

SERBIAN ACADEMY OF SCIENCES AND ARTS SASA Branch in Niš

Vlada B. Veljković, Ivana B. Banković Ilić, and Dejan U. Skala

HYDRODYNAMICS AND MASS TRANSFER
OF MULTIPHASE RECIPROCATING
PLATE COLUMNS



SERBIAN ACADEMY OF SCIENCES AND ARTS SASA Branch in Niš

Vlada B. Veljković, Ivana B. Banković Ilić, and Dejan U. Skala

HYDRODYNAMICS AND MASS TRANSFER OF MULTIPHASE RECIPROCATING PLATE COLUMNS

Academician Vlada B. Veljković, Serbian Academy of Sciences and Arts (SASA), Belgrade Prof. Ivana B. Banković Ilić, University of Niš, Faculty of Technology, Leskovac Prof. Dejan U. Skala, University of Belgrade, Faculty of Technology and Metallurgy, Belgrade

Hydrodynamics and Mass Transfer of Multiphase Reciprocating Plate Columns First edition, 2025

Publisher:

Serbian Academy of Sciences and Arts, SASA Branch in Niš

For Publisher:

Academician Vlada B. Veljković, SASA Branch in Niš

Reviewers:

Academician Velimir Radmilović, SASA, Belgrade, Serbia

Corresponding member Vladimir Srdić, SASA, Belgrade, and Faculty of Technology,

University of Novi Sad, Serbia

Prof. Nikola Nikačević, Faculty of Technology and Metallurgy, University of Belgrade, Serbia Prof. Dragan Govedarica, Faculty of Technology, University of Novi Sad, Serbia

Lector:

Žarko Radovanov

Printed by:

Unigraf - X-copy, Niš, Serbia

Circulation: 100

ISBN 978-86-6184-086-9

According to Decision 54/31 dated 27 June 2025, the Department of Technical Sciences of the Serbian Academy of Sciences and Arts has approved the manuscript for publication as a monograph.

CIP - Каталогизација у публикацији Народна библиотека Србије, Београд

66.063.8.021.3

VELJKOVIĆ, Vlada B., 1953-

Hydrodynamics and Mass Transfer of Multiphase Reciprocating Plate Columns / Vlada B. Veljković, Ivana B. Banković Ilić, and Dejan U. Skala. - 1st ed. - Belgrade

: SASA, Branch in Niš, 2025 (Belgrade: Unigraf - X-copy). - XIV, 245 str.: ilustr.; 25 cm

Tiraž 100. - Bibliografija: str. 205-232. - Registri.

ISBN 978-86-6184-086-9

- 1. Banković Ilić, Ivana B., 1963- [autor] 2. Skala, Dejan, 1946- [autor]
- а) Вибрационе мешалице -- Пренос масе

COBISS.SR-ID 175150857

PREFACE

This book delves into the intricate world of multiphase reciprocating plate columns as versatile contactors and reactors, covering their design, operation, and applications across thirteen comprehensive chapters. Drawing on the authors' earlier work, including a Serbian-language book from 2009, 1 recent reviews, 2,3 and many research articles, it provides a comprehensive resource for researchers, engineers, and practitioners keen on understanding and advancing in this field.

This book explores the complex realm of multiphase reciprocating plate columns, highlighting their design, operation, and applications across thirteen indepth chapters. Drawing on the authors' earlier work, including a Serbian-language book from 2009 and a recent review article, it provides a comprehensive resource for researchers, engineers, and practitioners aiming to deepen their knowledge and drive innovation in this field.

The introductory chapter defines mechanical agitation methods in multiphase systems, focusing on reciprocating plate columns and their role in enhancing mass transfer efficiency. It traces the historical development of these columns, highlighting their applications in fields like pharmaceuticals and biotechnology. Mechanical agitation methods, such as impellers or axially reciprocating plates, disperse drops and bubbles in turbulent liquid flows, increasing interfacial area and mass transfer rates. Reciprocating plate columns offer high mass transfer efficiency with low energy consumption, blending features of bubble columns and stirred reactors. Since Van Dijck's 1935 advancements, these columns have been widely adopted, especially in liquid-liquid dispersion, and continue to find new applications in diverse industries.

-

¹ Banković Ilić, I. B., Veljković, V. B., Skala, D. U. (2009) Hidrodinamičke i masenoprenosne karakteristike kolone sa vibracionom mešalicom za sisteme gas-tečnost i gas-tečnost-čvsta faza – monografija [Hydrodynamic and mass-transfer characteristics of reciprocating plate columns for gas/liquid and gas/liquid/solid systems], Leskovac: Tehnološki fakultet.

² Veljković, V. B., Banković-Ilić, I., Skala, D. (2024) Reciprocating plate column – fundamental research and application in Serbia from 1970 to 2020. Hemijska industrija 78, 187–203. https://doi.org/10.2298/HEMIND230320028V.

³ Banković-Ilić, I., Miladinović, M., Veljković, V. (2024) Continuous reciprocating plate and packed bed multiphase reactors in biodiesel production: Advancements and challenges. Hemijska industrija 78, 205–225. https://doi.org/10.2298/HEMIND230630010B.

Chapter two focuses on flow regimes and models in reciprocating plate columns. The reciprocating motion of perforated plates creates distinct flow patterns, with jets and surrounding vortices between adjacent plates, driving vigorous mixing through vertical liquid exchange and radial vortex formation. Turbulence at the jet-vortex interface enhances mixing and reduces dependence on molecular transfer. In gassed systems, gas bubbles undergo cyclic coalescence and dispersion. Regarding plate velocity and gas flow rate, four gas-liquid dispersion states can be formed: segregated, homogeneous, cellular, and slug bubbles. Liquid flow can be described by two models: the quasi-steady-state model, effective for large reciprocating amplitudes, and the acoustic flow model, for smaller amplitudes. Both models account for fluctuations in plate velocity, pressure drop, and power consumption during each reciprocation cycle.

In Newtonian liquids with turbulent flow (Re > 50), pressure variation and power consumption exhibit nearly quadratic and cubic relationships with reciprocating intensity, respectively; however, in laminar flow (Re < 10), these relationships are linear and quadratic. In gas-liquid systems, pressure variations and power consumption are lower than in single-phase systems due to reduced dispersion density and weaker interactions between the plates and the two-phase system. In liquid-solid systems, both pressure variation and power consumption increase with higher solid fractions, due to greater friction between solids, liquid, and plates. Gasliquid-solid systems exhibit lower pressure variations and power consumption than liquid-solid systems, due to lower dispersion density. The plate opening coefficient, representing resistance to fluid flow through plate openings, is key to determining pressure variation and power consumption in the column. In turbulent flow, it remains nearly constant and independent of the Reynolds number, while in laminar flow, it scales with the square root of the Reynolds number. Factors such as reciprocating amplitude and frequency, plate geometry, superficial gas and liquid velocities, and fluid properties influence this coefficient. Thus, experimental determination of the plate opening coefficient is vital for accurate power consumption calculations.

The next four chapters examine the reciprocating plate stack's motion, pressure variation, power consumption, and plate opening coefficient in single-liquid and multiphase systems. In multiphase systems, gas compressibility complicates pressure changes and power consumption, while the absence of a complete physical model hinders analysis in gas-liquid and gas-liquid-solid systems. Pressure variations at the column bottom arise from inertia, friction, gravity, and buoyancy, with periodic variations driven by non-steady plate motion. Overall liquid flow remains steady, with unsteady flow caused by plate movement. Key factors affecting

pressure variation, power consumption, and plate opening coefficient include liquid properties, operating conditions, plate geometry, and flow dynamics. In Newtonian liquids, turbulent flow (Re > 50) produces quadratic and cubic relationships between reciprocating intensity, pressure variation, and power consumption, while laminar flow (Re < 10) results in linear and quadratic relationships. Gas-liquid systems have lower pressure variations and power consumption due to reduced dispersion density and weaker plate interactions. In liquid-solid systems, higher solid fractions increase pressure variation and power consumption due to greater friction, while gas-liquid-solid systems exhibit lower values than liquid-solid systems. The plate opening coefficient, essential for calculating pressure variation and power consumption, remains constant in turbulent flow but scales with the square root of the Reynolds number in laminar flow. Experimental determination of this coefficient is crucial for accurate power consumption estimates.

Chapters seven and eight examine gas holdup and bubble size in gassed reciprocating plate columns. Various correlations have been proposed to relate gas holdup to operating conditions, fluid properties, and column geometry, with two main approaches: (1) using a modified hydrodynamic equation with relative velocity, and (2) employing an empirical equation based on power consumption and superficial gas velocity. The presence of solid particles significantly affects gasliquid dispersion by influencing bubble formation and coalescence, leading to higher gas holdup in a three-phase column compared to a two-phase column under identical conditions. Bubble size decreases with increasing dissipated energy, regardless of column diameter. As total specific power consumption (from mechanical agitation and aeration) increases, the Sauter bubble diameter decreases, following Kolmogorov's model of isotropic turbulence for water and glycerol solutions. However, this model is less accurate for *n*-butanol and sodium sulfite solutions. Higher superficial gas velocity increases gas holdup, while higher superficial liquid velocity reduces bubble size.

Chapter nine analyzes axial dispersion in reciprocating plate columns. While extensive research exists for axial dispersion in single-phase systems, recent studies on multiphase systems have produced conflicting results. Empirical correlations for calculating the axial dispersion coefficient in single-phase and gas-liquid systems are limited to the continuous (liquid) phase and specific column types. Variations among these correlations stem from differences in column geometry, plate design, and operating conditions and should be used with caution.

The next three chapters discuss the mass transfer properties in gassed reciprocating plate columns, including the mass transfer coefficient, specific interfacial area, and volumetric mass transfer coefficient. These properties are

influenced by reciprocating intensity, superficial gas and liquid velocities, and column geometry. When power consumption is below the 'critical' value, the mass transfer coefficient is proportional to power consumption raised to 0.25. Above the critical value, it decreases with increasing power consumption and is proportional to the Sauter bubble diameter. The mass transfer coefficient also decreases with increasing liquid and gas velocities. At low reciprocating intensities, the specific interfacial area may increase due to smaller bubbles or remain constant. At higher reciprocating intensities, the interfacial area increases with intensity, driven by higher gas holdup and smaller bubble size. Adding Rashig rings increases the specific interfacial area, while spheres have no effect. The volumetric oxygen mass transfer coefficient in reciprocating plate columns is generally higher than in bubble columns, air-lift reactors, and stirred tanks at the same superficial gas velocity.

The final chapter explores the use of continuous oscillatory reactors, specifically reciprocating plate and oscillatory flow reactors, in biodiesel production. These reactors offer advantages over conventional designs, including improved mixing, higher mass and heat transfer, compact size, and easier scale-up. They combine the continuous production benefits of tubular reactors with the effective mixing of stirred batch reactors. Even at low net flow rates, oscillatory reactors maintain plug flow patterns and high mixing intensity, which is controlled by oscillation or reciprocation, not by flow rate. Continuous reciprocating plate and oscillatory baffled reactors show significant potential to enhance biodiesel production through both homogeneous and heterogeneous catalysis, reducing costs and achieving high oil conversion under moderate conditions (e.g., lower temperatures, reduced methanol/oil ratios, shorter reaction times, and lower catalyst concentrations) compared to conventional batch reactors.

CONTENTS

PREFACE	i
1. INTRODUCTION	1
1.1 History of the reciprocating plate column origin and development	1
1.2. Classification of reciprocating plate columns	6
2. FLOW REGIME AND MODELS IN RECIPROCATING PLATE	
COLUMNS	17
2.1. Regime flow	17
2.2. Flow models	20
3. RECIPROCATING PLATE STACK VELOCITY	23
4. THE PRESSURE VARIATION AT THE BOTTOM OF	
RECIPROCATING PLATE COLUMNS	25
5. POWER CONSUMPTION IN RECIPROCATING PLATE COLUMNS	43
6. PLATE OPENING COEFFICIENT FOR RECIPROCATING PLATE	
COLUMNS	55
6.1. Influence of reciprocating intensity	61
6.2. Effect of superficial gas velocity	63
6.3. Effects of solid phase	64
7. GAS HOLDUP IN RECIPROCATING PLATE COLUMNS	67
8. BUBBLE SIZE IN GASSED RECIPROCATING PLATE COLUMNS	87
9. AXIAL MIXING	97
9.1. Flow models	97
9.1.1. Dispersion flow model	
9.1.2. Model of a series of <i>N</i> -compartments with ideal mixing	98
9.2. Determination of model parameters	
9.3 Coefficient of axial dispersion in reciprocating plate columns	99
9.4 Comparison of reciprocating plate columns with other multiphase	
devices	100
10. VOLUMETRIC MASS TRANSFER COEFFICIENT	
IN RECIPROCATING PLATE COLUMNS	105
11. SPECIFIC INTERFACIAL AREA IN RECIPROCATING PLATE	
	115
12. MASS TRANSFER COEFFICIENT IN RECIPROCATING PLATE	
COLUMNS	123
13. APPLICATION OF OSCILLATORY REACTORS IN BIODIESEL	
PRODUCTION	
13.1 Reciprocating plate column-type reactors in biodiesel production	130

13.1.1. Hydrodynamics of reciprocating plate reactors used for biodiesel	
production	138
13.1.1.1. Flow behavior and regime	138
13.1.1.2. Pressure variation at the reactor bottom and power	
consumption	140
13.1.1.3. Dispersed phase holdup	145
13.1.2. Drop size and drop size distribution	146
13.1.2.1. Non-reactive systems	146
13.1.2.2. Reactive systems	153
13.1.3. Specific interfacial area	156
13.1.4. Overview of previous research on biodiesel production	
in reciprocating plate reactors	156
13.1.5.1. Effect of operational parameters on biodiesel production	157
13.1.5.2. Two-step biodiesel production by a continuous base-catalyzed	
methanolysis of vegetable oils	160
13.1.5.3. Biodiesel production in a continuous pilot reciprocating	
plate reactor	161
13.1.5. Cosolvents in transesterifications in continuous flow reactors	163
13.3.6.1. Mean drop size and drop size distribution	166
13.3.6.2. Kinetic modeling of the potassium hydroxide-catalyzed	
methanolysis of sunflower oil in a reciprocating plate	
column in the presence of a cosolvent	169
13.1.6. Biodiesel production from waste pig-roasting lard in	
a continuous reciprocating plate reactor	178
13.1.7.1. Statistical modeling and optimization	181
13.1.7.2. Kinetic analysis	183
13.1.7. Comparison of reciprocating plate reactors with other	
reactor types	192
13.2.8. A short overview of other applications of reciprocating plate	
reactors in Serbia	194
13.2 Oscillatory flow reactors in biodiesel production	195
13.2.1. Reactor design and flow regime	195
13.2.2. Overview of previous research on biodiesel production	
in oscillatory flow reactors	197
13.2.3. Analysis of homogeneous transesterification reactions	199
13.2.3.1. Base catalysis	199
13.2.3.2. Acid catalysis	202

13.2.4. Analysis of heterogeneous transesterification reactions	202
13.2.4.1. Base catalysis	202
13.2.4.1. Acid catalysis	203
13.2.5. Advanced oscillatory flow reactor technology	
REFERENCES	205
List of Tables	233
List of Figures	235

Nomenclature

a, m⁻¹ Specific interfacial area *A*, m Amplitude of reciprocating motion $A_{\rm c}$, m² Cross-sectional area of the column A_{cr} , m Critical amplitude of reciprocating motion Af, m/s Reciprocating intensity $c_{\rm A}$, mol/m³ Triacylglycerol concentration in the oil phase c_{Ao} , mol/m³ Initial concentration of triacylglycerols c_R , mol/m³ Concentrations of methanol $c_{\rm B,o}$, mol/m³ Initial concentration of methanol $c_{A,s}$, mol/m³ Triacylglycerol concentrations on the interfacial area c_R , mol/m³ Concentrations of fatty acid methyl esters c_S , mol/m³ Concentrations of glycerol C1, C2, 1 Integration constants (Equations 13.27, 13.30) C_0 , 1 Plate opening coefficient $C_{\rm o}(t)$, 1 Instantaneous value of the plate opening coefficient \overline{C}_{α} , 1 Mean value of the plate opening coefficient $C_{a,av}$, 1 Time-averaged plate opening coefficient $C_{o,\max}$, 1 Maximum value of the plate opening coefficient $(C_{o,av})_{\downarrow \downarrow}$, 1 Plate opening coefficient calculated from the processed pressure signals at the column bottom $(C_{o,av})$, 1 Plate opening coefficient determined from the recorded pressure signals at the column bottom C_{Ψ} , C_{Π} , 1 Parameters of Equation (13.9) d, m Equivalent spherical diameter $d_{\rm av}$, m Average plate opening diameter $d_{\rm d}$, m Diameter of vibration disc, also diameter of the opening of the gas distributor d_i , m Drop diameter $d_{\rm o}$, m Plate opening diameter $d_{3,2}$, m Sauter-mean diameter D_i , m²/s Axial dispersion coefficient $D_{\rm c}$, m Column diameter E, min⁻¹ Residence time distribution Normalized form of the function of the residence time distribution density E_{Θ} , 1 f, s⁻¹ Frequency of reciprocating motion Friction term of the pressure variation at the column bottom, $f_{1,2}$, Pa Equation (4.8) $F_{\rm s}$, N Force exerted by the perforated plate stack on the system

F(s), 1 Laplace transform of the residence time distribution density F_p , N Force of interaction between the perforated plate stack and the system $F_{\rm b}$, N Buoyancy force exerted by the system on the perforated plate stack Gravitational acceleration g, m/s² h, m Distance between two reciprocating plates; interbaffle space; the reactor length, Equation (13.21) $h_{\rm o}$, m Total reactor height I=Af, m/s Vibration intensity $k_{\rm app}, k_{\rm m}, \min^{-1}$ Apparent pseudo-first order reaction rate constant k_c , m/s Triacylglycerol mass transfer coefficient $k_{\rm l}$, m/s Liquid mass transfer coefficient k_2 , m³/mol·min Rate constant of the irreversible pseudo-second-order reaction, Equation (13.26) \vec{k}_2 , \vec{k}_2 Reaction rate constants for the forward and reversible reactions, Equation (13.28) k_1a, k_2a, s^{-1} Volumetric mass transfer coefficient $K = \overline{k}_2/\overline{k}_2$, 1 Reciprocal value of the equilibrium constant for the overall methanolysis reaction, Equation (13.30) K, 1 Model parameter that takes the triacylglycerol affinity to the catalytic species (methoxide ions) l, m Length of the tie-rod l_b , m Mixing path caused by surface tension $l_{\rm c}$ / m Column length; the distance between sections 1 and 2, Fig. 4.1.a, Equation (4.5) $l_{\rm m}$, m Mixing path $m_{\rm e}$, kg Mass of emulsion $m_{\rm l}$, kg Mass of the liquid $m_{\rm s}$, kg Mass of the perforated plate stack $M = c_{Ao}/c_{Bo}$, 1 Initial molar ratio of triacylglycerol to methanol n_i , 1 Number of drops with diameter d_i Number of discs $n_{\rm d}$, 1 $n_{\rm p}$, 1 Number of plates N, 1 Number of sections with ideal mixing p, Pa Instantaneous pressure p_1, p_2, Pa Pressures at the top and bottom of the column, respectively Δp , Pa Instantaneous pressure variation at the column bottom Δp_{av} , Pa Time-averaged pressure fluctuation at the reactor bottom Δp^* , Pa Total pressure fluctuation at the bottom of the reactor Δp_{\min} , Pa Pressure variations at the column bottom corresponding to the upstroke

and downstroke of the plate stack

 Δp_{max} , Pa Pressure variations at the column bottom corresponding to

the downstroke of the plate stack

P, W Instantaneous power consumption P^* , W Maximum power consumption P_{av} , W Time-average power consumption

 P_{ac} , W Average power consumption (acoustic model)

 $P_{\rm g}^*$, W Maximum gassed power consumption

 $P_{g,cr}^*$, W Critical maximum gassed power consumption

 $P_{\rm g,p}$, W/m³ Specific pulsation power consumption $P_{\rm g,t}$, W/m³ Total pulsation power consumption q, 1 Backmixing through perforated plates

 Q_g , m³/h Gas flow rate Q_b , m³/h Liquid flow rate r, m Radius of the disc

s, 1 Ratio of the radius (equal to the amplitude of reciprocating motion A)

of the disc to the length of the tie-rod (A/l); Laplace operator

 $s_{\rm e}$, m Equivalent plate length

t, s Time

T, s Period of time u, m/s Superficial velocity

 u_c , m/s Superficial continuous phase velocity u_d , m/s Superficial dispersed phase velocity

 $u_{\rm g}$, m/s Superficial gas velocity

 $u_{g,o}$, m/s Superficial gas velocity in the opening of the distributor

*u*_l, m/s Superficial liquid velocity

 $u_{l,o}$, m/s Local instantaneous liquid velocity through the plate openings

 u_r , m/s Relative velocity u_R , m/s Slip velocity

 u_s , m/s Reciprocating plate stack velocity

 $u_{s,m}$, m/s Maximum reciprocating plate stack velocity

 U_0, U_1, U_2 Function of the Laplace transformation of the residence time distribution

density

v_o, mL/min Volumetric flow rate

V, m³ Volume

 $V_{\rm d}$, m³ Total dispersion volume

 $V_{\rm g}, \, {\rm m}^3$ Gas volume $V_1, \, {\rm m}^3$ Liquid volume

 x_4 , 1 Conversion degree of triacylglycerols

 x_{Ae} , 1 Equilibrium degree of triacylglycerol conversion

y, m Displacement of the reciprocating plate stack during one cycle

YY, YZ, 1 Function of the Laplace transform of the residence time distribution

density

z, m Distance between the center of the disc and the starting end of the tie-rod

 z_1, z_2, m Top and bottom of the column, respectively

Z, 1 Morton's number

Greek symbols

 α , 1 Backmixing coefficient

 δ , m Plate thickness

Δ Parameter, Equation (13.30) D_t , m²/s Axial dispersion coefficient ε, 1 Fractional free plate surface

 ε_b , W/kg Specific dissipated energy for overcoming surface tension forces

 ε_d , 1 Dispersed phase holdup

 $\varepsilon_{\rm g}$, 1 Gas holdup

 $\varepsilon_{g,0}$, 1 Gas holdup without pulsation

 $\varepsilon_{\rm s}$, 1 Solid phase content

 ε_t , W/kg Specific total dissipated energy

 \mathcal{E}_{τ} , m²/s Eddy diffusivity μ , Pa·s Dynamic viscosity $\rho_{\rm e}$, kg/m³ Density of emulsion $\rho_{\rm l}$, kg/m³ Liquid density

 ρ_s , kg/m³ Density of the perforated plate stack $\Delta \rho$, kg/m³ Density difference between phases

 σ , N/m Liquid surface tension

 σ_{θ}^{2} , 1 Variance of the retention time distribution

τ, s Residence time

 θ Mean change in the angular distance of the disc;

intensity of backmixing, Equation (9.1); normalized time

 ω , s⁻¹ Angular velocity $(2\pi f)$

Ψ, W/kg Specific power consumption, Equation (13.9)

Dimensionless criteria

$$Fr = \frac{(Af)^2}{gd_o}$$
 Froude number

$$\Phi = \frac{P}{n_p \rho_l (2Af)^3 D_c^2}$$
 Power number

$$Ga = \frac{d_o^3 g \rho^2}{\mu^2}$$
 Galileo number

 $Pe = \frac{u_l l_c}{D_l}$ Peclet number

 $Re = \frac{\rho_i u_i D_c}{\mu_l}$ Reynolds number

 $Re_0 = \frac{2A\pi f \rho_i d_0}{\mu_i}$ Reciprocation Reynolds number

 $Z = \frac{\rho_i \sigma^3}{g u^4}$ Dimensionless number

 $We = \frac{(Af)^2 d_o \rho}{\sigma}$ Weber number

Abbreviations

ALCDT Air-lift reactors with concentric draft tubes
ALELC Air-lift reactors with external loop circulation

ANN Artificial neural network

AM Axial mixing BC Bubble column

BRPC Baird-type reciprocating plate column

CMC Carboxymethylcellulose

DAG Diacylglycerol

DBSA 4-Dodecylbenzenesulfonic acid

FAME Fatty acid methyl ester FV Flow visualization

GIAP Plate with rectangular openings and a drain HRRPC Hybrid rotating-reciprocating plate column

HT Heat transfer i.d. Internal diameter

KRIMZ Plate with rectangular openings without a drain

KRPC Karr-type reciprocating plate column

MAG Monoacylglycerol

MRPD Mean relative percentage deviation

MT Mass transfer

OFR Oscillatory flow reactor

PBC Pulsation column

PRPC Procházka-type reciprocating plate column

PP Degree of polymerization

Re Reynolds number

RPR Reciprocating plate reactor
RSM Response surface methodology

SP Segmental passages
ST Stirred tank reactor
TAG Triacylglycerol

THF Tetrahydrofuran

VDC Vibrating disc column WCO Waste cooking oil

Subscripts

av Average

c Continuous phase

cr Critical

d Dispersed phase

e Emulsion g Gas l Liquid

max Maximum value

mod Value corresponding mathematical model

puls Pulsation s Solid

1. INTRODUCTION

Various mechanical agitation methods enhance mass transfer in multiphase contactors and reactors, significantly impacting their efficiency. This mechanical agitation is typically achieved using an impeller mounted on a rotating shaft or plates affixed to an axially reciprocating carrier. By imparting external energy to the multiphase system, mechanical agitation promotes the dispersion of drops or bubbles within a turbulent liquid flow environment. It, in turn, leads to a notable increase in interfacial area, volumetric mass transfer coefficient, and, consequently, interfacial mass transfer rates. Furthermore, solid particles are evenly dispersed throughout the suspension.

One standout example among multiphase contactors, which boasts both low energy consumption and a high interfacial mass transfer rate, is the reciprocating plate column.⁴ In constructing a reciprocating plate column, a column features numerous perforated plates securely fastened to a shared carrier, which can reciprocate in an up-and-down motion. This design optimally capitalizes on the advantageous effects of mechanical mixing while minimizing or eliminating any detrimental ones. Reciprocating plate columns, thus, combine the favorable attributes of traditional columns and stirred reactors, presenting an appealing alternative to conventional stirred vessels equipped with rotary stirrers.

1.1 History of the reciprocating plate column origin and development

As documented in his patent, the pioneering researcher Van Dijck made significant advancements in oscillatory fluid flow in 1935 (Van Dijck, 1935). His work introduced two notable methods:

(1) Hydraulic pulsation: This method involves inducing oscillatory fluid flow by pulsating one of the phases using an external mechanism while maintaining the internal structure of the column, including perforated plates and filling, in a steady-state condition. This technique, known as 'pulsed columns,' was originally designed for applications in the nuclear industry.

⁴ The terms 'reciprocating plate column' and 'reciprocating plate reactor' will be used for non-reactive and reactive systems, respectively.

(2) Axial reciprocation: Van Dijck's second method revolves around the axial reciprocating motion of a set of perforated plates within the column, commonly called reciprocating plate columns. Unlike pulsed columns, reciprocating plate columns have found their primary utility in the pharmaceutical industry (Baird et al., 1996).

In reciprocating plate columns, the oscillatory fluid flow is achieved by displacing the liquid through the openings in the plates, resulting in efficient mixing and mass transfer. This innovation has significantly impacted the nuclear and pharmaceutical industries by providing tailored solutions for different applications.

The reciprocating plate column remained largely overlooked for two decades until 1959, when Karr introduced a groundbreaking laboratory extraction column featuring perforated plates with a significantly expanded free surface area. This innovation, known as the Karr reciprocating plate extraction column (Karr, 1959), sparked renewed interest in reciprocating plate column technology. Subsequently, the utilization of reciprocating plate columns began to gain traction, particularly in the capacity of extractors. One of the key advantages of reciprocating plate columns is their ability to achieve uniform liquid-liquid dispersion with minimal axial mixing, requiring relatively modest external energy input compared to pulsation columns.

In the 1960s, reciprocating plate columns started to garner attention and application in absorption columns. Notably, Jealous and Johnson (1955) contributed to this development by defining pressure variations at the column bottom and quantifying the power consumption based on a quasi-steady-state flow model.

The seventies of the last century marked a period of intensified research that has continued to the present day. This ongoing exploration has centered on unraveling the hydrodynamic and mass-transfer characteristics of multiphase systems, especially their potential application as reactors for various aerobic bioprocesses and biodiesel production. Reciprocating plate columns have emerged as versatile tools in these endeavors, offering substantial promise for advancing these critical fields of study.

In Serbia, the initial investigations into Karr-type reciprocating plate columns were conducted during the 1970s by research teams hailing from the 'Boris Kidrič' Institute in Vinča and the Faculty of Technology and Metallurgy at the University of Belgrade (Kažić, 1979; Pavasović, 1975). Their research primarily focused on several key aspects, including the characterization of pressure variations at the column bottom and the mean power consumption in single-phase and two-phase (liquid-liquid) flows. They also delved into understanding the intricate mechanisms governing drop movement, dispersion, coalescence, and the occurrence of column flooding.

As the 1980s dawned, the application of Karr-type reciprocating plate columns expanded beyond liquid-liquid extraction columns. The Pavas in Belgrade and the Pharmaceutical and Chemical Products Factory Zdravlje in Leskovac employed these columns as absorption units (Skala, 1980; Veljković, 1985). The subsequent decades, spanning the 1990s and 2000s, have witnessed a continuation of this research journey, with contributions from the Faculty of Technology in Leskovac at the University of Niš.

During this period, significant strides were made in comprehending phenomena associated with fluid flow in the presence of solid particles, including spheres and Rashig rings. Researchers also explored oxygen mass transfer within multiphase systems and investigated the influence of the rheological properties of liquids on the hydrodynamics of reciprocating plate columns featuring various geometries. These efforts were underscored by a range of scholarly works authored by experts in the field (Aleksić, 2006; Banković-Ilić, 1993, 1999; Naseva, 2002; Nikolić, 2003; Stamenković et al., 2010a; Stamenković, 2005, 2014; Vasić, 2006).

The dynamic up-and-down motion of reciprocating plates within reciprocating plate columns offers distinct advantages over other systems. Compared to bubble columns, whether equipped with liquid circulation or not (Boyle, 1975; Gomaa et al., 1991), and stirred tanks, reciprocating plate columns demonstrate notably higher gas holdup. Additionally, they exhibit a substantial specific gas-liquid interfacial area (Al Taweel et al., 1995; Yang et al., 1986a). Reciprocating plate columns stand out due to several key features:

- (1) Reduced backmixing: reciprocating plate columns exhibit diminished backmixing tendencies (Skala, 1980). This characteristic enables a more controlled and efficient mixing process.
- (2) Extended gas bubble retention: reciprocating plate columns excel in prolonging the retention of gas bubbles within the dispersion. This extended interaction time between phases enhances mass transfer and reaction efficiency.
- (3) Enhanced contact area: reciprocating plate columns facilitate a greater contact area between phases while mitigating shear forces caused by the movement of perforated plates (Lo and Procházka, 1983). This balance optimizes the interfacial mass transfer process.
- (4) Ease of maintenance: reciprocating plate columns are known for their simple maintenance and uncomplicated construction (Lo and Procházka, 1983).
- (5) Scalability: reciprocating plate columns offer an advantage in scalability, with straightforward procedures for upscaling the system to accommodate larger fluid flows and capacities (Lo and Procházka, 1983).

In summary, reciprocating plate columns present a compelling choice for applications where gas-liquid interactions, mass transfer efficiency, and operational simplicity are paramount considerations. Their distinctive design and performance characteristics have positioned them as a preferred technology in various industrial processes.

Previous investigations encompassed a diverse range of reciprocating plate columns, featuring varying types and diameters from 2.5 to 30 cm. The perforated plates within these reciprocating plate columns exhibited openings ranging from 0.3 to 1.5 cm, contributing to fractional-free plate surfaces from 9% to 61%. During the research conducted in the 1980s, these studies predominantly employed 'pure' liquids. However, there has been a notable shift in recent years towards intensively examining gas-liquid, gas-liquid-solid, and liquid-liquid systems within reciprocating plate columns.

As for the liquid phase, researchers predominantly utilized Newtonian liquids, with water being the most commonly employed liquid. Nevertheless, certain studies used liquids with varying rheological characteristics and distinct physical properties. The solid phase in these investigations often featured spherical particles and Rashig rings. This research has been conducted globally, spanning several countries, including Canada, the United States, India, Russia, Japan, the Czech Republic, and Serbia, as detailed in Table 1.1. This international collaboration has enriched the understanding of reciprocating plate columns across various applications and contexts.

Reciprocating plate columns have found widespread application across many industries globally, including the chemical sector, hydrometallurgy, wastewater treatment, biotechnology, and pharmaceutical technology, as outlined in Table 1.2. Their versatility is exemplified through various noteworthy applications:

- 1) Aerobic wastewater treatment: reciprocating plate columns have been successfully employed in aerobic wastewater treatment processes, as evidenced by the work of Brauer (1991), Brauer and Sucker (1979), and Vogelpohl (1985).
- 2) Bioprocesses: They play a pivotal role in biosynthesis activities, such as pullulan biosynthesis (Audet et al., 1996; Lounes et al., 1995), dextran and enzyme production (Veljković, 1985; Veljković et al., 1990), antibiotic synthesis (Brauer, 1991; Reschke and Schügerl, 1985), citric acid production (Brauer, 1991), and ethanol manufacturing (Brauer, 1991; Nikolić, 2003).
- 3) Ester saponification reaction: reciprocating plate columns have been utilized effectively in ester saponification reactions (Harvey et al., 2003).

Table 1.1 Types of reciprocating plate columns (Banković-Ilić et al., 2009).

Plate туре	Reciprocating element	Characteristics	Country
Karr-type	Plates with	Column diameter up to 1.7 m	USA,
reciprocating	large openings	Large fractional free plate surface (50–60%)	Canada,
plate column	('open' type)	Large plate opening diameter (10–16 mm)	Western
		Plate modification – with a central opening	Europe,
		Inserted buffers along the column of larger	India,
		diameter reduce the radial flow non-uniformity	Serbia
		Operating mode: homogeneous	
Procházka-type	Plates with	Column diameter up to 1.2 m	Czech
reciprocating	downcomers	Small fractional free plate surface (4–30%)	Republic,
plate column	or segmental	Small plate opening diameter (2–5 mm)	Canada
	passages	With a drain in the form of a pipe or a segmental	
		passage in the form of a cut-off part of the plate	
		(free surface fraction of 10–25%)	
		Movement of plates: all in the same phase or every	
		other with a phase shift of 180°	
		Operating mode: segregated and homogeneous	
Vibrating disc	Discs	Discs without perforations	Japan
column		The fractional free plate surface depends on the disc	
		diameter-to-column diameter ratio (4-0.78%)	
		Static buffers between every two discs	
Karpačeva and	Plates with	Column diameter up to 1.5 m, height up to 11 m.	Former
Gorodetskiy-	rectangular	Fractional-free plate surface about 45%.	USSR
type	openings	Rectangular openings with bent ends that divert	
reciprocating		fluid flow radially to reduce axial mixing	
plate column		Plates with rectangular openings without (KRIMZ)	
Hybrid rotating-	Plates with	or with (GIAP) a drain Column diameter 10 cm, height 1.2 m.	India
reciprocating	uniform	The hybrid rotating and reciprocating motion of	maia
plate column	perforation	the plate stack is achieved through a bevel gear	
plate column	perioration	arrangement. The reciprocating motion is induced	
		by the central shaft, milled at the top, and	
		connected to an eccentric mechanism on the	
		vertical gear. Meanwhile, the rotating motion is	
		driven by the horizontal gear, which turns the	
		inner shaft as the vertical gear rotates.	

Reciprocating plate columns owe wide-ranging applications to their favorable hydrodynamic properties and efficient facilitation of oxygen mass transfer from the gaseous to the liquid phase. Consequently, they are classified as cutting-edge, highly efficient bioreactors (Deshusses, 1997). Particularly, reciprocating plate columns excel in processing heavily loaded industrial wastewater (Vogelpohl, 1985). These attributes have proven invaluable for enhancing growth and production bioprocesses involving fungi such as *Cyathus striatus* and *Aspergillus niger* (for the antibiotic striatine and citric acid production, respectively) and bacteria like *Zymomonas mobilis* (ethanol production) as highlighted by Brauer (1991).

Table 1.2 Application of reciprocating plate columns.

Plate	Application	Reference
Karr type	Copper extraction	Sharma and Baird (1978)
	Lysine biosynthesis	Šerbak et al. (1978)
	Treatment of wastewater	Brauer and Sucker (1979)
	Extraction of the product from the fermentation liquid	Karr et al. (1980)
	Penicillin extraction	Reschke and Schügerl (1985)
	Biosynthesis of dextransucrase	Veljković (1985), Veljković et al. (1990)
	Production of antibiotics, ethanol, and citric acid	Brauer (1991)
	Fermentation processes	Lounes et al. (1995)
	Fermentation of pullulan	Audet et al. (1996)
	Ester saponification reaction	Harvey et al. (2003)
	Rare earth separation and recovery	Liao et al. (2005)
	Extraction of phenol from water	Yung et al. (2012a,b,c)
	Caffeine extraction	Hu et al. (2003)
	Alcoholic fermentation with immobilized yeast cells	Nikolić (2003)
	Extraction of natural alkaloids	Wu et al. (2022)
	Biodiesel production	Stamenković et al. (2010a),
		Stamenković. (2014),
		Miladinović et al. (2019),
		Banković-Ilić et al. (2015)
Procházka	Production of ephedrine and erythromycin	Cited according to Baird et
type	Extraction of phenol and nitro-aromatic derivatives from wastewater	al. (1994)
KRIMZ,	Caprolactam extraction with organic solvents	Cited according to Baird et
GIAP	Extraction of cyclohexanone and cyclohexanol with benzene	al. (1994)

Abbreviations: GIAP – the plate with rectangular openings with a drain, and KRIMZ – the plate with rectangular openings without a drain.

Furthermore, reciprocating plate columns offer extensive possibilities for utilization as multiphase reactors, where the solid phase can take the form of catalyst particles, particle substrates, or carriers for immobilized enzymes or living cells, as indicated by Banković Ilić et al. (2009). This adaptability positions reciprocating plate columns as versatile tools for diverse applications across various industries.

1.2. Classification of reciprocating plate columns

Reciprocating plate columns exhibit variations based on several critical factors, including the type and geometry of the vibrating components and the inclusion of static buffers. The vibrating elements, typically in the form of plates or discs, may possess segmental passages and drains. Furthermore, the perforations within these vibrating elements come in diverse shapes and sizes. Depending on the specific plate design, as outlined by Lo et al. (1992), reciprocating plate columns can be

categorized into four distinct groups (Baird et al., 1994), as illustrated in Figures 1.1 and 1.2. A specialized hybrid device combines the rotating and reciprocating motions of the plate stack, facilitated by a bevel gear arrangement (Dhanasekaran and Karunanithi, 2012a,b,c,d). The reciprocating motion is induced by the central shaft, which is milled at the top and linked to an eccentric mechanism on the vertical gear. Simultaneously, the rotating motion is driven by the horizontal gear, which rotates the inner shaft as the vertical gear turns.

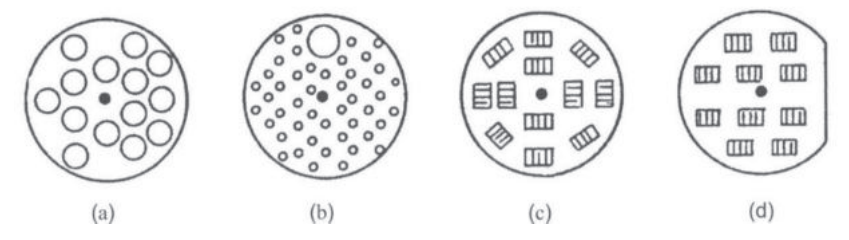


Figure 1.1 Types of reciprocating plate column plates (Lo et al., 1992): (a) Karr type, (b) Procházka type, (c) Karpacheva and Gorodetsky type without the drain on plates – KRIMZ, and (d) Karpacheva and Gorodetsky type with the drain on plates – GIAP.

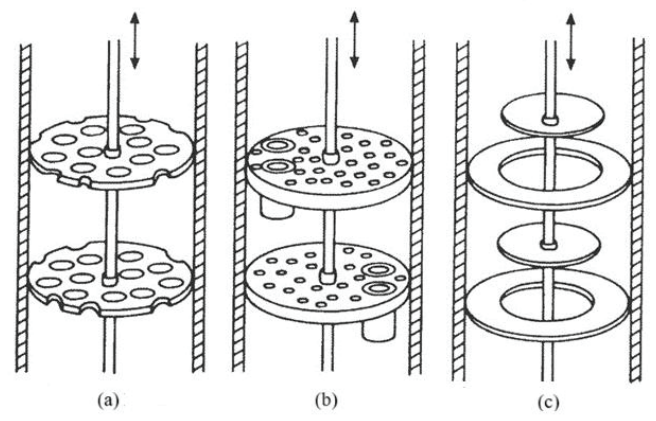


Figure 1.2 Types of reciprocating plate column (adapted from Baird et al., 1994): (a) Karrtype reciprocating plate column (KRPC), (b) Procházka-type reciprocating plate column (PRPC), and (c) vibrating disc column (VDC).

Table 1.3 provides an overview of prior research, highlighting essential geometric characteristics and operational conditions. These investigations have revealed that the hydrodynamic and mass-transfer characteristics within reciprocating plate columns are contingent on various factors. These include the reciprocating intensity, which is the product of amplitude and frequency, superficial gas velocity, the presence and concentration of solid phases, liquid properties, and the geometric attributes of the devices and plates. Understanding these intricate relationships is pivotal in optimizing the performance of reciprocating plate columns across a spectrum of applications.

Table 1.3 Overview of previous research related to the reciprocating plate column.^a

Continuation of Table 1.3 Overview of previous research related to the reciprocating plate column.

Reference	Aleksić (2006), Aleksić et al. (2002a,b; 2003, 2006)	Masuik and Rakoczy (2007)	Rama Rao and Baird (1986)	Gomaa et al. (1991)	Baird et al. (1992)	Gomaa and Al Taweel (2005)	Boyle (1975)
Subject	$\Delta p,P,arepsilon_{ m g},$ MT	<i>P</i> , MT, HT	$d\nabla$	$arepsilon_{ m g}, d_{ m b}, { m MT}$	AM	AM	Δp , P , ε_g , a , ΔM
ug cm/s	0.5–1.5	pu	0.04-	0-5.65	I	0-0.3	10-30 1.8-11
f Hz	2–6	0.124	0.75-	5-30	20- 100	0-25	10-30
A mm	2.35	0.02-	7–32	16- 32	pu	0-3.2	3.2-63.2
, w	0.263 0.319 0.454	pu	0.09	0.38	pu	0.38	0.15-
d_o cm	8.0	0.5–6	0.3-0.8	0.16	0.061 0.099	0.16	0.16-
h cm	v	0.04	5.6	$\frac{10}{30}$	15	0.1	5
n_p	15	1-5	2-10	pu	6	pu	10
l _c m	1.05	0.678 1–5	-	pu	6.0	2.22	1.47
D_c	9.2	0.248	9.3	10	5	0.1	10
Phase flow	Batch	Batch	→ ←	$\; \stackrel{\rightarrow}{\leftarrow} \;$	$\overset{\rightarrow}{\leftarrow}$	$\overset{\rightarrow}{\leftarrow}$	Batch or ↑
System	Water Air-water Air-water-solid Air-CMC solution (1%)- solid	Sugar beet molasses, machine oil, glycerol, and water	Air-water	Water - air	Water-kerosine	Air-water	Water, Air-water Batch or ↑↓
Type	RPC	RPC	RPC without SP	PRPC	PRPC	PRPC with SP	PRPC RPC without SP

Continuation of Table 1.3 Overview of previous research related to the reciprocating plate column.

	communication of the control of the	1011100	ord to	2001	110100	50250	21 211 22	na ordin	ma bun	2000			
Type	System	Phase	D_c	l_c	n_p	h	d_o	S	A	f	u_{g}	Subject	Reference
		flow	cm	m		cm	cm		mm	Hz	cm/s		
PRPC	pu	Batch or	10	1.47	10	10	0.32	0.15-	1.8-	pu	I	$d\nabla$	Landau et al.
without SP		$\overset{\rightarrow}{\leftarrow}$						67:0	6.9				(1976)
PRPC and RPC without SP	Air-water	→ ←	10	1.47	pu	pu	0.16-	0.15-0.23	1.6 - 3.2	5-30	<17	AM, a	Al Taweel et al. (1995)
BRPC	Water	Batch	19.4	6.0	5	5_	4	0.169	5-20	0.6 - 3	1	P	Baird and
						20	8 12	0.211					Rama Rao (1995)
BRPC	Air-water	Batch	15	3.96	1-10	22.5	7	0.235	1–10	2–5	<46.6	$P, \varepsilon_{ m g}$	Baird et al. (1996)
BRPC	Air-water	Batch	19	6.0	pu	19	6	pu	0-21	0.25-	pu	FV, MT	Mackley et al. (1998)
KRPC	Water	Batch	14.96	pu	47	5	1.43	0.531	3.17-	0.5-	I	P	Hafez and
					95 8 12	2.5 25 20	1.47	0.23	12.7	6.9			Baird (1978)
KRPC	Water	Batch	2.54	2.11	78	2.54	8.0	0.51	5- 19.6	0.5-	I	$\Delta p, P$	Kažić (1979)
KRPC	Water-toluene	pu	2.54	2.71	18	2.54	pu	0.51	20.5	0.275	I	$d\nabla$	Stevanović et al. (1980)
KRPC	Water, Airsulfite solution	→ ←	2.54	2.14	9	2.6	9.0/8.0	0.51	0.65-	0.483	0.8–3.2	$\begin{array}{l} \text{AM, } \varepsilon_{\text{g}}, \\ \text{MT} \end{array}$	Skala (1980)

Noh and Baird Veljković and Veljković and Rama Rao et Skala (1985) Skala (1986) Chen et al. Yang et al. Skala et al. Yang et al. Reference al. (1983) Veljković Skala and Veljković (1986a) 1986b(1987a)(1981)(1984)(1985)(1986) $\Delta p. P. \varepsilon_{\rm g}$ Δp , P, $\varepsilon_{\rm g}$ AM, MT $\Delta p, \, \varepsilon_{\rm g}, \, a$ Δp , MT Subject Δp , $\varepsilon_{
m g}$ $\varepsilon_{\rm g}, d_{\rm b}$ \overline{AM} MT $k_{1}a$ ಭ 0.8;2.90.72 - 50 - 8.220 - 14.30.027 -0.275 -0.275 u_g cm/s 2.75 \ \ \ 5.1 pu Continuation of Table 1.3 Overview of previous research related to the reciprocating plate column. 1.83-1 - 101 - 101.83 <10 0-5 pu pu <22.5 1 - 101 - 100.65 63.5 0.65 -18.8 <20 and pu pu 0.41 -60.00.29 0.53 0.53 0.41 0.53 0.41 0.61 0.51 0.51 0.51 0.3 - 0.80.7/0.5 9.0/8.0 0.7/0.5 9.0/8.00.7/0.5 9.0/8.01.37 1.27 cm 1.5 1.5 d_o 2.54 2.54 2.54 2.54 2.54 2.54 5.08 5.08 5.08 cm 5.6 2.5 5.0 5.0 2 - 1064 29 84 33 32 6533 84 84 33 1.46 2.14 3.96 3.96 ca N 4 2.54 2.54 2.54 5.08 5.08 2.54 5.08 2.54 9.3 cm D_c Batch Phase flow $\overset{\rightarrow}{\leftarrow}$ $\overset{\rightarrow}{\leftarrow}$ _ $\overset{\rightarrow}{\leftarrow}$ _ _ + $\overset{\rightarrow}{\leftarrow}$ dextran solutions sucrose solution, sucrose solution sucrose, sulfate, Air-kerosine fructose, and mixtures of Water, air-Water, air-Water, air-Tap water Air-water Air-water Air-water Air-water Air-water air-water Air-water sucrose, System Water KRPC KRPC KRPC KRPC KRPC KRPC KRPC KRPC KRPC KRPC

Rama Rao and Veljković and Veljković and Baird (1988) Skala (1988) Skala (1989) Veljković et Sundaresan and Varma Rama Rao Reference Baird and Skala and Veljković Baird and al. (1990) Rohatgi (1990a)(1988)(1988)(1989) Δp , $\varepsilon_{\rm g}$, $d_{\rm b}$ AM, MT Subject $arepsilon_{
m g}, d_{
m b}$ MT MT k_1a ŝ a0.6 - 4.60.8 - 3.10 - 0.990.2 - 1 u_g cm/s 3 5 pu pu Continuation of Table 1.3 Overview of previous research related to the reciprocating plate column. 0.75-1.6-4 <6.2 <6.2 6.25 0-5) Hz pu 0-2022.5 22.5 <20 mm <20 14-25 pu 50 \forall -60.00.306 0.57 0.57 0.51 0.51 0.57 0.51 0.41 0.51 0.41 ω 9.0/8.0 9.0/8.0 0.7/0.5 9.0/8.09.0/8.0 0.7/0.5 0.3-0.65 d_o 4. 4. cm 5.08 5.08 2.54 2.54 5.08 2.54 5.08 7.75 5.2 7.75 5.6 h cm 19 54 28 19 6533 65 32 65 33 6533 18 n_p 6 2.45 2.45 pu l_c N 2 2 a 5.08 2.54 2.54 2.54 2.54 5.08 cm 9.3 D_c Batch or Batch Phase flow $\overset{\rightarrow}{\leftarrow}$ $\stackrel{\rightarrow}{\leftarrow}$ $\stackrel{ o}{\leftarrow}$ $\overset{\rightarrow}{\leftarrow}$ $\overset{\rightarrow}{\leftarrow}$ $\stackrel{ o}{\leftarrow}$ $\overset{\rightarrow}{\leftarrow}$ sucrose solution, sulfite solutions sucrose, sulfate O₂-sucrose and Water, air, N2, fructose, and fermentation mixtures of Water, air-Water, air-Air-water, CO₂-water Air-water Air-water solutions, Air-water O₂-water sucrose, dextran System Water, Water, KRPC KRPC KRPC KRPC KRPC KRPC KRPC KRPC Type

Banković-Ilić Banković-Ilić Rama Rao et Holmes et al. Gagnon et al. et al. (2001a, et al. (1995) Sundaresan and Varma Skala et al. Rama Rao Banković-Ilić(1999), Reference al. (1991) Baird and (1990b)1998) (1991)(1993)(1997) $P, \varepsilon_{\rm g}, {
m MT}$ Δp , P, $\varepsilon_{\rm g}$, $d_b, k_1 a, a$ $\Delta p, P, \varepsilon_{\rm g}$ Subject $\varepsilon_{\rm g}, d_{\rm b}$ P, d_b AMMT ∇D 0.6 - 4.60.4 - 7.50.5 - 1.50.5 - 1.50 - 1.880 - 1.2 u_g cm/s 12.8 Continuation of Table 1.3 Overview of previous research related to the reciprocating plate column. 0-6.4 1 - 7.22-6 100 **^** 0.024 23.5 12.7 2.35 2.35 13-A mm $\frac{1}{4}$ pu 17 50 0.306 0.454 -60.00.54 0.25 0.57 0.51 0.51 0.54 0.51 0.51 0.5 9.0/8.00.635 0.635 -0.65 0.63 1.43 1.27 1.9 cm 0.3^{-} 0.8 8.0 8.0 2.54 2.54 2.54 5.24 h cm 2.5 pu 65 15 10 65 65 42 4 n_p 1.836 1.05 1.17 3.09 3.96 0.55 l_c Ш 2 a 14.96 5.08 2.54 2.54 22.8 2.54 9.2 7.62 cm D_c Batch Batch Phase flow $\overset{\rightarrow}{\leftarrow}$ $\overset{\rightarrow}{\leftarrow}$ $\overset{\leftarrow}{\leftarrow}$ $\stackrel{\rightarrow}{\leftarrow}$ $\overset{\rightarrow}{\leftarrow}$ $\overset{\rightarrow}{\leftarrow}$ ← Water, Air-water iquid-solid, gas-Air-water-solids solution-Rashig Water-kerosine (0,5%), glycerol CMC (1%, 2%) Water, butanol sulfite (0,8 M), Water-CaCl₂ (69%, 64%), Multi-phase (bilos-binpi gas-liquid; CO₂-water O₂-sulfite Air-water Air-water solutions. solution System rings with SP KRPC KRPC KRPC KRPC KRPC KRPC KRPC KRPC

2005b, 2006a, (2002), Stamenković (1999, 2001a, (1999, 2001a, Vasić (2006), Stamenković Aleksić et al. Nikolić et al. 2001b, 2003, 2001b, 2003, Naseva et al. Nikolić et al. et al. (2005) Vasić et al. Reference (2005a, (2002a) b. 2007) (2005),(2003);(2003);Nikolić Nikolić 2004) 2004) Δp , P, $\varepsilon_{\rm g}$, MT Δp , P, $\varepsilon_{\rm g}$, $k_{\rm I}a$ fermentati alcoholic AM, $\varepsilon_{\rm g}$, Subject ∇p ಯೆ 0.5 - 1.50.5 - 1.50.5 - 1.50.5 - 1.50-1.48 0-1.88 u_g cm/s Continuation of Table 1.3 Overview of previous research related to the reciprocating plate column. 2-4.5 2-4.5 2-5.5 2–6 2-6 2.35 2.35 2.35 mm 0.4660.466 0.454 $0.51 \\ 0.454$ 0.454 ω 0.78 0.78 0.8 8.0 0.8 d_o 2.54 5.0 cm Ч 65 15 15 15 1.836 0.856 1.05 1.05 0.97 0.97 l_c 16.6 2.54 9.2 16.6 9.5 cm D_c Batch Batch Phase flow $\overset{\rightarrow}{\leftarrow}$ $\overset{\rightarrow}{\leftarrow}$ $\overset{\rightarrow}{\leftarrow}$ Air-water-solids Air-water-solids Air-water-solids Air-water, Air-CMC solution solution (1%)water-solids Air-water Air-water Air-CMC System Water solids KRPC KRPC KRPC KRPC KRPC Type

	continuent of the continuent of branch of the continuent of the continuent of the continuent of the continuent		4										
Type	System	Phase	D_c	l_c	n_p	h	d_o	3	Ą	f	u_g	Subject	Reference
		flow	cm	m		cm	cm		mm	Hz	cm/s		
HRRPC Water,	Water,	→	10.0	1.2	15	4.5	8.0		1.0	0-1.5	3.18-	Axial	Dhanasekaran
	Air-water	•									7.43	mixing,	and
					16	4.5,				0-3.0	2.12-	$k_{1}a$	Karunanithi
						2.25					4.24		(2010a, b)
HRRPC Air-water	Air-water	$\overset{ o}{\leftarrow}$	10.0	1.2	16	2.0,	0.8,		1.0	0-3.0	2.12-	$\varepsilon_{\rm g}, d_{ m b}, a,$	Dhanasekaran
						3.5,	0.6,0.4				5.31	$k_{1}a$	and
						5.0							Karunanithi
													(2012a, b, c,
													(p
KRPC	Methanol-oil,	←	2.54	2.0	63	2.54	9.0/8.0	0.51	1.0	2-5	ı	Δp , P , $d_{\rm b}$,	Stamenković
	methanol-KOH-											a,	et al. (2010a)
	lio								2.35			biodiesel	
												production	
KRPC	Methanol-KOH-	←	2.54	2.0	63	2.54	9.0/8.0	0.51	1.0	2-4	I	ı	Stamenković
	oil		16.6	1.53	15	5	8.0	0.466	2.35	2	I		(2014)
KRPC	Methanol-oil,	←	2.54	2.0	63	2.54	9.0/8.0	0.51	1.0	2.0	I	$d_{ m b},$	Banković-Ilić
	methanol-KOH-											biodiesel	et al. (2015)
	lio											production	
KRPC	Methanol-KOH-	↓	2.54	2.0	63	2.54	9.0/8.0	0.51	1.0	2.0	ı	Kinetic	Miladinović et
	waste lard											modeling,	al. (2019)
												biodiesel	

reciprocating plate column, SP - segmental passages, and VDC - vibrating disc column. Symbols: a - specific interfacial area, db - bubble/drop size, Dl, ^a Abbreviations: AM – axial mixing, BRPC – Baird-type reciprocating plate column (plate with central hole), FV – flow visualization, HRRPC – hybrid rotating-reciprocating plate column, HT - heat transfer, KRPC - Karr-type reciprocating plate column, MT - mass transfer, PRPC - Procházka-type - axial dispersion coefficient, k_l – liquid mass transfer coefficient, $k_l a$ – volumetric mass transfer coefficient, Δp – pressure variation at the column bottom, P – power consumption, and ε_g – gas holdup.

2. FLOW REGIME AND MODELS IN RECIPROCATING PLATE COLUMNS

2.1. Regime flow

The fluid dynamics within a reciprocating plate column are intricately linked to the reciprocal motion of the perforated plates. This movement gives rise to distinctive flow phenomena between adjacent plates, as depicted in Figure 2.1 (Brauer, 1985, 1991). As the perforated plates ascend, they compel liquid jets to traverse the openings in a downward trajectory, forming individual ring vortices with cross sections labeled as 1a and 1b (Figure 2.1a). However, a pivotal transformation takes place when the direction of the perforated plate motion is altered, inducing a corresponding shift in the direction of fluid flow within the jets. Simultaneously, this alteration gives rise to the emergence of novel ring vortices (Figure 2.1b). For example, jet 2 becomes encircled by vortex 2, characterized by cross sections 2a and 2b. Remarkably, the fluid circulation within vortex 2 aligns with the circulation observed in vortex 1 despite the modification in the jet flow direction. Consequently, the reversal of perforated plate motion leads to the disintegration of ring vortex 1 while simultaneously fostering the formation of ring vortex 2. This intricate interplay of plate movement and fluid dynamics underscores the dynamic and responsive nature of reciprocating plate columns, contributing to their effectiveness in various applications.

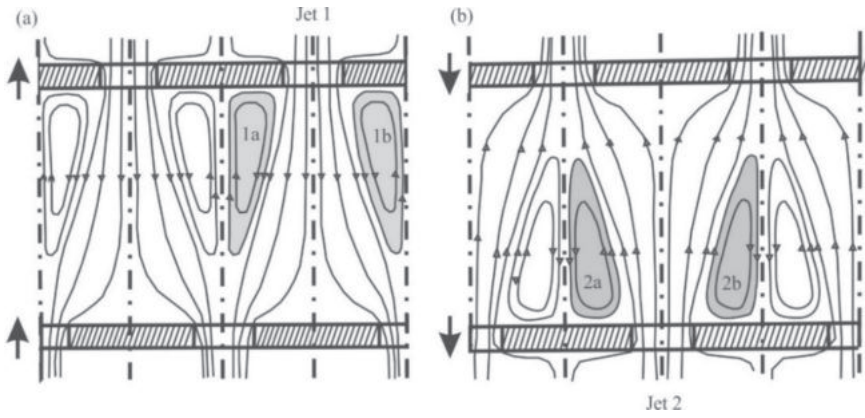


Figure 2.1 Characteristic fluid flow between two adjacent perforated plates in a single-phase system in a reciprocating plate column (Brauer, 1991): (a) upwards motion of plates and (b) downwards motion of plates.

The oscillating motion of the liquid jets, accompanied by the formation and dissolution of vortices, constitutes the secondary liquid flow within the reciprocating plate column. In contrast, the primary liquid flow involves the movement of the liquid through the column facilitated by a pump, but this superficial liquid velocity remains notably lower when compared to the maximum velocities of the jets and vortices. Each volume element within the reciprocating plate column corresponds to the interplate space occupied by one jet along with its surrounding ring vortex. The entire reciprocating plate column volume comprises numerous such elements arranged in parallel and sequence. As the perforated plates cyclically change position, the liquid undergoes a dual exchange. Firstly, it is exchanged between adjacent volume elements in the vertical direction due to the jet movements. Secondly, in the horizontal (i.e., radial) direction, this exchange results from the formation and dissipation of vortices. This periodic exchange of liquid engenders vigorous mixing within the interplate spaces, ensuring uniform conditions throughout the reciprocating plate column. The intensity of this mixing is further amplified by the turbulence generated at the interface of the jets and vortices, resulting from the shear forces at play. In this process, the energy transition from the jets to the ring vortices serves as an energy reservoir, supplying the requisite energy for the robust turbulent transfer of momentum. This mechanism significantly reduces the reliance on molecular transfer mechanisms (Brauer, 1991).

In multiphase reciprocating plate columns, the fluid dynamics are contingent on several factors, including the reciprocal motion of the plates, the superficial gas and liquid velocities, and the nature and concentration of solid particles. Under conditions of gassed flow, when the direction of jet flow changes twice during each cycle, gas bubbles are compelled to move in tandem with the liquid. This motion leads to cyclic occurrences of bubble coalescence and dispersion (Brauer, 1991). Furthermore, the interfacial mass transfer between gas and liquid, though unsteady, takes place under the most favorable conditions.

A visual examination of gas-liquid dispersion reveals four distinctive dispersion states, which vary depending on the reciprocating intensity and gas flow (Boyle, 1975; Veljković and Skala, 1986): segregated dispersion, homogeneous dispersion, cellular dispersion, and 'slug' bubbles. In Figure 2.2, photographic evidence shows cases of dispersed air bubbles within a gassed reciprocating plate column filled with water, captured at two different amplitudes and frequencies of the reciprocating plate motion. As the reciprocating amplitude and frequency increase, signifying higher reciprocating intensity and power consumption, there is a notable reduction in bubble size. Consequently, at a constant flow rate, the number of bubbles increases significantly, leading to an enhanced distribution of bubbles within the liquid. These

photographs vividly depict various dispersion states attainable in gassed reciprocating plate columns.

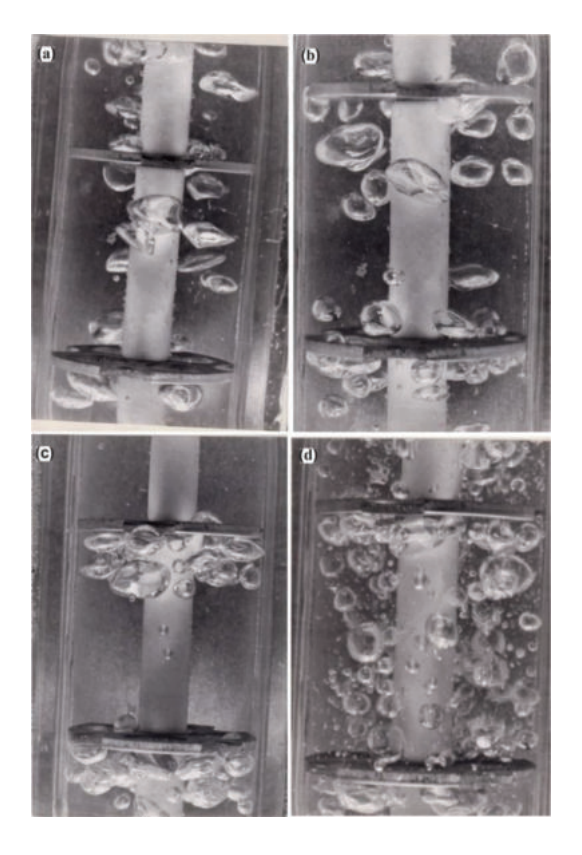


Figure 2.2 Photographs of the gas-liquid dispersion in a reciprocating plate column with the countercurrent gas-liquid flow: (a) A = 0.65 cm, f = 1.17 Hz, (b) A = 0.65 cm, f = 6.17 Hz, (c) A = 2.00 cm, f = 1.17 Hz, and (d) A = 2.00 cm, f = 6.17 Hz ($D_c = 2.54$ cm, $n_p = 65$, $d_o = 0.8$ cm, cm, $\varepsilon = 51\%$, $u_g = 0.823$ cm/s, and $u_l = 0.443$ cm/s).

A segregated dispersion state, often likened to a 'mixer-settler,' is observed at relatively low reciprocating intensities. Here, as the gas traverses the plate openings, it is fragmented into small bubbles of nearly uniform size (Figure 2.2a). Subsequently, as these bubbles pass through the plate openings, they coalesce into larger ones, accumulating beneath the following plate (Figure 2.2c). Consequently, while there is a modest rise in reciprocating intensity, the gas holdup experiences a slight decline.

At higher reciprocating intensities and gas flows, a homogeneous dispersion is formed. Shear forces, resulting from more intensive mixing, prevent the coalescence of bubbles created in the plate openings. As a result, bubbles are similar in size and shape (Figure 2.2b). As the gas flow increases, the bubble size and gas holdup increase. This flow regime provides optimal conditions for efficient mass transfer.

At a high gas holdup, there is an increased coalescence of tiny bubbles into larger, spherical, and densely packed bubbles in the spaces between the plates and the formation of a cellular dispersion (Figure 2.2d). As the bubble size increases, the mass transfer rate decreases.

A further increase in the gas flow rate leads to the formation of slug bubbles, which cannot be broken into smaller bubbles using a reciprocating plate stack. Gas 'slugs,' due to their number and the volume they occupy, limit the mass transfer in the reciprocating plate column. Therefore, the gas flow rate at which gas 'slugs' occur represents the maximum gas flow rate in the RCP (Boyle, 1975).

2.2. Flow models

The description of liquid flow within a reciprocating plate column relies on two fundamental models: the quasi-steady-state model and the acoustic flow model. During a single cycle of reciprocating plate movement, variables such as the velocity of the reciprocating plate, the pressure at the column bottom, and the power consumption exhibit time-varying patterns.

The quasi-steady-state flow model, formulated initially by Jealous and Johnson (1955) for pulsed extraction columns, has been extended to encompass reciprocating plate columns (Hafez and Procházka, 1974a; Hafez and Baird, 1978). It assumes these dynamic variations are steady-state and align with their respective mean values over an extended time interval. This model further assumes that the liquid flow within the reciprocating plate column is fully developed at each moment of the reciprocating plate's movement. It is a valuable tool for characterizing instantaneous alterations in the plate velocity, the pressure at the column bottom, and power consumption (as elaborated in Chapters 2, 3, and 4). One integrates the instantaneous changes over a single cycle interval to obtain mean values akin to a quasi-steady state. It is pertinent to note that the applicability of the quasi-steady-state flow model is corroborated when the reciprocating amplitude surpasses the threshold of 1 cm (Baird et al., 1996). This model plays a pivotal role in deciphering the dynamic fluid behavior within reciprocating plate columns, offering valuable insights into their operational characteristics.

In cases characterized by small reciprocating amplitudes, typically spanning a few millimeters, there exists a noticeable deviation of the measured mean power consumption from the Equation derived from the quasi-steady-state flow model, as initially outlined by Hafez and Baird (1978). This deviation was subsequently confirmed by Baird and Stonestreet (1995), specifically within a reciprocating plate

column featuring a central orifice. In response, they developed an alternative model known as the acoustic flow model. The essence of this model lies in the fact that most external energy dissipates close to the perforated plates, mirroring the behavior observed in acoustic flow systems (Panton and Goldman, 1976). Nonetheless, the impact of liquid viscosity varies with the frictional interaction between the liquid and the plates at different liquid velocities through the plate openings. These variations are particularly pronounced in regions where jets and vortices are generated (Panton and Goldman, 1976). In scenarios characterized by subsonic frequencies (below 20 kHz) and relatively substantial reciprocating amplitudes ranging from 0.5 to 4 mm, the kinematic liquid viscosity exerts minimal influence on energy dissipation, as Mackay et al. (1991) affirmed. Within the framework of the acoustic flow model, an introduction of eddy viscosity becomes imperative. This eddy viscosity is directly proportional to the product of the angular frequency squared and the mixing path, as articulated by Baird and Rama Rao (1995) and further supported by Baird et al. (1996). In turbulent flow regimes, this eddy viscosity effectively supplants the role of kinematic viscosity, accounting for the observed deviations and providing a more accurate representation of the energy dissipation process. Following this model, the power consumption is proportional to f^3A^2 , i.e.:

$$P = \frac{3\pi}{8} \cdot \frac{\rho_l n_p D_c (2\pi f)^3 A^2 l_m}{\varepsilon}$$
 (2.1)

where ρ_l is the liquid density, n_p is the plate number, D_c is the column diameter, A is the amplitude of reciprocation motion, f is the frequency of reciprocation motion, l_m is the mixing path, and ε is the fractional-free plate surface.

The 'acoustic' flow model is applicable for reciprocating amplitudes less than critical, which is defined as follows (Baird and Rama Rao, 1995):

$$A_{cr} = l_m \cdot \frac{9\pi}{4} \cdot \frac{C_o^2 \varepsilon}{1 - \varepsilon^2} \tag{2.2}$$

where $A_{\rm cr}$ is the critical amplitude, $l_{\rm m}$ is the mixing path, $C_{\rm o}$ is the plate opening coefficient, and ε is the fractional-free plate surface.

3. RECIPROCATING PLATE STACK VELOCITY

The defining characteristic of reciprocating plate columns lies in the motion of the reciprocating plate stack as it traverses the column, propelled by a driving mechanism housing a variable-speed motor. The transmission mechanism responsible for this dynamic movement is visually outlined in Figure 3.1. At its core, this mechanism features a disc linked to the plate stack carrier through an eccentric connection and a tie-rod. Notably, the disc maintains a steady angular velocity throughout its operation. This continuous angular motion directly translates into the reciprocating agitator's vertical oscillation within the column. Notably, the agitator exhibits the same angular frequency as the disc and an amplitude equivalent to the disc's radius, which coincides with the reciprocating amplitude. The ability to fine-tune the reciprocating amplitude and frequency is achieved through simple adjustments. Altering the disc's radius or modifying the motor's rotating speed offers a flexible way to customize these critical parameters.

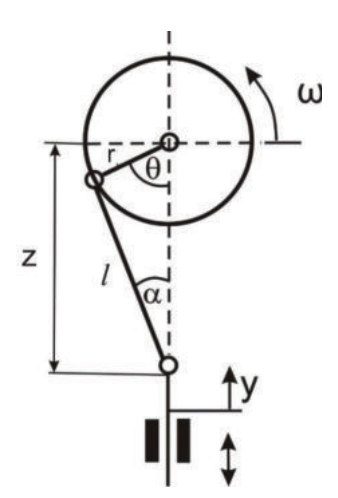


Figure 3.1 Scheme of the transmission mechanism (Banković-Ilić, 1993).

The displacement of the reciprocating agitator varies during one cycle:

$$y = l + r - z \tag{3.1}$$

where y is the displacement of the reciprocating agitator during one cycle, l is the length of the tie-rod, r is the radius of the disc, and z is the distance between the center of the disc and the starting end of the tie-rod.

The distance between the center of the disc and the starting end of the tie-rod is:

$$z = r\cos\theta + l\cos\alpha \tag{3.2}$$

where θ is the angular distance of the disc and α is the angular distance of the tie-rod, while the ratio of the radius of the disc and the length of the tie-rod is defined by Equation (3.3):

$$s = \frac{r}{l} = \frac{A}{l} \tag{3.3}$$

where s is the disc radius-to-tie-rod length, r is the radius of the disc, l is the length of the tie-rod, and A is the amplitude of the reciprocation motion.

The mean change in the angular distance of the disc is:

$$\theta = \omega t = 2\pi f t \tag{3.4}$$

where ω is the angular velocity, f is the frequency of the reciprocation motion, and t is time.

After expanding Equation (3.1) into the Taylor series and neglecting all terms except the first, the displacement of the reciprocating plate stack can be described as follows:

$$y = A(1 - \cos 2\pi f t) + \frac{s}{2} A \sin^2 2\pi f t$$
 (3.5)

The reciprocating plate stack velocity has the following form:

$$u_s = \frac{dy}{dt} = 2\pi A f \sin 2\pi f t \left(1 + s \cos 2\pi f t\right)$$
(3.6)

where u_s is the reciprocating plate stack velocity.

4. THE PRESSURE VARIATION AT THE BOTTOM OF RECIPROCATING PLATE COLUMNS

A theoretical analysis of pressure change and power consumption in a single-phase (liquid) system was performed by Hafez and Procházka (1974a, 1974b). In the case of two-phase (gas-liquid) systems, the theoretical analysis is more complex due to the compressibility of the gas phase. By neglecting the change in gas density due to the change in the pressure in the column at low gas velocities and agitation intensities, the limiting case of the simplified system behavior analysis is reached. The pressure variations observed at the column bottom are influenced by a combination of forces, as outlined in previous research (Hafez and Procházka, 1974a; Hafez and Baird, 1978). These forces include:

- (a) Inertia force resulting from the reciprocating plate movement and the motion of the liquid adjacent to the plates.
- (b) Friction force arising from mechanical contacts between the plates and the column wall and between the liquid and moving and stationary components within the column.
- (c) Gravity force due to the weight of the reciprocating plate stack.
- (d) Buoyancy force caused by the difference in pressure between the top and bottom of an immersed reciprocating plate stack, resulting from displacing a particular liquid volume.

Except for the pressure resulting from gravitational and buoyancy forces, the pressure variation at the column bottom has a periodic character. Hence, the induced liquid flow is in a non-steady state. At the same time, the reciprocating plate stack is also moved unsteadily.

The instantaneous pressure on the column bottom can be related to the instantaneous force applied to the perforated plate stack with the help of a momentum balance for a controlled volume of the reciprocating plate column filled with a liquid between $z = z_1$ and $z = z_2$ (Figure 4.1). In addition, for a continuous reciprocating plate column, both boundary surfaces are sufficiently far from the top and bottom plates of the reciprocating plate stack, so the flow through the column can be regarded as an ideal plug flow. Moreover, the system is closed as its boundaries move with the liquid.

In other words, it is assumed the controlled volume does not undergo acceleration. However, a slight liquid displacement occurs for a batch reciprocating plate column when the perforated plate carrier enters the controlled volume at $z = z_1$.

This effect can be ignored as the cross-sectional area of the perforated plate carrier is much smaller than that of the column. Furthermore, the system includes the reciprocating plate stack, so the forces that act between the perforated plates and the liquid, being the inner ones, are not included in the momentum balance. This frictional force is negligible in the case of liquids of low viscosity (Kažić, 1979).

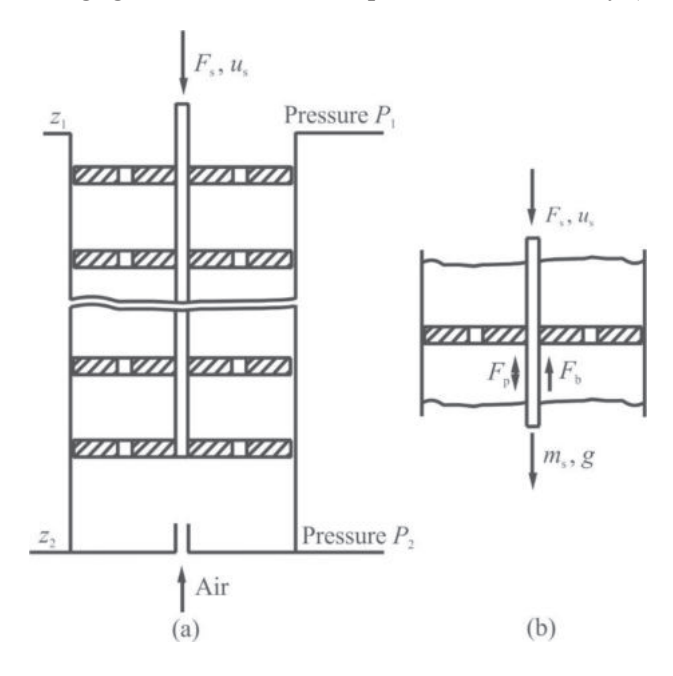


Figure 4.1 The momentum balance for the controlled volumes in a batch reciprocating plate column (Banković-Ilić, 1993): (a) an entire column with the reciprocating plate stack and (b) a column part comprising the liquid surrounding a reciprocating plate.

The pressure variation at the column bottom can be determined from the momentum balance for the controlled volume shown in Figure 4.1a:

$$m_{s} \frac{du_{s}}{dt} + m_{l} \frac{du_{l}}{dt} = (p_{1} - p_{2}) A_{c} + F_{s} + (m_{s} + m_{l}) g$$
(4.1)

where m_s and u_s are the mass and velocity of the perforated plate stack, m_l and u_l are the mass and superficial velocity of the liquid, p_1 and p_2 are the pressures at $z = z_1$ and $z = z_2$, F_s is the force exerted by the perforated plate stack on the system, A_c is the cross-sectional area of the column, g is the gravitational acceleration, and t is time.

For a particular case of a constant superficial liquid velocity ($u_1 = const.$), Equation (4.1) is simplified as follows:

$$m_{s} \frac{du_{s}}{dt} = (p_{1} - p_{2}) A_{c} + F_{s} + (m_{s} + m_{l}) g$$
(4.2)

The momentum balance for a moving plate in the controlled volume shown in Figure 4.1b is as follows:

$$m_s \frac{du_s}{dt} = F_s - F_p - F_b + m_s g \tag{4.3}$$

where F_p and F_b represent the force of interaction between the perforated plate stack and the system and the buoyancy force exerted by the system on the perforated plate stack, respectively.

The directions of forces, velocity, and acceleration in Equations (4.1), (4.2), and (4.3) are with a positive orientation pointing downwards. Only the normal components of the forces are considered.

The force corresponding to the friction of the perforated plates against the column wall is excluded. The analysis excludes the frictional forces between the perforated plates and the column wall (solid-solid friction). These forces represent an additional load on the drive motor shaft but are not considered in the plates and liquid interaction. A practical method involves measuring two forces to eliminate the influence of solid-solid friction: the total force exerted on the plate carrier during regular operation and the force generated when the plates move through an empty column with a wetted wall. A net force value that effectively isolates the impact of solid-solid friction is derived by subtracting the latter force from the former.

Regarding the liquid flow unsteadiness in the column, the analysis exclusively accounts for flow variations induced by the perforated plate movement. This approach aligns with the established understanding that the overall liquid flow within the column remains in a steady-state condition. Therefore, the only factor contributing to unsteady liquid flow is the motion of the perforated plates.

The buoyancy force exerted by the liquid on the perforated plate stack in motion is defined by the following expression:

$$F_b = \frac{m_s}{\rho_s} \rho_l g \tag{4.4}$$

where ρ_s and ρ_l are the densities of the perforated plate stack and of the liquid, respectively.

The force acting between a perforated plate and the system for the steady-state liquid flow is obtained by combining Equations (4.2), (4.3), and (4.4):

$$F_{p} = \left[\left(p_{2} - p_{1} \right) - \rho_{l} g l_{c} \right] A_{c} - m_{s} \frac{\rho_{l}}{\rho_{s}} g \tag{4.5}$$

where l_c is the distance between sections 1 and 2 (Figure 4.1a). The first term of the right side of Equation (4.5) depends on the perforated plate movement and consists of inertial and frictional components, which have a phase difference of 90° (Procházka and Hafez, 1972):

$$\left[(p_2 - p_1) - \rho_l g(z_2 - z_1) \right] A_c = \left[\rho_l \int_{z_1}^{z_2} \frac{\partial u_{l,o}}{\partial t} dz + f_{1,2} \right] A_c$$
 (4.6)

where $u_{1,0}$ is the local instantaneous liquid velocity through the plate openings and $f_{1,2}$ is the total mechanical energy losses per unit volume of liquid between cross-sections 1 and 2 (Figure 4a). The integral on the right side of Equation (4.6) expresses the effect of unsteady liquid flow through the plate openings. Therefore, for a stack of n_p perforated plates, Equation (4.6) should be multiplied by n_p .

Calculating the integral in Equation (4.6) presents challenges due to the complexity of the velocity profile within the system under analysis. An empirical parameter known as 'equivalent plate thickness' (s_e) was introduced as a pragmatic solution to simplify this calculation. It is defined as the height of the liquid column that, when passing through the plate opening, shows an inertia equal to that of the integral mentioned above. By adopting this concept, the inertial term can be expressed as follows (Hafez and Baird, 1978):

$$\rho_{l} \int_{z_{l}}^{z_{2}} \frac{\partial u_{l,o}}{\partial t} dz = \rho_{l} n_{p} s_{e} \frac{1 - \varepsilon}{C_{o}^{2} \varepsilon} \left(\frac{du_{s}}{dt} \right)$$

$$(4.7)$$

where C_0 is the plate opening coefficient (also known as the orifice coefficient), s_e is the equivalent plate thickness, n_p is the number of perforated plates, and ε is the fractional plate-free area.

Hafez and Procházka (1974b) correlated the equivalent plate thickness with the reciprocating amplitude and frequency, plate opening diameter, and fractional plate-free area. This empirical correlation was derived from experimental data for the equivalent plate thickness s_e using a quasi-steady-state flow model, assuming that the pressure drop attributed to the flow resistance is approximately the same for steady-state and unsteady-state flows.

Therefore, the friction term of the pressure variation at the column bottom is

$$f_{1,2} = n_p \rho_l \frac{1 - \varepsilon^2}{2C_o^2 \varepsilon^2} u_s |u_s| \tag{4.8}$$

In the derivation of Equation (4.8), it was assumed that the plate opening is constant throughout the cycle of the reciprocating movement of the perforated plate stack, and the fluid flow is fully developed. However, the plate opening coefficient varies with time depending on the instantaneous perforated plate stack velocity.

Based on Equations (4.6), (4.7), and (4.8), the instantaneous pressure variation at the column bottom is:

$$(p_2 - p_1) - \rho_l g(z_2 - z_1) = \rho_l n_p s_e \frac{1 - \varepsilon}{\varepsilon} \left(\frac{du_s}{dt}\right) + n_p \rho_l \frac{1 - \varepsilon^2}{2C_0^2 \varepsilon^2} u_s |u_s|$$

$$\tag{4.9}$$

The inertial component of the pressure variation reaches its maximum at the ends of the stroke and is proportional to Af^2 . In one cycle of the reciprocating plate movement, the average inertial component equals zero since there is no overall acceleration of the liquid in the column. On the other hand, the frictional component reaches its maximum halfway through the stroke when the reciprocating plate velocity is the highest and is proportional to $(Af)^2$. In practical conditions, the maximum of the frictional component is always larger than the maximum of the inertial component (Hafez and Baird, 1978) by at least two orders of magnitude (Harikrishnan and Varma, 1992).

Adopting the assumptions of the quasi-steady-state flow model, the instantaneous pressure variation at the column bottom (Δp) is:

$$\Delta p = n_p \rho_l \frac{1 - \varepsilon^2}{2C_0^2 \varepsilon^2} u_s |u_s| \tag{4.10}$$

The average pressure variation at the column bottom ($\Delta \overline{p}$) in one cycle of the reciprocating plate movement (from t = 0 to t = T) is:

$$\Delta \overline{p} = \frac{1}{T} \int_{0}^{T} |\Delta p| dt \tag{4.11}$$

By combining Equations (3.6) and (4.11), the average pressure variation at the column bottom is (Banković-Ilić et al., 1995):

$$\Delta p_{av} = n_p \rho_l \frac{1 - \varepsilon^2}{2C_0^2 \varepsilon^2} (2\pi A f)^2 \left(\frac{1}{2} + \frac{4s}{3\pi} + \frac{s^2}{8} \right)$$
 (4.12)

where s is the ratio of the reciprocating amplitude and the length of the tie-rod.

The total pressure variation at the column bottom is defined as the sum of the pressure variation during the reciprocating plate movement towards the bottom and top of the column:

$$\Delta p^* = \Delta p_{max} + |\Delta p_{min}| \tag{4.13}$$

where Δp_{\min} and Δp_{\max} are the pressure variations at the column bottom corresponding to the upstroke and downstroke of the plate stack, respectively. A typical instantaneous pressure variation at the column bottom for a non-gassed system (water) is shown in Figure 4.2.

According to Equation (4.10), the pressure variation at the column bottom during the downward and upward reciprocating plate movement is symmetrical, so it follows:

$$\Delta p_{max} = \left| \Delta p_{min} \right| = n_p \rho_l \frac{1 - \varepsilon^2}{2C_0^2 \varepsilon^2} (2\pi A f)^2 \tag{4.14}$$

while the total pressure variation at the column bottom is:

$$\Delta p^* = n_p \rho_l \frac{1 - \varepsilon^2}{C_0^2 \varepsilon^2} (2\pi A f)^2 \tag{4.15}$$

where A and f are the amplitude and frequency of reciprocating plate movement; the product of amplitude and frequency (Af) is referred to as reciprocating intensity.

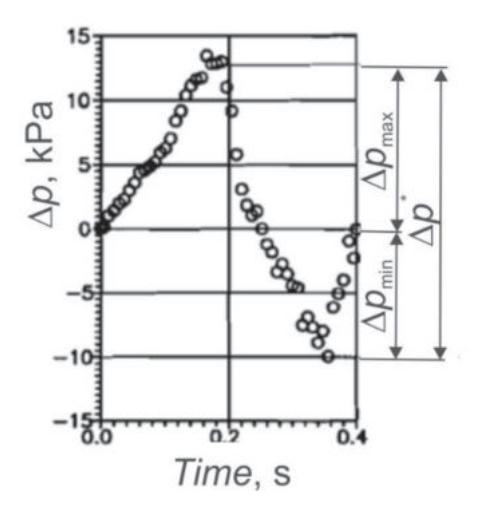


Figure 4.2 A typical instantaneous pressure variation at the column bottom Δp for a non-gassed system (water, A = 2.35 cm, and f = 2.5 s⁻¹).

However, it was shown that $\Delta p_{\text{max}} > \Delta p_{\text{min}}$ regardless of the reciprocating intensity (Banković-Ilić et al., 1995). The pressure variation at the column bottom is asymmetrical due to the slightly faster reciprocating plate downward movement caused by the weight of the reciprocating agitator (Rama Rao and Baird, 1988).

Based on Equations (4.15) and (4.12), the ratio of the total and average pressure variations at the column bottom is as follows:

$$\frac{\Delta p^*}{\Delta p_{av}} = \frac{2}{\frac{1}{2} + \frac{4s}{3\pi} + \frac{s^2}{8}}$$
 (4.16)

Table 4.1 provides a comprehensive overview of the underlying theoretical Equations used to compute pressure variations at the bottom of pulsed columns and reciprocating plate columns. However, it is worth noting that the absence of a fully established physical model presents a challenge in the context of gas-liquid and gas-liquid-solid phase systems. For gas-liquid systems, the Equations for the pressure variation at the column bottom are corrected for the liquid holdup (Banković-Ilić et al., 1995; Boyle, 1975; Veljković and Skala, 1986). Empirical correlations in Table 4.2, moving beyond pure theory, are based on these foundational Equations to provide more practical estimates for pressure variations at the bottom of reciprocating plate columns.

Table 4.1 Theoretical correlations for the pressure variation at the bottom of pulsation and reciprocating plate columns.

Column	Phase flow	Correlation	Reference
		Correlation	Reference
PBC	arrangement	$\Delta p = \frac{n_p \rho_l (1 - \varepsilon^2)}{2C_o^2 \varepsilon^2} \left(\frac{dy}{dt}\right)^2$	Thornton (1957)
PBC		$\Delta p = \frac{n_p \rho_l (1 - \varepsilon)(1 - \varepsilon^2)}{2C_o^2} u_s^2$	Miyauchi and Oya (1965)
RPC	Af = 0	$\Delta p = \frac{n_p \rho_l u_l^2 (1 - \varepsilon^2)}{2C_o^2 \varepsilon^2}$	Noh and Baird (1984)
	$\uparrow \uparrow$	$\Delta p = \frac{n_p \rho_l (u_{lo} u_{lo} - u_l^2)}{2C_o^2}$	
		$\Delta p_{av} = \frac{n_p \rho_l (1 - \varepsilon^2)}{2C_o^2 \varepsilon^2} \left[\frac{1 - \varepsilon}{1 + \varepsilon} \frac{(2\pi Af)^2}{2} + u_l^2 \right]; (2\pi Af) \ll \frac{u_l}{(1 - \varepsilon)}$	
		$\Delta p_{av} = \frac{n_p \rho_l u_l^2}{2C_o^2} \left[\frac{4(1-\varepsilon)}{\pi \varepsilon^2} \frac{2\pi A f}{u_l} - 1 \right]; (2\pi A f) \gg \frac{u_l}{(1-\varepsilon)}$	
RPC	Af = 0	$\Delta p = \frac{n_p \rho_l u_l^2 (1 - \varepsilon^2)}{2C_o^2 \varepsilon^2}$	Yang et al. (1986a)
RPC	$\uparrow \uparrow$	$\Delta p_{av} = \frac{n_p \rho_l (1 - \varepsilon)}{2C_o^2} \left[\frac{2}{\pi} \left(\frac{1}{C_{od}^2} + \frac{1}{C_{ou}^2} \right) u_l (2\pi A f) + \frac{1 - \varepsilon}{4} \left(\frac{1}{C_{od}^2} - \frac{1}{C_{od}^2} \right) \right]$	$\frac{1}{C_{ou}^{2}}\bigg)(2\pi Af)^{2}\bigg]$
RPC	$\uparrow \downarrow \\ \uparrow \uparrow$	$\Delta p = \frac{n_p \rho_l (1 - \varepsilon^2)}{2C_o^2 \varepsilon^2} (u - u_s)^2$	Harikrishnan and Varma (1992)
RPC	Batch	$\Delta p_{av} = \frac{n_p \rho_l (1 - \varepsilon^2)}{2C_o^2 \varepsilon^2} (2\pi A f)^2 \left(\frac{1}{2} + \frac{4s}{3\pi} + \frac{s^2}{8} \right)$	Banković- Ilić et al. (1995)

Abbreviations: PBC – pulsed bubble column and RPC – reciprocating plate column.

Many factors inherently influence the pressure variations encountered at the column bottom. These encompass the physical and rheological properties of the liquid, the specific operating conditions employed, the number and geometry of plates within the system, and the prevailing hydrodynamic flow conditions. As a tangible illustration, consider Procházka-type reciprocating plate columns: in cases where perforated plates feature segmental passages, the total pressure variation at the base is notably reduced, typically by a factor of 10 to 15 when compared to perforated plates lacking such segmental passages (Boyle, 1975; Landau et al., 1976).

Table 4.2 Empirical correlations for the pressure variation at the column bottom of reciprocating plate columns.

System		Correlation	Reference	
'Pure' liquid	Distilled water, sucrose solution, and a model dextran fermentation broth	$\Delta p^* \propto n_{\rm p} \rho_{\rm l} (Af)^2$	Veljković and Skala (1986)	
	Water	$\Delta p^* = 0.113 n_{\rm p} \rho_{\rm l} (Af)^2$	Banković-Ilić et al.	
		$\Delta p_{av} = 0.0317 n_{\rm p} \rho_{\rm l} (Af)^2$	(1995)	
	Water	$\Delta p^* = 0.082 n_{\rm p} \rho_{\rm l} (Af)^2$	Banković-Ilić	
		$\Delta p_{av} = 0.023 n_{\rm p} \rho_{\rm l} (Af)^2$	(1999)	
	Water	$\Delta p^* = 657.2 (Af)^{1.57}$	Aleksić et al.	
		$\Delta p_{av} = 457.8 (Af)^{1.96}$	(2002a)	
	CMC (1%) solution	$\Delta p^* = 314.5 (Af)^{1.21}$		
		$\Delta p_{av} = 115 (Af)^{1.2}$		
	Water	$\Delta p^* = 899 (Af)^{1.617}$	Vasić et al. (2005a)	
		$\Delta p_{av} = 615.6 (Af)^2$		
	Sunflower oil (batch)	$\Delta p^* = 2.081 (Af)^{1.35}$	Stamenković et al.	
		$\Delta p_{av} = 0.542 (Af)^{1.32}$	(2010)	
	Sunflower oil (continuous)	$\Delta p^* = 1.652 (Af)^{1.31}$		
		$\Delta p_{av} = 0.591 (Af)^{1.39}$		
Gas-liquid	Air-water	$\Delta p^* = 0.0647 n_p \rho_l (1 - \varepsilon_g) (Af)^2$	Banković-Ilić et al. (1995)	
		$\Delta p_{av} = 0.0176 n_p \rho_l (1 - \varepsilon_g) (Af)^2$	(1993)	
	Air-water	$\Delta p^* = 0.1087 n_p \rho_l (1 - \varepsilon_g) (Af)^2$	Banković-Ilić	
		$\Delta p_{av} = 0.0322 n_p \rho_l (1 - \varepsilon_g) (Af)^2$	(1999)	
	Air-water	$\Delta p^* = 711.9 (Af)^{1.67}$	Aleksić et al.	
		$\Delta p_{av} = 425.4 (Af)^{1.93}$	(2002a)	
	Air-CMC (1 %) solution	$\Delta p^* = 321.5 (Af)^{1.14}$		
		$\Delta p_{av} = 115.1(Af)^{1.21}$		
	Air-water	$\Delta p^* = 899(1 - \varepsilon_g)(Af)^{1.617}$	Vasić et al. (2005a)	
		$\Delta p_{av} = 615.6(1 - \varepsilon_g)(Af)^2$		
	Air-CMC (0.5 %) solution	$\Delta p^* = 862.3(1 - \varepsilon_g)(Af)^{1.57}$		
		$\Delta p_{av} = 473.4(1 - \varepsilon_g)(Af)^{1.85}$		
	Air-CMC (1 %) solution	$\Delta p^* = 740.6(1 - \varepsilon_g)(Af)^{1.46}$		
		$\Delta p_{av} = 390.9(1 - \varepsilon_g)(Af)^{1.71}$		
Liquid-solid	Water-solid (spheres, 8.4 mm, 5	$\Delta p^* = 0.279 n_p \rho_l (Af)^2$	Banković-Ilić et al.	
	spheres per each second or third interplate space)	$\Delta p_{av} = 0.0322 n_p \rho_l (Af)^2$	(1993)	

Continuation of Table 4.2 Empirical correlations for the pressure variation at the column bottom of reciprocating plate columns.

System		Correlation	Reference			
Liquid-solid	Water-solid (spheres: 8 mm,	$\Delta p^* = 699.7 (Af)^{1.56}$	Aleksić et al.			
	0.35–3.2%)	$\Delta p_{av} = 458.4 (Af)^{1.95}$	(2002a)			
	CMC (1%) solution-solid	$\Delta p^* = 248.4 (Af)^{0.93}$				
	(0.35–3.2%)	$\Delta p_{av} = 92.3 (Af)^{1.0}$				
	Water-solid (spheres: 8.4 mm,	$\Delta p^* = 610.7 (Af)^{1.31}$	Vasić et al. (2005a)			
	3.8%)	$\Delta p_{av} = 324.6 (Af)^{1.58}$				
	Water-solid (6.6%)	$\Delta p^* = 425.5 (Af)^{10.97}$				
		$\Delta p_{av} = 265.4 (Af)^{1.29}$				
	CMC (0.5%) solution-solid (3.8%)	$\Delta p^* = 683.7 (Af)^{1.34}$				
		$\Delta p_{av} = 419.6 (Af)^{1.64}$				
	CMC (0.5%) solution-solid (6.6%)	$\Delta p^* = 416.9 (Af)^{0.91}$				
		$\Delta p_{av} = 187.2 (Af)^{1.09}$				
	CMC (1%) solution-solid (3.8%)	$\Delta p^* = 1276.4 (Af)^{1.54}$				
		$\Delta p_{av} = 676.1 (Af)^{1.78}$				
	CMC (1%) solution-solid (6.6%)	$\Delta p_{av} = 255 (Af)^{1.18}$				
		$\Delta p^* = 479 (Af)^{120}$				
Gas-liquid-	Air-water-solid (spheres, 8 mm, 0.35-3.2%)	$\Delta p^* = 413.8 (Af)^{1.43}$	Aleksić et al.			
solid		$\Delta p_{av} = 327.5 (Af)^{1.84}$	(2002a)			
	Air-CMC (1%) solution-solid (0.35-	$\Delta p^* = 173 (Af)^{0.86}$				
	3.2%)	$\Delta p_{av} = 70.1 (Af)^{0.93}$				
	Air-water-solid (spheres: 8.4 mm,	$\Delta p^* = 610.7(1 - \varepsilon_g)(Af)^{1.31}$	Vasić et al. (2005a)			
	3.8%)	$\Delta p_{av} = 324.6(1 - \varepsilon_g)(Af)^{1.58}$				
	Water-solid (6.6%)	$\Delta p^* = 425.5(1 - \varepsilon_g)(Af)^{10.97}$				
		$\Delta p_{av} = 265.4(1 - \varepsilon_g)(Af)^{1.29}$				
	Air-CMC (0.5%) solution-solid	$\Delta p^* = 683.7(1 - \varepsilon_g)(Af)^{1.34}$				
	(3.8%)	$\Delta p_{av} = 419.6(1 - \varepsilon_g)(Af)^{1.64}$				
	Air-CMC (0.5%) solution-solid	$\Delta p^* = 416.9(1 - \varepsilon_g)(Af)^{0.91}$				
	(6.6%)	$\Delta p_{av} = 187.2(1 - \varepsilon_g)(Af)^{1.09}$				
	Air-CMC (1%) solution-solid	$\Delta p^* = 1276.4(1 - \varepsilon_g)(Af)^{1.54}$				
	(3.8%)	$\Delta p_{av} = 676.1(1 - \varepsilon_g)(Af)^{1.78}$				
	Air-CMC (1%) solution-solid	$\Delta p^* = 947(1 - \varepsilon_g)(Af)^{1.20}$				
	(6.6%)	8				
Liquid-liquid	Sunflower oil-methanol (1:6	$\Delta p_{av} = 255(1 - \varepsilon_g)(Af)^{1.18}$ $\Delta p^* = 1.158(1 - \varepsilon_d)(Af)^{1.28}$	Stamenković et al.			
_	mol/mol)	$\Delta p_{av} = 0.428(1 - \varepsilon_d)(Af)^{1.37}$	(2010)			

The rheological properties of the liquid significantly influence the pressure variations at the column bottom (Aleksić et al., 2002a; Banković-Ilić, 1999; Vasić et al., 2005a). Table 4.3 gives an overview of liquids and their physical properties, which have been used in researching the hydrodynamics of reciprocating plate columns. Regardless of the column diameter, the pressure variation at the column bottom directly correlates with the liquid's viscosity due to the more intense friction between the liquid and the reciprocating plates. For Newtonian liquids in the turbulent flow regime (Re > 50), the pressure variation at the column bottom exhibits a nearly quadratic relationship with the reciprocating intensity, as illustrated in Figure 4.2.

Table 4.3 Physical properties of liquids (20 °C) used in the hydrodynamic research in reciprocating plate columns.

Liquid	Density,	Surface	Viscosity,	
	kg/m^3	tension, N/m	mPa·s	
Distilled water	998	0.0726	1.05	
n-Butanol, ^a 0,5%	997	0.0568	1.22	
Sodium sulfite, ^a 0,8 mol/L	1099	0.0831	1.34	
Glycerol, ^a 40%	1102	-	3.8	
Glycerol, ^a 64%	1166	0.0773	14.6	
Glycerol	1258	0.0634	942	
CMC, a,b 1% ($D_c = 9.2$ cm)	1004	-	K = 0.128 $K = 0.274$	
			$n = 0.77^{\circ}$ $n = 0.66^{d}$	
CMC, a,b 1% ($D_c = 2,54$ cm)	1005	-	K = 0.128 $K = 0.274$	
			$n = 0.77^{\circ}$ $n = 0.66^{d}$	
CMC, a,b 2% ($D_c = 9.2 \text{ cm}$)	1009	-	K = 0.643 $K = 1.017$	
			$n = 0.72^{\circ}$ $n = 0.63^{d}$	
CMC, a,b 2% ($D_c = 2.54$ cm)	1010	-	K = 1.022 $K = 1.022$	
			$n = 0.66^{\circ}$ $n = 0.66^{\circ}$	

^a Aqueous solutions. ^b CMC – Sodium salt of CMC; the solutions have pseudoplastic behavior; K – coefficient of consistency ($Pa \cdot s^n$); n – flow index (-). ^c One-phase and two-phase (gas-liquid) systems. ^d Two-phase (gas-solid) and three-phase (gas-liquid-solid) systems.

This observation lends credence to the applicability of the quasi-steady-state flow model (Hafez and Procházka, 1974a, 1974b). Furthermore, it implies that frictional losses play a pivotal role in determining the pressure variations at the column bottom. However, when dealing with non-Newtonian liquids, a departure from this established model becomes evident, with a more pronounced deviation arising as the fluid becomes increasingly pseudoplastic. Within the laminar flow regime, exemplified by a 2% CMC solution, characterized by Re values below 10, the dependence of the pressure variation at the column bottom on the reciprocating intensity is almost linear (Banković-Ilić, 1999).

In gas-liquid systems, it is observed that the pressure variations at the column bottom are relatively smaller when compared to single-phase systems ('pure' liquid) (Aleksić et al., 2002a; Baird and Rama Rao, 1997; Banković-Ilić et al., 1993, 1995, 1996, 2004a; Boyle, 1975; Lounes and Thibault, 1993; Stamenković et al., 2004; Vasić et al., 2005a; Veljković and Skala, 1986). This difference arises primarily due to the lower dispersion density and weaker interactions between the reciprocating plates and the two-phase system, in contrast to the interactions observed in "pure" liquid systems. Notably, an increase in the superficial liquid velocity (Baird and Rama Rao, 1997; Rama Rao and Baird, 1986), coupled with a reduction in superficial gas velocity (Aleksić et al., 2002a; Banković-Ilić, 1999), contribute to an increase in the pressure variation at the column bottom of three diameters 2.54 cm, 9.2 cm, and 16.6 cm, as illustrated in Figures 4.3, 4.4 and 4.5. It is worth noting that this effect remains consistent regardless of the rheological properties inherent to the liquid phase (Aleksić et al., 2002a). Furthermore, an increase in the superficial gas velocity results in a decrease in dispersion density and frictional interactions within the system, thereby reducing pressure variations at the column bottom. Additionally, following Equations (4.11) and (4.14), an increase in the number of plates coupled with a decrease in fractional free plate surface leads to an escalation in the pressure variations at the column bottom (Rama Rao and Baird, 1986).

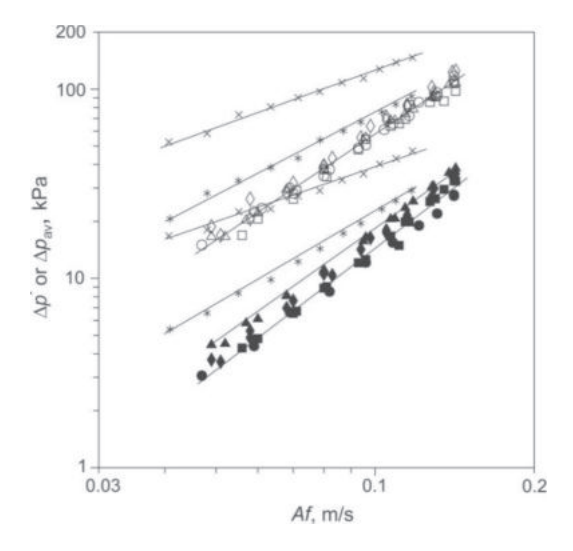


Figure 4.3 Dependence of the total and mean pressure variation at the column bottom filled with "pure" liquids on the reciprocating intensity: $D_c = 2.54$ cm (Δp^* – open symbols and $\Delta p_{\rm av}$ – black symbols; water – circles, glycerol – triangles, 0.5% n-butanol – squares, 0.8 M Na₂SO₄ – rhombuses, 1% CMC – stars, and 2% CMC—crosses) (Banković-Ilić, 1999).

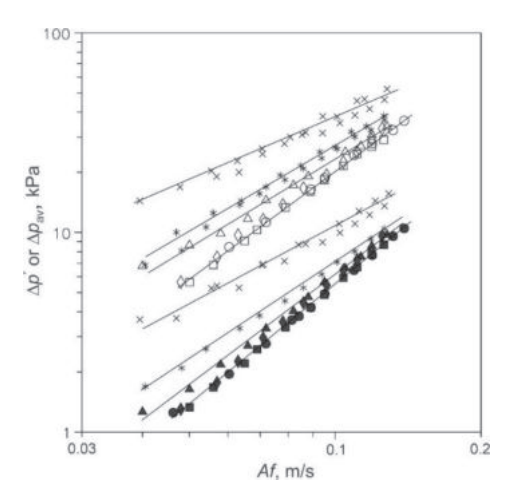


Figure 4.4 Dependence of the total and mean pressure variation at the column bottom filled with "pure" liquids on the reciprocating intensity: $D_c = 9.2$ cm (Δp^* – open symbols and $\Delta p_{\rm av}$ – black symbols; water – circles, glycerol – triangles, 0.5% n-butanol – squares, 0.8 M Na₂SO₄ – rhombuses, 1% CMC – stars, and 2% CMC – crosses) (Banković-Ilić, 1999).

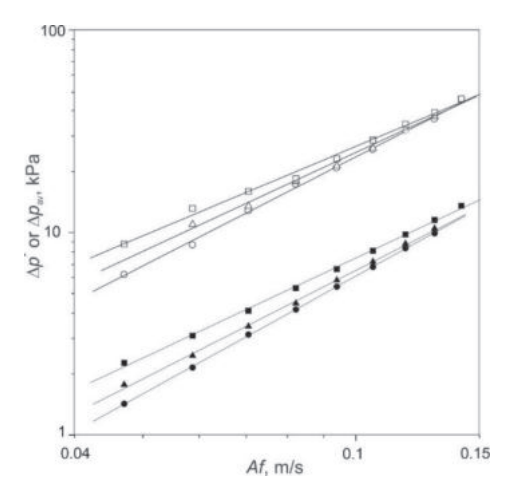


Figure 4.5 Dependence of the total (open symbols) and mean (close symbols) pressure variation at the column bottom filled with "pure" liquids on the reciprocating intensity: $D_c = 16.6$ cm, water – circle, 0.5% CMC – triangle, and 1.0% CMC – square (Vasić et al., 2005a).

The effect of increasing reciprocating intensity on the pressure variation at the column bottom exhibits an interesting behavior (Banković-Ilić, 1999; Banković-Ilić et al., 1995; Rama Rao and Baird, 1986; Veljković and Skala, 1986). Initially, the pressure variation at the column bottom shows a linear increase with reciprocating intensity, but beyond a certain critical point, it reaches a maximum and subsequently decreases, especially within the unstable operation regime. The critical reciprocating intensity at which the pressure variation at the column bottom shows a maximum

depends on the superficial gas velocity, the reciprocating amplitude, the number of perforated plates (Veljković and Skala, 1986), and the rheological properties of the liquid (Banković-Ilić, 1999). Up to the point of reaching this critical reciprocating intensity, the average pressure variation at the column bottom is proportional to $(Af)^n$, with the value of the exponent typically falling within the range of 1.67 to 2.1 for Newtonian liquids (Banković-Ilić, 1999; Vasić et al., 2005a). In contrast, for viscous non-Newtonian liquids, the exponent typically lies in the range of 1.2 to 1.3 (Aleksić et al., 2002a; Banković-Ilić, 1999). Notably, a decrease in the value of the exponent suggests a transition in the flow regime, shifting from turbulent to a regime more closely resembling laminar flow.

Enhancing the liquid flow rate (Baird and Rama Rao, 1997; Rama Rao and Baird, 1986), alongside reducing the gas phase flow rate (Aleksić et al., 2002a; Banković-Ilić, 1999), both contribute to a noticeable increase in the pressure variation at the column bottom within the two-phase system, as depicted in Figure 4.6. Importantly, this effect remains consistent regardless of the specific rheological properties inherent to the liquid phase (Aleksić et al., 2002a).

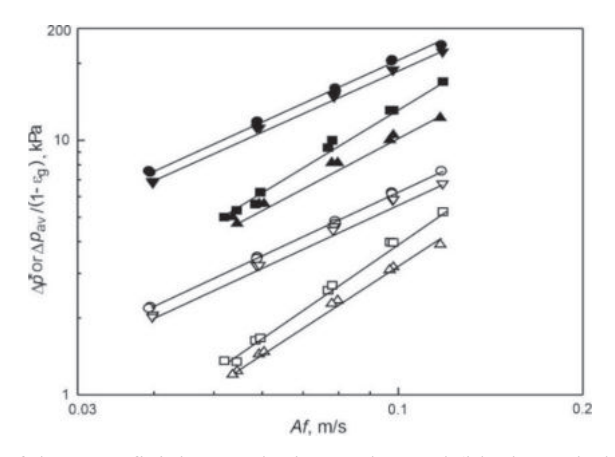


Figure 4.6 Effect of the superficial gas velocity on the total (black symbols) and mean (open symbols) pressure variation at the column bottom (distilled water: $u_{\rm g}$ (cm/s): 0.5 – squares and 1.5 – triangles; aqueous CMC solution: $u_{\rm g}$ (cm/s): 0.5 – circles and 1.5 – inverted triangles) (Aleksić et al., 2002a).

When the gas flow rate through the column increases, it reduces dispersion density and frictional interactions within the system. Consequently, this reduction results in a decrease in the pressure variation at the column bottom. Furthermore, augmenting the number of reciprocating plates while concurrently reducing the fractional free plate surface has intensified the pressure variation at the column bottom (Rama Rao and Baird, 1986), in line with the theoretical Equations (4.11) and (4.14).

Regardless of the type of solid phase placed in the spaces between the perforated plates (spheres or Rashig rings), the pressure variation at the column bottom in the case of a two-phase liquid-solid phase system is greater if the solids fraction is larger (Aleksić et al., 2002a; Banković-Ilić, 1999; Banković-Ilić et al., 2004a). It results from a greater frictional interaction of solid particles with the liquid and plates. By increasing the reciprocating intensity, the pressure variation at the column bottom increases (Figure 4.7a).

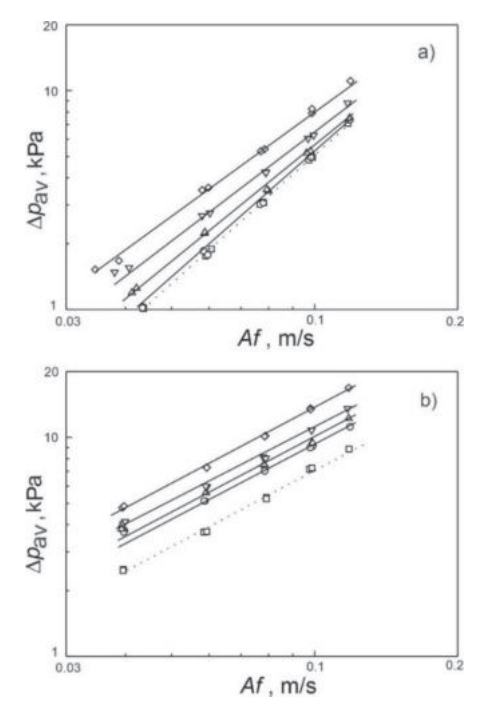


Figure 4.7 Dependence of the mean pressure variation at the column bottom on the reciprocating intensity for two-phase (liquid-solid) systems: (a) distilled water and (b) aqueous 1% CMC solution (ε_s , %: $0 - \square$, $0.35 - \circ$, $0.87 - \Delta$, $1.74 - \nabla$, and $3.2 - \delta$ (Aleksić et al., 2002a).

The slope of the straight lines depends on the solids fraction and the characteristics of the liquid, i.e., the flow regime. In the case of Newtonian liquids, this slope is approximately 2, regardless of the type of solid particles. In the case of Rashig rings and Newtonian fluid, the slope decreases with increasing solids fraction. When a solid phase is inserted into the interspaces between the plates, the effective free cross-section of the plates through which the liquid flows decreases, thus changing the liquid flow regime (Aleksić et al., 2002a; Vasić et al., 2005a). In the case of non-Newtonian liquids (Figure 4.7b), the slope of the straight lines is less than 2, which, based on the analogy with the behavior of "pure" liquids, is explained

by a change in the flow regime in the presence of a solid phase. When Rashig rings are present in the column, the slope of the straight lines is slightly lower in the presence of solid particles (1,0) than in their absence (1,2). Hence, the contribution of reducing the free section of the perforated plates due to the presence of solid particles to the regime change is not significant.

Under the same operating conditions, the pressure variation at the column bottom with a three-phase system is smaller than in a two-phase liquid-solids system due to a lower dispersion density (Aleksić et al., 2002a; Banković-Ilić, 1993, 1999; Banković-Ilić et al., 1993, 1996; Stamenković et al., 2004). In the case of viscous solutions (glycerol and CMC), the pressure variation at the column bottom is greater than in the case of water due to greater frictional interaction (Banković-Ilić et al., 1996). Reciprocating intensity, superficial gas velocity, type, and solids fraction affect the total and mean pressure variation at the column bottom. A decrease in the superficial gas velocity contributes to an increase in the pressure variation at the column bottom due to a reduced gas holdup and an apparent increase in the dispersion density (Figure 4.8). The effect of superficial gas velocity is more evident in the case of spheres (diameter 8.3 mm) than in Rashig rings (diameter and height each 8 mm). At the lowest superficial gas velocity, the pressure variation at the column bottom is greater in the presence of spheres than in their absence. Increasing the reciprocating intensity increases the pressure variation to a maximum value, then decreases (Banković-Ilić et al., 1995); Rashig rings, while the case is reversed at the highest (Veljković and Skala, 1986). This change is observed in a 2.54 cm i.d.

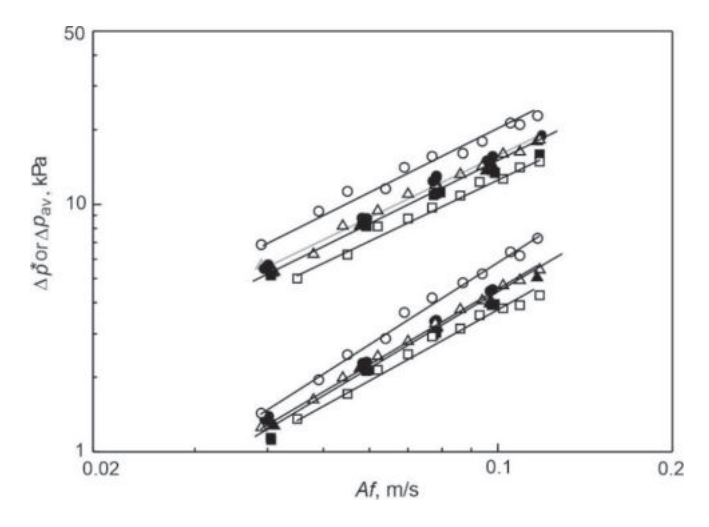


Figure 4.8 Effect of the superficial gas velocity on the total and the mean pressure variation at the column bottom (spheres – open symbols and Rashig rings – black symbols; $u_{\rm g}$ cm/s: 0.5 – squares, and 1.5 – triangles (Aleksić et al., 2002a).

reciprocating plate column. In the area of low reciprocating intensity, before reaching the critical reciprocating intensity, the pressure variation at the column bottom is proportional to $(Af)^n$, where the exponent n is close to 1, regardless of the column geometry. In the 9.2 and 16.6 cm i.d. reciprocating plate columns, a maximum is not observed, regardless of the properties of the liquid phase. An increase in the solids fraction contributes to an increase in the pressure variation at the column bottom due to greater frictional interactions in the system (Banković-Ilić, 1999; Banković-Ilić et al., 1996; Vasić et al., 2005a).

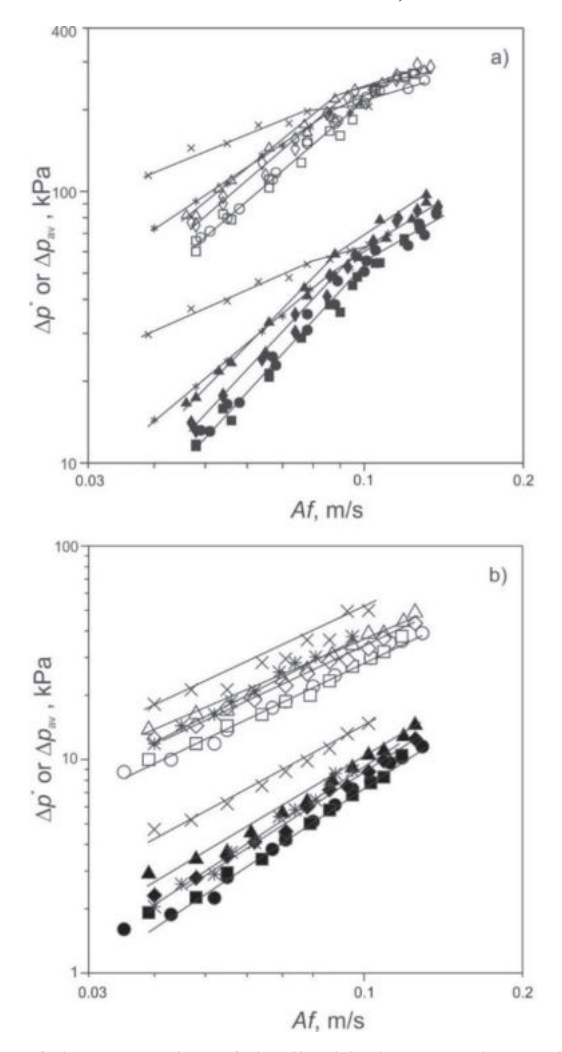


Figure 4.9 Influence of the properties of the liquid phase on the total and mean pressure variation at the column bottom with a two-phase (liquid-solid) system: (a) $D_c = 2.54$ cm and $\varepsilon_s = 6.6\%$ and (b) $D_c = 9.2$ cm and $\varepsilon_s = 3.8\%$ (Δp^* – open symbols and Δp_{av} – black symbols; water – circles, 64% glycerol – triangles, 0.5% n-butanol – squares, 0.8 M Na₂SO₄ – rhombuses, 1% CMC – stars, and 2% CMC—crosses) (Banković-Ilić, 1999).

The properties of the liquid affect the total and mean pressure variation at the column bottom, independently of the column diameter and the type of system (Banković-Ilić, 1999). Larger pressure variations at the column bottom are in the case of liquids with a lower surface tension than water under the same reciprocating intensity and superficial gas velocity (Rama Rao and Baird, 1986). More viscous liquids increase friction between the plates and the liquid and, thus, the pressure variation at the column bottom (Banković-Ilić, 1999; Lounes and Thibault, 1993). In the case of a non-Newtonian liquid (aqueous CMC solution), due to the more intense friction between the liquid and the plates, the total and mean pressure variations at the column bottom are higher than in the case of water (Figure 4.9) (Aleksić et al., 2002a; Banković-Ilić, 1999; Stamenković et al., 2004; Vasić et al., 2005a), under the same operating conditions. Increasing the degree of polymerization, i.e., CMC's molar mass, affects the pressure variation at the column bottom, regardless of the type of system (Banković-Ilić et al., 2004a).

5. POWER CONSUMPTION IN RECIPROCATING PLATE COLUMNS

The total external energy in multiphase-agitated contactors depends on aeration intensity and mechanical agitation. Compressed gas energy is significant at higher gas flow rates and is calculated based on the gas flow rate. The energy of mechanical agitation is determined based on the quasi-steady-state flow model (Jealous and Johnson, 1955). The intensity of mechanical agitation in reciprocating plate columns is related to the amplitude and frequency of reciprocation, the system's physical properties, and the column's construction. An overview of the theoretical Equations for power consumption is given in Table 5.1.

The instantaneous power consumption delivered by the reciprocating agitator to the system is equal to the product of the instantaneous reciprocating plate stack velocity u_s and the force exerted by the reciprocating plates on the system F_p :

$$P = |u_s| F_p = A_c |\Delta p \cdot u_s| \tag{5.1}$$

where Δp is the instantaneous pressure variation at the column bottom and A_c is the cross-sectional area of the column.

Using Equation (4.9) for the instantaneous pressure variation at the column bottom gives the most commonly used equation for calculating power consumption:

$$P = n_p \rho_l A_c \frac{1 - \varepsilon^2}{2C_o^2 \varepsilon^2} u_s^2 |u_s|$$
 (5.2)

where P is the power consumption, n_P is the number of plates, ρ_1 is the liquid density, A_c is the cross-sectional area of the column, ε is the fractional free plate surface, C_0 is the plate opening coefficient, and u_s is the reciprocating plate stack velocity.

The mean power consumption is calculated by integrating the instantaneous power consumption, assuming that C_0 does not vary with time (Banković-Ilić, 1993; Lounes and Thibault, 1993):

$$P_{av} = \frac{16\pi^2}{3} n_p \rho_l A_c \frac{1 - \varepsilon^2}{C_o^2 \varepsilon^2} (Af)^3 \left(\frac{3}{5} s^2 + 1\right)$$
 (5.3)

where P_{av} is the average power consumption, and s is the ratio of the reciprocating amplitude and the length of the tie-rod.

The total power consumption (P^*) in incompressible systems is defined as the product of the total pressure variation at the column bottom and the maximum reciprocating plate stack velocity:

mns.	Reference		$\begin{cases} $	Thornton (1957)	Miyauchi and Oya (1965)	Baird and Lane (1973)	Noh and Baird (1984)	Harikrishnan and Varma (1992)	Banković-Ilić et al. (1993,1995), Lounes and Thibault (1993)
Table 5.1 Review of theoretical equations for the calculation of power consumption in pulsed and reciprocating columns			$P = A_c \left\{ \left(\rho_l l_c - \rho_{puls} l_{puls} \right) g + \left(\rho_l l_c + \rho_{puls} l_{puls} \frac{A_c}{A_{puls}} \right) \frac{d^2 y}{dt^2} + \frac{1}{2} \left[\frac{n_p \rho_l (1 - \varepsilon^2)}{0,36\varepsilon^2} + \left(\frac{A_c}{A_{puls}} - 1 \right)^2 \right] \frac{dy}{dt} \right\} \frac{1}{2} \frac{1}{2}$			$\frac{1-\varepsilon^2)\rho_{SL}}{\sigma^2\varepsilon^2h}(Af)^3$	$\left[^{q}\right) ^{3}$		$\left(\frac{s^2}{5} + 1\right)$
soretical equations for the calcula	Equation		$P = A_c \left\{ (\rho_l l_c - \rho_{puls} l_{puls}) g + \left(\rho_l \right) \right\}$	$\frac{P}{V} = \frac{n_{p}\rho_{l}\pi^{2} (1 - \varepsilon^{2}) (Af)^{3}}{2l_{c}C_{o}^{2} \varepsilon^{2}}$	$\frac{P}{V} = \left(\frac{1}{h} + \frac{1}{l_c}\right) \frac{\rho_l \varepsilon (1 - \varepsilon) (1 - \varepsilon^2) \left u_s^3\right }{2C_o^2}$	$\frac{P}{V} = \Delta \rho \varepsilon_g g \left(\frac{u_d}{\varepsilon_d} - \frac{u_c}{1 - \varepsilon_d} \right) + \frac{2\pi^2 (1 - \varepsilon^2) \rho_{sr}}{3C_o^2 \varepsilon^2 h} (Af)^3$	$\frac{P}{V} = \frac{\rho_{av}}{h} \frac{1 - \varepsilon^2}{C_o^2 \varepsilon^2} \left[\frac{2\pi^2}{3} (Af)^3 + \frac{1}{2} (u_c + u_d)^3 \right]$	$\frac{P_{ov}}{V} = \frac{D_c}{I_c} \left[u \left(u^2 + \frac{3(2\pi Af)^3}{2} \right) \right]$	$P_{uv} = \frac{16\pi^2}{3} n_p \rho_l A_c \frac{1 - \varepsilon^2}{C_o^2 \varepsilon^2} (Af)^3 \left(\frac{3s^2}{5} + 1 \right)$
Review of the	Phase flow	arrangement				$\mathop{\rightarrow}\limits_{\leftarrow}$	←	$\begin{array}{c} \leftarrow \rightarrow \\ \leftarrow \leftarrow \end{array}$	Batch
Table 5.1	Column	type	PBC	PBC	PBC	RPC	RPC	RPC	RPC

Abbreviations: PBC - pulsed bubble column and RPC - reciprocating plate column.

$$P^* = A_c \Delta p^* u_{s,m} = 8\pi^3 n_p \rho_l A_c \frac{1 - \varepsilon^2}{C_o^2 \varepsilon^2} (Af)^3 \left[\sin 2\pi f t \left(1 + s \cdot \cos 2\pi f t \right) \right]_{\text{max}}$$
 (5.4)

since the pressure variation at the column bottom and the reciprocating plate stack velocity are in phase (Hafez and Procházka, 1974b).

At low reciprocating amplitudes, the acoustic flow model is applicable. For the turbulent regime of fluid flow through a plate orifice, the Equation describing the pressure variation at the column bottom due to friction (Panton and Goldman, 1976) is modified by introducing eddy diffusivity ε_{τ} , which varies proportionally with the square of the frequency of the reciprocation motion and the mixing path (Baird and Rama Rao, 1995; Baird et al., 1996):

$$\varepsilon_{\tau} = \left(2\pi f t\right)^2 l_{\rm m} \tag{5.5}$$

where f is the frequency of the reciprocation motion and $l_{\rm m}$ is the mixing path. The average power consumption is proportional to the third power of the frequency and the square of the amplitude:

$$P_{\rm ac} = \frac{3\pi}{8} n_{\rm p} \rho_{\rm l} D_{\rm c}^2 (2\pi f)^3 A^2 \frac{l_{\rm m}}{\varepsilon}$$
 (5.6)

where $P_{\rm ac}$ is the average power consumption according to the acoustic model.

The dependence of the dimensionless power number on the Reynolds number is also used to determine the power consumption of reciprocating plate columns. The power number of a reciprocating agitator is analogous to the power number of a rotary stirrer. The power number has a constant value in the turbulent flow regime and depends on the opening coefficient C_0 and the fractional plate-free area ε :

$$\Phi = \frac{P_{\text{av}}}{n_{\text{p}}\rho_{1}(2Af)^{3}D_{c}^{2}} = \frac{\pi^{3}}{6} \frac{1-\varepsilon^{2}}{\varepsilon^{2}} \frac{1}{C_{o}^{2}} \left(\frac{3}{5}s^{2}+1\right)$$
 (5.7)

where Φ is the power number.

In the laminar regime, the power number depends on the Reynolds number (Lounes and Thibault, 1993):

$$\Phi \propto Re^{0.5} \tag{5.8}$$

In the case of applicability of the acoustic flow model, the power number is as follows (Baird et al., 1996):

$$\Phi = \frac{3\pi^4}{8\varepsilon} \cdot \frac{l_{\rm m}}{A} \tag{5.9}$$

The mean and total power consumption of single-phase and multi-phase systems in reciprocating plate columns depends on several factors, including reciprocating intensity, superficial gas velocity, plate number and geometry, the cross-sectional area of the column, and the physical properties of the phases (Table 5.2).

Table 5.2 Empirical correlations for the power consumption of reciprocating plate columns

System	2 Empirical correlations for the pe	Correlation	Reference
'Pure'	Water	$P_{av} = 2.688 \cdot 10^{-4} n_p \rho_l (2\pi Af)^3$	Pavasović (1975)
1	Water	$P_{av} = 1.742 \cdot 10^{-3} n_p \rho_l (2\pi Af)^3$	Kažić (1979)
	Distilled water, sucrose solution, and a model dextran fermentation broth	$P^* = 2.567 \cdot 10^{-3} n_p \rho_l (2\pi Af)^3$	Veljković and Skala (1986)
	Water	$P^* = 0.34 n_p \rho_l (Af)^3$	Banković-Ilić et al. (1995)
		$P_{av} = 0.0642 n_p \rho_l (Af)^3$	
	Water	$P^* = 5.49 n_p \rho_l (Af)^3$	Banković-Ilić (1999)
		$P_{av} = 1.157 n_p \rho_l (Af)^3$	(111)
	Sunflower oil (batch)	$P^* = 6.840 (Af)^{2.36}$	Stamenković et
		$P_{av} = 1.345 (Af)^{2.33}$	al. (2010)
	Sunflower oil (continuous)	$P^* = 5.432 (Af)^{2.32}$	
		$P_{av} = 1.434 (Af)^{2.39}$	
Gas- liquid	Air-distilled water, sucrose solution, and a model dextran fermentation broth	$P^* = 1.804 \cdot 10^{-3} n_p \rho_l (1 - \varepsilon_g) (2\pi A f)^3$	Veljković and Skala (1986)
	Air-water	$P^* = 0.310n_p \rho_l (1 - \varepsilon_g) (Af)^3$ $P_{av} = 0.0664n_p \rho_l (1 - \varepsilon_g) (Af)^3$	Banković-Ilić et al. (1993)
	Air-water	$P_{av}^* = 0.199 n_p \rho_l (1 - \varepsilon_g) (Af)^3$ $P_{av}^* = 0.0403 n_p \rho_l (1 - \varepsilon_g) (Af)^3$	Banković-Ilić et al. (1995)
	Air-water	$P_{av}^* = 4.481 n_p \rho_l (1 - \varepsilon_g) (Af)^3$ $P_{av}^* = 1.034 n_p \rho_l (1 - \varepsilon_g) (Af)^3$	Banković-Ilić (1999)
Liquid-	Water-solid (spheres, 8.4 mm, 5	$P^* = 0.88n_p \rho_l (Af)^3$	Banković-Ilić et
solid	spheres per each second or third interplate space)	$P = 0.88n_p \rho_l (Af)^3$ $P_{av} = 0.152n_p \rho_l (Af)^3$	al. (1993)
Gas-	Water	$P^* = 0.31 n_n \rho_i (1 - \varepsilon_\sigma) (Af)^3$	Banković-Ilić et
liquid- solid		$P_{av} = 0.0664 n_p \rho_l (1 - \varepsilon_g) (Af)^3$	al. (1993)
Liquid- liquid	Sunflower oil-methanol (1:6 mol/mol)	$P^* = 3.829(1 - \varepsilon_d)(Af)^{2.29}$	Stamenković et al. (2010)
	,	$P_{av} = 1.393(1 - \varepsilon_d)(Af)^{2.48}$	

Additionally, the type, size, and fraction of solids play a significant role (Aleksić et al., 2003; Naseva et al., 2002). Furthermore, power consumption varies with the flow regime of the liquid through the plate openings, which changes with the viscosity of the liquid (Banković-Ilić, 1999). In the laminar region, the total and mean power consumption are correlated with the square of the reciprocating intensity Af, whereas in the turbulent region, the correlation is with the third power of the

reciprocating intensity. Empirical correlations for power consumption have the following form:

$$P^* \text{ or } P_{\text{av}} = k \left(Af \right)^n \left(1 - \varepsilon_g \right) \tag{5.10}$$

where n = 2 in the laminar flow regime and n = 3 in the turbulent flow regime. Under the same operating conditions, the power consumption is greater in a column with an aqueous CMC solution, a non-Newtonian liquid, than with water due to the more intense frictional interaction between the plates and the liquid (Figure 5.1).

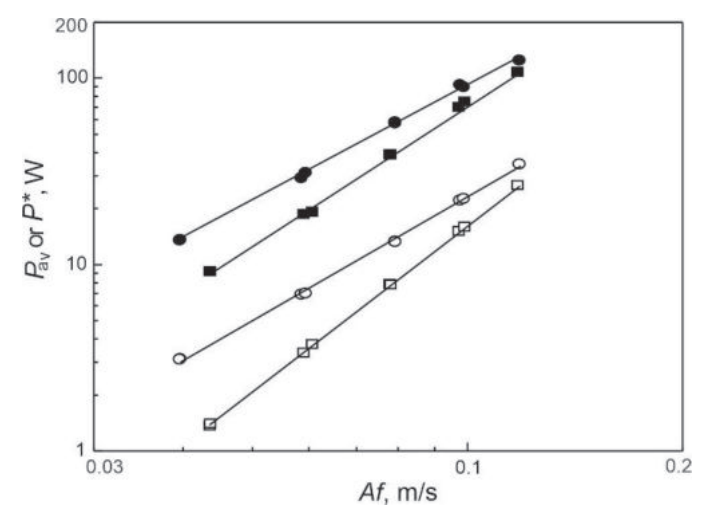


Figure 5.1 The influence of reciprocating intensity on the mean and total power consumption of 'pure' liquids (P_{av} – open symbols and P^* – black symbols; distilled water – squares and aqueous CMC solution – circles) (Aleksić et al., 2003).

As can be seen in Figure 5.2, which shows the dependence of the power number on the Reynolds number, the general conclusion, which is valid for the mixing of "pure" liquids in stirred vessels, is also applicable to reciprocating plate column: the power number decreases linearly with increase of the Reynolds number in the laminar regime, so that $\Phi \propto \text{Re}_o^{-0.5}$ and $P \propto (Af)^2$ while it does not depend on the Reynolds number in the turbulent regime: $\Phi = const$ and $P \propto (Af)^3$. When the flow regime through the plate openings changes from turbulent to laminar, the value of n in Equation (5.10) changes from 3 to 2. The column and plate geometries have a negligible influence on the laminar flow regime. However, as the column diameter increases for a constant fractional plate-free area, the power number increases in the turbulent region. Conversely, when the column diameter remains constant, the fractional plate-free area directly impacts the power number.

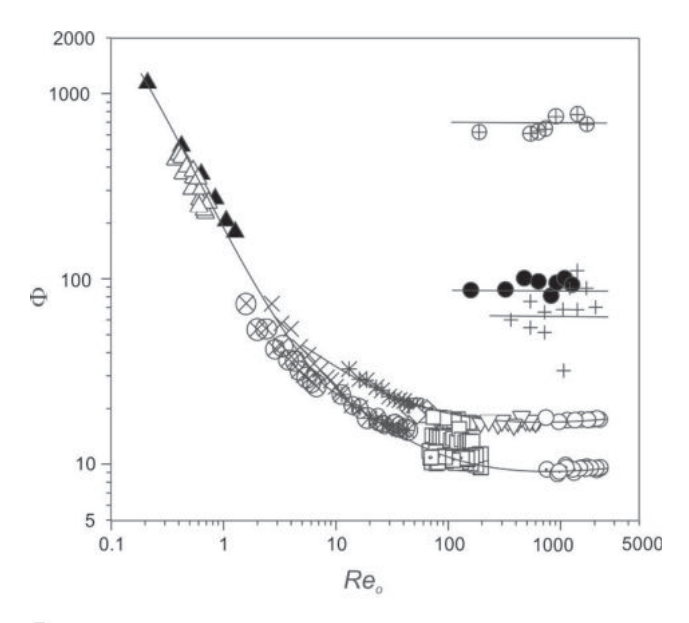


Figure 5.2 Dependence of the power number of 'pure' liquids on the Reynolds number: 1) $D_c = 14.96$ cm, $\varepsilon = 0.12 - \oplus$ and $\varepsilon = 0.53 - +$: water (Hafez and Baird, 1978); 2) $D_c = 10.2$ cm, $\varepsilon = 0.28$: water $- \bullet$ and 100% glycerol $- \blacktriangle$ (Lounes and Thibault, 1993); and 3) $D_c = 2.54$ cm, $\varepsilon = 0.51$: water $- \odot$, 64% glycerol $- \Box$, 1% CMC $- \odot$, and 2% CMC $- \odot$; $D_c = 9.2$ cm, $\varepsilon = 0.45$: water $- \odot$, 100% glycerol $- \Delta$, 69% glycerol $- \Diamond$, 64% glycerol $- \Box$, 40% glycerol $- \blacktriangledown$, 1% CMC $- \ast$, and 2% CMC $- \times$ (Banković-Ilić, 1999).

An increase in liquid viscosity leads to higher power consumption due to increased frictional interaction between the plates and the liquid (Banković-Ilić et al., 1995). This effect is observed in both Newtonian liquids, such as aqueous glycerol solutions (Banković-Ilić, 1999), and non-Newtonian liquids, such as aqueous CMC solutions (Banković-Ilić et al., 1998b; Naseva, 2002). Furthermore, with higher concentrations and degrees of polymerization under unchanged operating conditions, a corresponding increase in power consumption occurs (Figure 5.3).

The power consumption of gas-liquid dispersion also depends on the gas holdup in the column (Figure 5.4). Increasing superficial gas velocity generally decreases power consumption across various reciprocating plate column geometries, as higher gas holdup reduces frictional interaction between the fluid and reciprocating plates (Aleksić et al., 2003; Banković-Ilić, 1999; Banković-Ilić et al., 1998a; Baird and Rama Rao, 1997; Lounes and Thibault, 1993; Vasić et al., 2006a; Veljković, 1985; Veljković and Skala, 1986). In both single-phase and two-phase systems, regardless of column diameter or liquid type, total and mean power consumptions are generally lower in two-phase systems under similar conditions due to reduced frictional interaction between plates and liquid.

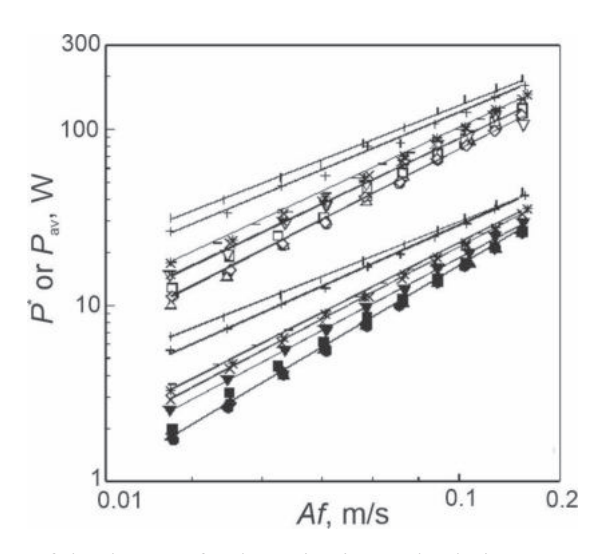


Figure 5.3 Influence of the degree of polymerization and solution concentration on the total (open symbols) and mean (black symbols) power consumption of 'pure' liquids (liquid: aqueous carboxymethylcellulose solutions; PP 50: 0.5% – circles, 1% – triangles, and 2% – squares; PP 200: 0.5% – rhombuses, 1% – inverted triangles, and 2% – +; PP 500: 0.5% – crosses and 1% – stars; and PP 1000: 0.5% – dashes and 1% – up dashes) (Naseva, 2002).

The presence of a solid phase in the interplate spaces significantly impacts total and mean power consumption. Due to friction between solid particles (such as spheres or Rashig rings), the liquid, and the plates, power consumption increases in two-phase (liquid-solid) systems with higher solids fractions (Aleksić et al., 2003; Banković-Ilić, 1999; Naseva et al., 2002). This effect holds when compared to single-phase systems operating under identical conditions, irrespective of the rheological properties of the liquid phase (Figure 5.5). The slope of the $log(P_{av})$ -to- $\log(P^*)$ relationship on $\log(Af)$ depends on the properties of the liquid and the solids fraction, generally decreasing with increasing solids fraction (Figure 5.6). For distilled water, the slope of mean power consumption changes from approximately 3 in single-phase systems to 2.5 with the highest solids fraction (Aleksić et al., 2003). This change likely results from reduced effective fractional plate-free area for liquid flow and a shift in flow regime from turbulent to transitional in the presence of solid particles. In contrast, the mean power consumption slope for non-Newtonian CMC solutions with pseudoplastic behavior stabilizes around 2, regardless of solids fraction, due to laminar or transitional flow through plate openings, whether solids are present or not (Aleksić et al., 2003).

An increase in the superficial gas velocity at a constant reciprocating intensity reduces power consumption. It occurs because the increased gas holdup decreases frictional interaction, regardless of the liquid's rheological properties (Figure 5.7).

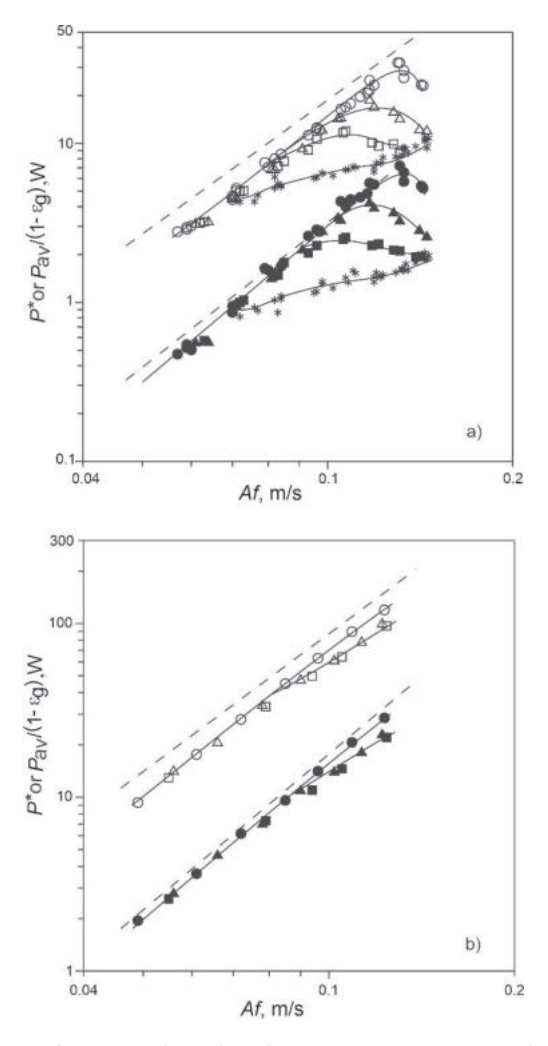


Figure 5.4 Dependence of corrected total and mean power consumption of two-phase (gas-liquid) systems on reciprocating intensity at a constant superficial gas velocity: a) $D_c = 2.54$ cm and b) $D_c = 9.2$ cm (liquid: water; P^* – open symbols and $P_{\rm av}$ – black symbols; single-phase system – dashed line, $u_{\rm g}$ cm/s: 0.5 – squares, 1.0 – triangles, 1.5 – squares, and 3.0 – stars (Banković-Ilić, 1999).

The influence of the solids fraction on the power consumption of three-phase systems is determined by the rheological properties of the liquid, the superficial gas velocity, and the reciprocating intensity (Figure 5.6). At a smaller solids fraction (Naseva et al., 2002), the increase in gas holdup compensates for the intensified frictional interaction caused by spherical particles, resulting in reduced power consumption. For a non-Newtonian fluid with a lower CMC concentration (0.5%), the power consumption is similar for two-phase and three-phase systems when

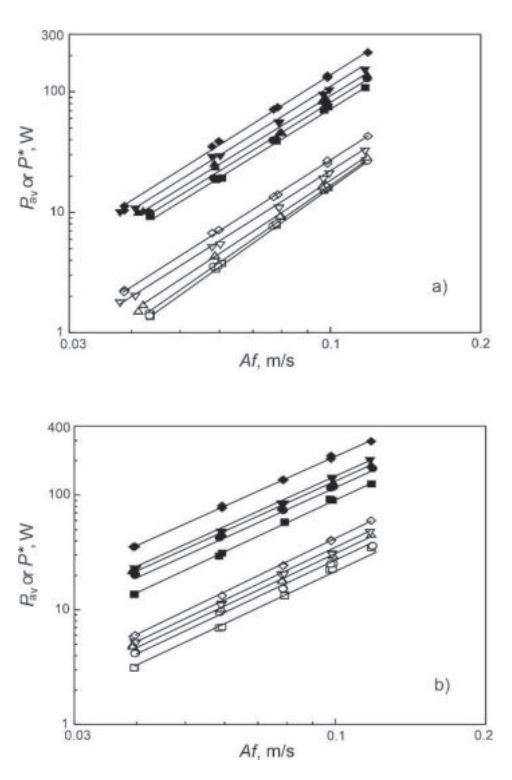


Figure 5.5 Dependence of mean and total power consumption of two-phase (liquid-solid) systems on reciprocating intensity ($D_c = 9.2$ cm): (a) distilled water and (b) aqueous 1% CMC solution (ε_s , % vol.: 0 – squares; 0.35 – circles; 0.87 – triangles; 1.74 – inverted triangles, and 3.2 – rhombuses; P^* – black symbols and P_{av} – open symbols) (Aleksić et al., 2003).

divided by the liquid holdup. However, with a larger solids fraction, the power consumption is higher. In a more concentrated solution (1% CMC), the presence of a solid phase increases the corrected power consumption at the lowest superficial gas velocity (Naseva et al., 2002, 2003), but does not affect power consumption at higher superficial gas velocities due to the adverse effect of increased gas holdup (Naseva et al., 2002). The solid phase in the column increases friction, leading to greater pressure variation at the column bottom and higher power consumption. Consequently, the power consumption of a system with introduced gas is lower than that of a system without gas, owing to reduced frictional interaction.

The rheological properties of the liquid significantly influence power consumption. For non-Newtonian liquids, power consumption is higher than for water due to more intense frictional interactions between the liquid, reciprocating plates, and solid particles (Aleksić et al., 2003; Banković-Ilić, 1999; Banković-Ilić et al., 1996). Under the same operating conditions, the power consumption of a three-

phase system increases with the degree of polymerization of CMC, as the increased viscosity leads to more intense friction between the plates, spheres, and liquid (Naseva et al., 2003). Similarly, in Newtonian solutions, an increase in liquid viscosity also results in higher power consumption (Banković-Ilić et al., 1996).

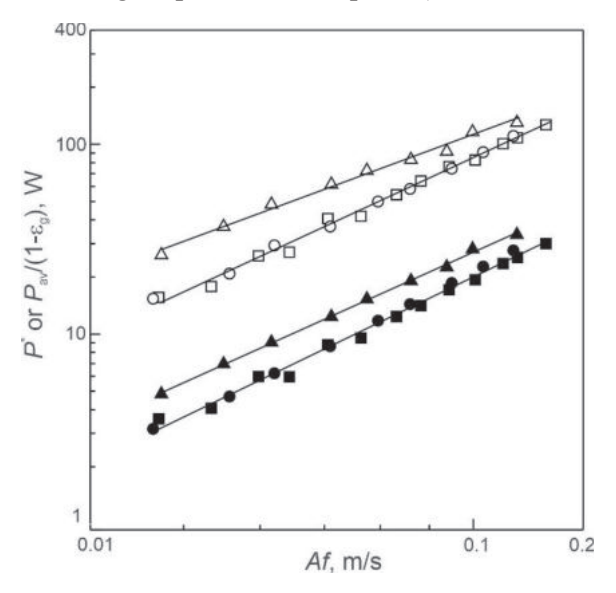


Figure 5.6 Effect of a solid phase (spheres: 8.3 mm) on the total and mean power consumption (liquid: 0.5 % CMC solution; $D_c = 9.2$ cm; u_g , cm/s: 0.5 cm/s; liquid-solid system – squares; three-phase system: ε_s , %: 3.84 – circles; 6.61 – triangles; P^* – open symbols and P_{av} – black symbols) (Stamenković et al., 2002).

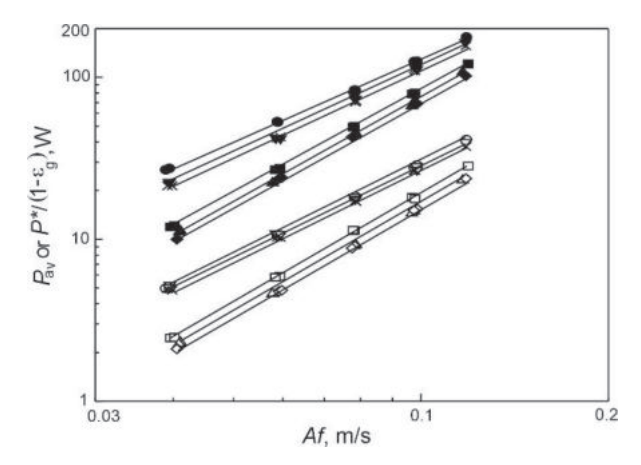


Figure 5.7 Effect of superficial gas velocity on the power consumption of three-phase systems (distilled water; Rashig rings (0.8 cm): 3.2%; D_c : 9.2 cm; P^* – black symbols and $P_{\rm av}$ – open symbols; $u_{\rm g}$, cm/s: 0.5 – squares, 1.0 – triangles, and 1.5 – rhombuses; 1% CMC solution: $u_{\rm g}$, cm/s: 0.5 – circles, 1.0 – inverted triangles, and 1.5 – stars) (Aleksić et al., 2003).

The power consumption of a liquid-solid system follows a proportional relationship of $(Af)^n$, where the exponent depends on the diameter of the column and the type of liquid (Banković-Ilić, 1999). For Newtonian liquids, the slope of the total and average power consumption as a function of reciprocating intensity is higher in smaller diameter columns (approximately 3) compared to larger diameter columns (approximately 2). This difference is likely due to increased frictional interactions caused by a greater number of solid particles in the interplate spaces of larger-diameter columns. In the case of non-Newtonian liquids, this slope approaches a value of 2. Solutions with higher concentrations of CMC, characterized by greater pseudoplasticity, exhibit deviations from values observed in Newtonian liquids (Banković-Ilić, 1999). For three-phase systems, the slope of the power consumption dependence on reciprocating intensity is close to 2. However, this slope tends to be slightly smaller when there is a higher fraction of the solid particles, irrespective of the column diameter.

Earlier research in a smaller diameter column indicated that within a solids fraction range of 3.8–6.6%, the number of solid particles in the interplate space and their distribution along the column height has a negligible effect on power consumption (Banković-Ilić, 1993; Banković-Ilić et al., 1993; 1996; Skala and Veljković, 1996). However, a detailed analysis of power consumption for all tested liquids in two columns (diameters 2.54 and 9.2 cm) revealed that the number and arrangement of the solid particles (Figure 5.8) do impact power consumption.

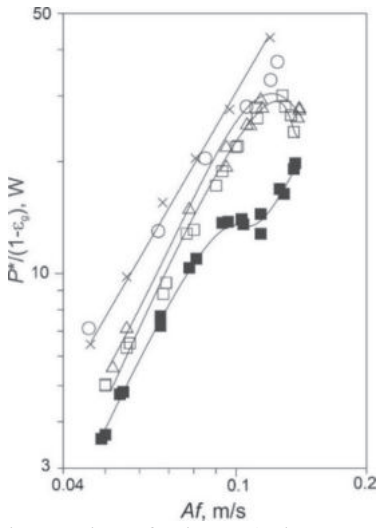


Figure 5.8 The influence of the number of spheres (spheres: 8.3 mm) in the interplate space on the total power consumption of a three-phase system (liquid: water; D_c : 2.54 cm; $u_g = 0.5$ cm/s: 5 spheres per interplate space $- \circ$, 5 spheres per second interplate space $- \Delta$, 5 spheres per third interplate space $- \Box$, and 10 spheres per second interplate space $- \Box$; $u_g = 1.5$ cm/s: 5 spheres per second interplate space $- \times$) (Banković-Ilić, 1999).

Specifically, power consumption in the three-phase system increases with a higher solids fraction due to increased frictional interactions, with this effect being particularly significant in the case of water.

The shape and type of solid particles significantly influence overall power consumption (see Figure 5.9). Under nearly identical operating conditions (solids fraction and gas flow rate) with a superficial gas velocity of 0.5 cm/s, spheres exhibit higher power consumption compared to Rashig rings. However, at higher superficial gas velocities, the trend reverses due to varying effects of solid particles and gas flow rate on power consumption and gas holdup.

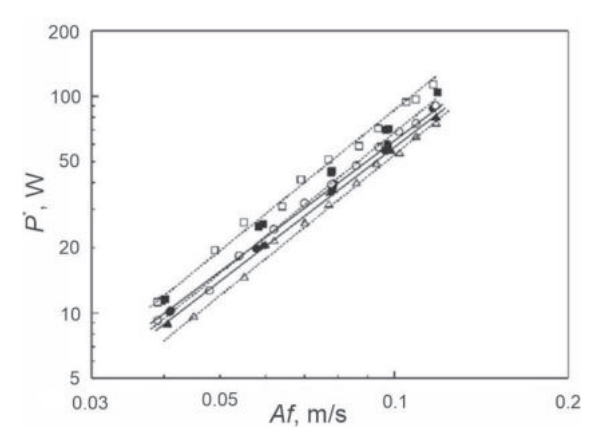


Figure 5.9 The influence of the type of solid particles ($D_c = 9.2$ cm; spheres: 8.3 mm, ε_s : 3.8 vol.% – open symbols; and Rashig rings: 8×8 mm, ε_s : 3.2 vol.% – black symbols) on the total power consumption of three-phase systems as a function of the reciprocating intensity at different superficial gas velocities: (liquid: distilled water; u_g , cm/s: 0.5 – squares, 1.0 – circles, and 1.5 – triangles) (Aleksić et al., 2003).

6. PLATE OPENING COEFFICIENT FOR RECIPROCATING PLATE COLUMNS

Equation (5.3) can be used to calculate the energy required for mechanical agitation in reciprocating plate columns, assuming that the reciprocating amplitude exceeds the critical threshold and the plate opening coefficient is constant. Knowing the value of the plate opening coefficient is, therefore, critical for calculating the pressure variation at the column bottom and the power consumption. Physically, the plate opening coefficient represents the resistance to fluid flow through the plate openings. Under turbulent flow conditions, the average value of the plate opening coefficient is nearly constant and independent of the Reynolds number (usually adopted $\overline{C}_0 = 0.6$), while in the laminar regime, it is proportional to the square root of the Reynolds number (Lounes and Thibault, 1993):

$$\overline{C}_o = k \operatorname{Re}^{0.5} \tag{6.1}$$

The plate opening coefficient is influenced by several factors, including the reciprocating amplitude and frequency, the geometric characteristics of the plates (Hafez and Procházka, 1974a,b; Hafez and Baird, 1978), the superficial liquid velocity (Noh and Baird, 1984), the superficial gas velocity, and the physical properties of the liquid (Lounes and Thibault, 1993; Boyle, 1975), as shown in Table 6.1. Therefore, calculating the average power consumption using Equation (5.3) is reliable only when the experimentally determined values of the plate opening coefficient are known.

The mean value of the plate opening coefficient in the turbulent regime of liquid flow through the plate openings can be calculated using Equations (4.11) and (4.14). This calculation is based on measured values of the total and mean pressure variations at the column bottom. It can be performed using individual measurements of these pressure variations at the corresponding reciprocating intensity:

$$\overline{C}_o = \left[n_{\rm p} \rho_{\rm l} \left(1 - \varepsilon_{\rm g} \right) \frac{1 - \varepsilon^2}{\varepsilon^2} \frac{\left(2\pi A f \right)^2}{\Delta p^*} \right]^{0.5}$$
(6.2)

$$\overline{C}_o = \left[n_{\rm p} \rho_{\rm l} \left(1 - \varepsilon_{\rm g} \right) \frac{1 - \varepsilon^2}{2\varepsilon^2} \left(\frac{1}{2} + \frac{4s}{3\pi} + \frac{s^2}{8} \right) \frac{\left(2\pi Af \right)^2}{\Delta p_{\rm av}} \right]^{0.5}$$

$$(6.3)$$

or from the slope of the linear relationship between the pressure variations at the column bottom and the squared reciprocating intensity (Banković-Ilić et al., 1997).

	Reference		Kažić (1979)	Veljković and Skala	(1986)	Banković-Ilić et al.	(1995)	Yang et al. (1986a)	Noh and Baird	(1984)	Rama Rao and Baird	(1988)	Hafez and Procházka	(1974a, 1974b)	Rama Rao and Baird		.7–0.95 Lounes and Thibault	(1993)	$1d \propto Re^{0.5}$		Hafez and Baird	(1978)	Baird and Rama Rao	(1995)	Baird et al. (1996)
	\overline{C}_o	$(Af > 0^a)$	1.16	1.02		0.99		0.79	0.6°	11	0.4 - 0.6				0.6^{d}		0.4 ^b and 0.7–0.95	0.39-0.49	$0.2-0.6$ and $\propto \text{Re}^{0.5}$	0.2 - 0.66			0.6^{d}		0.6^{d}
	\overline{C}_o	(liquid flow, $Af = 0$)	1.20					$\propto \mathrm{Re}^{0.54}$	0.42 - 0.75	depending on u _l	0.97		6.0-8.0								0.55-0.58				
geometry on the mean plate opening coefficient.	System		Water	Water, aqueous	sucrose solution	Water		Air-water	Tap water	ı	Water		Water		Water, kerosene		Water	Air-water	Glycerol	Air-glycerol	Water		Water		Water
te opening	\mathcal{A}	cm	0.5 - 1.96	0.1 - 1.0		1.3 - 2.35		0 - 1.88	<2.25		2.5		0.1 - 1.2		0.7 - 3.2		1.25-5				0.31-	1.27	0.5-2		0.1 - 1
ıean pla	3		0.51	0.41		0.51		0.53	0.61		0.57		$2-7.4 \ 0.04-$	0.362	0.094 -	0.306	0.28				0.123 -	0.531	0.169 -	0.423	0.235 - 0.377
n the m	d_o	mm	8	7		∞		1.5	13.7		14		2–7.4		3-8		6.35				7.5	14.7	4-12		70
netry o	δ	mm	pu	1		_		1.5	pu		1.4		2-4		pu		1.25				1.4		1.5		7
m geon	h	cm	2.54	2.5,	5.0	2.54		2.54	5.08		5.2-	7.75	5-10		5.6		2				2.4-	25	5-20		22.5
Table 6.1. Influence of the system	n_p		78	33,65		65		84	29		19–54		30		2 - 10		18				12-47		5		1-10
ence of	D_c	cm	2.54	2.54		2.54		5.08	5.08		5.08		8.5		9.3		10.16				14.96		19.4		15
1. Influ	Phase	flow	Batch	Batch		Batch		\leftarrow	\downarrow		Batch		Batch		$\overset{\rightarrow}{\leftarrow}$		Batch				Batch		Batch		Batch
Table 6.	Type of Phase	RPC	KRPC	KRPC		KRPC		KRPC	KRPC		KRPC		RPC,	no SP	RPC,	no SP	RPC				KRPC,	RPC	BRPC		BRPC

Abbreviations: KRPC - Karr-type reciprocating plate column, RPC - reciprocating plate column, and SP - segmental passages a Calculated from Δp^{*} . b Calculated from Δp_{av} . c According to Rama Rao and Baird (1988). d Adopted value.

This calculation method is not applicable in laminar and transitional flow regimes due to the dependence of the plate opening coefficient on the Reynolds number. Instead, Equation (6.1) is substituted into Equation (4.9) and then integrated into the calculation. The mean value of the plate opening coefficient in these regimes is determined as follows (Lounes and Thibault, 1993):

$$\bar{C}_{o} = \left[\frac{2n_{p}\rho_{1}(1-\varepsilon_{g})}{\Delta p_{av}} \left(\frac{1-\varepsilon^{2}}{\varepsilon^{2}} \right) \right]^{0.5} (2Af)$$
(6.4)

Banković-Ilić et al. (1997) developed a procedure to calculate the plate opening coefficient independently of the fluid flow regime. This method assumes that the plate opening coefficient varies with time during one cycle of the reciprocating motion. The variation in the plate opening coefficient over time is due to changes in the reciprocating plate stack velocity, and consequently, the liquid velocity through the plate openings (Hafez and Procházka, 1974a, b; Hafez and Baird, 1978). First, the instantaneous value of the plate opening coefficient is calculated based on the instantaneous pressure variation at the column bottom and the instantaneous reciprocating plate stack velocity (Banković-Ilić et al., 1997):

$$C_{o} = \left[n_{p} \rho_{l} \left(1 - \varepsilon_{g} \right) \frac{1 - \varepsilon^{2}}{2\varepsilon^{2}} \frac{u_{s} \left| u_{s} \right|}{\Delta p} \right]^{0.5}$$

$$(6.5)$$

Then, its average value is calculated as follows:

$$C_{\text{o,av}} = \left| \frac{1}{T} \int_{0}^{T} C_{\text{o}}(t) dt \right| \tag{6.6}$$

where $C_{0,av}$ is the time-averaged plate opening coefficient, $C_0(t)$ is the instantaneous plate opening coefficient, T is the period of time under consideration, and t is time. A recorded or processed signal of the pressure variation at the column bottom can be used in this calculation.

Figure 6.1 illustrates typical variations in the square of the plate opening coefficient, the pressure variation at the column bottom, and the reciprocating plate stack velocity over one movement cycle. The pressure changes asymmetrically during the up-and-down movement of the reciprocating plates (Banković-Ilić et al., 1995; Rama Rao and Baird, 1988). The figure shows the recorded and processed pressure signals, along with the square of the plate opening coefficient calculated using Equation (6.5). The maxima of all the curves are in phase, indicating that the plate opening coefficient reaches its peak value when friction losses are at their highest and drops to zero when the reciprocating plate stack velocity and pressure variation at the column bottom are zero. Consequently, the maximum values of the plate opening coefficient, calculated based on the processed pressure variation signal

at the column bottom, are approximately 30% higher than the corresponding mean value (Table 6.2).

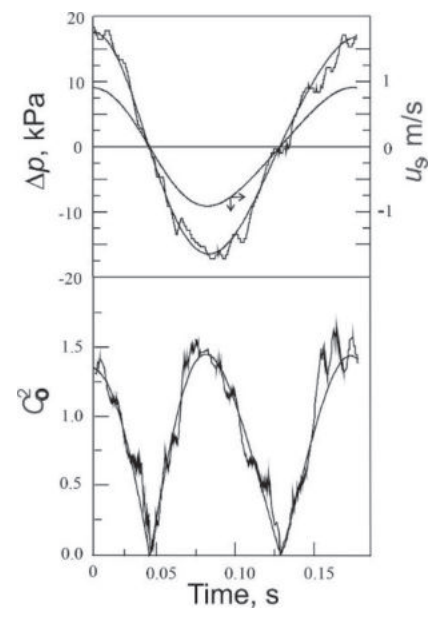


Figure 6.1 Changes in the vibrating plate velocity, the pressure at the column bottom, and the square of the plate opening coefficient with time during one cycle of reciprocating motion (liquid: distilled water; $D_c = 9.2$ cm; f = 5.9 Hz; Δp and C_o^2 : solid line – recorded signal, and dashed line – processed signal) (Banković-Ilić et al., 1997).

The values of the plate opening coefficient calculated from the processed pressure signals are slightly lower (by 4.5%) than those determined from the recorded pressure signals at the column bottom (Figure 6.2). Occasionally, the plate opening coefficient exceeds 1, which is not unexpected, particularly at higher frequencies and in two-phase gas-liquid systems. At higher frequencies, interference occurs between the plates and the fluid streams through the individual openings. When the plates move quickly, the time required to reach maximum column pressure is too short, which would otherwise be attained if the plates were moving at a constant speed (Lounes and Thibault, 1993).

The values of the plate opening coefficient vary depending on whether they are calculated based on the total or mean pressure variation at the column bottom. Additionally, different researchers have reported varying findings. For instance, Banković-Ilić et al. (1997) found that, in the turbulent flow regime, the plate opening coefficient calculated from the mean pressure variation at the column bottom is slightly higher (about 6.9%) than that calculated from the total pressure variation at the column bottom, regardless of column geometry and liquid properties (Table 6.2).

Table 6.2 The plate opening coefficient calculated by Eqs. (6.2), (6.3), and (6.6) for single-phase systems (Banković-Ilić et al., 1997).

Liquid	D_c		$C_{ m o,av}$	10		$C_{o,\max}$	Comax
	cm			Ĩ		`	$C_{o,av}$
		Calculated based	Calculated based	Calculated based on	Calculated based	Calculated based	Co,av calculated
		on the processed	on the recorded	the mean pressure	on the mean	on the processed	based on the pro-
		pressure signal, Equation $(6.6)^a$	pressure signal, Equation $(6.6)^a$	variation, Equation (6.3) ^b	pressure variation Equation $(6.2)^b$	pressure signal	cessed pressure signal
Water	2.54	1.06	1.14	1.26	1.12	1.35	1.28
	9.2	0.95	0.97	1.11	1.08	1.23	1.30
n-Butanol				1.26	1.09		
(0.5%)		0.93	0.98	1.11	1.08	1.20	1.29
Sodium sulfite		1		1.26	1.18		
(0.8 mol/dm^3)	9.2	96.0	1.02	1.11	1.09	1.29	1.34
Glycerol		0.91	0.94	1.12	1.08	1.19	1.30
(40%)							
Glycerol		96.0			1.10	1.29	1.35
(64%)		96.0	1.05	1.13	1.09	1.27	1.32
CMC (1%)							1.33
							1.32
CMC (2%)	2.54						1.33
	9.2						1.28

^a Mean value in the area Af for which the turbulent regime applies. ^b Calculated from the slope of the dependence Δp^* or Δp_{ω} on $(Af)^2$.

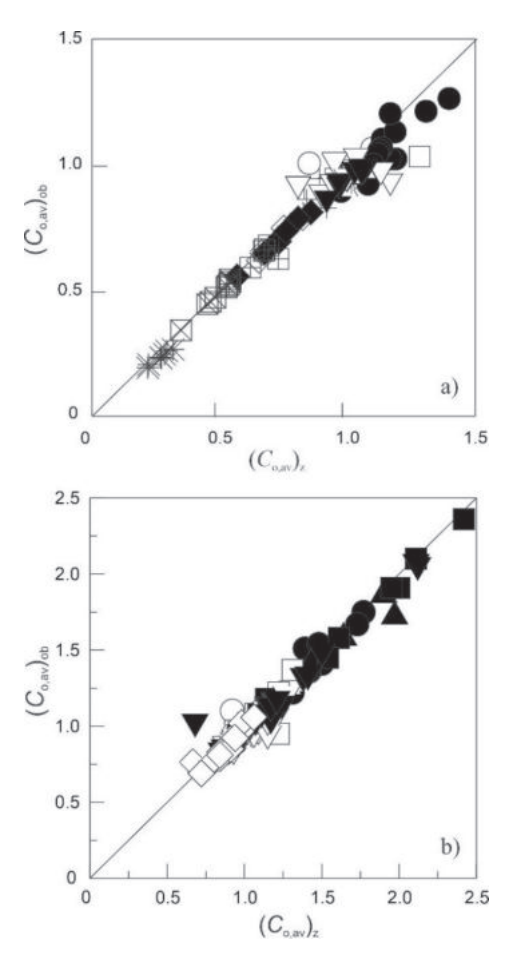


Figure 6.2 Comparison of plate opening coefficients determined based on the processed and recorded pressure signals at the column bottom: (a) gas-liquid and (b) liquid (D_c , cm: 2.54 – black symbols, and 9.2 – open symbols; water – circles, 0.5% n-butanol – triangles, 0.8M sodium sulfite – squares, 40% glycerol – +, 64% glycerol – inverted triangles, 100% glycerol – *, 1% CMC – rhombuses, and 2% CMC – + squares and × squares, respectively; adapted from Banković-Ilić et al., 1997).

Conversely, other researchers (Rama Rao and Baird, 1988; Lounes and Thibault, 1993) reported that, for water, the plate opening coefficient calculated from the total pressure variation at the column bottom is significantly higher than the value calculated from the mean pressure variation at the column bottom.

In the turbulent liquid flow regime (single-phase system), the mean plate opening coefficient calculated using Equation (6.6) based on the processed pressure signal is 16.2% lower than the mean plate opening coefficient calculated from the mean pressure variation at the column bottom using the same Equation (Table 6.2). This discrepancy is due to different assumptions made in deriving these equations.

Equations (6.2) and (6.3) assume a single, constant value of the plate opening coefficient throughout the reciprocating cycle, whereas Equation (6.6) accounts for the time-varying nature of the plate opening coefficient. Additionally, the mean plate opening coefficient calculated using Equation (6.3) is 9.9% lower than the maximum value in both single- and two-phase systems. Conversely, in the laminar flow regime, there is relatively good agreement between the values of the plate opening coefficient calculated using Equations (6.4) and (6.6), as shown in Figure 6.3.

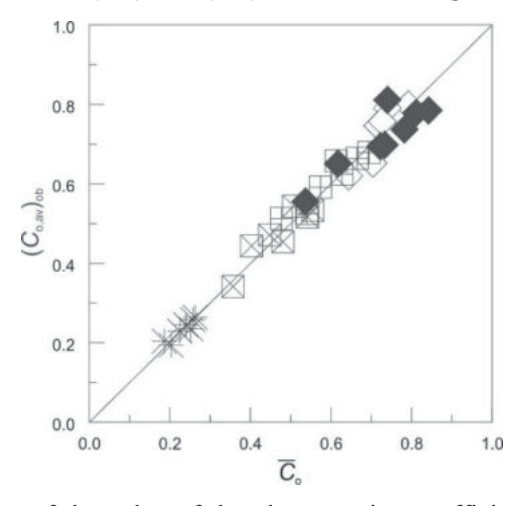


Figure 6.3 Comparison of the value of the plate opening coefficient calculated based on Equations (6.4) and (6.6) for the laminar regime of the liquid flow (symbols the same as in Figure 6.2) (Banković-Ilić et al., 1997).

6.1. Influence of reciprocating intensity

Figure 6.4 shows the dependence of the plate opening coefficient, calculated from the processed signal of the pressure variation at the column bottom, on the reciprocating intensity for single-phase systems. For low-viscosity liquids (water and aqueous solutions of *n*-butanol, sodium sulfite, and 40% glycerol) and medium-viscosity liquids (64% glycerol solution), the plate opening coefficient remains constant across the entire range of reciprocating intensity. In this case, the plate opening coefficient is independent of the liquid phase properties, as indicated by the data in Table 6.2. However, for more viscous liquids (glycerol and CMC solutions), the plate opening coefficient increases with increasing reciprocating intensity. In this case, the plate opening coefficient decreases with increasing viscosity due to the more intense frictional interaction between the perforated plates and the liquid.

As the viscosity of the liquid increases, the flow regime through the plate openings changes, as illustrated in Figure 6.5. This figure shows the dependence of the plate opening coefficient, calculated from the instantaneous pressure variation at

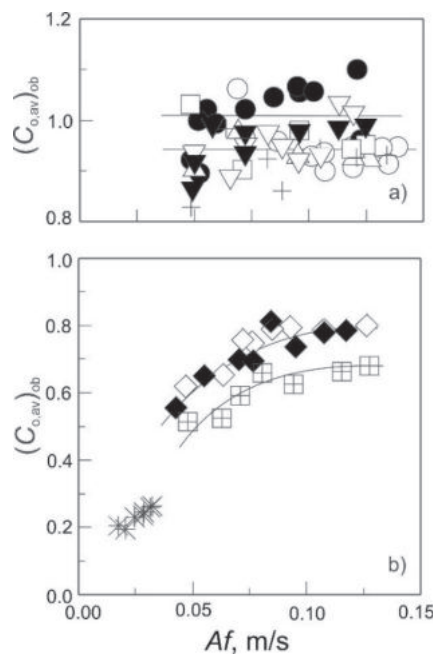


Figure 6.4 The influence of reciprocating intensity on the plate opening coefficient for (a) Newtonian liquids of low and medium viscosity and (b) highly viscous Newtonian and non-Newtonian liquids (symbols as in Figure 6.2) (Banković-Ilić et al., 1997).

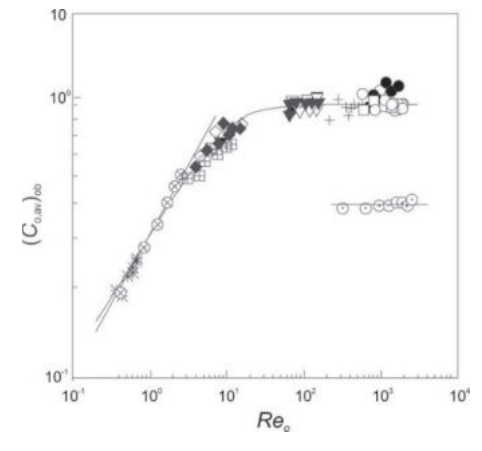


Figure 6.5 Dependence of the plate opening coefficient calculated based on the processed pressure signal on the Reynolds number (symbols as in Figure 6.2; Lounes and Thibault, 1993: water ⊙ and glycerol □) (Banković-Ilić et al., 1997).

the column bottom, on the Reynolds number in the plate opening. For Reynolds numbers greater than 50, the flow regime is turbulent, and the plate opening coefficient is constant and close to 1. Conversely, a laminar regime exists for Reynolds numbers less than 10. Based on data for the plate opening coefficient in the case of glycerol and CMC solutions in reciprocating plate columns of different

diameters, the following dependence was established: the plate opening coefficient is proportional to the square root of the Reynolds number:

$$C_{0.3V} = 0.30 \,\mathrm{Re}^{0.4} \tag{6.7}$$

aligning relatively well with the findings of Lounes and Thibault (1993), as indicated by the dashed line in Figure 6.5.

6.2. Effect of superficial gas velocity

Figure 6.6 illustrates the dependence of the plate opening coefficient, calculated based on the mean pressure variation at the column bottom (Equation 6.3), on the reciprocating intensity at different constant superficial gas velocities. In contrast, Figure 6.7 shows the dependence of the plate opening coefficient calculated from the slope of the linear part of the log $[\Delta p/(1-\varepsilon_g)]$ -to-log (Af) relationship. An increase in the plate opening coefficient with increasing reciprocating intensity and superficial gas velocity is observed, regardless of the liquid's rheological properties. The plate opening coefficient is higher in two-phase systems than in single-phase systems at the same reciprocating intensity because the pressure variation at the column bottom decreases with increasing superficial gas velocity due to the lower density of the gasliquid dispersion. This effect is further enhanced by the increased local gas holdup near the plate at higher frequencies and superficial gas velocities, leading to a further reduction in pressure variation at the column bottom and an increase in the plate opening coefficient above one (Lounes and Thibault, 1993).

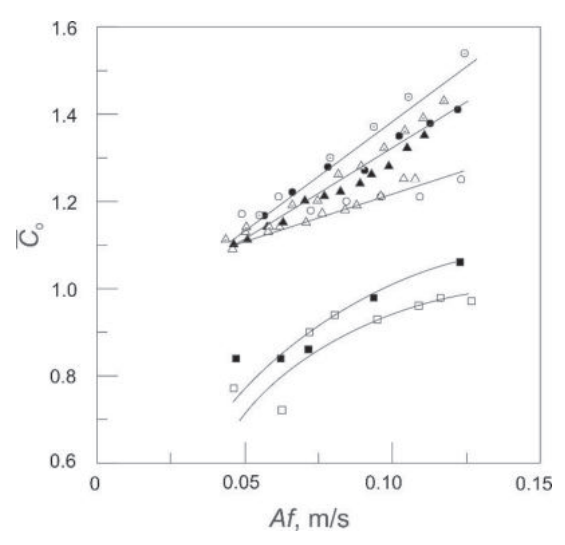


Figure 6.6 The dependence of the plate opening coefficient calculated from the mean pressure variation at the column bottom on the reciprocating intensity ($D_c = 9.2 \text{ cm}$; u_g , cm/s: 0.5 – open symbols, 1.0 – black symbols, and 1.5 – bullet symbols; water – circles, 64% glycerol – triangles, and 1% CMC – squares) (Banković-Ilić et al., 1997).

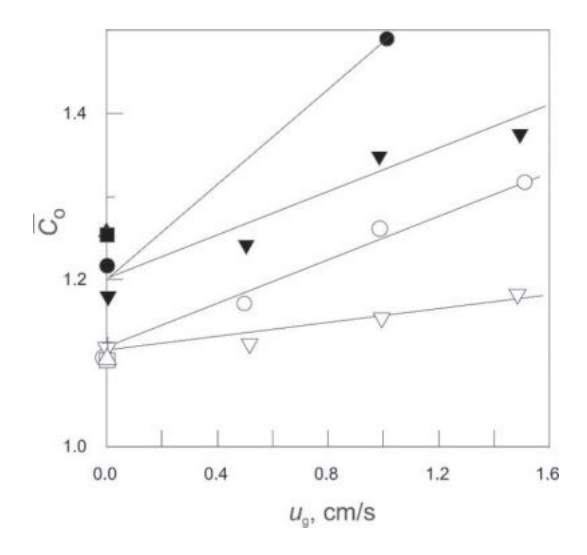


Figure 6.7 Dependence of the mean plate opening coefficient, calculated based on the slope of the linear part of the log $[\Delta p/(1-\varepsilon_g)]$ versus log (Af) relationship, on the superficial gas velocity (symbols the same as in Figure 6.2) (Banković-Ilić et al., 1997).

6.3. Effects of solid phase

Figures 6.8 and 6.9 show the dependence of the mean plate opening coefficient, calculated from the mean pressure variation at the column bottom, on the Reynolds number for three-phase and two-phase (liquid-solid) systems in reciprocating plate

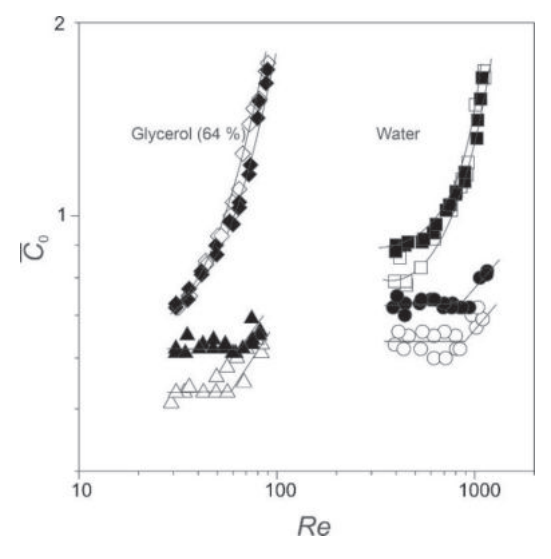


Figure 6.8 Dependence of the mean plate opening coefficient on the Reynolds number in two-phase (liquid-solid phase: water – circles and 64% glycerol – tringles) and three-phase (gas-liquid-solid: water – squares and 64% glycerol – rhombuses; u_g , cm/s: 0.5) systems (D_c = 2.54 cm; ε_s ,%: 6.6 – open symbols and 3.8 – black symbols) (Banković-Ilić, 1999).

columns of varying diameters. In the case of a liquid-solid system in a column with a 2.54 cm diameter, the mean plate opening coefficient remains approximately constant with increasing Reynolds number until a certain point, after which it increases. This breaking point corresponds to the critical reciprocating intensity, where the minimum pressure during the upward movement of the reciprocating plates approaches absolute vacuum. If the reciprocating intensity exceeds this critical value, the mean pressure variation at the column bottom becomes lower than expected based on lower reciprocating intensities, leading to an apparent increase in the mean plate opening coefficient beyond the breaking point.

In three-phase systems, the plate opening coefficient increases continuously with increasing reciprocating intensity, similar to two-phase (gas-liquid) systems. The higher plate opening coefficient in three-phase systems compared to gas-liquid systems is attributed to gas compression and increased local gas holdup at higher frequencies, which reduce the pressure variation at the column bottom. The mean plate opening coefficient also decreases with a higher solids fraction, regardless of column diameter, due to increased pressure variation at the column bottom. Compared to three-phase and one-phase systems, the mean plate opening coefficient in two-phase (liquid-solid) systems is lower (0.99; Banković-Ilić et al., 1995) due to greater pressure variation at the column bottom.

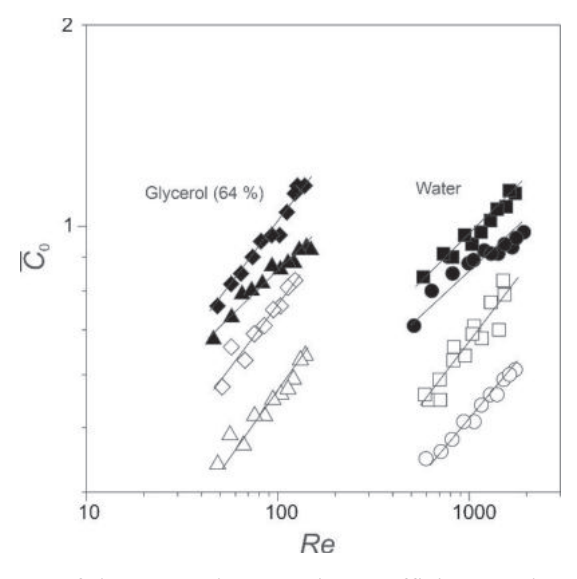


Figure 6.9 Dependence of the mean plate opening coefficient on the Reynolds number in two-phase (liquid-solid) and three-phase (gas-liquid-solid) systems ($D_c = 9.2$ cm; symbols as in Figure 6.8) (Banković-Ilić, 1999).

In a 9.2 cm diameter column, the plate opening coefficient increases with the Reynolds number, regardless of the liquid and solids fractions. For a two-phase system (glycerol-spheres), this relationship can be represented by an Equation of the following form:

$$\overline{C}_{o} = k \operatorname{Re}^{m} \tag{6.8}$$

where m is 0.54 and 0.62 for the solids fraction of 3.8% and 6.6%, respectively. Equations (6.7) and (6.8) exhibit a similar form, indicating that both the presence of solid particles and the physical properties of the liquid have comparable effects on the plate opening coefficient.

7. GAS HOLDUP IN RECIPROCATING PLATE COLUMNS

The gas holdup is a key hydrodynamic parameter in multiphase reactors, as it influences both the mean gas retention time and the specific gas-liquid interfacial area. Methods for measuring gas holdup in reciprocating plate columns can be categorized into continuous and discontinuous techniques (Skala, 1980). Continuous methods include light, radioactive, manometric, mean retention time, and electrical resistance approaches. In contrast, the discontinuous method involves halting both the gas flow and reciprocating plate motion after reaching a steady state within the column. The gas holdup is then determined by the ratio of the dispersed gas volume to the total dispersion volume.

$$\varepsilon_g = \frac{V_g}{V_d} \tag{7.1}$$

Designing multiphase reactors is greatly enhanced when a reliable correlation for gas holdup is available. Numerous correlations have been proposed to relate gas holdup in reciprocating plate columns to operating conditions, fluid properties, and column geometry (see Table 7.1). These efforts to establish a universal correlation for gas holdup in two-phase reciprocating plate columns can be categorized into two main approaches.

The first approach involves using the general hydrodynamic equation with a modified relative velocity (Rama Rao et al., 1983; Rama Rao and Baird, 1988):

$$\frac{u_g}{\varepsilon_g} + \frac{u_l + Af}{1 - \varepsilon_g} = 0.55 \frac{\varepsilon_g}{1 - \varepsilon_g} + 0.19 \tag{7.2}$$

where u_g and u_l are the superficial gas and liquid velocities, respectively, A and f are the amplitude and frequency of the reciprocation motion, respectively, and ε_g is the gas holdup.

Equation (7.2) is applicable for countercurrent fluid flow in reciprocating plate columns within a specific range of diameters (5.08 cm and 9.3 cm), plate opening diameters (0.3–1.4 cm), and the fractional free plate surface (9–57%) provided that the gas holdup is less than 0.2. However, this correlation does not accurately reflect the changes in gas holdup with varying reciprocating intensities. Depending on the context, the gas holdup either remains constant (Rama Rao and Baird, 1988; Yang et al., 1986a) or decreases (Rama Rao et al., 1983; Veljković and Skala, 1986) as the reciprocating intensity increases at specific superficial gas and liquid velocities. Veljković (1985) demonstrated that this type of Equation does not hold under all

Table 7.1 Empirical correlations for the gas holdup in pulsation and vibration devices

radire in cioni	ical colletations for any gas inc	table /: Thiphical collectanoin for the gas motary in passation and rectanois	
Device type and dimensions	Operating variables and system Correlation	Correlation	Reference
PBC $D_c = 0.076 \text{ m}$ $I_c = 3 \text{ m}$	A = 0-9.4 cm f = 1.09-1.35 Hz $u_g = 0.0082-0.024 \text{ m/s}$ $u_l = 0$ Air-water	$\begin{split} \varepsilon_g &= 0.46 P_{g,p}^{0.33} u_g^{03} \\ \varepsilon_g &= 0.67 P_{g,J}^{0.42} u_g^{0.50} \\ P_{g,p} &= 141.9 (1 - \varepsilon_g) (2\pi A f)^3 \\ P_{g,f} &= P_{g,p} + P_{g,sgas}, \ P_{g,sgas} = u_g \rho_{lg} \ (Af)_{cr} = 0.048 \ m/s \end{split}$	Baird and Garstang (1972)
PBC $D_c = 0.1 \mathrm{m}$ $I_c = 1.7 \mathrm{m}$	A = 0-2 cm f = 0-4.17 Hz $u_g = 0.002-0.02$ m/s Air-fermentation medium	$\varepsilon_g = Q_g \exp(-2Af + 11.85) + 3.04(Af)^2 - 38.37(Af) + 2.78$	Serieys et al. (1978)
PBC $D_c = 0.05; 0.1 \text{m}$ $l_c = 1.2; 2.2 \text{ m}$	A = 2.5 cm f = 0.25-5.0 Hz $u_g = 0.007-0.044 \text{ m/s}$	$\varepsilon_g = 0.122 u_g^{09}$ (air-water) $\varepsilon_g = 0.623 u_g^{0.69}$ (air-1% CMC)	Murthi et al. (1987)
VDC $D_c = 0.05 \text{ m}$	A = 0-1.2 cm f = 0-7 Hz $u_g = 0.0115-0.0772 \text{ m/s}$ $u_l = 0.001-0.0112 \text{ m/s}$ CO_2 -water	$\begin{split} \mathcal{E}_{g} &= \mathcal{E}_{g,o} + \Delta \mathcal{E}_{g} \\ \boldsymbol{\varepsilon}_{g,o} &= 0.0043 u_{g}^{0.7} u_{l}^{-0.08} \left(\frac{d_{d}}{D_{c}} \right)^{0.5} \left(\frac{d_{o}}{D_{c}} \right)^{-0.5} \left(\frac{h}{D_{c}} \right) \\ \Delta \boldsymbol{\varepsilon}_{g} &= 0.0034 \left(\frac{d_{d}}{D_{c}} \right)^{2.0} \left(\frac{d_{o}}{D_{c}} \right)^{-0.56} n_{d} (Af - Af_{cr}) \end{split}$	Tojo et al. (1974a)

Continuation Table 7.1 Empirical correlations for the gas holdup in pulsation and vibration devices.

Device type and dimensions	Operating variables and system Correlation	Correlation	Reference
VDC $D_c = 0.172 \text{ m}$ $I_c = 0.78 \text{ m}$	A = 1-3 cm f = 0-4.3 Hz $u_g = 0.0037-0.012$ m/s $u_I = 0-0.0033$ m/s CO_2 -water Air-glycerol solution	$\begin{split} \mathcal{E}_{\mathcal{G}} &= \mathcal{E}_{\mathcal{S},o} + \Delta \mathcal{E}_{\mathcal{G}} ; \\ \boldsymbol{\varepsilon}_{g,o} &= 0.89 \left(\frac{d_d}{D_c} \right)^{0.5} \left(\frac{d_o}{D_c} \right)^{-0.15} \left(\frac{u_g}{gh} \right)^{0.34} \left(\frac{u_f^2}{gh} \right)^{-0.04} \\ \Delta \mathcal{E}_g &= 0.0024 \left(\frac{d_d}{D_c} \right)^{2.0} \left(\frac{d_o}{D_c} \right)^{-0.56} \frac{\mu h_l}{\sigma h} \left(Af - Af_{cr} \right) \end{split}$	Miyanami et al. (1978)
RPC, KRIMZ type $D_c = 0.08 \text{ m}$ $l_c = 0.04 \text{ m}$	Af < 0.40 m/s $u_g = 0.0079-0.0715 \text{ m/s}$ $u_l = 0.0012 \text{ m/s}$ Air-water Air-sulfite solution	For $(Af) > (Af)_{cr}$ and $u_g < 0.06$ m/s: $\varepsilon_g = 1 - 1.044 \exp \left[-4 \left(\frac{u_g}{u_{g,o}} \right)^{0.33} \left(\frac{u_g}{gh} \right) \right]$ $Za (Af) < (Af)_{cr} i u_g > 0.06 \text{ m/s:}$ $\varepsilon_g = 1 - \exp \left[-3 \left(\frac{u_g}{u_{g,o}} \right)^{0.33} \left(\frac{u_g}{gh} \right) \right]$	Gorodeckiy et al. (1980)
RPC $D_c = 0.093$; 0.153 m $l_c = 1.0$ m	A = 1.4-6.35 cm f = 0.75-6.35 Hz $u_g = 0.0004-0.051$ m/s $u_l = 0.0124-0.0372$ m/s Air-water	Segregated dispersion: $ \varepsilon_{g} = 0.049 W e^{0.37} \text{Re}^{-0.05} \left(\frac{D_{c}}{d_{o}} \right)^{0.59} n_{p}^{0.4} \left(\frac{\sigma_{c}}{\sigma_{c} - \sigma_{d}} \right)^{0.25} $ Homogeneous dispersion: $ \varepsilon_{g} = 0.017 W e^{0.37} \text{Re}^{-0.147} F r^{0.16} \left(\frac{D_{c}}{d_{o}} \right)^{0.36} n_{p}^{0.66} \left(\frac{\sigma_{c}}{\sigma_{c} - \sigma_{d}} \right)^{-0.88} $	Rama Rao et al. (1983)

Continuation Table 7.1 Empirical correlations for the gas holdup in pulsation and vibration devices.

Device type and	Device type and Operating variables and system	Correlation	Reference
dimensions			
RPC $D_c = 0.05$ m;	$u_g = 0-0.07 \text{ m/s}$ $u_l = 0-0.07 \text{ m/s}$	$\boldsymbol{\varepsilon}_g = 0.0448 u_g^{0.81} u_f^{-0.055}$	Chen et al. (1986)
$l_c = 4m$ RPC $D_c = 0.025 \text{ m}$ $l_c = 1.875 \text{ m}$	Air-water $A = 1-10 \text{ mm}$ $f = 0.48-8.8 \text{ Hz}$ $u_g = 0.00274-0.031 \text{ m/s}$ $u_f = 0.00181 \text{ m/s}$	Segregated dispersion: $\frac{u_r}{1-\varepsilon_g} = 0.436u_g^{0.22} \exp(-0.122\varepsilon_g u_g^{-0.88})$	Skala and Veljković (1987b)
RPC, plates with segmental passages	Air-water Air-sucrose solution $A = 0.16-0.32$ cm $f = 5-30$ Hz $u_g = 0-0.0565$ m/s	Homogeneous dispersion:	Gomaa et al. (1991)
$D_c = 0.01 \text{ m}$	$u_l = 0.005-0.028 \text{ m/s}$ Air-water	Za $u_g > 0, 1 \text{ m/s}$: $\varepsilon_g = \varepsilon_{g,o} \left[1 + 0.844 \left(Af - Af_{or} \right)^{0.11} \right]; \varepsilon_{g,o} = \frac{0.188 \left(1 + 1.73 u_I \right)}{h^{0.35}}$	
RPC $D_c = 0.093 \text{ m}$ $I_c = 1 \text{ m}$	A = 1.4-5.0 cm f = 0.75-3 Hz $u_g = 0.6-4.6 \text{ m/s}$ $u_l = 0.409-3.681 \text{ m/s}$ Air-water CO ₂ -water	Segregated dispersion: $\varepsilon_g = 0.85 F r^{0.42} G a^{0.04} \left(\frac{u_g}{u_f + Af} \right)^{0.13} \varepsilon^{0.03}$ Homogeneous dispersion: $\varepsilon_g = 8.68 F r^{0.38} G a^{-0.04} \varepsilon^{-0.19} W e^{0.3}$	Sundaresan and Varma (1990a)

Continuation Table 7.1 Empirical correlations for the gas holdup in pulsation and vibration devices.

Device type and Operating variables and system dimensions	Correlation 70.45 0.03/	Reference
[= 1.2–2.35 cm = 1–7.2 Hz	$\angle a$ $Af > 0.03$ m/s: $oldsymbol{arepsilon}_g = 2.515(P^*)^{0.20} u_g^{0.83}$	Banković-Ilić et al. (1993)
$u_g = 0.4-1.5 \text{ m/s};$ $u_l = 0 \text{ m/s}$ $\varepsilon_s = 3.8 \text{ and } 6.6\%$ Air-water-spheres		
A = 1.2 - 2.35 cm	Segregated dispersion:	Banković-Ilić et al.
$u_g = 0.4-1.5 \text{ m/s}$	Eg = 7.4(2)	(5251)
$u_l = 0 \text{ m/s}$	$\boldsymbol{\varepsilon}_g = 6.2(P^*)^{0.2} u_g$	
Air-water Air-sucrose solution	$oldsymbol{arepsilon}_g = 44.55 (Af)^{00} oldsymbol{u}_g$	
4 = 2.35 cm	Za $Af > 0.03$ m/s:	Banković-Ilić
f = 2-6 Hz	$oldsymbol{arepsilon}_g = 1.38(P^*)^{0.27} u_g^{0.73}$	(1999)
$t_g = 0.5-1.5 \text{ m/s};$ $t_l = 0 \text{ m/s}$		
Air-water		
4 = 2.35 cm	Polymerization degree: 200:	Naseva et al. (2002)
f = 2 - 5.5 Hz	$m{arepsilon}_{g} = 0.043(P_{av})^{0.39} m{u}_{g}^{0.53}$	
$u_{\rm g} = 0.5 - 1.5 \text{ m/s};$		
$u_l = 0 \text{ m/s}$	Polymerization degree: 1000:	
$\epsilon_s = 0, 3.84 \text{ and } 6.61\%$	$m{arepsilon}_g = 0.043(P_{av})^{0.31}m{u}_g^{0.44}$	
Air-CMC solution (0.5% and		
%)-spheres		

Continuation Table 7.1 Empirical correlations for the gas holdup in pulsation and vibration devices.

Device type and dimensions	Operating variables and system	Correlation	Reference
RPC $D_c = 0.092 \text{ m}$ $I_c = 1.05 \text{ m}$	A = 2.35 cm f = 1.6 Hz $u_g = 0.5 - 1.5 \text{ m/s};$ $u_l = 0 \text{ m/s}$ $c_s = 0 - 3.2\%$ A ir-water-Rashio rinos (8 mm)	For $A \not f > 0.03 \text{ m/s}$: $\varepsilon_g = 1.145(P_w)^{0.428} u_g^{0.662}$ $\varepsilon_g = 0.393(P^*)^{0.495} u_g^{0.628}$ $\varepsilon_g = 1.06(P_f)^{0.456} u_g^{0.663}$	Aleksić et al. (2002b)
RPC $D_c = 0.025 \text{ m}$ $(I_c = 2 \text{ m}) \text{ and}$ $D_c = 0.092 \text{ m}$ $(I_c = 1.05 \text{ m})$	A = 1 cm, 2,35 cm f = 2-4.5 Hz $u_g = 0-0.02 \text{ m/s}$; $u_l = 0.06 \text{ m/s}$	Two-phase (air-water): $\varepsilon_g = 1.369 u_g^{0.962} D_c^{-0.483} + 172.26 u_g^{0.33} D_c^{0.453} (\mathcal{A}f)^{221}$ Three-phase (air-water-spheres): $\varepsilon_g = 1.369 u_g^{0.962} D_c^{-0.483} + 66.942 u_g^{0.294} D_c^{0.268} (\mathcal{A}f)^{1.693} \varepsilon_g^{0.238}$	Nikolić et al. (2004)
RPC $D_c = 0.092 \text{ m}$ $l_c = 1.05 \text{ m}$	A = 2.35 cm f = 1-5.5 Hz $u_g = 0.5-1.5 \text{ m/s};$	For $Af > 0.04$ m/s and polymerization degree of 50: $\epsilon_g = 0.053 (P_o)^{0.39} u_g^{0.005}$	Stamenković et al. (2005)
i i	u _l = 0 m/s c _s =0; 3.84 and 6.61% Air-CMC (0.5, 1, and 2%) solution-spheres	For $Af > 0.04$ m/s and polymerization degree of 200: $\varepsilon_g = 0.041 (P_{\omega})^{0.4} u_g^{0.54}$	
RPC $D_c = 0.092 \text{ m}$ $I_c = 1.05 \text{ m}$	Air-water-Rashig rings (12 mm) $A = 2.35 \text{ cm}$ $f = 1.6 \text{ Hz}$	$m{arepsilon}_g = 1.991(P_w)^{0.404} \mu_g^{0.787}$	Aleksić (2006)
	$u_g = 0.5 - 1.5 \text{ m/s},$ $u_l = 0 \text{ m/s}; g_s = 03.2\%$ Air-water-Rashig rings (12 mm)	$m{arepsilon}_g = 0.335(P_{o_0})^{0.291} m{u}_g^{0.527}$	

Continuation Table 7.1 Empirical correlations for the gas holdup in pulsation and vibration devices.

Device type and imensions	Operating variables and system Correlation	Correlation	Reference
d.	A = 0.01 m f = 0.3 Hz $u_g = 2.12-6.31 \text{ cm/s};$ $u_l = 0.14-0.28 \text{ m/s}$	Mixer-settle region: $\varepsilon_g = 0.035 \left(\frac{4f}{u_l} \right)^{-0.068} \left(\frac{u_g}{u_l} \right)^{0.378} \text{Re}^{0.364} \left(\frac{d_o}{h} \right)^{0.095}$	Dhanasekaran and Karunanithi (2012a)
		Emulsion region: $\varepsilon_g = 0.019 \left(\frac{Af}{u_l} \right)^{0.456} \left(\frac{u_g}{u_l} \right)^{0.235} \text{Re}^{0.65} \left(\frac{d_o}{h} \right)^{0.56}$	

Abbreviations: HRRCP - hybrid rotating-reciprocating plate column, PBC - pulsed bubble column, RPC - reciprocating plate column, and VDC - vibration disc column. aeration and agitation conditions, particularly when examining a broader range of operating conditions and different geometries with varying physical properties.

Dhanasekaran and Karunanithi (2012a) developed a hybrid column integrating features from bubble columns, stirred tanks, and reciprocating plate columns through a novel bevel gear arrangement. This hybrid design modified the internal geometry of the gas-liquid contactor by combining rotary and reciprocating motions. Their study revealed that, under countercurrent conditions, the gas holdup in the hybrid column mirrored that of a traditional reciprocating plate column for an air-water system. Key parameters such as reciprocating intensity, superficial gas and liquid velocities, perforation diameter, and plate spacing significantly influenced gas holdup in both the mixer-settler and emulsion regions. Specifically, the gas holdup in the hybrid column was found to be 1.2–1.7 times higher in the mixer-settler region and 2.1–2.7 times higher in the emulsion region compared to reciprocating plate columns.

A Box-Behnken experimental design within the response surface methodology was employed to predict the relationship between experimental variables—reciprocating intensity, superficial gas and liquid velocities, plate opening diameter, and plate spacing—and the resulting gas holdup (Dhanasekaran and Karunanithi, 2012b). The study analyzed the linear, quadratic, and interactive effects of these variables on gas holdup. The reciprocating intensity and plate spacing were found to have a particularly strong influence, while the interaction between reciprocating intensity and plate spacing, as well as the plate perforation with superficial gas and liquid velocities, showed significant effects on gas holdup. The correlations between these experimental parameters and gas holdup were effectively modeled using the response surface methodology.

Another approach involves using an empirical equation based on power consumption and superficial gas velocity to calculate gas holdup in both stirred vessels (Calderbank, 1958) and pulsation columns (Baird and Garstang, 1972). Skala and Veljković (1987b) were the first to develop a correlation specifically for gas holdup in reciprocating plate columns of this type:

$$\varepsilon_g = k(P^*)^a u_g^b \tag{7.3}$$

where ε_g is the gas holdup, P^* is the maximum power consumption, u_g is the superficial gas velocity, and a, b, and k are the parameters. This correlation, derived from data on the volume mass transfer coefficient (Skala and Veljković, 1988), is valid within the homogeneous regime. In this context, power consumption influences gas holdup less than gas flow energy, as mechanical energy in reciprocating plate columns is primarily dissipated near the plates. When aeration is the dominant factor

over agitation ($Af < Af_{cr}$), the gas holdup is dependent solely on the superficial gas velocity.

In two-phase reciprocating plate columns, at lower reciprocating intensities, the gas holdup either decreases (Banković-Ilić et al., 1995; Lounes and Thibault, 1993; Rama Rao et al., 1983; Sundaresan and Varma, 1990a; Veljković and Skala, 1986) or remains constant (Boyle, 1975; Rama Rao and Baird, 1988; Yang et al., 1986a) until there is a change in the dispersion structure. This decrease is attributed to the combined effects of gas bubble and reciprocating plate velocities, which enhance bubble movement, lead to coalescence, and result in the accumulation of bubbles beneath the plates (segregated dispersion). When solid particles (such as spheres or Rashig rings) are introduced, the gas holdup increases with higher reciprocating intensity and superficial gas velocity (Aleksić et al., 2002; Banković-Ilić, 1999; Naseva et al., 2002; Skala and Veljković, 1987a; Skala and Veljković, 1996; Skala et al., 1993; Veljković et al., 1996). Unlike two-phase systems, however, a distinct transition from segregated to homogeneous dispersion is not typically observed. Following the minimum gas holdup, there is a near-linear increase with further increases in reciprocating intensity. This rise is marked by a sharp transition from a homogeneous to an unstable regime. At higher reciprocating intensities, the gas holdup increases significantly due to the comminution of bubbles, which is a result of enhanced shearing forces and increased resistance to gas flow through the plate openings, leading to prolonged gas retention in the column (Veljković and Skala, 1986).

The 'critical' reciprocating intensity is the point at which gas holdup in a two-phase system reaches its minimum value. This intensity is influenced by factors such as the type of plates, the physical properties of the liquid, and the superficial gas velocity. In a Karr-type reciprocating plate column, the 'critical' reciprocating intensity is relatively insensitive to changes in superficial gas velocity (Veljković and Skala, 1986). The transition from segregated to homogeneous dispersion is determined by the properties of the gas-liquid system and the geometry of the plates (Rama Rao et al., 1983). In contrast, for a Prohaska-type reciprocating plate column, the 'critical' reciprocating intensity increases with higher superficial gas velocity (Gomaa et al., 1991). For a vibrating disc column, however, it is more dependent on the physical properties of the liquid (Miyanami et al., 1978).

Typical relationships between gas holdup and reciprocating intensity at a given superficial gas velocity in a three-phase reciprocating plate column are illustrated in Figure 7.1. At low reciprocating intensities, gas holdup measurements were not taken, so the characteristic transition from segregated to homogeneous dispersion observed in two-phase systems was not recorded. Generally, for reciprocating

intensities greater than approximately 4 cm/s, gas holdup increases with increasing reciprocating intensity, regardless of the column diameter, because enhanced mixing promotes bubble dispersion through shear forces, leading to a more homogeneous bubble distribution between the plates.

In a column with a small diameter (2.54 cm), solid particles act similarly to perforated plates at low reciprocating intensities, helping to prevent bubble coalescence and thus maintaining lower gas holdup. As reciprocating intensity increases, the dispersion of bubbles improves due to more intensive agitation and interactions with solid particles, causing a sharp rise in gas holdup until it reaches a plateau. In contrast, in a larger column (9.2 cm diameter), solid particles primarily facilitate bubble comminution, regardless of superficial gas velocity or solids fraction. In the largest column (16.6 cm diameter), however, a higher gas holdup is observed at higher superficial gas velocities with a smaller solids fraction. It is due to changes in the liquid flow regime through the plate openings, resulting from a reduction in the effective free section of the plates caused by the presence of solid particles (Vasić, 2005).

The effect of the superficial gas velocity on the gas holdup is very pronounced, regardless of the type of system and column geometry (Figure 7.1). At low superficial gas velocities (less than 3 cm/s), the gas holdup increases proportionally with increased superficial gas velocity due to increased resistance to gas flow through the plate openings. So it was before in columns of different diameters in the presence of liquids with different rheological behavior (Aleksić et al., 2002b, 2004; Banković-Ilić, 1999; Banković-Ilić et al., 1994, 1995, 1996, 2004b; Gomaa et al., 1991; Lounes and Thibault, 1993; Rama Rao and Baird, 1988; Rama Rao et al., 1983; Stamenković et al., 2005; Vasić et al., 2005b, 2006b; Veljković and Skala, 1986; Skala and Veljković, 1987a). At higher superficial gas velocities, regardless of the type of system, gas "plugs" appear in the reactor, and the gas holdup reaches its maximum value and does not change when the superficial gas velocity is further increased (Banković-Ilić et al., 1995; Skala et al., 1993). In Prohaska-type reciprocating plate columns, the gas holdup does not depend on the superficial gas velocity if it is greater than 10 cm/s (Gomaa et al., 1991).

The impact of superficial liquid velocity on gas holdup in two-phase systems remains debated. Some studies suggest no significant effect of superficial liquid velocity on gas holdup (Chen et al., 1986; Rama Rao et al., 1983; Sundaresan and Varma, 1990a; Yang et al., 1986a), while others argue that increasing superficial liquid velocity enhances gas holdup (Boyle, 1975; Gomaa et al., 1991; Rama Rao and Baird, 1988; Veljković and Skala, 1986). Notably, this enhancement is typically observed at superficial liquid velocities exceeding 1.2 cm/s (Skala, 1980). Additi-

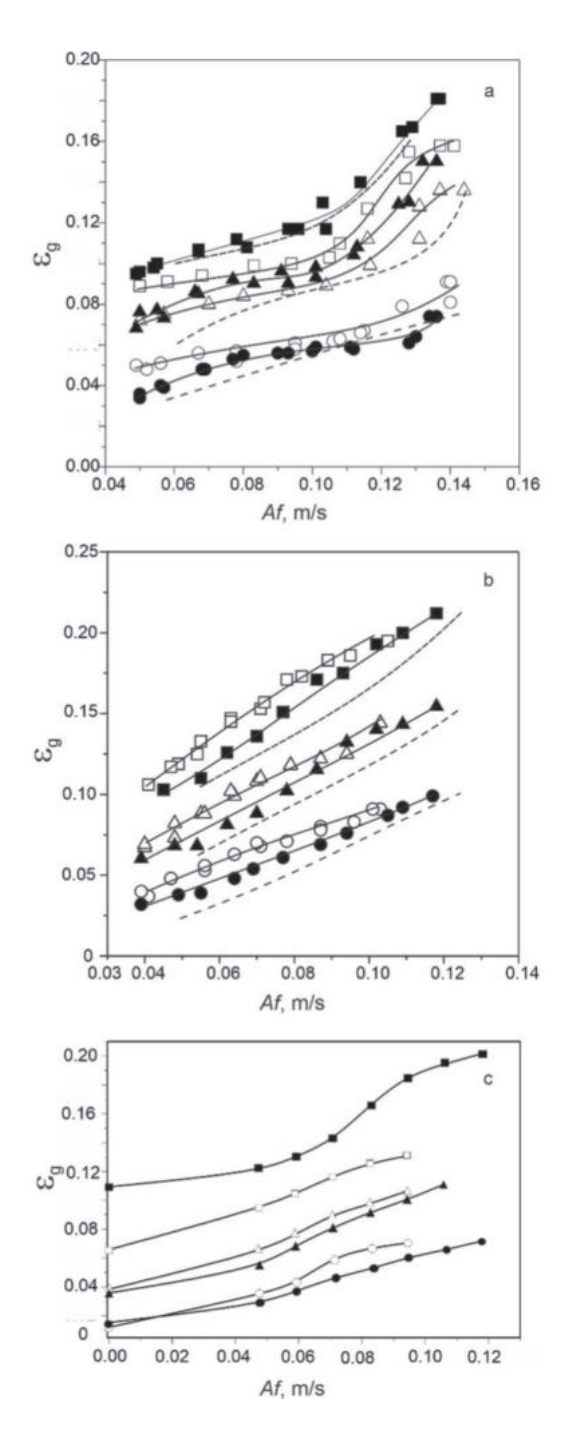


Figure 7.1 Dependence of gas holdup on reciprocating intensity: (a) $D_c = 2.54$ cm, (b) $D_c = 9.2$ cm (Banković-Ilić, 1999), and (c) $D_c = 16.6$ cm (Vasić, 2005) (liquid: water; ε_s , %: 0 – lines [u_g , cm/s: 0 – - - -, 0.5 – ----, and 1.5 – —], 3.8 – black symbols, and 6.6 – open symbols; u_g , cm/s: 0.5 – circles, 1.0 – triangles, and 1.5 – squares).

onally, concurrent upward flow generally achieves higher gas holdup compared to counter-current flow under similar operating conditions (Sundaresan and Varma, 1990a). Conversely, the influence of superficial liquid velocity on gas holdup in three-phase systems appears negligible (Skala and Veljković, 1987a; Skala et al., 1993).

The geometry of the plate plays a crucial role in determining gas holdup within the column. In segregated mode, bubble size is primarily governed by the diameter of the plate openings, whereas in homogeneous mode, it is influenced by the bubble dispersing process. Increasing the diameter of the plate openings in segregated mode leads to a decrease in gas holdup, while in homogeneous mode, the impact is negligible. Conversely, increasing the number of plates, thereby decreasing the distance between them, enhances gas holdup by reducing mean bubble diameter and increasing resistance to bubble movement (Gomaa et al., 1991; Rama Rao and Baird, 1988; Rama Rao et al., 1983; Veljković and Skala, 1986). Irrespective of the rheological properties of the liquid and the presence of a solid phase, reducing the fractional plate-free area (Figure 7.2) results in increased gas holdup. This occurs because reduced fractional plate-free area facilitates gas dispersion and impedes the flow of gas and liquid through the plate openings (Aleksić, 2006).

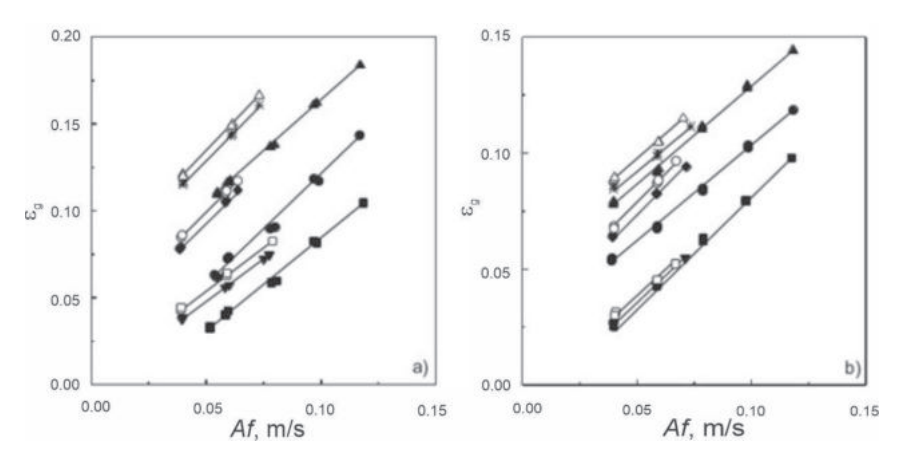


Figure 7.2 The influence of the free surface of the plate on the gas holdup of the two-phase systems: a) distilled water and b) 1% CMC solution (ε , %: 45,4; u_g , cm/s: 0,5 – \blacksquare , 1,0 – \bullet , and 1,5 – \blacktriangle ; ε , %: 31,9; u_g , cm/s: 0,5 – \blacktriangledown , 1,0 – \bullet , and 1,5 – \ast ; ε , %: 26,3; u_g , cm/s: 0,5 – \square ; 1,0 – \circ , and 1.5 – Δ) (Aleksić, 2006).

The presence of solid particles significantly impacts gas-liquid dispersion. The reciprocating movement of the plates forces the solid particles to move, which helps equalize the turbulent forces between the plates, prevents coalescence, and promotes bubble reduction. This movement of solid particles also reduces the intensity of backmixing and stabilizes column operation (Skala and Veljković, 1987a). As a

result, gas holdup is higher in a three-phase column compared to a two-phase column under identical operating conditions (Figure 7.1). The difference in gas holdup between three-phase and two-phase columns increases with higher reciprocating intensity.

Increasing the fraction of Rashig rings in the spaces between the plates up to 3.2% enhances gas holdup as the solids fraction increases (Figure 7.3). For spherical particles up to 11.2%, gas holdup initially rises, peaks at a solids fraction of 6.6%, and then declines (Skala et al., 1993). This variation in gas holdup is attributed to the effect of solid particles on bubble dispersion and coalescence. At lower solids fractions, particles can move relatively freely between the plates, following the reciprocating motion. This movement reduces bubble size and increases gas holdup. However, as the solids fraction increases, particles occupy more space between the plates, restricting their movement and forming a 'vibrating layer.' At higher superficial gas velocities, this 'vibrating layer' cannot effectively disrupt the gas stream, leading to channeled gas movement and the formation of larger gas bubbles, which decreases gas holdup (Skala et al., 1993).

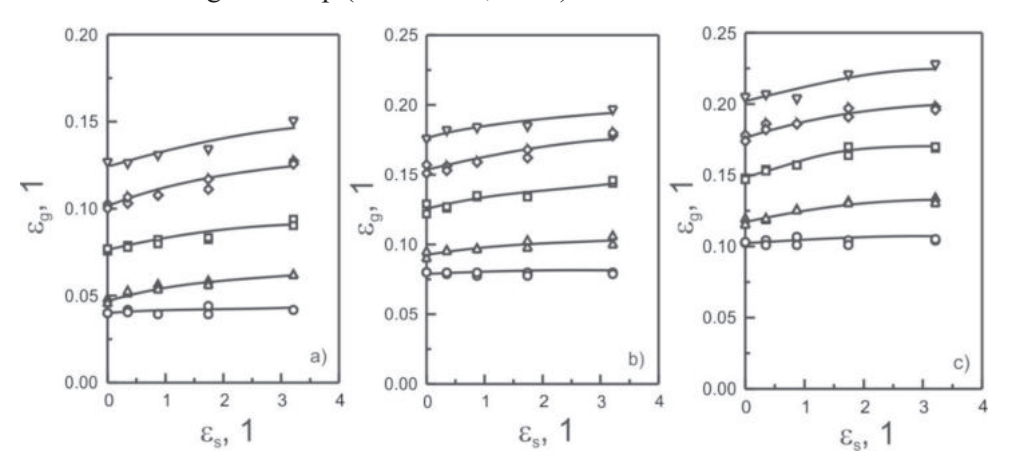


Figure 7.3 Influence of the fraction of Rashig rings on the gas holdup: u_g , cm/s: a) 0.5, b) 1.0, and c) 1.5 (Af, cm/s: 0.045 – circles, 0.06 – triangles, 0.08 – squares, 0.1 – rhombuses, and 0.12 – inverted triangles) (Aleksić et al., 2002b).

An increase in the size of Rashig rings affects gas holdup (Figure 7.4) due to the higher input power at the same reciprocating intensity (Banković-Ilić et al., 2004b). Additionally, Rashig rings disperse gas more efficiently than similarly sized spheres in reciprocating plate columns of the same geometry under identical operating conditions (Figure 7.5).

The physical properties of the liquid significantly influence gas holdup. In solutions of n-butanol, glycerol, and sodium sulfite, the gas holdup is higher than in

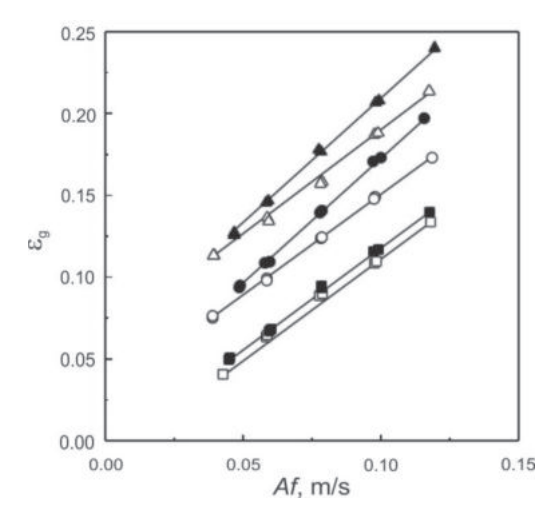


Figure 7.4 The effect of the size of Rashig rings on the gas holdup (distilled water; ϵ , %: 45.4; ϵ _s, % vol.: 2.66; diameter of Rashig rings, mm: 8 – open symbols and 12 – black symbols; u_g, cm/s: 0.5 – squares, 1.0 – circles, and 1.5 – triangles) (Banković-Ilić et al., 2004b).

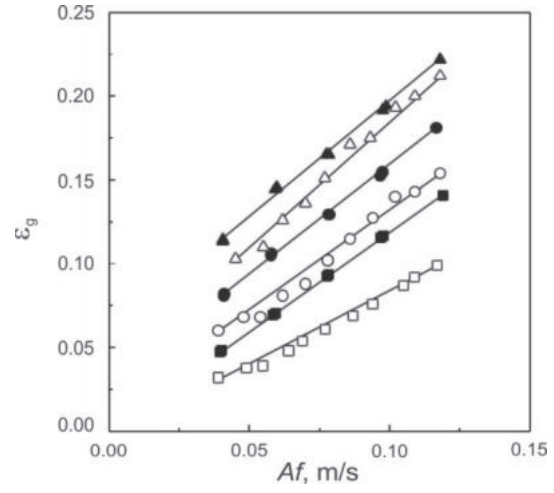


Figure 7.5 Comparison of the effect of solid particles on the gas holdup (distilled water; ε , %: 45.4; u_g , cm/s: 0.5 – squares, 1.0 – circles, and 1.5 – triangles; Rashig rings with a diameter of 8 mm: black symbols; ε_s , % vol.: 3.20; spheres with a diameter of 8.3 mm: open symbols; ε_s , % vol.: 3.80) (Aleksić, 2006).

water, regardless of the system type (Banković-Ilić, 1999). Pure liquids tend to promote bubble coalescence, while the presence of dissolved substances, such as electrolytes and aliphatic alcohols, inhibits coalescence (Petrović, 1989). The highest gas holdup is observed in *n*-butanol solutions due to the prevention of bubble coalescence, with water exhibiting the lowest gas holdup, irrespective of column

diameter. In non-Newtonian solutions of CMC, gas holdup depends on the solution concentration and the molar mass of CMC, reflecting changes in the rheological properties of the liquid phase (Naseva et al., 2002).

Regardless of the degree of polymerization, gas holdup in a two-phase system decreases with more concentrated solutions (Figures 7.6 and 7.7). For instance, gas holdup decreases as liquid pseudoplasticity increases (i.e., as the flow index decreases, as shown in Table 7.2) due to higher CMC concentrations. This trend has been observed in CMC solutions within a bubble column (Kawase et al., 1992) and an air-lift reactor with external liquid recirculation (Gavrilescu et al., 1998), resulting from enhanced bubble coalescence in viscous solutions. Similar effects of rheological properties on gas holdup were observed in a three-phase system with CMC PP 200 solution (Figure 7.6).

Table 7.2 Physical properties of CMC solution (Naseva et al., 2002).

	,			
Property	CMC PP 200	•	CMC PP 1000	0
	0.5 %	1.0 %	0.5 %	1.0 %
Density (kg/m ³)	1003	1006	1003	1006
Coefficient of consistency (Pas ⁿ)	0.0154	0.0671	0.4585	3.435
Flow index	0.93	0.85	0.60	0.46
Surface tension (N/m)	0.0871	0.087	0.0883	0.0789

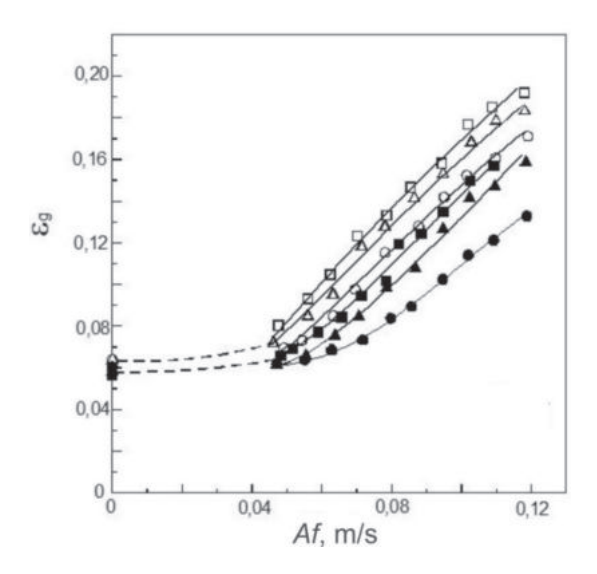


Figure 7.6 Effect of CMC (PP 200) concentration on gas holdup of two-phase and three-phase systems at $u_g = 0.5$ cm/s (ε_s , %: 0 – circles, 3.84 – triangles, and 6.61 – squares; CMC, %: 0.5 – open symbols and 1.0 – black symbols; adapted from Naseva et al., 2002).

The gas holdup in the three-phase system using a CMC (PP 1000) solution (Figure 7.7) is influenced by the combined effects of reciprocating intensity, superficial gas velocity, solids fraction, and the rheological properties (viscosity) of the liquid on bubble dispersion and coalescence in the spaces between the plates.

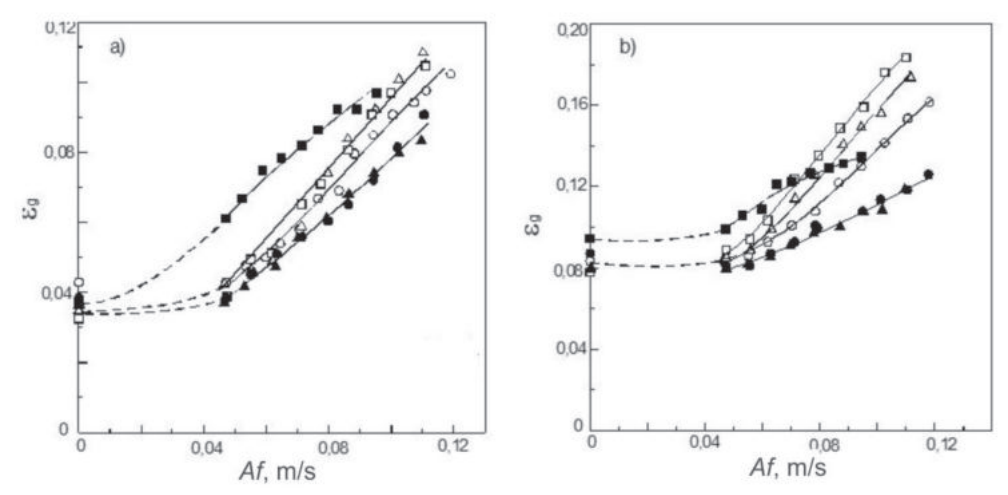


Figure 7.7 Effect of CMC concentration (PP 1000) on the gas holdup of two-phase and three-phase systems at (a) $u_g = 0.5$ cm/s and (b) $u_g = 1.5$ cm/s (&, %: 0 – circles, 3.84 – triangles, and 6.61 – squares; CMC, %: 0.5 – open symbols and 1.0 – black symbols) (Naseva et al., 2002).

In a solution of lower concentration (0.5%), gas holdup in a three-phase system is higher than in a two-phase system, regardless of superficial gas velocity. However, at lower superficial gas velocities, gas holdup remains similar for both solids fractions (Figure 7.7a). In contrast, at higher superficial gas velocities, gas holdup increases with a higher solids fraction (Figure 7.7b). This suggests that at lower superficial gas velocities, the spheres' contribution to bubble comminution reaches its maximum effect at a smaller solids fraction, so increasing the number of spheres does not further enhance gas holdup (Figure 7.7a). Conversely, at higher superficial gas velocities, the additional dispersing capacity of a larger number of spheres becomes effective, leading to increased gas holdup (Figure 7.7b).

In a higher concentration solution (1%), gas holdup is similar in both two-phase and three-phase systems with a smaller solids fraction (Figures 7.7a and 7.7b) because the positive effect of the spheres on bubble comminution is offset by the negative effect of increased viscosity, which promotes bubble coalescence. However, increasing the number of spheres between the plates enhances the dispersing capacity, leading to an increase in gas holdup as the solids fraction rises from 3.84% to 6.61% by volume.

In a three-phase system with a CMC (PP 1000) solution, gas holdup is higher in more concentrated solutions across the entire range of reciprocating intensities at lower superficial gas velocities (Figure 7.7a) and at lower reciprocating intensities (< 7 cm/s) at higher superficial gas velocities (Figure 7.7b). This effect of liquid viscosity on gas holdup (Naseva et al., 2002) is attributed to a shift in the flow regime toward laminar conditions. Consequently, the 'maximum' dependence of gas holdup on the solids fraction (Skala et al., 1993) occurs at higher solids fractions.

The effect of the degree of polymerization of CMC on gas holdup is influenced by solution concentration, reciprocating intensity, and solids fraction (Figure 7.8). For instance, in both two-phase and three-phase systems with a 0.5% CMC solution, a higher degree of polymerization results in lower gas holdup due to increased pseudoplasticity, which promotes bubble coalescence (Figure 7.8a). In systems with a 1% CMC solution and a solids fraction of 3.84%, the degree of polymerization does not significantly impact gas holdup at low reciprocating intensities. However, at higher reciprocating intensities, gas holdup is reduced in solutions with a higher degree of polymerization.

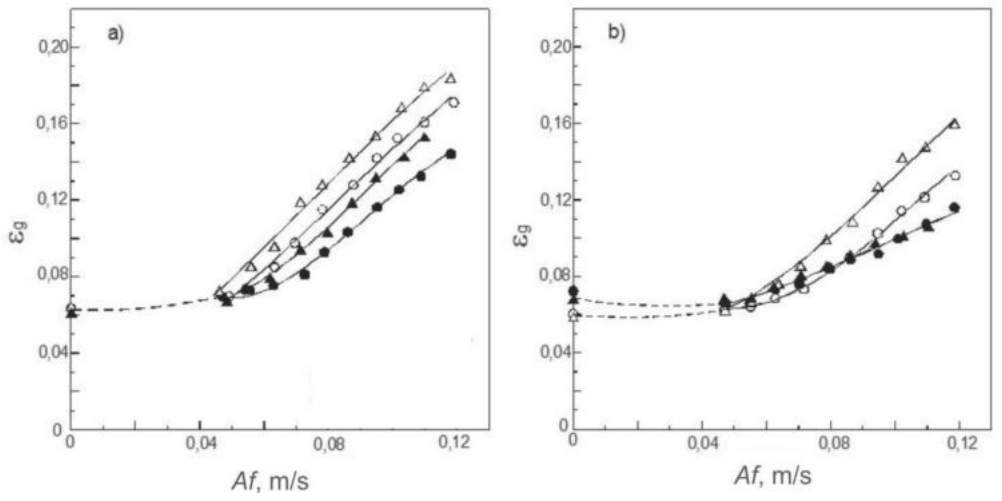


Figure 7.8 The influence of the degree of polymerization of the CMC solution on the gas holdup of two-phase and three-phase systems at $u_g = 1$ cm/s: a) 0.5 % CMC and b) 1.0 % CMC (ε_s , %: 0 – circles and 3.84 – triangles; CMC: PP 200 – open symbols and PP 1000 – black symbols) (Naseva et al., 2002).

Figure 7.9 compares gas holdup in Karr-type reciprocating plate columns of different diameters. At identical specific power consumption and superficial gas velocity, gas holdup remains roughly consistent across three reciprocating plate columns with similar geometric characteristics (Vasić et al., 2005b).

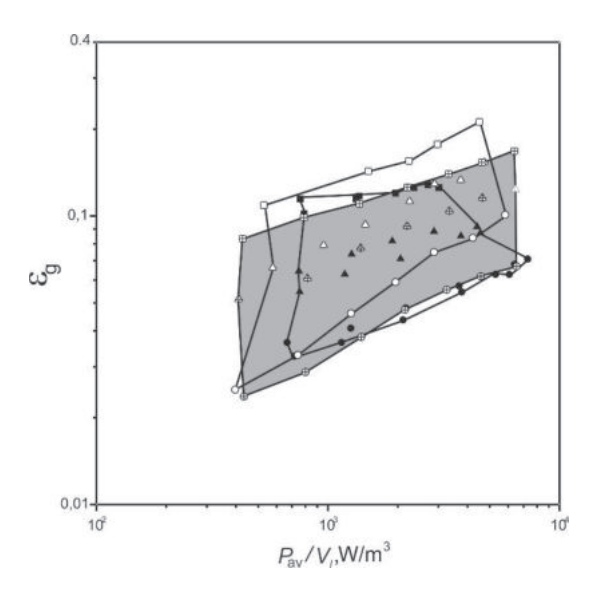


Figure 7.9 Dependence of the gas holdup on the specific power consumption (u_g , cm/s: 0.5 – circle, 1.0 – triangle, and 1.5 – square): $D_c = 2.54$ cm – black symbols; $D_c = 9.2$ cm – open symbols (Banković-Ilić, 1999); and $D_c = 9.2$ cm – crossed out symbols (Vasić et al., 2005b).

Comparisons of gas holdup between reciprocating plate columns and other two-phase contactors, such as bubble columns, packed columns, and tray columns, reveal that reciprocating plate columns achieve significantly higher gas holdup. Specifically, gas holdup in reciprocating plate columns is 50-60% greater than in pulsed bubble columns and approximately 25% higher than in vibrating disc columns under similar operating conditions (Gomaa et al., 1991). This enhanced gas holdup in reciprocating plate columns with segmental passage plates, compared to bubble columns and stirred vessels, is attributed to the effective mixing and bubble comminution facilitated by gas passage through the plate openings (Boyle, 1975).

Figure 7.10 illustrates gas holdup data for various systems, including stirred tanks (ST), bubble columns (BC), air-lift reactors with concentric draft tubes and external loop circulation (ALCDT and ALELC, respectively), and reciprocating plate columns. Reciprocating plate columns achieve the highest gas holdup at lower superficial gas velocities, due to the impact of mechanical mixing on the bubble comminution process (Banković-Ilić, 1999; Banković-Ilić et al., 2001b). As a result, reciprocating plate columns are particularly well-suited for complex reactions in three-phase (gasliquid-solid) systems.

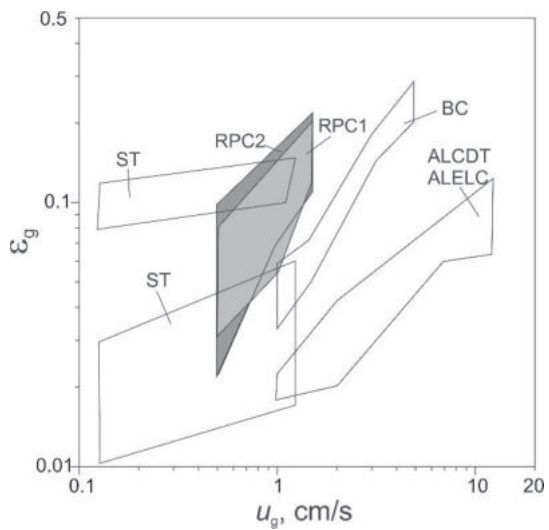


Figure 7.10 Comparison of gas holdup in different reactors (system: gas-liquid) (Banković-Ilić, 1999): RPC1 – $D_{\rm c}$ = 2.54 cm (Banković-Ilić, 1999), RPC2 – $D_{\rm c}$ = 9.2 cm (Banković-Ilić, 1999), BC (Stegeman et al., 1996), ALCDT (Al-Masry and Dukkan, 1998), ALELC (Gavrilescu et al., 1997, and ST – stirred tank (Gagnon et al., 1998).

8. BUBBLE SIZE IN GASSED RECIPROCATING PLATE COLUMNS

The dispersion state is influenced by processes involving the formation, dispersion, and coalescence of gas bubbles (Sundaresan and Varma, 1990a). Bubble formation occurs due to instabilities in the gas flow as it passes through openings in the plate, causing the flow to break into individual bubbles. The dispersion of these bubbles is governed by energy dissipation from reciprocating plates, influenced by the balance between stabilizing surface tension forces and disruptive local forces such as shear (Veljković, 1994). Non-uniform dynamic forces on the bubble surface can lead to deformation and eventual breakup. According to Kolmogorov's model of isotropic turbulence (Kolmogorov, 1941), the maximum stable size of a bubble in a turbulent field depends on the liquid's surface tension and the dissipated energy:

$$d_{3,2} = k \frac{\sigma^{0.6}}{\rho_1^{0.2} \left(P/V_1 \right)^{0.4}} \tag{8.1}$$

where $d_{3,2}$ is the Sauter bubble diameter, P is the power consumption, V_1 is the liquid volume, ρ_1 is the liquid density, σ is the surface tension, and k is the constant; k = 0.36 for Karr-type plates (Baird and Lane, 1973) and k = 0.36 for KRIMZ, GIAP, and Procházka-type plates (Kostanyan et al., 1980).

As illustrated in Figure 8.1, the bubble diameter decreases with increasing dissipated energy, regardless of the column diameter. As the total specific power consumption—encompassing mechanical agitation and aeration—increases, the Sauter bubble diameter aligns well with Equation (8.1) for water and glycerol solutions. However, this agreement is less accurate for *n*-butanol and sodium sulfite solutions.

Bubble coalescence occurs due to the increased bubble density in the space between the plates and is influenced by the physical properties and composition of the liquid, as well as the characteristics of the gas-liquid interface. For instance, electrolytes, polyalcohols, and fatty acids in aqueous solutions can reduce coalescence (Veljković, 1994). Comminution and coalescence are particularly notable at higher reciprocating intensities and flow velocities. The impact of these processes is affected by operating conditions (such as agitation intensity and gas and liquid flow rates), the geometric features of the device and the reciprocating agitator, and the physical properties of the liquid. These effects are also reflected in the correlations for bubble size in reciprocation devices, as summarized in Table 8.1.

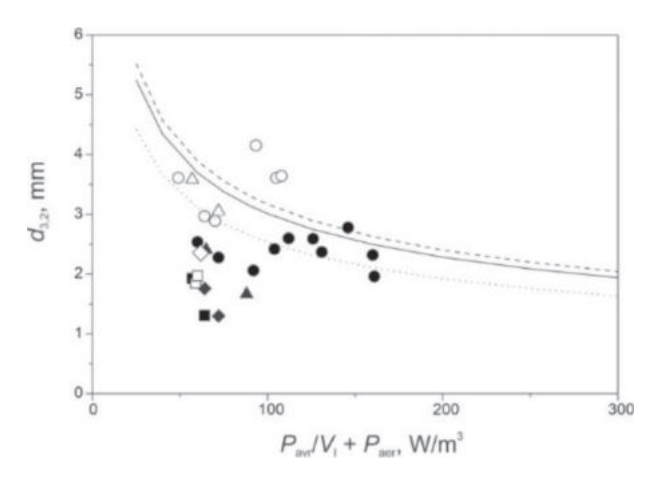


Figure 8.1 Effect of agitation on bubble size (Experiments – symbols; Equation (8.1) – lines; D_c , cm: 9.2 – open symbols and 2.54 – black symbols; water – circles, solid line, 64% glycerol – triangles, solid line, 0.5% n-butanol – squares, dotted line, and 0.8M Na₂SO₄ – rhombuses, dashed line) (Banković-Ilić, 1999).

Table 8.1 Empirical correlations for Sauter and mean bubble diameters

Type of device	System	Correlation	Reference
RPC	Air-water	$d_{3,2} = 1.15(Af)^{-0.6} \left(\frac{u_g}{u_l}\right)^{0.2}$	Parthasarathy (1981)
RPC	Air-water	Segregated dispersion - $[(Af) < 5cm/s]$: $d_{3,2} = 0.65(Af)^{-0.33}u_g^{0.06}u_l^{-0.206}d_o^{-0.1}\varepsilon^{0.21}$ Homogeneous dispersion - $[(Af) > 5cm/s]$:	Sundaresan and Varma (1990a)
RPC, SP	Air-water	$d_{3,2} = 0.42(Af)^{-0.17} u_g^{0.3} u_l^{-0.38} d_o^{-0.1} \varepsilon^{0.16}$ For $u_g < 0.1$ m/s: $d_{3,2} = \frac{0.044 u_g^{0.56}}{1 + 0.052(Af - Af_{cr})^{0.1}}$ For $u_g \ge 0.1$ m/s: $d_{3,2} = \frac{0.088}{1 + 8.716(Af - Af_c)^{0.05}}$	Gomaa et al. (1991)
HRRPC	Air-water	For $u_g \ge 0.1$ m/s. $u_{3,2} = \frac{1}{1 + 8.716(Af - Af_{cr})^{0.05}}$ $d = 2.778 \left(\frac{u_g}{Af}\right)^{0.13}$	Dhanasekaran and Karunanithi (2012c)
VDC	CO ₂ -water	$Af < (Af)_{cr} = 2.4 \text{ cm/s}$: $d_{av} = d_0 (= 0.55cm)$	Tojo et al. (1974a)
VDC	CO ₂ -water	$Af \ge (Af)_{cr.} d_{av} = d_0 + 0.0262 Af$ $\varepsilon_g < 0.21:$ $d_{3,2} = 0.12 d_d \left(\frac{d_d}{D_c}\right)^{-0.97} \cdot \left(\frac{\rho (2\pi Af)^2 d_d}{\sigma}\right)^{-0.32}$	Miyanami et al. (1978)

Abbreviations: HRRPC – hybrid rotating-reciprocating plate column, RPC – reciprocating plate column, SP – segmental passages, and VDC – vibrating disc column.

The photographic method is commonly employed to determine bubble size in reciprocating plate columns. To minimize the effects of reflection and refraction, a chamber filled with distilled water is placed around the column. Multiple images are captured for each operating condition, with a minimum of 250 bubbles analyzed. For ellipsoidal bubbles, the longer (d_1) and shorter (d_2) axes are measured, and the equivalent spherical diameter is then calculated using the following Equation (Skala, 1980):

$$d = \sqrt{d_1 \cdot d_2} \tag{8.2}$$

The bubbles are then classified based on their diameters. Given that bubble sizes are typically non-uniform, the mean bubble diameter is computed from the individual bubble measurements as follows:

$$d_{av} = \frac{\sum_{i=1}^{n} n_i d_i}{\sum_{i=1}^{n} n_i}$$
(8.3)

or Sauter bubble diameter:

$$d_{3,2} = \frac{\sum_{i=1}^{n} n_i d_i^3}{\sum_{i=1}^{n} n_i d_i^2}$$
(8.4)

where n_i is the number of babbles having the size of d_i .

As illustrated in Figure 8.2, increasing reciprocating intensity leads to a reduction in mean bubble diameter in reciprocating plate columns and vibrating disc columns due to the enhanced external energy input driving bubble comminution (Banković-Ilić, 1999; Gomaa et al., 1991; Skala, 1980; Sundaresan and Varma, 1990a; Veljković and Skala, 1988; Yang et al., 1986a). This reduction is more pronounced with higher liquid flow rates, as the turbulent forces contribute significantly to bubble comminution. The effect of bubble size reduction through turbulent forces is generally greater than that achieved by bubble collisions with plates (Skala, 1980). Additionally, the Sauter bubble diameter decreases with increasing reciprocation acceleration $A\hat{f}$, as the turbulent forces in the plate openings become more effective at reducing bubble size (Veljković and Skala, 1988). When the total power consumption is below a critical value, the Sauter mean diameter remains unaffected by agitation intensity. However, when power consumption exceeds this critical threshold, the mean diameter decreases (Veljković and Skala, 1988). The reduction in bubble size with increased reciprocating intensity is further enhanced in the presence of coalescence inhibitors (Veliković, 1985).

An increase in gas flow rate significantly impacts bubble size due to enhanced coalescence (Banković-Ilić, 1999; Gomaa et al., 1991; Veljković and Skala, 1988; Yang et al., 1986a), particularly noticeable at low superficial gas velocities (Gomaa et al., 1991). Higher superficial gas velocities lead to a broader distribution of bubble sizes, often manifesting multiple peaks at elevated gas flow rates (Sundaresan and Varma, 1990a).

There is disagreement among researchers regarding the influence of liquid flow rate on bubble size. One group suggests this influence can be disregarded (Gomaa et al., 1991; Rama Rao and Baird, 1988; Rama Rao et al., 1983), whereas others argue that bubble size decreases with increasing superficial liquid velocity, attributed to turbulent forces generated at plate openings (Yang et al., 1986a; Veljković and Skala, 1988). Increased superficial liquid velocity promotes narrower bubble size distributions, influencing dispersion formation (Sundaresan and Varma, 1990a).

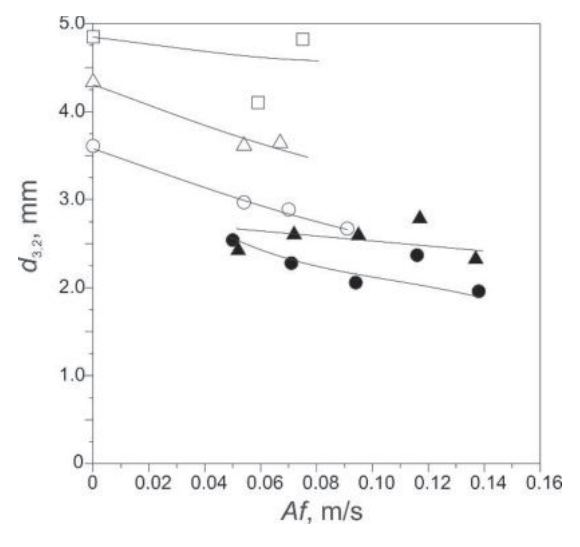


Figure 8.2 Dependence of the Sauter bubble diameter on reciprocating intensity (liquid: water; D_c , cm: 2.54 – black symbols and 9.2 – open symbols; u_g , cm/s: 0.5 – circles, 1.0 – triangles, and 1.5 squares) (Banković-Ilić, 1999).

The effect of liquid properties on bubble size is visually demonstrated in Figure 8.3, which displays photos of dispersed air bubbles in a gassed reciprocating plate column filled with water or aqueous solutions of glycerol, *n*-butanol, and sodium sulfite. These images were taken at comparable reciprocating plate movement frequencies (approximately 3 cm/s) and a superficial gas velocity of 0.5 cm/s. In comparison to water (Figure 8.3a), bubbles are smaller in liquids that either enhance bubble reduction due to viscous forces (e.g., aqueous glycerol solutions, Figure 8.3b) or inhibit bubble coalescence through interfacial phenomena (e.g., aqueous solutions

of *n*-butanol and sodium sulfite, Figures 8.3c and 8.3d). This difference is more pronounced in these aqueous solutions with the increased reciprocating intensity, leading to more efficient mixing. Under identical aeration and agitation conditions, bubble sizes are smaller in aqueous solutions of *n*-butanol and sodium sulfite compared to aqueous glycerol solutions. In the bubble dispersion process, interfacial phenomena have a greater impact on bubble size than viscous forces.

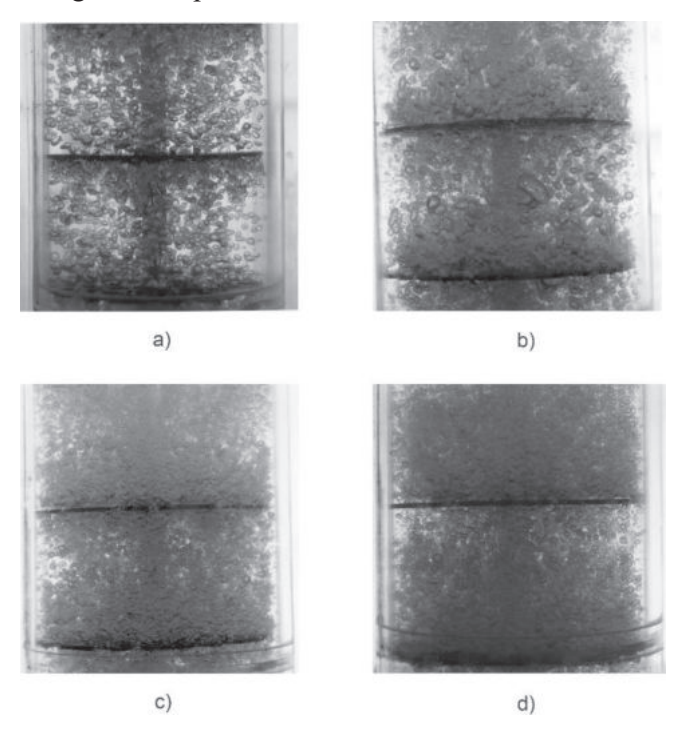


Figure 8.3 The effect of liquid properties on bubble size in a gassed reciprocating plate column ($D_c = 9.2$ cm) filled with (a) water, (b) 64% glycerol, (c) 0.8 M Na₂SO₄, and (d) 0.5% *n*-butanol ($f \approx 3 \text{ s}^{-1}$, $u_g = 0.5 \text{ cm/s}$).

The influence of liquid properties on bubble size can be quantified using the Sauter mean bubble diameter under consistent aeration and agitation conditions (Banković-Ilić, 1999). The Sauter mean bubble diameter decreases with an increase in the plate opening diameter and a decrease in the fractional plate-free area (Sundaresan and Varma, 1990a). In a segregated mode of operation, the bubble size in the column decreases, whereas it remains unchanged in the homogeneous mode (Sundaresan and Varma, 1990a). Skala et al. (1993) explored the relationship between mean bubble diameter and solids fraction. They observed that an increase in the solids fraction from 4% to 6% results in a slight increase in the mean bubble diameter. However, when the solids fraction is increased to approximately 12%, the

mean bubble size increases significantly. Additionally, the mean bubble diameter decreases with an increase in reciprocating intensity and a decrease in superficial gas velocity in a three-phase system.

Dhanasekaran and Karunanithi (2012c) developed a correlation to determine the mean bubble diameter in an air-water system, achieving 94% accuracy across the tested experimental conditions (see Table 8.1). When comparing their findings with the correlations from Rama Rao et al. (1983) and Sundaresan and Varma (1990a) for calculating bubble diameters in reciprocating plate columns, it was observed that the hybrid column yielded smaller and more uniformly distributed bubbles.

Bubble size distribution in reciprocating plate columns is typically represented by normal, lognormal, and Gamma distributions (Rama Rao and Baird, 1988; Skala, 1980; Sundaresan and Varma, 1990a; Veljković and Skala, 1988; Yang et al., 1986a). The bimodal distribution of bubble size is explained by the balance between bubble dispersion and coalescence (Skala, 1980). Under high or low mixing intensities, a polydisperse system is created, characterized by a single peak either in the small or larger bubble diameter range. At low gas flow rates, in water and aqueous solutions of sodium sulfite, n-butanol, and glycerol, bubble coalescence is prevented, leading to the presence of numerous tiny bubbles (Figures 8.4a and 8.5).

Increasing the reciprocating intensity shifts the maximum of the distribution curve towards smaller bubble diameters (Figure 8.4b). At high superficial gas velocities, bubble coalescence is favored, and with high power consumption, bubble comminution becomes significant. This results in the presence of both large and small bubbles in the gas-liquid dispersion, producing a distribution curve with two maxima (Veljković and Skala, 1988). This bimodal distribution is evident when the bubble size distribution widens, showing two peaks on the histogram (Figure 8.4c, Banković-Ilić, 1999). In aqueous solutions of sodium sulfite, *n*-butanol, and glycerol, a single peak in the small bubble size range is observed on the distribution histogram (Figure 8.5).

For a 9.2 cm i.d. reciprocating plate column, the presence of a large number of tiny bubbles in all tested liquids is notable (Figures 8.6, 8.7, and 8.8). In water, the bubble size distribution histogram exhibits one peak in the area of tiny bubbles and another peak in the area of larger bubble diameters, irrespective of agitation intensity (Figures 8.6a and 8.6b). Without agitation, a multimodal distribution is observed at all gas flow rates (Figure 8.7a) and at the highest gas flow rate with the highest reciprocating intensity (Figure 8.7b). For other Newtonian liquids and the non-Newtonian CMC solution, an unimodal distribution is observed, with a peak in the area of tiny bubbles (Figure 8.8).

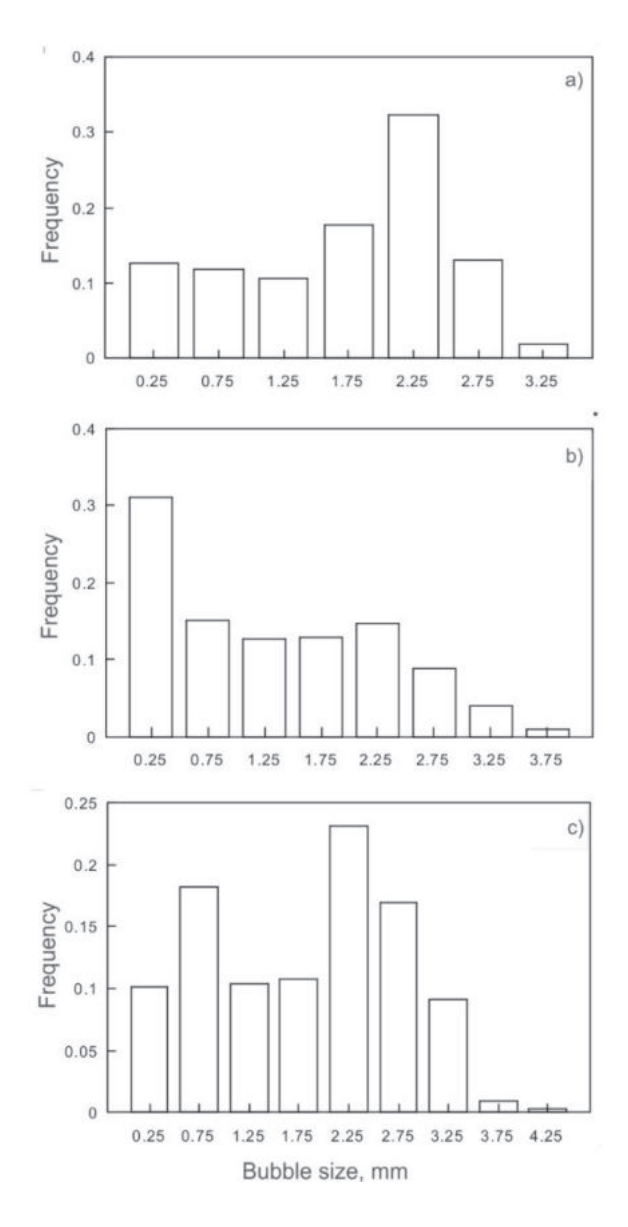


Figure 8.4 Bubble size distribution histograms: (a) $u_g = 0.5$ cm/s and f = 3 s⁻¹, (b) $u_g = 0.5$ cm/s, and f = 4.9 s⁻¹, and (c) $u_g = 1$ cm/s and f = 4 s⁻¹ ($D_c = 2.54$ cm; liquid: water) (Banković-Ilić, 1999).

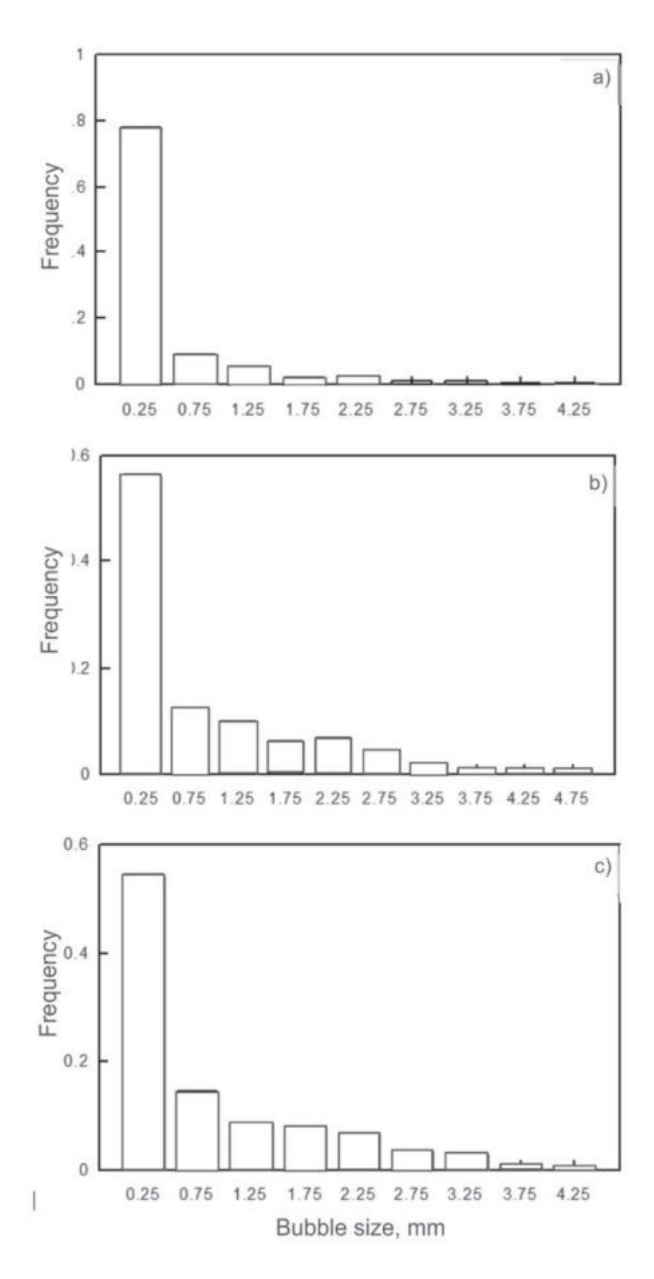


Figure 8.5 Bubble size distribution histograms: (a) 64% glycerol, $f = 1.8 \text{ s}^{-1}$, (b) 0.5% n-butanol, $f = 2.1 \text{ s}^{-1}$, and (c) 0.8M Na₂SO₄, $f = 2.2 \text{ s}^{-1}$ ($D_c = 2.54 \text{ cm}$; $u_g = 0.5 \text{ cm/s}$) (Banković-Ilić, 1999).

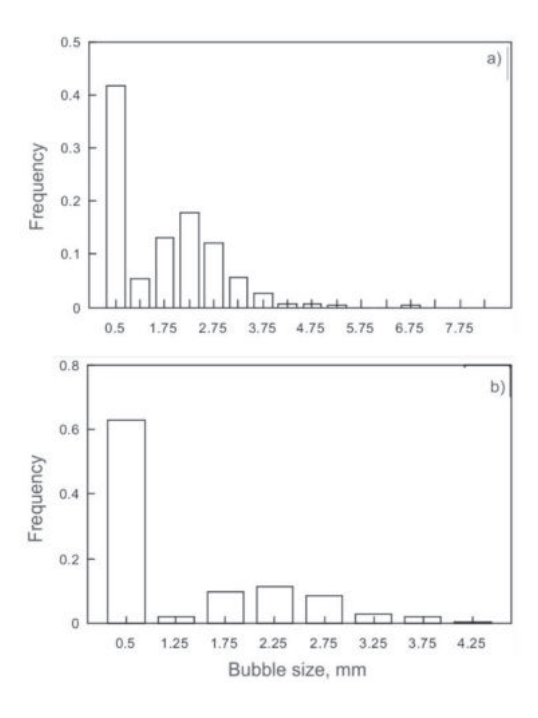


Figure 8.6 Bubble size distribution histograms: (a) $f = 2.3 \text{ s}^{-1}$ and (b) $f = 3.7 \text{ s}^{-1}$ ($D_c = 9.2 \text{ cm}$; $u_g = 0.5 \text{ cm/s}$; liquid: water) (Banković-Ilić, 1999).

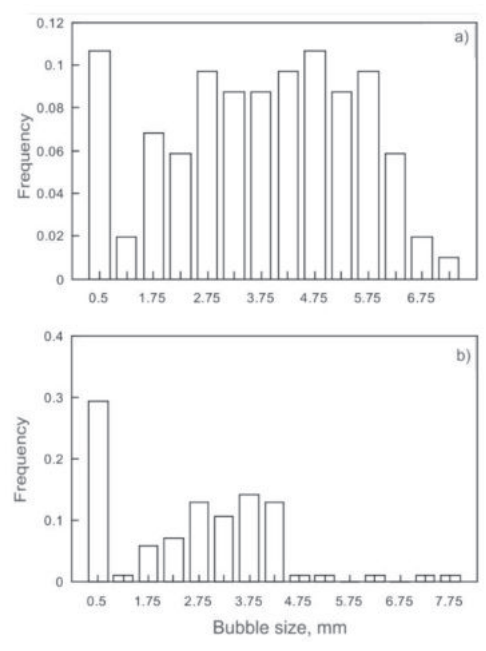


Figure 8.7 Bubble size distribution histograms: $(u_g = 1.5 \text{ cm/s})$: (a) $f = 0 \text{ s}^{-1}$ and (b) $f = 3.2 \text{ s}^{-1} (D_c = 9.2 \text{ cm}; \text{ liquid: water})$ (Banković-Ilić, 1999).

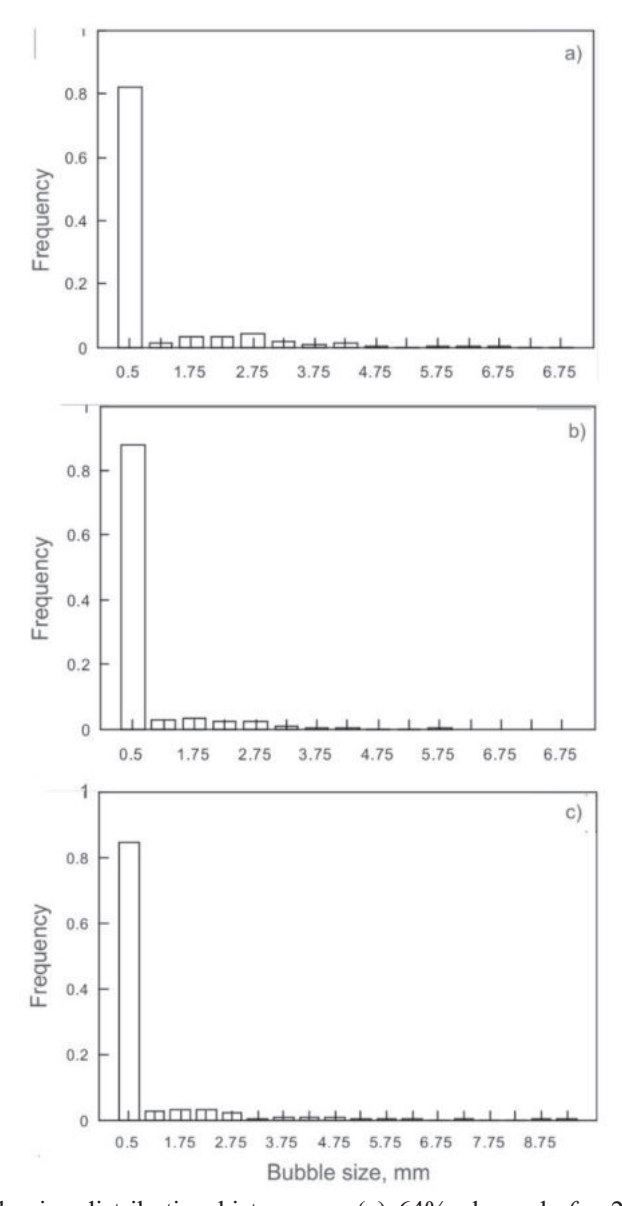


Figure 8.8 Bubble size distribution histograms: (a) 64% glycerol: $f = 2.4 \text{ s}^{-1}$, (b) 0.8 M Na₂SO₄: $f = 2 \text{ s}^{-1}$, and (c) 1% CMC: $f = 1.9 \text{ s}^{-1}$ ($D_c = 9.2 \text{ cm}$; $u_g = 0.5 \text{ cm/s}$) (Banković-Ilić, 1999).

9. AXIAL MIXING

In real column-type multiphase contactors, there is no ideal plug flow of the liquid phase. Deviations from ideal plug flow occur due to channeling, recirculation, or the formation of immobile zones. Flow non-ideality is often quantified by the intensity of mixing in the direction of or perpendicular to fluid flow, i.e., by the axial or radial mixing (dispersion) coefficients. In an ideal plug flow, there is no axial mixing, and the axial mixing coefficient is zero. Conversely, in flow with ideal mixing, the axial mixing coefficient is maximal. In smaller-diameter columns, radial mixing is usually negligible.

When designing column-type chemical reactors with countercurrent flow, a slight degree of axial dispersion is desirable to maintain a high concentration gradient (driving force) in the axial direction.

9.1. Flow models

The following models are used to describe the actual flow in continuous reactors (Skala and Mićić, 1982):

- Combined model: Includes ideal mixing, channeling, and plug flow in different proportions.
- Convective model: Characterized by a defined velocity distribution.
- **Dispersion model**: Based on the analogy between fluid mixing during flow and the diffusion process.
- Compartmental (backflow) model: Consists of a series of *N*-compartments with ideal mixing that are interconnected, forming a cascade.
- **Circulation model**: Assumes varying flow velocities inside the reactor that change over time.

The dispersion model is suitable for processes where continuous differential contact occurs between the phases, while the cascade model is appropriate for devices composed of multiple compartments.

9.1.1. Dispersion flow model

The dispersion flow model, also known as the diffusion model, uses the same mathematical expressions to describe mixing as those used for diffusion mass transfer. The model is based on the following assumptions (Pratt and Baird, 1983):

- The backmixing of each phase can be characterized by a constant turbulent diffusion coefficient.
- The velocity and concentration of each phase are constant across the crosssection.
- The volumetric mass transfer coefficient is constant, or its mean value in the column can be used.
- The volumetric flow rates of the phases are constant.
- The equilibrium relation is linear.

The dispersion model defines two extreme cases depending on the turbulence intensity, i.e., the mixing intensity in the column: ideal plug flow and ideal mixing. Due to variations in the axial dispersion coefficient, which is influenced by the reciprocating intensity, the required volume of a reciprocating plate column is slightly larger than that predicted for no backmixing and significantly larger if complete mixing occurs in the column. Assuming a constant fluid flow rate through the reciprocating plate column and negligible radial mixing, the residence time distribution is a symmetric function similar in shape to the Gaussian normal distribution (Levenspiel, 1979).

$$E = \frac{1}{2} \left(\frac{Pe}{\pi} \right)^{0.5} \exp \left[-\frac{Pe(1-\Theta)^2}{4} \right]$$
 (9.1)

where E is the residence time distribution, Pe is the Peclet number, and θ is the normalized time.

9.1.2. Model of a series of N-compartments with ideal mixing

In the case of reciprocating plate columns, a compartmental model can be effectively employed, consisting of a series of N perfectly mixed compartments of equal volume, with or without backflow between compartments. The tracer impulse response, which represents the tracer concentration in the output flow of these compartments, provides information about the residence time density distribution of the fluid (Skala and Mićić, 1982). The model parameters, such as the intensity of backmixing (θ) and the number of compartments (N), are determined by solving a system of N differential Equations. When backflow intensity is negligible, the reciprocating plate column can be represented using a one-parameter model, where N is the sole parameter derived from solving the system of Equations.

9.2. Determination of model parameters

Regardless of the model used to describe fluid flow in reciprocating plate columns, the model parameters can be determined using various methods, including

the linear method, the method of moments, or the "fitting" of experimental data to the theoretical fluid flow model. The different flow models and the methods for calculating their parameters in reciprocating plate columns are summarized in Table 9.1.

9.3 Coefficient of axial dispersion in reciprocating plate columns

The efficiency of multiphase reciprocating plate columns depends significantly on fluid flow characteristics and is optimized when flow approaches the ideal plug flow. Increased axial mixing tends to reduce the impact of mechanical agitation on the mass transfer rate of the gaseous reactant (Baird et al., 1992; Lounes and Thibault, 1993, 1996; Yang et al., 1986b).

In reciprocating plate columns, high mass transfer rates and relatively low axial dispersion coefficients can be achieved. While extensive literature exists on axial dispersion for 'pure' liquids, particularly in the context of extraction columns, recent studies have expanded to multiphase systems. However, findings across different studies often appear contradictory, which remains challenging to reconcile:

- The coefficient of axial dispersion either increases (Kagan et al., 1973; Miyauchi and Oya, 1965) or decreases (Kim and Baird, 1976a; Stevens and Baird, 1990) with an increase in the distance between plates.
- The axial dispersion coefficient may increase (Miyauchi and Oya, 1965) or decrease (Mar and Babb, 1959) with larger plate openings.
- The axial dispersion coefficient either shows no significant dependence on column diameter (Kagan et al., 1973; Kim and Baird, 1976b) or exhibits a weak dependency (Karr et al., 1987).
- The axial dispersion coefficient generally increases approximately linearly with reciprocating intensity (Kim and Baird, 1976a; Miyauchi and Oya, 1965; Stevens and Baird, 1990; Lounes and Thibault, 1993), though higher amplitudes also appear to influence this increase (Lounes and Thibault, 1993).
- Turbulent fluid flow between plates and circulation caused by gas bubbles enhance axial mixing compared to single-phase systems (Baird and Rama Rao, 1991).
- Increasing the superficial gas velocity in a gas-liquid system results in a higher axial dispersion coefficient, with a more pronounced effect at elevated superficial gas and liquid velocities (Nikolić et al., 2004).
- The axial dispersion coefficient increases with higher superficial liquid velocity due to increased resistance to liquid and gas flow through the plate openings

- and the impact of liquid jets on mixing throughout the interplate space, which promotes backmixing (Nikolić et al., 2004).
- The presence of solid particles between plates significantly affects the axial
 dispersion coefficient's dependence on the superficial gas velocity at low
 reciprocating intensities, though this effect diminishes with increased
 reciprocating intensity. Additionally, the axial dispersion coefficient in a threephase system decreases with rising reciprocating intensity, irrespective of
 superficial gas velocity (Nikolić et al., 2004).

Empirical correlations for calculating the axial dispersion coefficient in single-phase and two-phase systems are provided in Table 9.2. These correlations apply only to the continuous (liquid) phase and the specific column types in which the axial dispersion studies were conducted. Variations among the correlations arise from differences in column geometries, reciprocating plate designs, and operating conditions. Therefore, it is crucial to use these literature correlations with caution, as they apply only to particular systems and column geometries (Stevens and Baird, 1990).

9.4 Comparison of reciprocating plate columns with other multiphase devices

Figure 9.1 compares the axial dispersion coefficients of different multiphase contactors, including reciprocating plate columns, bubble columns, and packed columns. The type of contactor, its geometric characteristics, and operating conditions significantly influence the axial dispersion coefficient. Two reciprocating plate columns with nearly identical diameters (Nikolić, 2003; Parthasarathy et al., 1984) show similar axial dispersion coefficients within the same range of reciprocating intensities (Figure 9.1a), despite differing flow velocity ranges (Figure 9.1b). A similar pattern is observed for two additional reciprocating plate columns of comparable diameter under the same operating conditions (Nikolić, 2003; Lounes and Thibault, 1996) (Figure 9.1c). In contrast, packed columns (Satter and Levenspiel, 1966) and bubble columns (Baird and Rice, 1975) exhibit less pronounced backmixing compared to reciprocating plate columns.

Table 9.1 Models and methods of calculating flow model parameters in reciprocating plate columns.

Flow model	Model	Methods of cal	Methods of calculating flow model parameters	eters	Reference
	parameter	Method of	Linear methods	Optimization method	I
Compartmental – a series of N perfectly mixed compartments without backflow	N	$N = \frac{1}{\sigma_0^2} = \frac{I_{\alpha^2}^2}{\sigma_i^2}$	$F_{(s) \bmod} = \left(\frac{t_{av} \cdot s}{N}\right)^{-N}$	$E_{\theta, \operatorname{mod}} = \theta^{N-1} \cdot \frac{N^N \cdot e^{(-\theta N)}}{(N-1)^{N-1} \cdot e^{(1-N)} \cdot \sqrt{2\pi(N-1)}}$	Skala and Mićić (1982)
Compartmental – a series of N perfectly mixed compartments with backflow	α ; N	$\sigma_{\theta}^{2} = \frac{1+2\alpha}{N}$	$YY = \frac{1}{N^2} s + \frac{1+2\alpha}{t_{sr}N}$ $YZ = \frac{1+2\alpha}{t_{sr}N} + \frac{1}{t_{sr}^2}$	$F_{\rm (s)mod} = \left\{ \frac{1}{2\pi} \left[1 + 2\alpha + \frac{I_m}{N} S - \sqrt{1 + 2 \frac{I_m}{N} S (1 + 2\alpha) + \left(\frac{I_m}{N} S \right)^2} \right] \right\}^N$	Skala (1980); Skala and Mićić (1982)
Dispersion	$D_{l}(\mathrm{Pe})$	$D_l = \frac{u_l \cdot L}{Pe}$	$-\frac{1}{U_0} = t_{\omega} \cdot \frac{s}{U_0^2} - \frac{1}{Pe}$ $\frac{1}{U_1^2} = \frac{4s}{t_{\omega} Pe} + \frac{1}{t_{\omega}^2}$	$E_{\theta, \text{mod}} = \frac{1}{2} \left(\frac{Pe}{\pi \theta} \right)^{0.5} \cdot \exp \left[\frac{-Pe(1-\theta)^2}{4\theta} \right]$	Skala and Mićić (1982)

^a Based on the corresponding model's transfer function (Laplace transform).

Table 9.2 Empirical correlations for the axial dispersion coefficient in reciprocating plate columns.

System	Dc, cm	Operating conditions	Correlation	Reference
Water \downarrow	2.54	A = 0-1.4 cm; f = 0-10 Hz; $u_1 = 0.1-1.1 \text{ cm/s}$	$\ln D_l = \ln \left(D_l \right)_{l=0} + \left(Af \right)^{0.56} \exp \left(-1, 44 \cdot u_c + 0, 912 \right)$ $\left(D_l \right)_{l=0} = 5, 15 \cdot u_l^{0.471}$	Skala (1976)
Water ↑	5.0	A = 0.15-0.45 cm; f = 0.4-10 Hz; $u_1 = 0.3-0.5$ cm/s	$D_{l} = 0, 3 \frac{h - 2m_{l}}{h - 4, 5} \cdot \frac{2Afd_{o}^{2}}{\varepsilon}$	Nemecek and Procházka (1974)
			$2m_1 = \begin{cases} 1.05 \left(\frac{2.4J}{\varepsilon^2} \right) & \text{for } 2m_1 < 0.65 (h + 2.35) \\ 0.5 (h + 2.35) & \text{for other values} \end{cases}$	
Water↓	5.0	A < 0.012 cm; f = 20-100 Hz; $u_1 = 0.23-0.44 \text{ cm/s}$	$\frac{D_l}{h \cdot u_l} = 0.5 + \alpha$	Baird et al. (1992)
Water ↑	5.08	A = 1.8 - 2.9 cm; f = 0.5 Hz; $u_1 = 0.15 - 0.3 \text{ cm/s}$	$D_{i} = \left[I_{m} + \left(I_{b} - I_{m} \right) \left(\varepsilon_{b} / \varepsilon_{t} \right)^{0.34} \right]^{4/3} \varepsilon_{t}^{1/3}$ $I_{m} = 0.301 \text{ cm: } I_{b} = 4.02 \text{ cm}$	Baird and Rama Rao (1991)
Water, HCl, glucose, and Polyox solutions \downarrow	5.08	A < 2.35 cm; f = 0.5-6 Hz; $u_1 = 0-1.2 \text{ cm/s}$	$D_i = 1.98 \cdot A^{1.74} f^{0.96} h^{-0.69}$ for Teflon plates $D_i = 5.56 \cdot A^{1.77} f^{1.00} h^{-1.32}$ for stainless steel plates	Kim and Baird (1976a)
HCl solution ↓	5.08	A < 2.35 cm; f = 0.5-6 Hz; $u_1 = 0-1.2 \text{ cm/s}$	$D_l \propto A^{1.80} f^{1.00} d_o^{1.8} \delta^{-0.3} h^{-1.3}$	Kim and Baird (1976b)

Continuation of Table 9.2 Empirical correlations for the axial dispersion coefficient in reciprocating plate columns.

System	D_c , cm	Operating conditions	Correlation	Reference
Water ↓	5.08	A = 1-1.85 cm; f = 2.2-3.8 Hz; $u_1 = 0.5-1.32 \text{ cm/s}$	$D_{_{_{_{_{_{_{_{_{_{_{_{_{_{_{_{_{_{_{$	Stevens and Baird (1990)
Air-water ↓↑	2.54	A = 0.65-1.5 cm; f = 0.5-6.18 Hz; $u_1 = 0.38-1.2 \text{ cm/s};$ $u_g = 0.8-3.2 \text{ cm/s}$	K_1 , K_2 — nondimensional constants $D_i = 90.5 \cdot u_R^{-0.964}$ $D_i = 81.47 \cdot u_I^{-0.54} u_R^{-0.75+0.19 \cdot u_L}$ $u_R = \frac{u_S}{\varepsilon_S} + \frac{u_I}{1 - \varepsilon_S} + 2.4f$	Skala (1980)
Air-water ↓↑	3.2	A = 0-1.5 cm; f = 0.4-3 Hz; $u_1 = 0.05-0.58 \text{ cm/s};$ $u_2 = 0.044 \text{ cm/s}$	$D_{l} = 1.754 \cdot A \cdot f \cdot h^{0.67} \cdot d_{o} \cdot D_{c}^{-0.67} \cdot \varepsilon^{-1.0}$	Miyauchi and Oya (1965)
Water ↓ Air-water ↓↑ Water ↓ - spherical particles (8.3 mm) Air-water ↓↑ - spherical particles (8.3 mm)	2.54	$A_{\rm g} = 1 \text{ i } 2.35 \text{ cm};$ f = 2-4.5 Hz; $u_{\rm l} = 0.24-0.87 \text{ cm/s};$ $u_{\rm g} = 0-1.48 \text{ cm/s}$	$D_{l} = 0.49 (Af)^{1.11} u_{l}^{0.31}$ $D_{l} = 3.37 \cdot (Af)^{0.17} \cdot u_{l}^{0.38} \cdot u_{g}^{0.07}$ $D_{l} = 1.26 \cdot (Af)^{1.42} u_{l}^{0.52} e_{g}^{0.03}$ $D_{l} = 1.39 (Af)^{0.47} u_{l}^{0.42} u_{g}^{0.03} \cdot \varepsilon_{s}^{-0.26}$	Nikolić et al. (2004)
Water↓ Air-water ↓↑	10	A = 1 cm; f = 0 - 1.5 Hz; $u_1 = 0.32 - 1.17 \text{ cm/s};$ $u_g = 3.18 - 7.43 \text{ cm/s}$	$D_{l} = 0.6551u_{l}L\left(\frac{Af}{u_{l}}\right)^{-0.3032}\left(\frac{dou_{l}\rho_{l}}{u_{l}}\right)^{-0.4527}$ $D_{l} = 0.00066u_{l}c\left(\frac{u_{g}}{u}\right)^{0.146}\left(\frac{d_{o}Af\rho_{l}}{\mu}\right)^{-0.1594}\left(\frac{d_{o}^{3}g\rho_{l}^{2}}{\mu^{2}}\right)^{0.3943}$	Dhanasekaran and Karunanithi, 2010a ^a

^a Hybrid rotating-reciprocating plate bubble column.

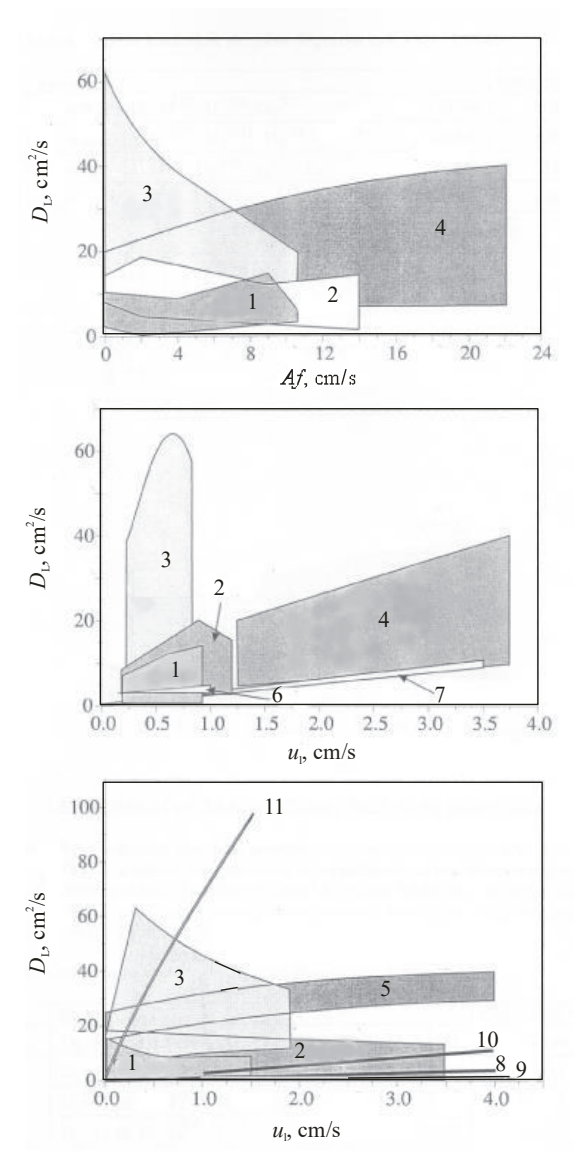


Figure 9.1 Comparison of the axial dispersion coefficient of different multiphase devices: dependence of the axial dispersion coefficient on (a) reciprocating intensity, (b) superficial liquid velocity, and (c) superficial gas velocity: reciprocating plate column: 1) $D_c = 2.54$ cm (Nikolić et al., 2004); 2) $D_c = 2.54$ cm (Skala, 1980); 3) $D_c = 9.2$ cm (Nikolić, 2003); 4) $D_c = 9.3$ cm (Parthasarathy et al., 1984); 5) $D_c = 10.2$ cm (Lounes and Thibault., 1996); packed column (Rashig rings): 6) $D_c = 5.1$ cm (Michell and c, 1972); 7) $D_c = 10.2$ cm (Sater and Levenspel, 1966); and bubble column: 8) $D_c = 1.97$ cm (Cova, 1974); 9) $D_c = 4$ cm (Ohki and Inoue, 1970); 10) $D_c = 6.6$ cm (Kato and Nishiwaki, 1972); 11) $D_c = 9.2$ cm (Baird and Rice, 1975).

10. VOLUMETRIC MASS TRANSFER COEFFICIENT IN RECIPROCATING PLATE COLUMNS

The efficiency of multiphase contactors hinges on the interphase mass transfer rate of the reactant per unit volume of dispersion, known as the volumetric mass transfer coefficient ($k_{l}a$), which denotes the aeration capacity in the liquid phase. Methods for determining volumetric oxygen mass transfer coefficient are categorized into steady-state and non-steady-state approaches, depending on whether the concentration of the diffusing component in the liquid phase changes over time. Steady-state methods involve continuous liquid phase flow through the reactor. Direct measurement involves assessing absorbed gas levels, typically oxygen, at both inlet and outlet using suitable instrumentation. Indirect methods rely on balancing oxygen absorption and consumption rates from the gas phase.

Non-steady-state methods are applicable when the liquid phase operates in batches. The dynamic (absorption) method monitors dissolved oxygen changes in the output gas stream continuously using appropriate instruments. The chemical method utilizes reactions (e.g., sulfite oxidation) to determine oxygen mass transfer rates. In this approach, the volumetric oxygen mass transfer coefficient is computed based on experimentally derived oxygen absorption rates and solubility.

As the reciprocating amplitude and frequency, or reciprocating intensity, increase, the volumetric oxygen mass transfer coefficient in the liquid also rises due to greater power consumption and enhanced gas bubble dispersion (Banković-Ilić et al., 2000, 2001a; Baird and Rama Rao, 1988; Lounes and Thibault, 1994; Rama Rao and Baird, 2003; Skala, 1980; Sundaresan and Varma, 1990b; Vasić et al., 2005; Yang et al., 1986b). This increase is insignificant at lower and significant at higher reciprocating intensities (Yang et al., 1986b). The change in the volumetric oxygen mass transfer coefficient is influenced by the flow regime and typically becomes noticeable at reciprocating intensities greater than 3 cm/s (Yang et al., 1986b) or 5 cm/s (Skala, 1980; Sundaresan and Varma, 1990b). At low reciprocating intensities, the system operates in a segregated regime, with gas-to-liquid mass transfer dependent primarily on aeration intensity (Lounes et al., 1995; Skala and Veljković, 1988; Veljković, 1985). As the gas flow rate increases, the volumetric mass transfer coefficient reaches a maximum value due to the increased energy transferred from the gas to the liquid. It leads to a higher gas holdup in the column and enhanced bubble dispersion as they pass through the plate openings, causing reciprocating plate columns to function similarly to bubble columns with perforated plates (Veljković, 1985). With increased reciprocating intensity and a constant gas flow rate, the intensification of gas bubble dispersion results in a greater specific interfacial surface area and a higher volumetric oxygen mass transfer coefficient. In such conditions, mixing becomes the primary factor influencing the mass transfer rate between the gas and the liquid.

There is limited data in the literature regarding the impact of liquid flow rate on the volumetric oxygen mass transfer coefficient. Some researchers report that the volumetric oxygen mass transfer coefficient remains unchanged with increasing superficial liquid velocity (Sundaresan and Varma, 1990b) or do not address this influence (Skala and Veljković, 1988; Veljković, 1985). In contrast, other studies indicate that a higher liquid flow rate enhances the volumetric oxygen mass transfer coefficient (Baird and Rama Rao, 1988; Yang et al., 1986b). The effect of liquid flow rate is influenced by the geometry of the reciprocating agitator and the fluid velocity, stemming from the turbulent currents generated as the liquid flows through the plate openings. Additionally, the direction of phase flow affects the volumetric oxygen mass transfer coefficient, with concurrent flow generally resulting in higher coefficients compared to countercurrent flow (Sundaresan and Varma, 1990b).

The relationship between the volumetric oxygen mass transfer coefficient and the properties of the liquid is complex, as these properties can influence both the mass transfer coefficient and the specific interfacial area. For instance, adding a small concentration of a non-electrolyte, such as alcohol, can increase the volumetric oxygen mass transfer coefficient (Liu and Chen, 1993). Veljković (1985) quantified the impact of liquid physical properties on the volumetric oxygen mass transfer coefficient in reciprocating plate columns using the dimensionless Morton's number, which incorporates the physical properties of the liquid (Van Dierendonck et al., 1971):

$$Z = \frac{\rho_l \sigma^3}{g \mu_l^4} \tag{10.1}$$

where Z is Morton's number, ρ_l is the liquid density, σ is the superficial tension, μ_l is the liquid dynamic viscosity, and g is the gravitational acceleration.

The volumetric oxygen mass transfer coefficient exhibits a slight increase with increasing Morton's number (Veljković, 1985). For liquids with similar surface tension and density, the coefficient decreases as viscosity increases. In sucrose solutions, Veljković (1985) observed that the volumetric oxygen mass transfer coefficient decreased with higher solution concentrations, attributed to increased viscosity, while changes in bubble size and interfacial area were minimal.

The geometrical characteristics of a reciprocating plate column significantly impact the volumetric oxygen mass transfer coefficient. Increasing the number of

reciprocating plates under constant aeration and mixing conditions leads to a higher volumetric oxygen mass transfer coefficient (Skala and Veljković, 1988; Veljković, 1985). More plates enhance energy dissipation, reduce bubble coalescence, and increase the specific interfacial area (Lounes and Thibault, 1994; Veljković, 1985). Conversely, an increase in the diameter of plate openings and free surface area tends to decrease the volumetric oxygen mass transfer coefficient, likely due to reduced power consumption (Lounes and Thibault, 1994; Sundaresan and Varma, 1990b).

The effect of the solid phase on the volumetric oxygen mass transfer coefficient has been explored in several studies (Banković-Ilić, 1999; Sundaresan and Varma, 1990b). Adding Rashig rings (2.5% by volume) to each interplate space results in a 30% increase in the volumetric oxygen mass transfer coefficient. This enhancement is attributed to the solid phase's role in improving bubble comminution (Sundaresan and Varma, 1990b). In a three-phase system, increasing reciprocating intensity and gas flow rate enhances the mass transfer rate, as higher power consumption promotes more effective bubble reduction (see Figure 10.1). The volumetric oxygen mass transfer coefficient is generally higher in three-phase systems compared to two-phase systems due to more efficient mixing and the beneficial effects of the solid particles. However, increasing the solids fraction does not significantly impact the volumetric oxygen mass transfer coefficient.

Similar to other contact devices with mechanical agitation, the volumetric oxygen mass transfer coefficient in reciprocating plate columns can be correlated with factors such as power consumption (total, mean, or specific), reciprocating intensity, superficial gas and liquid velocities, and geometric characteristics of the column (see Table 10.1). The exponents for power consumption and superficial gas velocity range from 0.25 to 0.74 and 0.44 to 1.55, respectively. At low reciprocating intensities, mass transfer is primarily dependent on the gas flow rate, while at higher reciprocating intensities, the influence of power consumption and agitation becomes comparable. The correlation for volumetric oxygen mass transfer in reciprocating plate columns with small plate opening diameters and fractional plate-free area (Lounes and Thibault, 1994) closely matches that of turbine-mixed vessels (Gagnon et al., 1998; Linek et al., 1987). Additionally, some correlations for the volumetric oxygen mass transfer coefficient also incorporate superficial liquid velocity (Baird and Rama Rao, 1988; Yang et al., 1986b).

Dhanasekaran and Karunanithi (2010b, 2012d) conducted a study using a hybrid rotating-reciprocating plate column to investigate the effects of multiple parameters on the mass transfer coefficient in an air-sodium sulfite solution system, specifically focusing on the oxygen absorption from air into deoxygenated water. They employed the response surface methodology combined with a Box-Behnken design to develop

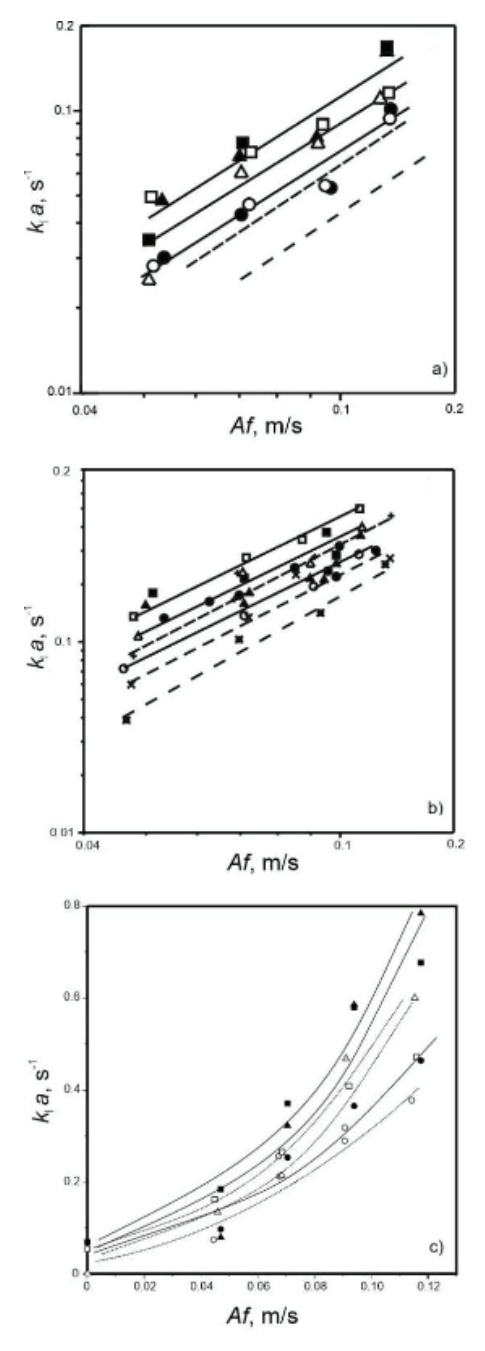


Figure 10.1 Dependence of the volumetric oxygen mass transfer coefficient on reciprocating intensity (gas-liquid system – dashed line; gas-liquid-solid system – solid line) : (a) D_c = 2.54 cm (Skala and Veljković, 1988), (b) D_c = 9.2 cm (Banković-Ilić, 1999), (c) D_c = 16.6 cm (Vasić, 2005b): (liquid: 0.8 M Na₂SO₄, ε _s, %: 0, u_g, cm/s: 0.5 – *, 1.0 – ×, and 1.5 – +; ε _s, %: 3.8 – open symbols, and 6.6 – black symbols, u_g, cm/s: 0.5 – circles, 1.0 – triangles, and 1.5 – squares).

Table 10.1 Correlations for volumetric oxygen mass transfer coefficient.

Reference	Veljković (1985); Skala and Veljković (1988)	Yang et al. (1986b)	Baird and Rama Rao (1988)	Sundaresan and Varma (1990b)		Lounes and Thibault (1994)	Lounes et al. (1995)
Correlation	$k_l a = 0.467 \left(P_g^*\right)^{0.25} u_g^{0.6}$	$k_l a = 0.00401 (Af)^{0.18} u_g^{0.42} u_l^{0.918}$	$k_l a = 4.86 \left(\frac{1}{g} / V_l \right)^{0.364} u_g^{1.55}$ $k_l a = 3.90 \left(\frac{1}{g} / V_l \right)^{0.246} u_g^{0.623} u_l^{0.825}$	Segregated regime, $Af < 5 \text{ cm/s}$: $k_t a = 0.0033 (Af)^{0.1} u_g^{0.25} d_o^{-0.2} \varepsilon^{-0.5}$	Homogeneous regime: $Af \ge 5$ cm/s: $k_i a = 0.0033 (Af)^{0.18} u_g^{0.2} d_o^{-0.12} \varepsilon^{-0.52}$ $k_i a = 0.0043 (Af)^{0.18} u_g^{0.2} d_o^{-0.12} \varepsilon^{-0.52}$	$k_l a = 0.00723 \left(P_g / V_l \right)^{0.59} u_g^{0.44}$	$k_t a = 0.281 \left(P_g / V_t \right)^{0.632} u_g^{1.138}$ $P_g / V_t < 600 \text{ W/m}^3;$ $k_t a = 1.677 \left(P_g / V_t \right)^{0.296} u_g^{1.142}$ $P_g / V_t > 600 \text{ W/m}^3;$ $k_t a = 0.0196 \left(P_g / V_t \right)^{1.017} u_g^{1.195}$
Method	Sulfite Physical (O ₂ -water) Dynamical	Physical $(O_{2}$ -water)	Physical (O ₂ -water)	Physical (CO ₂ - water)		Physical (O ₂ -water)	Physical (O ₂ -water)
Operating conditions Method $(u_g, u_l, cm/s; P_g/V_l, W/m^3)$	$u_{\rm g} < 2.5$ or $u_{\rm g} < 5.0$ Effects of $u_{\rm l}$ are	$0.72 < u_{\rm g} < 4.98$	$0.49 < u_g < 0.99$ $23 \le P_g/V_1 \le 3620$ $0.99 < u_1 < 3.95$	$0.6 < u_g < 4.6$ $0.41 < u_l < 3.68$		$0.68 < u_{\rm g} < 1.86$ $290 \le P_{\rm g}/V_{\rm l} \le 7200$	$0.65 \le u_{\rm g} \le 0.40$ $35 \le P_{\rm g}/V_{\rm l} \le 6600$
S	0.41 or 0.51	0.53	0.57	0.09-		0.28	0.33
d_o mm	7 or 8	15	41	3-65		6.35	6.35
<i>l_c</i> m	2	3.96	7	0.56		1.26	3.85
u^b	65 or 33	84	54	10		18	18
D_c	2.54	5.08	5.08	9.3		10.16 18	20.6 18
Phase flow	Batch, ↑↓	← ←	Batch	$\begin{array}{ccc} \leftarrow & \rightarrow \\ \leftarrow & \leftarrow \end{array}$	← → ←	Batch	Batch
Column Phase type flow	KRPC	KRPC	KRPC	KRPC		RPC	RPC

Banković-Ilić (1999) Gagnon et al. (1998) Lounes et al. (1995) Karunanithi (2010b, Vasić et al. (2005b, Dhanasekaran and Aleksić (2006) Reference 2012d) $\varepsilon_s = 3.8\%$: $k_l a = 2.33 (P_{av}/V_l)^{0.803} u_g^{0.572}$ $\varepsilon_{\rm s} = 6.6\%: \ k_i a = 0.6 \left(P_{\rm ov}/V_i\right)^{0.572} u_{\rm g}^{0.316}$ a = 0.028 - 0.084, b = 0.86 - 1.05a = 0.73 - 0.92, b = 0.50 - 0.61 $u_g^{1.624}$ $u_g^{1.043}$ $k_I a = 0.0039 \left(P_g/V_I\right)^{0.735} u_g^{0.668}$ $k_l a = 0.995 (P_{\omega})^{0.776} u_g^{0.854}$ $k_l a = 0.719(P_{\alpha v})^{0.74} u_{g}^{0.63}$ $k_l a = 0.0075 \cdot u_l^{1.031} \varepsilon_{g}^{0.2539}$ $k_1 a = 0.336 \cdot 10^{-4} \left(P_g / V_I \right)^{1.308} u_s$ $k_l a = 0.775 \left(P_g / V_l \right)^{0.159} u$ $P_{\rm g}/V_1 > 600 \text{ W/m}^3$: $P_{\rm g}/V_1$ < 600 W/m³: $P_{\rm g}/V_1 < 200~{
m W/m^3}$: $P_{\rm g}/V_1 > 200 \text{ W/m}^3$: $k_l a \propto \left(P_g/V_l\right)^a u_g^b$ $k_l a \propto \left(P_g/V_l\right)^a u_g^b$ Correlation Continuation of Table 10.1 Correlations for volumetric oxygen mass transfer coefficient. (O₂-water) $(O_2-50\%$ glycerol) Physical Physical Operating conditions Method Sulfite Sulfite Sulfite Sulfite $35 \le P_{\rm g}/V_1 \le 6600$ $u_1 = 0.035 - 0.105$ $0.65 \le u_{\rm g} \le 0.40$ $\epsilon_s = 0.35 {-} 3.2\%$ $u_{\rm g} = 2.12 - 4.24$ $\varepsilon_s = 0 - 6.6\%$ $\varepsilon_s = 0 - 6.6\%$ P_{ϱ}/V_b , W/m³) $(u_g, u_l, \text{cm/s};$ $u_g = 0-1.2$ $u_{\rm g} < \!\! 1.5$ $u_{\rm g} < 1.5$ $u_{\rm g} < 1.5$ 0.454 0.454 0.466 0.33 0.5-0.51 W 6.35-6.35 d_o mm 8.0 3.85 0.55 0.97 1.05 1.05 1.2 l_c 18 6 12 33 16 15 n_p 20.6 22.8 16.6 2.54 9.2 9.2 D_c 10 Batch Batch Batch Batch Column Phase flow $\overset{\leftarrow}{\leftarrow}$ HRRPC KRPC KRPC KRPC KRPC RPC

Abbreviations: HRRPC - hybrid rotating-reciprocating plate column, KRPC - Karr-type reciprocating plate column, and RPC - reciprocating plate column.

a second-order Equation that relates key experimental variables—reciprocating intensity, superficial gas and liquid velocities, plate spacing, and perforation diameter. The resulting response surfaces established a correlation between these parameters and the mass transfer coefficient, validating the second-order polynomial model Equation (Dhanasekaran and Karunanithi, 2012d).

The volumetric oxygen mass transfer coefficient is generally higher in reciprocating plate columns compared to bubble columns, air-lift reactors, and stirred tanks at the same superficial gas velocity, for both two-phase (Figure 10.2) and three-phase systems (Figure 10.3). This enhancement is attributed to the effective mechanical mixing, which improves bubble dispersion and increases the specific interfacial area.

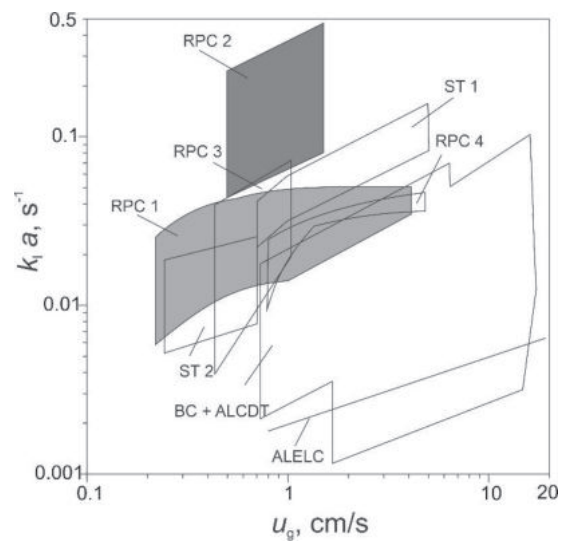


Figure 10.2 Comparison of the volumetric oxygen mass transfer coefficient in different devices for the gas-liquid system (Banković-Ilić, 1999): RPC1 – D_c = 2.54 cm (Veljković, 1985); RPC2 – D_c = 9.2 cm (Banković-Ilić, 1999); RPC3 – D_c = 9.3 cm (Sundaresan and Varma, 1990a); RPC4 – D_c = 5.08 cm (Yang et al., 1986); BC and ALCDT – (Al-Masry and Dukkan, 1998; Petrović, 1989); ALELC – (Weiland and Onken, 1981); ST1 – (Bouaifi and Roustan, 1998); and ST2 – (Chavarria-Hernandez et al., 1996).

In a two-phase system, the volumetric oxygen mass transfer coefficient is influenced by the reciprocating plate column's geometry (see Figures 10.4 and 10.5). For instance, at the same specific power consumption (Figure 10.4), a higher coefficient was observed in the reciprocating plate column with the largest diameter (16.6 cm). Additionally, at higher total power consumption, the highest volumetric oxygen mass transfer coefficient is achieved in the 9.2 cm diameter column (Figure 10.5), likely due to more efficient mixing and smaller bubble sizes.

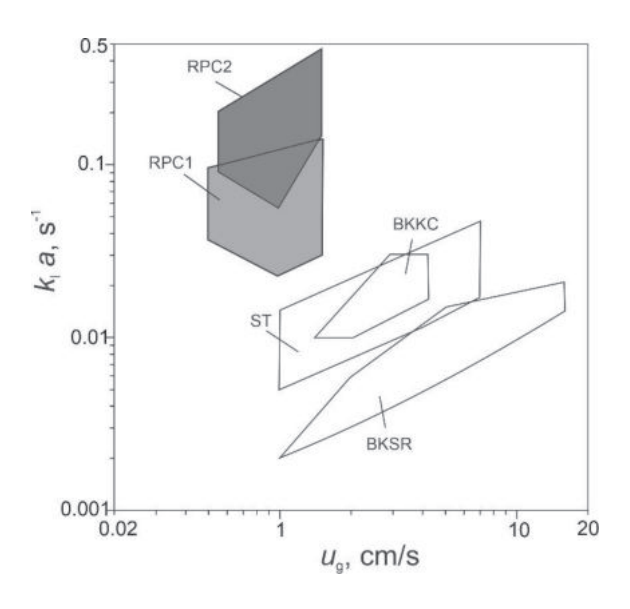


Figure 10.3 Comparison of volumetric oxygen mass transfer coefficient in different devices for the gas-liquid-solid phase system: RPC1 – D_c = 2.54 cm (Banković-Ilić, 1999); RPC2 – D_c = 9.2 cm (Banković-Ilić, 1999); BKKC (Petrović, 1989); BKSR (Pošarac, 1988); and SM (Roman and Tudose, 1997).

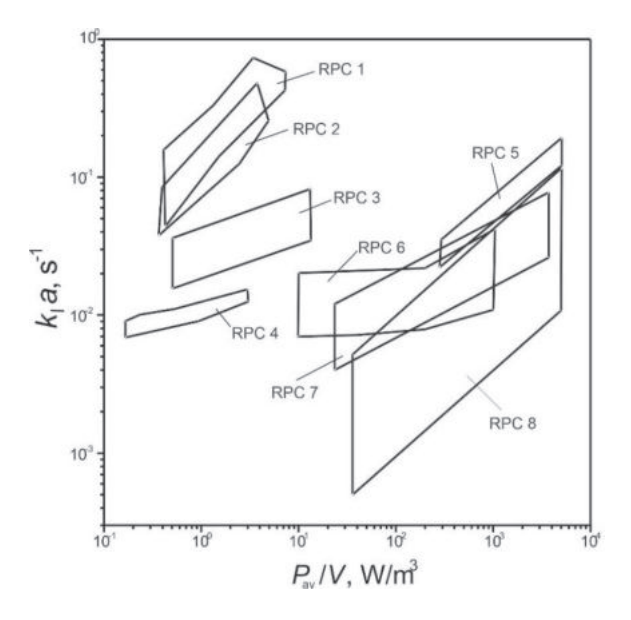


Figure 10.4 Comparison of volumetric mass transfer coefficient in Karr-type reciprocating plate columns of different geometries for the gas-liquid system: RPC1 – D_c = 16.6 cm (Vasić et al., 2007); RPC2 – D_c = 9.2 cm (Banković Ilić, 1999); RPC3 – D_c = 2.54 cm (Veljković, 1985); RPC4 (Rama Rao and Baird, 2003); RPC5 (Gagnon et al., 1998); RPC6 (Baird and Rama Rao., 1988); RPC7 (Lounes et al., 1995); and RPC8 (Lounes and Thibault., 1994).

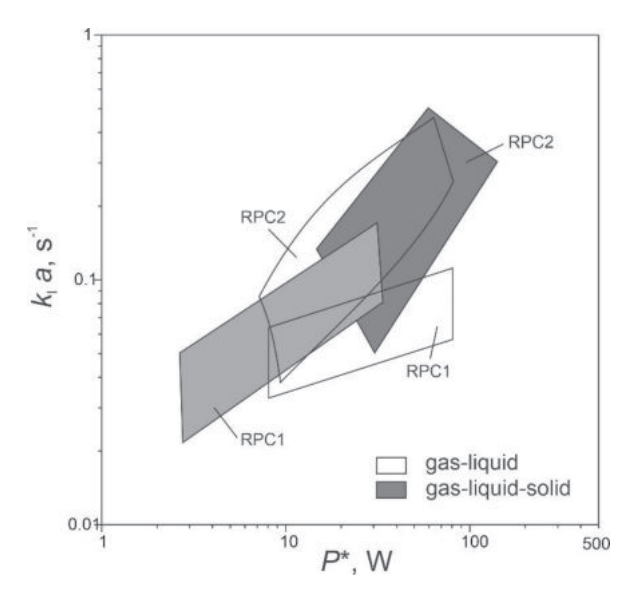


Figure 10.5 Comparison of the volumetric mass transfer coefficient in reciprocating plate columns of different geometries: $D_c = 2.54$ cm (RPC1) (Skala and Veljković, 1988) and $D_c = 9.2$ cm (RPC2) (Banković-Ilić, 1999).

A comparison of the effects of solid particle shape (spheres vs. Rashig rings) on the volumetric oxygen mass transfer coefficient in reciprocating plate columns of the same diameter (Figure 10.6) reveals that the coefficient values are approximately the same across different superficial gas velocities.

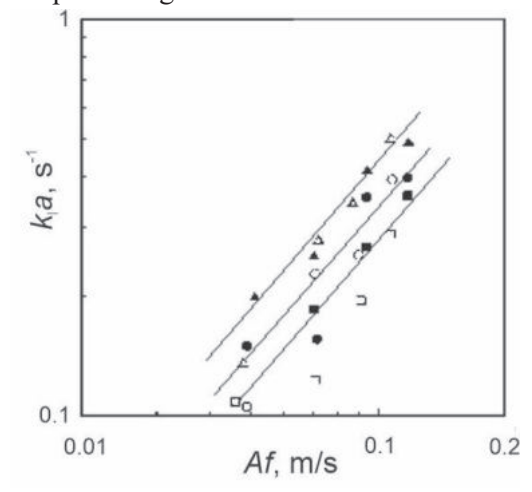


Figure 10.6 The influence of the shape of solid particles on the volume coefficient of oxygen mass transfer (spheres with a diameter of 8.3 mm; ε_s , % vol.: 3.80; open symbols; u_g ; cm/s: 0.5 – squares, 1.0 – circles and 1.5 – triangles (Banković-Ilić, 1999); Rashig rings with a diameter of 8 mm; ε_s , % vol.: 3.20; black symbols; u_g ; cm/s: 0.5 – square, 1.0 – circle and 1.5 – triangle (Aleksić, 2006).

11. SPECIFIC INTERFACIAL AREA IN RECIPROCATING PLATE COLUMNS

The specific gas-liquid interfacial area plays a crucial role in maximizing reactor productivity. Various methods are employed to quantify this parameter in gas-liquid contactors, categorized into physical and chemical approaches. Physical methods ascertain local values of the specific interfacial area, typically utilizing principles such as light attenuation due to scattering, refraction, and reflection. Conversely, chemical methods involve predicting the rate of gas absorption followed by a chemical reaction with a known kinetic expression. Veljković (1985) demonstrated that this method determines the average specific interfacial area.

In the area of low reciprocating intensities, the interfacial area either increases due to the decrease in bubble size (Sundaresan and Varma, 1990b) or remains unchanged because the bubble size and gas holdup do not change (Skala, 1980; Veljković and Skala, 1988; Yang et al., 1986a). The mixing intensity does not affect the interfacial area if Af < 2 cm/s (Yang et al., 1986a). At higher reciprocating intensities, the interfacial area increases with increasing intensity due to an increased gas holdup in the reactor and the decrease in bubble size (Figure 11.1, Banković-Ilić, 1999).

The specific interfacial area is influenced by the fluid-dynamic conditions within the multiphase contactor and the properties of the interacting phases. Numerous researchers have investigated the impact of reciprocating intensity and superficial gas velocity on the specific interfacial area in reciprocating plate columns (Al Taweel et al., 1995; Banković-Ilić, 1999; Banković-Ilić et al., 2001b; Gomaa et al., 1991; Sundaresan and Varma, 1990b; Vasić et al., 2006; Veljković and Skala, 1988; Yang et al., 1986a). The variation in the specific interfacial area with reciprocating intensity is dependent on the flow regime within the column (Veljković and Skala, 1988). At low reciprocating intensities, the specific interfacial area may increase due to a reduction in bubble size (Sundaresan and Varma, 1990b) or remain constant if bubble size and gas holdup are unchanged (Skala, 1980; Veljković and Skala, 1988; Yang et al., 1986a). Mixing intensity does not influence the specific interfacial area when Af < 2 cm/s (Yang et al., 1986a). However, at higher reciprocating intensities, the interfacial area increases with the intensity, attributed to increased gas holdup and decreased bubble size (Figure 11.1, Banković-Ilić, 1999).

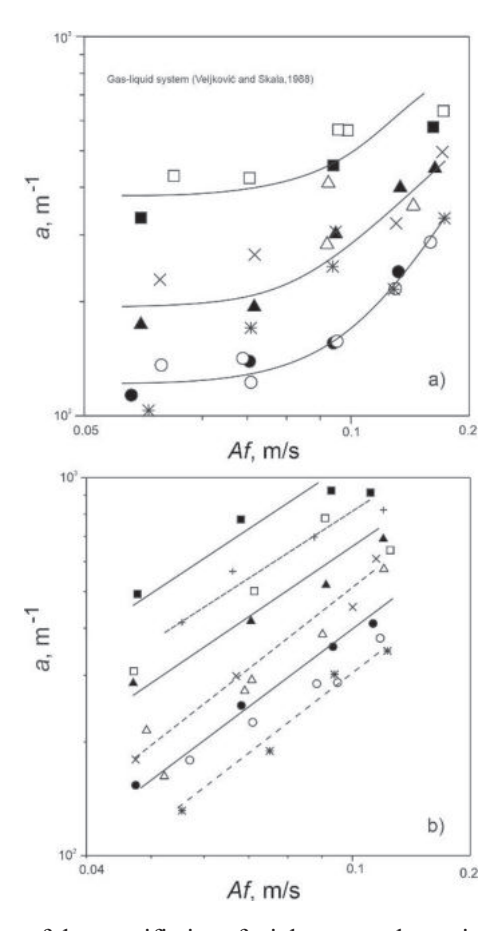


Figure 11.1 Dependence of the specific interfacial area on the reciprocating intensity: (a) D_c = 2.54 cm and (b) D_c = 9.2 cm (liquid: 0.8 M sodium sulfite, ε_s , %: 0, u_g , cm/s: 0 - *, 0.5 - ×, and 1.5 - +; ε_s , %: 3.8 - open symbols, and 6.6 - black symbols, u_g , cm/s: 0.5 - circles, 1.0 - triangles, and 1.5 - squares) (Banković-Ilić (1999).

The influence of superficial gas velocity on the specific interfacial area also depends on the flow regime and is particularly significant at low reciprocating intensities (Figure 11.1). At low superficial gas velocities, increasing the reciprocating intensity helps to break up the bubbles, thereby increasing the specific interfacial area (Banković-Ilić, 1999; Veljković and Skala, 1986a). At higher superficial gas velocities, where a larger volume of gas is present in the column, bubbles grow in size and pack more densely, promoting their coalescence (Skala, 1980). Despite the increase in bubble size, the specific interfacial area can still rise due to the greater gas holdup within the column (Gomaa et al., 1991; Sundaresan and Varma, 1990b; Veljković and Skala, 1988; Yang et al., 1986a).

There is no consensus among researchers regarding the influence of superficial liquid velocity, likely due to variations in the operating conditions of different studies. Some researchers (Veljković and Skala, 1988) argue that superficial liquid velocity has a negligible effect on the specific interfacial area, as it minimally impacts bubble size and gas holdup. In contrast, others (Al Taweel et al., 1995; Gomaa et al., 1991; Sundaresan and Varma, 1990b; Yang et al., 1986a) report that increasing the superficial liquid velocity enhances the specific interfacial area by reducing bubble size. Additionally, the mode of gas and liquid flow influences the interfacial area in reciprocating plate columns. Due to higher gas holdup, the specific interfacial area is greater in concurrent flow compared to countercurrent flow (Sundaresan and Varma, 1990b).

The influence of liquid properties on the specific interfacial area has been relatively understudied. The presence of electrolytes inhibits bubble coalescence due to the electrostatic potential at the gas-liquid interface, resulting in smaller bubble diameters and a slight increase in specific interfacial area compared to water (Banković-Ilić, 1999; Boyle, 1975; Veljković, 1985). However, Veljković and Skala (1988) indirectly concluded that the coalescent properties of the liquid do not significantly affect the interfacial area in reciprocating plate columns, based on similar specific interfacial area values determined by chemical and photographic methods. It contrasts with stirred vessels or bubble columns, where liquid coalescent properties play a more significant role. In reciprocating plate columns, the presence of electrolytes, which prevent bubble coalescence, and the action of reciprocating plates, which break and redisperse bubbles as they pass through the plate openings, exert approximately equal effects. However, under the same aeration and mixing conditions, the specific interfacial area determined by the photographic method is smaller in a glycerol solution than in water (Banković-Ilić, 1999).

The complexity of the influence of liquid physical properties on the specific interfacial area is illustrated in Figure 11.2 (Banković-Ilić, 1999), which shows the relationship between gas holdup, Sauter mean bubble diameter, and specific interfacial area with respect to Morton's number. As Morton's number increases, gas holdup initially rises to a maximum value before decreasing, while bubble size decreases to a minimum value before increasing again. Consequently, with increasing Morton's number, the specific interfacial area rises to a maximum value and then declines. Glycerol solution, due to its high viscosity, behaves differently from other Newtonian liquids.

The geometric characteristics of the column also influence the specific interfacial area. Increasing the diameter of the openings and the fractional plate-free area reduces both gas holdup and the specific interfacial area. These changes occur

despite a slight decrease in bubble size with larger opening diameters and a significant increase in bubble size with a greater fractional plate-free area (Sundaresan and Varma, 1990b).

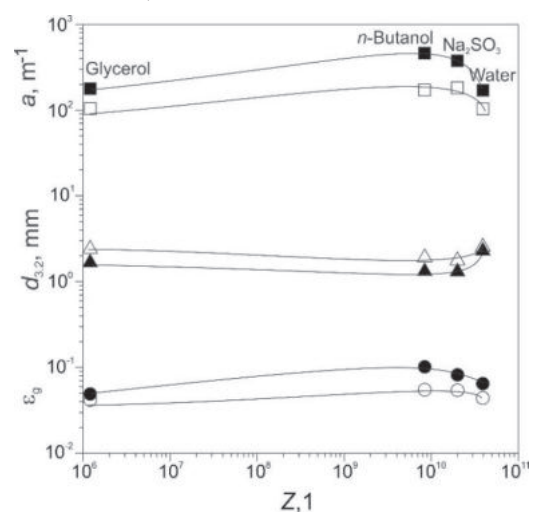


Figure 11.2 Dependence of gas holdup, Sauter bubble diameter, and specific interfacial area on Morton's number (Z) ($D_c = 2.54$ cm, u_g , cm/s: 0.5; Af, cm/s: 5.2 – open symbols and 7.1 – black symbols) (Banković-Ilić, 1999).

Adding Rashig rings (2.5% vol.) to each interplate space increases the specific interfacial area by about 30% (Sundaresan and Varma, 1990b). In contrast, the presence of spheres (Figure 11.1a) does not affect the specific interfacial area, despite higher power consumption compared to the two-phase (gas-liquid) system under the same operating conditions (Banković-Ilić, 1999). For example, in a column with a diameter of 9.2 cm (Figure 11.1b), the specific interfacial area is greater with a higher solids fraction than in the two-phase (gas-liquid) system.

Changes in the specific interfacial area with varying reciprocating intensity reveal a 'critical' reciprocating intensity corresponding to a 'critical' power consumption. This 'critical' reciprocating intensity depends on the gas flow rate (Skala, 1980), while 'critical' power consumption is also influenced by the 'critical' gas holdup (Veljković and Skala, 1988). When reciprocating intensity is below the critical level, the specific interfacial area depends on superficial gas velocity rather than reciprocating intensity (Skala, 1980; Veljković and Skala, 1988; Yang et al., 1986a). Under these conditions, reciprocating plate columns behave like bubble columns (Veljković and Skala, 1988). When reciprocating intensity exceeds the critical value, the dispersion state is influenced by both aeration and agitation intensity. It is understandable, as both aeration and agitation affect bubble breakup and coalescence processes, which in turn impact bubble size and the interfacial area.

Correlations for calculating the specific interfacial area in reciprocating plate columns, as published in the literature (Table 11.1), consider both power consumption and superficial gas velocity, with aeration having a more significant effect on the specific interfacial area than mechanical mixing.

Comparing the specific interfacial area in reciprocating plate columns of different diameters (Banković-Ilić et al., 2001b) reveals that, due to higher power consumption, the specific interfacial area is greater in larger diameter columns, both in two-phase (gas-liquid) and three-phase (gas-liquid-solid) systems (Figure 11.3). At the same superficial gas velocity, the specific interfacial area in gas-liquid systems (Figure 11.4) is several times greater in reciprocating plate columns than in stirred vessels and column-type reactors, such as bubble columns and airlift reactors (Banković-Ilić et al., 2001b). This is due to higher gas holdup and smaller bubble sizes in reciprocating plate columns, resulting from the contribution of mechanical mixing to bubble dispersion.

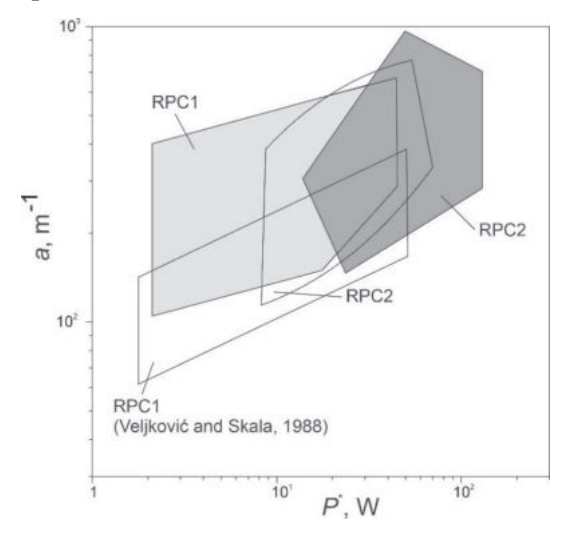


Figure 11.3 Comparison of the specific interfacial area in reciprocating plate columns of different geometry: $D_c = 2.54$ cm (RPC1) and $D_c = 9.2$ cm (RPC2); gas-liquid system – open area and gas-liquid-solid system – solid area (Banković-Ilić, 1999).

Dhanasekaran and Karunanithi (2012c) developed a correlation to determine the specific interfacial area in an air-water system, taking into account vibration intensity, gas, and liquid superficial velocities, and column geometric characteristics (see Table 11.1). They observed a significant increase in the interfacial area when transitioning from the mixer-settler regime to an emulsion regime. In the mixer-settler region, the Reynolds number for the liquid phase plays a more prominent role in enhancing the interfacial area, while the Weber number has equal significance in both flow regimes.

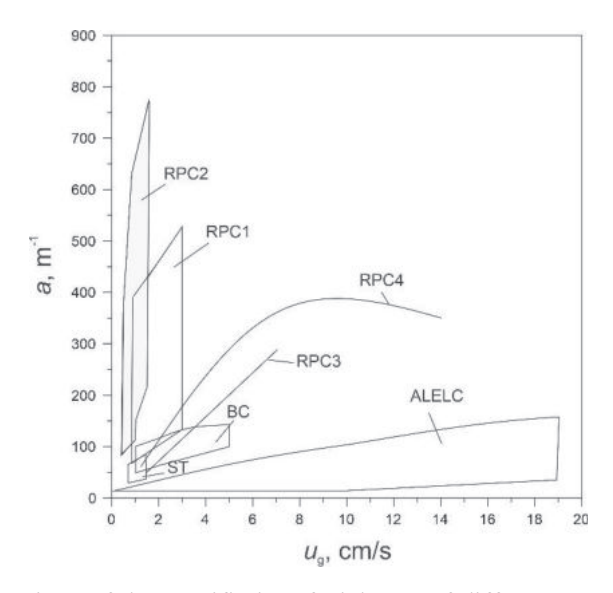


Figure 11.4 Comparison of the specific interfacial area of different reactors for gas-liquid systems (Banković-Ilić, 1999): RPC1 – D_c = 2.54 cm (Skala, 1980), RPC2 – D_c = 9.2 cm (Banković-Ilić, 1999), RPC3 (Yang et al., 1986a), RPC4 (Gooma et al., 1991), BC (Stegeman et al., 1996), ALELC (Ghirardini et al., 1992), and ST (Bouaifi and Roustan, 1998).

Table 11.1 Correlations for the specific interfacial area in reciprocating plate columns.

Column	Phase	$D_{\tilde{c}}$	n_n	h	d_{ρ}	3	٥	¥	Method	Correlation	Reference
type flow	flow	cm	d	cm	mm		s %	cm			
KRPC	Batch	2.54	65 33	2.5- 5.0	8 L	0.51	0	2.35	Sulfite and photographic	For $P_g^* > P_{g,cr}^*$: $a = 1783 (P_g^*)^{3} u_g^{36}$ For $P_g^* < P_{g,cr}^*$: $a = 1583 u_g^{36}$	Veljković (1985) Veljković and Skala (1988)
KRPC	←	5.08	84	2.54	15	0.53	0	0 - 1.88	Photographic	$a = 0.333 (Af)^{0.593} u_g^{0.912} u_i^{0.133}$	Yang et al. (1986a)
KRPC	← ←	9.3	10	5.6	3-	0.09-	0	I	Sulfite	For $Af \ge 5$ cm/s: $a = 0.284 (Af)^{0.8} u_g^{1.05} u_l^{0.35} d_o^{-0.1} \varepsilon^{-0.3}$	Sudaresan and Varma (1990b)
	$\overset{\rightarrow}{\leftarrow}$									For $Af \le 5$ cm/s: $a = 0.63 (Af)^{0.2} u_g^{0.7} u_l^{0.3} d_o^{-0.2} \varepsilon^{-0.1}$	
PRPC	<i>→ ←</i>	10	1	$\frac{10}{30}$	1.6	0.23 ^a 0.38 ^b	0	0.16-	Transmitted light intensity measurement	For $u_g < 0.1 \text{ m/s}$: $a = \frac{425u_g^{0.5} (1+8.15u_f) \left[1+5.5 (Af - Af_{cr})^{0.43} \right]}{h^{0.14}}$	Gomaa et al. (1991)
										For $u_g \ge 0.1$ m/s:	
										$a = \frac{24.5(1+2.31u_f)}{h^{0.38}}$	
KRPC Batch	Batch	2.54	65		∞ ∞	0.51 0–6.6 2.35 0.454	9-9-0	2.35	Sulfite	$a = 18883(P_w)^{0.31} u_g^{0.97}$	Banković-Ilić (1999)
HRRPC	→ ←	10	10,	2.25-4.5	0.4-	1	0	_	Calculation from gas holdup and bubble diameter	Calculation from For the mixer-settler region: gas holdup and $a = \frac{2.27}{d_o} \left(\frac{u_g}{u_f}\right)^{0.19} \left(\frac{Af}{u_f}\right)^{0.05} \left(\frac{h}{d_o}\right)^{-0.98} \text{Re}^{3.86} \text{ We}$ bubble diameter $a = \frac{2.27}{d_o} \left(\frac{u_g}{u_f}\right)^{0.19} \left(\frac{Af}{u_f}\right)^{0.69} \left(\frac{h}{d_o}\right)^{2.50} \text{Re}^{0.003} \text{ We}^{0.74}$ $a = \frac{2.27}{d_o} \left(\frac{u_g}{u_f}\right)^{0.19} \left(\frac{Af}{u_f}\right)^{0.69} \left(\frac{h}{d_o}\right)^{2.50} \text{Re}^{0.003} \text{ We}^{0.74}$	Dhanasekaran and Karunanithi (2012c)

 $Abbreviations: HRRPC-hybrid\ rotating-reciprocating\ plate\ column,\ KRPC-Karr-type\ reciprocating\ plate\ column,\ and\ RPC-reciprocating\ plate\ column.$

12. MASS TRANSFER COEFFICIENT IN RECIPROCATING PLATE COLUMNS

The mass transfer coefficient in the liquid film of reciprocating plate columns is influenced by reciprocating intensity, superficial gas and liquid velocities, column geometric characteristics, and bubble size, as can be seen in Table 12.1, where the correlations found in the literature are summarized. When power consumption is below the 'critical' value, then $k_l \propto (P_g^*)^{0.25}$ (Veljković and Skala, 1988). This relationship is similar to that observed in vibrating disc columns, where the mass transfer coefficient is proportional to the total power consumption with an exponent of 0.24 (Miyanami et al., 1978), and in classic stirred vessels, where it is proportional to the power consumption raised to the power of 0.14–0.30 (Yoshida and Muira, 1963).

Table 12.1 Correlations for mass transfer coefficient.

Phase	D_c	n_p	d_o	\mathcal{E}	Correlation	Reference
flow	cm		mm			
↑ ↓	2.54	33, 65	8	0.51	For $P_g < P_{g,cr}$ $k_l = 2.94 \cdot 10^{-4} P_g^{0.25}$ For $P_g > P_{g,cr}$ $k_l = 2.62 \cdot 10^{-4} P_g^{-0.05}$	Veljković and Skala (1988)
					$k_l = 0.0564 d_{3,2}$	
$\uparrow \uparrow$	5.08	84	15	0.53	$k_I = 0.0119 \cdot 10^{-2} \left(Af \right)^{-0.45} u_g^{-0.733} u_I^{0.605}$	Yang et al. (1986b)
↑↓ Or ↑↑	9.3	9	3–65	0.09– 0.306	Segregated dispersion $Af < 5 \text{ cm/s}$: $k_l \propto (Af)^{-0.1} u_g^{-0.5} u_l^{-0.3} \varepsilon^{-0.4}$ Homogeneous dispersion $Af > 5 \text{ cm/s}$: $k_l \propto (Af)^{-0.6} u_g^{-0.3} u_l^{-0.35} \varepsilon^{-0.2}$	Sundaresan and Varma (1990b)
Batch	9.2	15	8	0.45	$k_{l} = 20.24 d_{3,2}^{1.743}$	Banković- Ilić (1999)

When power consumption exceeds the 'critical' value, both the Sauter bubble diameter and the mass transfer coefficient decrease (Baird and Rama Rao, 1988; Sundaresan and Varma, 1990b; Veljković, 1985; Veljković and Skala, 1988). In this

regime, the mass transfer coefficient decreases with increasing power consumption and is proportional to the Sauter bubble diameter (Veljković and Skala, 1988). The exponent *n* for reciprocating plate columns is reported as -0.05 (Veljković and Skala, 1988) or -0.015 (Yang et al., 1986b), whereas for vibrating disc columns, it is -0.15 (Miyanami et al., 1978).

The dependence of the mass transfer coefficient on the Sauter bubble diameter has been confirmed in vibrating disc columns (Miyanami et al., 1978), pulsating columns (Baird and Garstang, 1972), classical stirred vessels (Miller, 1974), and bubble columns (Akita and Yoshida, 1974). Although the decrease in the mass transfer coefficient with increasing agitation intensity has not been fully elucidated, it is associated with a reduction in bubble diameter (Veljković and Skala, 1988).

The mass transfer coefficient decreases with increasing liquid and superficial gas velocities (Sundaresan and Varma, 1990b; Yang et al., 1986b). Higher superficial gas velocity increases gas holdup, while higher superficial liquid velocity reduces bubble size. Both effects decrease the relative velocity between the liquid and gas phases, leading to a reduction in the mass transfer coefficient (Sundaresan and Varma, 1990b). Conversely, Baird and Rama Rao (1988) observed that the mass transfer coefficient decreases with increasing bubble diameter but increases with higher superficial gas velocity. They attributed this to the removal of adsorbed, surface-active contaminants by turbulent forces and the ongoing breakup and coalescence of bubbles.

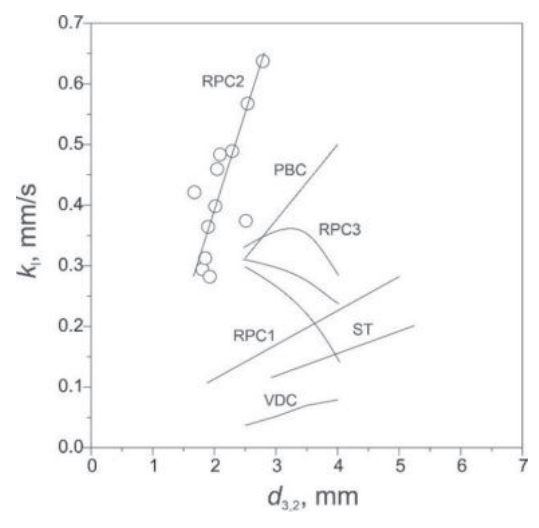


Figure 12.1 Comparison of the mass transfer coefficient in the liquid film in different devices for the gas-liquid system (adapted from Banković-Ilić, 1999): RPC1 – D_c = 2.54 cm (Veljković and Skala, 1986), RPC2 – D_c = 9.2 cm (Banković-Ilić, 1999), RPC3 (Baird and Rama Rao, 1988), PBC – pulsed bubble column (Baird and Garstang, 1972), VDC – vibration disc column (Mianami et al., 1978), and ST (Miller, 1974).

An increase in the fractional plate-free surface results in a decrease in the mass transfer coefficient in the liquid film, both in segregated and homogeneous regimes (Sundaresan and Varma, 1990b). Additionally, the mass transfer coefficient decreases with a higher solids fraction (Sundaresan and Varma, 1990b).

Compared to stirred vessels, pulsed columns, and vibrating disc columns, reciprocating plate columns exhibit a higher mass transfer coefficient for the same Sauter bubble diameter (Figure 12.1). Except for one study involving reciprocating plate columns (Baird and Rama Rao, 1988), the mass transfer coefficient generally increases with larger bubble size, regardless of column type.

13. APPLICATION OF OSCILLATORY REACTORS IN BIODIESEL PRODUCTION

Biodiesel represents a sustainable alternative to fossil diesel owing to its non-toxic, biodegradable properties, compatibility with most diesel engines with minimal adaptation, and renewable sourcing (Živković et al., 2017). It is predominantly manufactured on an industrial scale through homogeneous base-catalyzed methanolysis of vegetable oils, leveraging the cost-effectiveness of methanol and its rapid reaction kinetics. During this process, triacylglycerols in vegetable oils react with methanol in the presence of base catalysts such as potassium hydroxide, sodium hydroxide, or methoxides, yielding fatty acid methyl esters, commonly known as biodiesel, and glycerol.

Effective mixing plays a crucial role in methanolysis due to the immiscibility of vegetable oil and methanol phases. Vigorous mixing enhances collision frequency between reactants, ensures uniformity of the reaction mixture, disperses methanol as fine droplets in the oil phase, and maximizes interfacial contact between the immiscible reactants. This promotes efficient mass transfer of triglycerides, essential for sustaining the reaction (Stamenković et al., 2007, 2008).

Biodiesel is primarily produced using two types of reactors: batch reactors and continuous-flow reactors. Batch reactors are cost-effective, easy to operate, flexible, and simple to clean, making them ideal for small-scale production. However, they have several drawbacks, including limited production capacity, lower productivity, higher energy consumption, greater labor costs, and inefficiencies due to their startup and shutdown cycles, which can also lead to significant variations in product quality.

In contrast, continuous-flow reactors are designed to address the limitations of batch processes, enabling large-scale biodiesel production with enhanced efficiency. These reactors allow for better control of reaction parameters, such as temperature and droplet size, and more effective mixing of reagents, resulting in a more consistent quality of biodiesel. Additionally, continuous processes require fewer steps for scaling up and involve fewer unit operations during product isolation compared to batch processes. Continuous-flow reactors also significantly reduce residence time, often exhibiting plug-flow behavior, which contributes to more efficient and cost-effective production. Overall, continuous processes can produce biodiesel of

comparable or even superior quality to batch reactors, with lower investment and operating costs.

In recent years, the industry has increasingly focused on developing continuous processes to replace traditional batch reactors, driven by advantages in cost, safety, and product quality (Calabrese and Pissavini, 2011). Continuous reactors are typically designed as either continuous stirred-tank reactors or plug flow reactors, where reactants are continuously fed, and products are continuously removed, with constant agitation ensuring uniform chemical composition and temperature.

Most continuous stirred-tank reactors are equipped with mechanically agitated systems, commonly utilizing impellers. In some cases, multistage mechanically agitated reactors, such as those equipped with six standard Rushton turbines, are used for enhanced mixing efficiency (Leevijit et al., 2006, 2008). In plug flow reactors, the design and flow regime of the reactor dictate the degree of mixing. Plug flow reactors, with or without static mixers, have been extensively studied, including tube reactors (He et al., 2007; Lertsanthapornsuk et al., 2008; Peterson et al., 2002). Additionally, combined plug flow and continuous stirred-tank reactor configurations have been explored (Noureddini et al., 1998).

Some studies have investigated plug flow (tubular) reactors supplied with external energy sources for inducing oscillatory fluid flow through them, resulting in a novel technology known as oscillatory reactors. There are two major types of continuous oscillatory reactors: reciprocating plate reactors and oscillatory flow reactors, albeit they achieve this in different ways. Oscillatory flow is induced in these reactors by reciprocating plate movement or piston drive action in interaction with the baffles while the fluid flows through the reactor. A breakdown of their major characteristics, advantages, and drawbacks is presented in Table 13.1.

Oscillatory reactors offer several advantages over conventional reactors, such as uniform mixing, including higher mass and heat transfer, compact reactor design, and ease of scale-up (Abbott et al., 2013; Lo et al., 1992; Lounes and Thiboult, 1994). It is well known that this technology offers the combined benefits of continuous production from tubular reactors and effective mixing in stirred batch reactors. On the other hand, it can provide a higher degree of mixing with plug flow patterns even at a low net flow rate. The mixing intensity in these reactors is independent of the net flow and controlled by the oscillation or reciprocating conditions (Abbott et al., 2013; Harvey et al., 2001; Lo et al., 1992).

The flow pattern with a very high degree of mixing is created in the tubular reactors by stationary baffles and the oscillatory fluid flow or reciprocating movement of perforated plates. The movement of liquid within the interbaffle or interplate spaces causes the uniform formation of vortices, which greatly enhances

both the mass and heat transfer inside the reactor (Stephens and Mackley, 2002). The fluid condition in these reactors can be regulated through the frequency and amplitude of the oscillatory motion and the reactor geometry.

Table 13.1 Major characteristics, advantages, and drawbacks of oscillatory reactors.

	Reciprocating plate reactors (RPRs)	Oscillatory flow reactors (OFRs)
Properties	Reciprocating (up-and-down) motion of perforated plates within the tubular reactor. Induced oscillatory flow patterns in the fluid, enhancing mixing and heat transfer.	Use a piston, pump, or diaphragm and stationary baffles within the tubular reactor to create oscillatory flow patterns. Exploit hydrodynamic instability to induce chaotic mixing and enhanced mass transfer.
Advantages	Effective for mixing viscous fluids and achieving uniform reaction conditions. Suitable for reactions where mass transfer limitations are critical. Scalable from lab-scale to industrial application. The possibility of applying large fluid flows. Uniform liquid-liquid dispersion.	Excellent for enhancing mixing and heat transfer without moving parts. Suitable for reactions where mass transfer limitations are critical. Scalable from lab-scale to industrial applications. Uniform mixing at lower shear strains compared to stirred tank reactors. Good for liquid-liquid heterogeneous reactions.
	Frequent renewal of the interfacial contact area. Higher gas hold-up, larger specific interfacial area, reduced backmixing, and prolonged bubble residence time in the dispersion compared to bubble columns.	Low capital and operating costs. Long reactions in a significantly low length/diameter ratio.
Drawbacks	Mechanical complexity due to moving parts (plates or surfaces). Potential for wear and maintenance issues over time. Complicated design and operation in continuous mode.	Requires very long dimensions to create better mixing in the reactor. Incompatibility with processes involving very viscous liquids. Complicated design and operation in continuous mode.

The oscillatory reactor technology is particularly adapted to liquid-liquid reactions, such as transesterification, because it allows good inter-phase contacting, enhanced mixing, and sufficiently long residence times for reaction. Therefore, this novel technology has received increasing attention in biodiesel production in recent years. For this production, using continuous tubular reactors, achieving effective mixing of immiscible reactants is crucial for overcoming mass transfer resistance and maximizing biodiesel yield. Therefore, continuous reciprocating plate columntype (Banković Ilić et al., 2015, 2024; Miladinović et al., 2019; Stamenković et al., 2010a, 2013) and oscillatory baffled (Harvey et al., 2003) reactors have significant potential for enhancement of biodiesel production by transesterification of homogeneous and heterogeneous catalysts and reduction of biodiesel cost (Avilaa et

al., 2022; Banković Ilić et al., 2024; Gopi et al., 2022; Gupta et al., 2020; Masngut et al., 2010; Mazubert et al., 2014). A high biodiesel yield or oil conversion can be achieved under moderate conditions, such as at lower reaction temperatures, lower methanol to oil molar ratios, and shorter reaction times with lower catalyst concentrations by using a continuous reactor as compared with the conventional batch reactor (Banković Ilić et al., 2024).

The continuous flow reciprocating plate and oscillatory flow reactors show considerable promise for enhancing biodiesel production via transesterification using homogeneous catalysts, while also contributing to cost reduction (Banković Ilić et al., 2024; Harvey, 2003). These reactors enable high biodiesel yields and efficient oil conversion under moderate operating conditions. Compared to conventional batch reactors, continuous reactors can achieve these results with lower reaction temperatures, reduced methanol/oil molar ratios, shorter reaction times, and lower catalyst concentrations, making the process more efficient and cost-effective (Banković Ilić et al., 2024). Table 13.2 compares the performances of biodiesel production in reciprocating plate and oscillatory flow reactors.

13.1 Reciprocating plate column-type reactors in biodiesel production

Given that the primary challenge in commercializing biodiesel production is its high cost, recent research has focused on developing cost-reduction strategies. One promising approach is the use of novel reactor designs that outperform traditional systems, particularly in terms of energy efficiency. Energy consumption accounts for a significant portion of the total energy input in biodiesel production. Reciprocating plate column-type reactors, or simply reciprocating plate reactors (RPRs), are particularly effective for enhancing the methanolysis process. They maximize the interfacial surface area between the two immiscible reactants while maintaining relatively low energy requirements (Stamenković et al., 2010a). This is crucial because the mass transfer of triacylglycerols to the interface between vegetable oil and methanol can limit the methanolysis rate in reciprocating plate reactors, as observed in stirred tank reactors (Stamenković et al., 2008).

Reciprocating plate reactors are multiphase contactors featuring equally spaced perforated plates that move vertically to induce mixing. The plates, designed with large holes and operated at low frequencies, ensure uniform energy dissipation throughout the reactor. Due to their favorable hydrodynamic and mass transfer properties, reciprocating plate reactors have been widely studied over recent decades for their applications in various multiphase systems, including liquid-liquid. These reactors have found commercial use in the chemical, petrochemical, and pharmaceutical industries, supporting processes such as liquid-liquid extraction,

Table 13.2 Continuous reciprocating plate column and oscillatory flow reactors for biodiesel production.

r.		-	-	1 1 1	E			c c
Reactor type	Keactor geometry	reedstock	Catalyst,	Alcohol,	ı empe-	Kesidence	Biodiesel yield	Kererence
			loading	alcohol/oil molar ratio	rature, °C	time, min	(conversion), %	
RPR, a series of	$D_c = 25.4 \text{ mm}, d_o = 6/8 \text{ mm}, h = 6.6 \text{ mm}$	Sunflower	KOH, 1%	Methanol,	30	12	(80), first	Stamenković et
two reactors,	2.54 cm, l = 2 m, A = 10 mm, f	011		0:1			reactor	al. (2013)
each followed	$= 2 \text{ Hz}, \ \varepsilon = 51\%, \ n_{\rm p} = 63$					30	(98-100),	
by a separator							second reactor	
RPR	$D_c = 25.4 \text{ mm}, d_o = 6/8 \text{ mm}, h =$	Sunflower KOH, 1%	KOH, 1%	Ethanol,	30-70	13	(94.3-97.3)	Stamenković et
	2.54 cm, $l = 2$ m, $A = 10$ mm, f	oil		6:1				al. (2010b)
	$= 3 \text{ Hz}, \ \varepsilon = 51\%, \ n_p = 63$							
RPR, 190	$D_{\rm c} = 16.6 \text{ mm}, d_{\rm o} = 8 \text{ mm}, h = 5$	Rapeseed	KOH, 1%	Methanol,	30	13	(96.0-98.3)	Stamenković et
spheres (8.3	cm, $l = 1.53$ m, $A = 23.5$ mm, f	oil		6:1				al. (2010c)
mm) per	$= 2 \text{ Hz}, \ \varepsilon = 46.6\%, \ n_p = 15$							
merpiale space								
RPR	$D_c = 25.4 \text{ mm}, d_o = 6/8 \text{ mm}, h =$	Sunflower KOH, 1%	KOH, 1%	Methanol,	30	13	5.96	Stamenković
	2.54 cm, $l = 2$ m, $A = 10$ mm, f	oil		Methanol,				(2014),
	$= 2 \text{ Hz}, \ \varepsilon = 51\%, \ n_p = 63$			Methanol,				Stamenković et
				6:1				al. (2010a)
RPR	$D_c = 25.4 \text{ mm}, d_o = 6/8 \text{ mm}, h =$	Sunflower	KOH, 1%	6:1	20	13	(78–80) (0 and	Banković Ilić et
	2.54 cm, $l = 2$ m, $A = 10$ mm, f	oil				26	1% THF)	al. (2015)
	$= 2 \text{ Hz}, \ \varepsilon = 51\%, \ n_p = 63$						(81–84) (10 and	
							30% THF)	
RPR	$D_c = 25.4 \text{ mm}, d_o = 6/8 \text{ mm}, h =$	Waste pig-	KOH, 0.5–	4.5:1–7.5:1	09	10	(>99 predicted)	Miladinović et
	2.54 cm, l = 2 m, A = 10 mm, f	roasting	1.0				(0.9% KOH,	al. (2019)
	$= 2 \text{ Hz}, \ \varepsilon = 51\%, \ n_{\rm p} = 63$	lard					4.5:1)	
							(96.2) (1%	
							KOH, 4.5:1)	
OFR, sharp	$D_c = 25 \text{ mm}, l = 1,5 \text{ m}, A = 0-$	Rapeseed	NaOH,	Methanol,	50	10	(99.1)	Harvey et al.
baffles,	17 mm, $f = 0.2 - 12 \text{ Hz}$	oil	0.324	5:1		20	(96,6)	(2003)
continuous			g/mL			30	(96,6)	
					09	10	(96,6)	
						15	(9,66)	

Continuation of Table 13.2 Continuous reciprocating plate column and oscillatory flow reactors for biodiesel production.

	-	5		•			1	
Reactor type	Reactor geometry	Feedstock Catalyst,	Catalyst,	Alcohol,	Tempe-		Biodiesel yield	Reference
			loading	alcohol/oil	rature,	time, min	(conversion), %	
				molar ratio	$^{\circ}$ C			
OFR, meso,	$D_c = 5 \text{ mm}, d_o = 1.6 \text{ mm}, l = 20$	Refined	CH ₃ ONa,	Methanol,	09	Up to 40	(66<)	Zheng et al.
batch	mm, $A = 2$ mm, $f = 10$ Hz, $\varepsilon = 10\%$	vegetable oil	4.2%	6:1				(2007)
OFR, meso,	l = 730 mm	;			09	49	(66 <)	
continuous								
OFR, meso,	$D_c = 5 \text{ mm}, \ \varepsilon = 51\%, \text{ central}$	Rapeseed	KOH, 1%	Methanol,	09	20–25	88	Phan et al.
continuous	sharp-edge baffles used (discs	oil		5:1				(2011)
	3.5×0.5 mm; spacing 7.5 mm),			4:1			42	
	A = 4 mm, f = 6 Hz							
	Helically baffle (1.1 mm wire							
	coiled at a pitch of 7.5 mm)							
	A = 2 mm, f = 6 Hz			3:1		Up to 20	50-80	
	A = 4 mm, f = 6 Hz			9:1		Up to 5	06-02	
	Sharp-edge helical baffle, $A = 4$			5:1		20	80	
	mm, $f = 6 \text{ Hz}$			7:1		20	85	
				9:1		30	06	
OFR, baffled,	$D_c = 5 \text{ mm}, l = 0.34 \text{ m (4 tubes)},$	Rapeseed	КОН,	6:1	09	5, 10, and	(97) (1.5%	Phan et al.
continuous;	$d_0 = 2.5 \text{ mm}, h = 7.5 \text{ mm}, \varepsilon =$	oil	CH_3ONa ,			15	KOH, 5 min)	(2012)
Integral orifice	25%		0.5 - 1.5%				(94-96) (sodium	
baffles							methoxide, 5–	
Sham-adged	1.7 mm flat wire coiled at						10 min) (76) (1 5%	
helically baffles	7.5mm pitch, inner diameter 2.6						KOH, 10 min)	
with a central rod	mm, 1.2 mm rod							
Wire wool baffle	Knitted stainless-steel wire mesh (0.5 mm), packed loosely						(77%) (1.5% KOH, 10 min)	
	(10% of the tube)							

Continuation of Table 13.2 Continuous reciprocating plate column and oscillatory flow reactors for biodiesel production.

	•	5		'n			•	
Reactor type	Reactor geometry	Feedstock	Catalyst,	Alcohol,	Tempe-	Residence	Biodiesel yield	Reference
			loading	alcohol/oil	rature,	time, min	(conversion), %	
				molar ratio	O _o			
OFR (pulsed	$D_c = 63.5 \text{ mm}, l = 0.55 \text{ m}, f = 1 -$	Jatropha	KOH, 1%	Methanol,	09	10	(266.7)	Syam et al.
loop reactor),	9 Hz, (optimal 6 Hz)	oil		6:1				(2012)
orifice baffles,			CH_3ONa				(888)	
continuous								
OFR, orifice	$D_c = 63.5 \text{ mm}, d_o = 8 \text{ mm}, l =$	WCO		Methanol,	40	9	(92.1)	Mazubert et al.
baffle,	2.1 m, $h = 26$ mm, $A = 1.5-25$			6:1				(2014)
continuous	mm, $f = 0.4 - 1.7 \text{ Hz}$							
OFR, tri-orifice	$D_c = 15 \text{ mm}, l = 1.1 \text{ m}, h = 5-9$	WCO	KOH, 1%	Methanol,	40-09	5	81.9	Soufi et al.
baffles, batch	cm (optimal 5 cm), $f = 2.4-4.9$ Hz (optimal 4.1 Hz)			6:1	(optima			(2017)
OFR, single	$D_c = 5 \text{ mm}, l = 0.92 \text{ m}, h = 15.3$	WCO, 2-3	WCO, 2-3 NaOH, 1%	Methanol,	09	20–30	78.8 (2 kg oil,	García-Martín
orifice haffles	cm $d_s = 5$ cm $f = 0.33 - 0.67$ Hz	kσ		6.1–10.1			6.1 0 67 Hz 30	et al (2018)
batch		o F					min)	
OFR, meso,	$D_c = 5 \text{ mm}, l = 0.77 \text{ m}, h = 7.5$	Rapeseed	DBSA,	Methanol,	09	09	(100) (10:1,	Al-Saadi et al.
continuous	mm, $d_o = 2.5$ mm, $A = 1-8$ mm,	oil	0.031 -	3:1-10:1			1.25 M catalyst)	(2019)
	f = 2 - 7 Hz	15.3 cm	0.499			09	(100)(10:1,	
			mol/L oil				0.99 M catalyst)	
			(DBSA/oil			120	(99.8) (6.5:1,	
			0.03:1-				0.5 M catalyst)	
			0.48:1 mol/mol)					
OFR, meso,	$D_c = 5 \text{ mm}, l = 0.77 \text{ m}, h = 7.5$	Rapeseed	KOH, 0.5-	Methanol,	40–60	3–29	(99) (optimal:	Al-Saadi et al.
continuous	mm, $d_0 = 2.5$ mm, $A = 1-8$ mm, $f = 2-7$ Hz	oil	2%	4:1–13:1			13:1, 2% KOH, 50 °C. 16 min)	(2020)
		Low-grade KOH, 2%	KOH, 2%	6:1-18:1	50	0.5-8	(90) (optimal	
		rapeseed oil					2.75% FFA, 18:1, 4.25 min	

Continuation of Table 13.2 Continuous reciprocating plate column and oscillatory flow reactors for biodiesel production.

		1						
Reactor type	Reactor geometry	Feedstock	Catalyst,	Alcohol,	Tempe-	Residence	Biodiesel yield	Reference
			loading	alcohol/oil molar ratio	rature, °C	time, min	(conversion), %	
OFR, meso, continuous	$D_c = 11 \text{ mm}, l = 0.45 \text{ mm}, d_o = 6 \text{ mm}, h = 14.5 \text{ mm}, A = 8 \text{ mm}, f = 4.5 \text{ Hz}$	MCO	KOH, 2.5– 3.5%	Methanol, 9:1–15:1	99	40–60 s	(99.7) (11:1, 3.0% catalyst, 60 s residence time)	Santikunaporn et al. (2020)
Rotating flask OFR, solar-powered	Six rows of double bottles, fitted with baffles, arranged on both sides of the rotating shaft	Coconut	KOH, 1%	Methanol, 6:1	09	30	93.7	Muhammed Niyas et al. (2023)
OFR, meso, continuous	$D_c = 5 \text{ mm}, l = 1-3 \text{ m}, d_o = 2 \text{ mm}, h = 13 \text{ mm}, A = 1-5 \text{ mm}, f = 10-30 \text{ Hz}$	WCO	КОН, -	Methanol, 4:1–8:1	1	1-2.3 m/s (fluid velocity)	83 (6.5:1, 2.75 m, 2.28 m/s)	Taki et al. (2022)
OFR, meso, followed by a hydrodynamic reactor, continuous	$D_c = 5 \text{ mm}, l = 1-3 \text{ m}, d_o = 2 \text{ mm}, h = 13 \text{ mm}, A = 1-5 \text{ mm}$ $f = 10-30 \text{ Hz}$	Sunflower	KOH, 0.75– 1.25%	Methanol, 6:1–12:1	30-50	30–90 s	89 (92 predicted; 8.5:1, 1% KOH, 51 °C, 90 s)	Taki et al. (2023)
OFR, meso, continuous, preceded by cold plasma pretreatment (25–75 s)	$D_c = 5 \text{ mm}, l = 0.5 \text{ m}, d_o = 2 \text{ mm}, h = 13 \text{ mm}, A = 1-5 \text{ mm}, f = 10-30 \text{ Hz}$	Sunflower	KOH, 0.5– 1.25%	Methanol, 1:6–1:12		30–90 s	(94.8) (60 s plasma exposure; 7.2:1, 1.1% KOH, 86 s)	Taki et al. (2024)
OFR, single orifice baffle, continuous	$D_c = 5 \text{ mm}, l = 1-3 \text{ m}, d_o = 2.5 \text{ mm}, h = 7.5 \text{ mm}, A = 1-5 \text{ cm}, f = 10-30 \text{ Hz}$	Sunflower oil	KOH, 0.75– 1.25%	Methanol, 6:1–12:1	30–50	pu	(89) (40 °C, 9:1, 1% KOH, 3 m reactor length)	Kouhifaiegh et al. (2024)
OFR, no baffles, with a rod crank, batch	$D_c = 20 \text{ mm}, l = 80 \text{ mm}, f = 0.8-5.8 \text{ Hz}$	Sunflower oil	KOH, 0.7% Calcined	Methanol, 6:1	09	120	95 94.4	Khelafi et al. (2022)
			date seed					

Continuation of Table 13.2 Continuous reciprocating plate column and oscillatory flow reactors for biodiesel production.

Reactor type	Reactor geometry	Feedstock Catalyst,	Catalyst,	Alcohol,	Tempe-	Residence	Tempe- Residence Biodiesel yield	Reference
			loading	alcohol/oil rature, time, min	rature,	time, min	(conversion), %	
				molar ratio	သွ			
OFR, orifice	$D_c = 63.5 \text{ mm}, l = 1.1 \text{ m}, f = 1-9$ Palm fatty Sulfonated Methanol,	Palm fatty	Sulfonated	Methanol,	09	50	94.2	Kefas et al.
baffles,	Hz (optimal 6 Hz)	acid	glucose,	9:1				(2019)
continuous		distillate	2.5%					
OFR, orifice	$D_c = 10 \text{ mm}, l = 0.38 \text{ m}, d_o =$	Oleic acid	Oleic acid Calcined	Methanol, 50–70 5–40	50-70	5-40	(96) (RSM, 60	Ali et al. (2022)
baffles,	9.5 mm, $h = 15$ mm, $A = 2-8$	(model of	(model of dolomite,	6:1			$^{\circ}$ C, $f = 4.3 \text{ Hz}, A$	
continuous	mm, $f = 1 - 4.3 \text{ Hz}$	WCO)	CaO/MgO				= 8 mm, 40 min	
							residence time)	
OFR, helical	$D_c = 10 \text{ mm}, l = 0.38 \text{ m}, d_o =$	Oleic acid	Oleic acid Calcined	Methanol,	50-70 5-40	5-40	(98.6, predicted) Ali et al. (2023)	Ali et al. (2023)
baffles,	9.5 mm, $h = 15$ mm, $A = 2-8$	(model of dolomite,	dolomite,	6:1			(ANN, $60 ^{\circ}\text{C}$, f	
continuous	mm, $f = 1 - 4.3 \text{ Hz}$	WCO)	CaO/MgO				= 5.6 Hz, A =	
							9.2 mm, 45 min	
							residence time)	

Abbreviations: ANN – artificial neural network, DBSA – 4-dodecylbenzenesulfonic acid, FFA – free fatty acid, h – interbaffle space, OFR – oscillatory baffled reactor, RSM – response surface methodology, and WCO – waste cooking oil. multiphase reactions, aerobic bioprocesses, and biodiesel production (Baird et al., 1994; Lo et al., 1992; Stamenković et al., 2010a).

The energy generated by the reciprocating motion of the plates is transferred to the liquid-liquid system, creating a dispersion of small droplets. This dispersion results in a longer residence time and uniform shear mixing across the reactor's cross-section. The key advantages of reciprocating plate reactors include the axial and radial uniformity in phase dispersion and the frequent renewal of the interfacial area (Parthasarathy et al., 1984).

The design, optimization, and operation of reciprocating plate reactors as continuous flow systems for biodiesel production via base-catalyzed methanolysis of vegetable oils require a detailed understanding of both reaction kinetics and key hydrodynamic and mass-transfer characteristics. Critical factors include the dispersed phase hold-up, drop size (Sauter mean diameter and drop size distribution), axial dispersion of both phases, and the liquid mass transfer coefficient.

The dispersed phase hold-up and drop size are crucial in determining the residence time of the dispersed phase and the interfacial area, both of which directly impact the mass transfer rate between the immiscible liquid phases in the reactor. In liquid-liquid extraction systems without chemical reactions, it is well established that drop size influences both residence time and the column's maximum capacity, thereby affecting efficiency (Kumar and Hartland, 1996; Pietzsch and Pilhofer, 1985).

Historically, the ideal plug flow model has been used to describe flow regimes in reciprocating plate reactors, but it has often failed to predict performance accurately for many practical applications. Axial dispersion, which measures the deviation from ideal plug flow, significantly affects reciprocating plate reactor performance and productivity. Continuous-phase axial dispersion, in particular, reduces the effective driving force for mass transfer.

Additional considerations for reciprocating plate column reactor design and operation include pressure variation at the reactor bottom and power consumption due to reciprocating plate motion. Understanding pressure variations is essential for sizing equipment for liquid phase transport and for identifying construction requirements, such as preventing cavitation at high agitation intensities. Average power consumption is critical for operating cost estimation, while maximum power consumption is necessary for selecting the appropriate driving motor.

All these characteristics are influenced by the reactor's geometry (e.g., its diameter and height, number of perforated plates, hole diameter, and free fraction plate area), operating conditions (e.g., reciprocating intensity and superficial velocities of the dispersed and continuous phases), physical properties of the liquid

phases, the presence of emulsifiers, and temperature. Optimizing reciprocating plate reactor design involves maximizing performance by increasing the interfacial area for mass transfer, which is directly linked to the dispersed phase drop size and hold-up.

The hydrodynamic and mass transfer performance of reciprocating plate reactors has been extensively studied, with much of the research focused on developing correlations to predict key characteristics. Kumar and Hartland (1995) developed a correlation for dispersed phase hold-up based on power input, phase flow rates, physical properties, and column geometry for various column types, including Karrtype reciprocating plate extraction columns. They further extended their work by developing a unified model that correlates drop size with system parameters across pulsed, packed, and reciprocating columns (Kumar and Hartland, 1996). These correlations have shown reasonable accuracy in predicting dispersed phase hold-up and drop size across a range of operating conditions and column diameters (Stella et al., 2008).

Stella et al. (2006) also compiled available correlations for predicting the backmixing coefficient of the continuous phase in Karr-type reciprocating plate reactors. However, it is important to note that these correlations are generally accurate only for the specific systems and geometries for which they were developed. To ensure a correlation applies to the system under investigation, researchers must compare the calculated values with experimental data.

For the methanol-sunflower oil system, whether with or without a catalyst, there is currently scarce data available on the crucial hydrodynamic and mass transfer characteristics of reciprocating plate reactors (Stamenković et al., 2010a). Therefore, the hydrodynamics of systems with and without methanolysis reactions should be examined to assess whether simpler, non-reactive systems can effectively model the more complex reactive systems used in biodiesel production. The selection of model liquid-liquid systems should be based on typical conditions for base-catalyzed methanolysis of vegetable oils, such as a methanol/oil molar ratio of 6:1 and a potassium hydroxide catalyst concentration of 1% by oil weight. Additionally, exploring lower methanol/oil ratios, such as 3:1, could be important for reducing methanol distillation costs. Previous research has demonstrated that potassium hydroxide-catalyzed methanolysis of vegetable oils in stirred tank reactors can achieve high conversion rates at ambient temperatures within relatively short reaction times (Stamenković et al., 2008). Consequently, considering lower reaction temperatures, such as 30 °C or below, could further reduce reactor heating costs compared to industrial-scale operations, which typically operate near methanol's boiling point (around 60 °C).

13.1.1. Hydrodynamics of reciprocating plate reactors used for biodiesel production

Considering the hydrodynamics of reciprocating plate reactors used in biodiesel production will begin with analyzing the flow structure within the reactor, as it significantly influences the breakage process of the dispersed phase (methanol). This, in turn, plays a critical role in controlling the mass transfer rate between the two immiscible phases. Subsequent analyses will focus on pressure variations at the reactor bottom and power consumption in both single- and two-phase systems. Furthermore, dispersed phase hold-up under varying operating conditions will be addressed, followed by an analysis of Sauter-mean drop size and drop size distribution in both reactive and non-reactive systems. Finally, the specific interfacial area in both types of systems will be discussed.

The methanol—oil dispersion is assumed to be a pseudo-fluid with density and viscosity defined as follows (Stamenković et al., 2007), respectively:

$$\rho_e = \varepsilon_d \rho_d + (1 - \varepsilon_d) \rho_c \tag{13.1}$$

and

$$\mu_e = \mu_c \left[1 + 2.5\varepsilon_d \left(\frac{\mu_d + 0.4\mu_c}{\mu_d + \mu_c} \right) \right] \tag{13.2}$$

where ρ_d , ρ_c , and ρ_e are densities of the dispersed phase (methanol), the continuous phase (sunflower oil), and the emulsion of methanol in sunflower oil, μ_d , μ_c , and μ_e are dynamic viscosities of the dispersed, continuous, and emulsion phase, and ε_d is the dispersed phase holdup. The physical properties of methanol and sunflower oil are given in Table 13.3.

Table 13.3 Physic	al properties	of the liquid phase	(Stamenković et al., 2010a).
-------------------	---------------	---------------------	------------------------------

Liquid	Physical properties	Tempera	ature, °C
	_	20	30
Methanola	Density, kg/m ³	791.7	781.6
	Viscosity, mPa·s	0.58	0.51
Sunflower oil	Density, kg/m ³	922.0	918.5
	Viscosity, mPa·s	92.0	74.2

^a From CRC Handbook of Chemistry and Physics, 69th ed., 1988.

13.1.1.1. Flow behavior and regime

Optimal flow in liquid-liquid reactors generally requires the continuous phase to exhibit plug flow characteristics. The flow behavior in reciprocating plate reactors

can be evaluated using the axial dispersion model under specified operational conditions. With a substantial number of perforated plates (totaling 63), minimal axial mixing is anticipated, making the axial dispersion model particularly suitable. This model is characterized by a single parameter, either the axial dispersion coefficient or the Peclet number of the continuous phase:

$$Pe_c = \frac{u_c h_o}{E_c} \tag{13.3}$$

where Pe_c is the continuous-phase Peclet number, u_c is the superficial continuous phase velocity, h_0 is the dispersion height in the reactor, and E_c is the continuous-phase axial dispersion coefficient.

In an ideal plug flow reactor, axial dispersion is absent (Pe $\rightarrow \infty$), whereas an ideal continuous stirred-tank reactor exhibits complete axial dispersion (Pe = 0). Real flow reactors typically have a Peclet number between these extremes. For a continuous phase in a flow reactor, plug flow conditions are generally considered to be present if Pe > 100 (Kayode Coker, 2001). Based on kinetic data from a basecatalyzed methanolysis reaction in a batch-stirred tank reactor, with a methanol/oil molar ratio of 6:1, 1% potassium hydroxide loading (by oil weight), and a reaction temperature of 30°C (Stamenković et al., 2008), a conversion rate exceeding 80% for sunflower oil is achievable with a residence time greater than 12 min. This corresponds to a superficial continuous-phase velocity of 13.3 cm/min in a 2.54 cm i.d. reciprocating plate reactor under consideration. For reciprocating motion with amplitudes ranging from 1.0 to 2.35 cm and frequencies between 2.0 and 4.0 Hz, the single-phase axial dispersion coefficient, calculated using the correlation of Rama Rao and Baird (1998), ranges from 2.4 to 11.4 cm²/s. Under two-phase conditions, similar or even lower axial dispersion coefficients are expected (Rama Rao and Baird, 1998). With these estimated values of single-phase axial dispersion and the superficial continuous-phase velocity, the continuous-phase Peclet number is calculated to range between 187 and 887, indicating that plug flow conditions are present in the continuous-phase within the reciprocating plate reactor (Stamenković et al., 2010a).

Given the applied superficial continuous-phase velocity and reciprocating intensities, the flow of the continuous phase through the reactor is expected to be laminar, as indicated by the bulk flow Reynolds number (Stamenković et al., 2010a):

$$Re = \frac{\rho_{c} u_{c} D_{c}}{u_{c}} = 33.7 \tag{13.4}$$

where Re is the bulk flow Reynolds number, D_c is the column diameter, u_c is the superficial continuous phase velocity, and ρ_c and μ_c are the continuous phase density and dynamic viscosity, respectively.

The range of the reciprocation Reynolds number, based on the plate opening diameter, is given by Equation (13.3) (Stamenković et al., 2010a):

$$Re_o = \frac{\rho_c (2\pi A f) d_o}{\mu_c} = 10 \text{ to } 47$$
 (13.5)

where Re_o is the reciprocation Reynolds number, d_o is the internal opening plate diameter, A and f are the amplitude and frequency of reciprocating plate motion, and μ_c is the dynamic viscosity of the continuous phase. This range (10–47) suggests the potential for both laminar and transitional flow through the plate orifices (Aleksić et al., 2002b).

13.1.1.2. Pressure variation at the reactor bottom and power consumption

Figure 13.1 shows the total and time-averaged pressure variations at the reactor bottom, along with the total and time-averaged power consumption under batch or single-phase (sunflower oil) conditions at 30 °C, as a function of reciprocating intensity. As reciprocating intensity increases—whether by increasing the amplitude or frequency of the motion—both the pressure variations at the reactor bottom (Figure 13.1a) and the power consumption (Figure 13.1b) rise, driven by increased frictional losses. No significant difference is observed in pressure variations or power consumption between batch and single-phase conditions at the same reciprocating intensity, indicating that the frictional loss due to liquid flow through the reactor is negligible compared to that caused by the reciprocating motion of the perforated plate stack (Stamenković et al., 2010a).

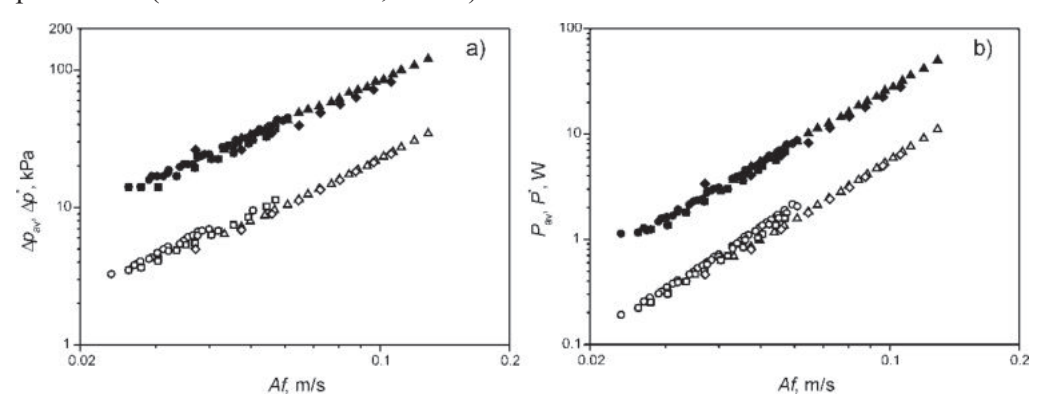


Figure 13.1 Pressure variation at the reactor bottom (a) and power consumption (b) as a function of reciprocating intensity under batch or single-phase conditions (sunflower oil; 30°C; batch reactor; *A*, cm: 1.0 circle and 2.35 triangle; single-phase flow reactor; *A*, cm: 1.0 square and 2.35 diamond; time-averaged pressure variation and power consumption: open symbols; maximum pressure variation and power consumption: black symbols) (Stamenković et al., 2010a).

Figure 13.2 presents the total and time-averaged pressure variations at the reactor bottom, along with total and time-averaged power consumption, under two-phase (methanol-sunflower oil, without catalyst) flow conditions as a function of reciprocating intensity. Similar to the single-phase flow, both the pressure variations and power consumption increase with higher reciprocating intensity, whether due to increased amplitude or frequency, as a result of greater frictional losses. When the temperature is raised from 20 °C to 30 °C, for the same methanol/oil molar ratio, there is a decrease in both pressure variations and power consumption, attributed to the reduction in the dispersion's density and viscosity. Additionally, increasing the methanol/oil molar ratio from 3:1 to 6:1 at a constant temperature, which increases the superficial dispersed phase velocity, results in a further decrease in pressure variations and power consumption. This reduction is due to changes in the physical properties of the dispersion caused by its altered composition.

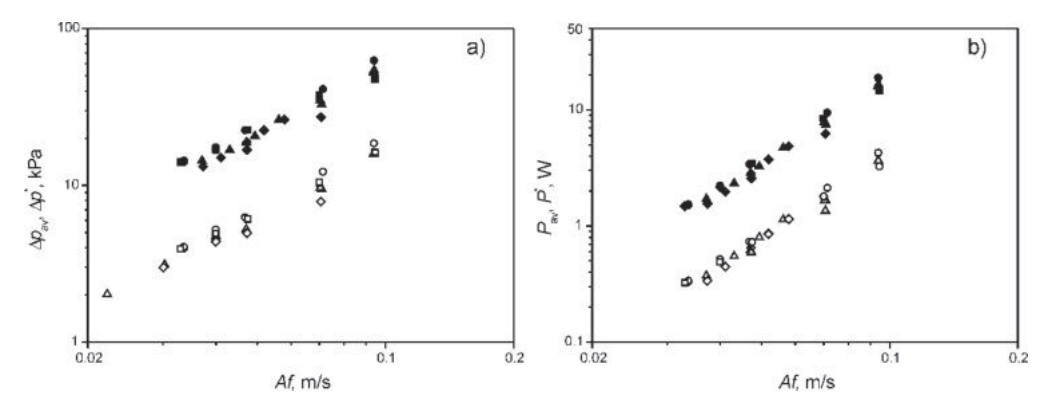


Figure 13.2 Pressure variation at the reactor bottom (a) and power consumption (b) as a function of reciprocating intensity under two-phase co-current flow conditions (A, cm: 1.0 and 2.35; sunflower-methanol molar ratio, 1:3: 20 °C - circles, and 30 °C - up triangles; sunflower-methanol molar ratio, 1:6: 20 °C - squares, and 30 °C - diamonds; time-averaged pressure variation and power consumption: open symbols; maximum pressure variation and power consumption: black symbols) (Stamenković et al., 2010a).

Given their dependence on the liquid phase density, the total and time-averaged pressure variations at the reactor bottom, as well as the total and time-averaged power consumption divided by the system density under batch, single-phase, and two-phase flow conditions, are correlated with the reciprocating intensity using Equation (13.6) (Stamenković et al., 2010a):

$$\frac{\Delta p_{\text{av}}}{\rho_e}, \frac{\Delta p^*}{\rho_e}, \frac{P_{\text{av}}}{\rho_e} \text{ or } \frac{P^*}{\rho_e} = k(Af)^n$$
(13.6)

where $\Delta p_{\rm av}$ is the time-averaged pressure variation at the reactor bottom, Δp^* is the maximum pressure variation at the bottom of the reactor, $P_{\rm av}$ is the time-averaged

power consumption, P^* is the maximum power consumption, k – is the coefficient of proportionality, Af – is the reciprocating intensity, and ρ_e is the system (emulsion) density.

The parameters k and n in Equation (13.6) are determined using the least squares method, and their values are presented in Tables 13.4 and 13.5 for the total and time-averaged pressure variations at the reactor bottom, as well as for the total and time-averaged power consumption under batch, single-phase flow, and two-phase flow conditions. A strong agreement between the experimental and calculated values for both pressure variations and power consumption under batch and single-phase conditions is evidenced by linear correlation coefficients close to or exceeding 0.99 and low standard deviations (mostly below $\pm 5\%$). For two-phase flow conditions, higher but still acceptable deviations ($\pm 13\%$ or less) were observed between the experimental and calculated values for both pressure variations and power consumption.

According to the quasi-steady state flow model, under steady conditions with superimposed oscillatory and turbulent flows, the pressure variation at the reactor bottom and the power consumption for single-phase operations follow power laws with exponents of 2 and 3, respectively (Banković-Ilić et al., 1995; Hafez and Baird, 1978; Veljković and Skala, 1986). In laminar flow, these exponents are 1 and 2, respectively. For transitional flow, the exponents fall within the ranges 1 < n < 2 and 2 < n < 3 (Aleksić et al., 2002b). Figure 13.3 and Tables 13.4 and 13.5 illustrate slopes of approximately 1.35 and 2.35 for the pressure variation and power consumption, respectively, indicating laminar to transitional flow through plate orifices.

Table 13.4 Parameters of correlations for time-averaged and maximum pressure variations at the reactor bottom, Equation (13.4) (Stamenković et al., 2010a).

System	Number of data		Δ	p _{av}			4	\p*	
	01 data	k	n	Error,	$R^{\rm a}$	k	n	Error,	$R^{\rm a}$
				%				%	
Batch	60	0.542	1.32	± 6.4	0.978	2.081	1.35	± 2.0	0.999
Single-phase	23	0.591	1.39	± 4.5	0.994	1.652	1.31	± 4.9	0.987
flow									
Batch +	83	0.564	1.35	± 2.5	0.979	1.91	1.33	± 2.2	0.990
single-phase									
flow									
Two-phase	19	0.428	1.37	\pm 8.9	0.982	1.158	1.28	\pm 12.8	0.972
flow									

^a Coefficient of linear correlation for the log form of Equation (13.4).

Table 13.5 Parameters of correlations for time-averaged and maximum power consumption,
Equation (13.4) (Stamenković et al., 2010a).

System	Number		i	Pav				P^*	
	of data	k	n	Error	R^{a}	k	n	Error	R
				%				%	
Batch	60	1.345	2.33	± 5.0	0.994	6.840	2.36	± 1.9	0.999
Single-	23	1.434	2.39	\pm 4.4	0.998	5.432	2.32	± 4.9	0.996
phase flow									
Batch +	83	1.391	2.35	± 2.6	0.994	6.276	2.34	± 3.1	0.997
single-phase									
flow									
Two-phase	19	1.303	2.45	± 11.9	0.991	3.829	2.29	\pm 12.8	0.991
flow									

^a Coefficient of linear correlation for the log form of Equation (13.4).

Figure 13.3 shows that the total and time-averaged pressure variations at the reactor bottom, as well as the total and time-averaged power consumption, divided by the system density, decrease with reciprocating intensity in two-phase flow compared to single-phase flow. This reduction becomes more pronounced as the methanol/oil molar ratio increases. Given that the density of the methanol-sunflower oil dispersion is less than 2% lower than that of pure sunflower oil, the observed reductions in pressure variations and power consumption are likely due to changes in the viscosity of the two-phase system.

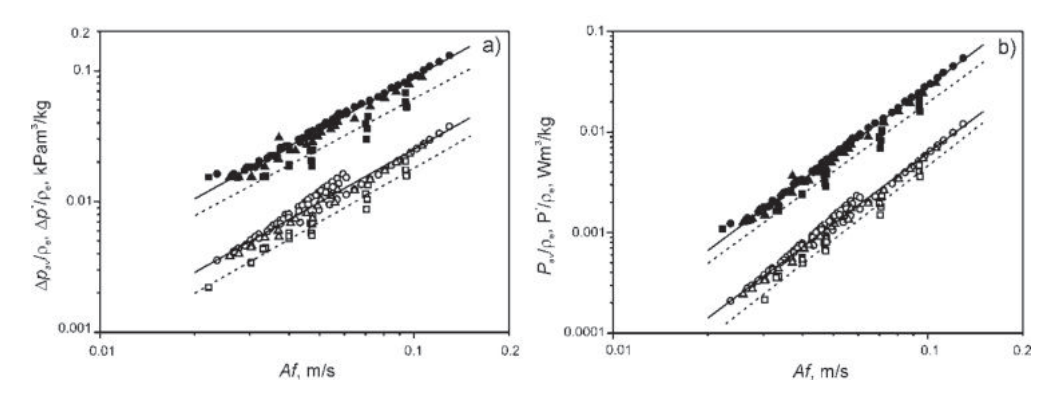


Figure 13.3 The dependences of $\frac{\Delta p_{\text{av}}}{\rho_{\text{e}}}$, $\frac{\Delta p^*}{\rho_{\text{e}}}$, $\frac{P_{\text{av}}}{\rho_{\text{e}}}$ or $\frac{P^*}{\rho_{\text{e}}}$ on the reciprocating intensity

(batch conditions: circles; single phase flow: triangles; and two-phase flow: squares; time-averaged pressure variation and power consumption: open symbols, and total pressure variation and power consumption: black symbols; Equation (13.6) for batch and single phase flow: solid lines, and Equation (13.6) for two-phase flow: dashed lines) (Stamenković et al., 2010a).

Figure 13.4 illustrates the power number as a function of the reciprocation Reynolds number, with additional data from the literature (Banković-Ilić, 1999) for comparison. The curve mirrors those observed in conventional stirred tank reactors. In the laminar flow regime (approximately Re_o<20), the power number decreases with increasing the reciprocation Reynolds number, while it remains constant in the turbulent flow regime (approximately Re_o>50). The slope of the line in the laminar flow regime is -0.5, consistent with earlier studies (Aleksić et al., 2002b; Lounes and Thibault, 1993). Experimental data for distilled water and a 64% aqueous glycerol solution fall within the turbulent flow regime.

The pivotal parameter in the mathematical framework of the quasi-steady state flow model is the plate opening coefficient. It has been established that the plate opening coefficient remains constant only under turbulent flow conditions (Lounes and Thibault, 1993), and can be readily computed from either time-averaged or total pressure fluctuations at the reactor bottom (Banković-Ilić et al., 1997). However, due to its dependence on the reciprocation Reynolds number, this method is unsuitable for laminar or transitional flow regimes. To address this challenge in plate opening coefficient estimation, the approach introduced by Banković-Ilić et al. (1997) offers a viable alternative that is independent of the flow regime. Initially, the instantaneous plate opening coefficient is computed by Equation (6.5) using instantaneous pressure variations at the reactor bottom and the velocity of the reciprocating plate. Subsequently, the time-averaged plate opening coefficient is derived through the integration according to Equation (6.6).

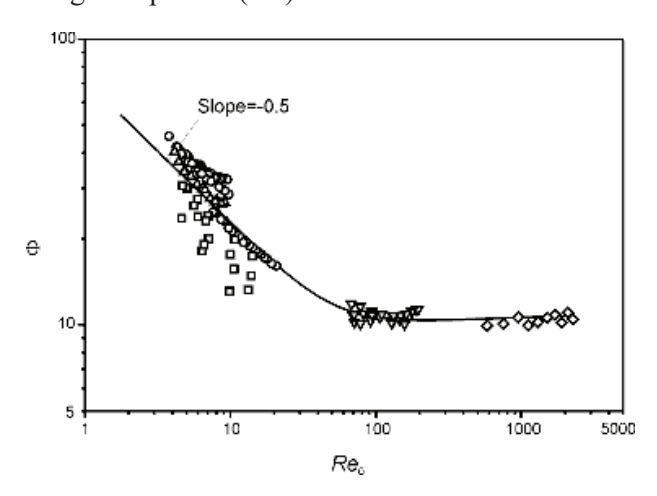


Figure 13.4 The power number as a function of the reciprocation Reynolds number (present study: sunflower oil, batch – circles, sunflower oil, single phase flow – up triangles, and sunflower oil-methanol, concurrent flow – squares; water, batch – diamonds; and a 64% aqueous solution of glycerol, batch – down triangles) (Stamenković et al., 2010a).

In both batch and continuous single-phase flow reciprocating plate reactors, the plate opening coefficient has been shown to depend on the reciprocation Reynolds number, with values ranging from 0.4 to 1.0 within the range of $4 < \text{Re}_0 < 20$ (Figure 13.5). For higher reciprocation Reynolds numbers in batch reciprocating plate reactors, the plate opening coefficient slightly exceeds 1.0 (Banković-Ilić et al., 1997).

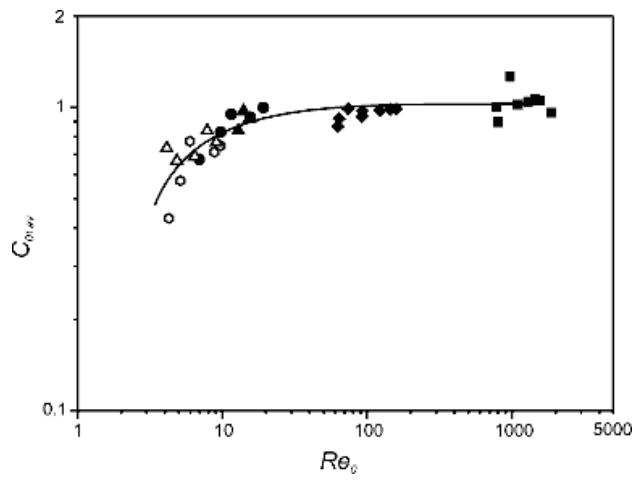


Figure 13.5 The plate opening coefficient as a function of the reciprocation Reynolds number (present study: sunflower oil, batch – circles, and single-phase flow – up triangles; water, batch – squares, and 64% glycerol, batch – diamonds; A, cm: 1.0 – open symbols, and 2.35 – black symbols) (Stamenković et al., 2010a).

13.1.1.3. Dispersed phase holdup

Figure 13.6 presents experimental data on dispersed phase holdup as a function of reciprocating intensity in a reciprocating plate reactor operated at two different amplitudes (1.0 and 2.35 cm) and frequencies (2.0 and 3.0 Hz) of reciprocation, along with two methanol/oil molar ratios (3:1 and 6:1) and two temperatures (20 and 30 °C). The dispersed phase holdup is observed to increase with rising reciprocating intensity up to 5 cm/s, likely due to the intensification of drop breakage. This nonlinear increase at relatively low reciprocating intensities (below 5 cm/s) has been previously documented in larger diameter reciprocating plate reactors (50–450 mm) with countercurrent phase flows (Smith et al., 2008; Stella et al., 2008). The observed increase in holdup is probably due to drop size reduction with enhanced agitation intensity (Baird et al., 1994). However, at reciprocating intensities exceeding 5 cm/s, the dispersed phase holdup appears to plateau, potentially indicating a limited degree of further drop size reduction. Additionally, holdup is higher at the oil/methanol molar ratio of 1:6. In countercurrent phase flows through reciprocating plate reactors, dispersed phase holdup increases not only with reciprocating intensity but also with

the dispersed phase superficial velocity (Banković-Ilić et al., 1997; Stella et al., 2008), while it remained unaffected by the continuous phase superficial velocity (Smith et al., 2008). Due to the large variability in the experimental holdup values, temperature effects could not be discerned.

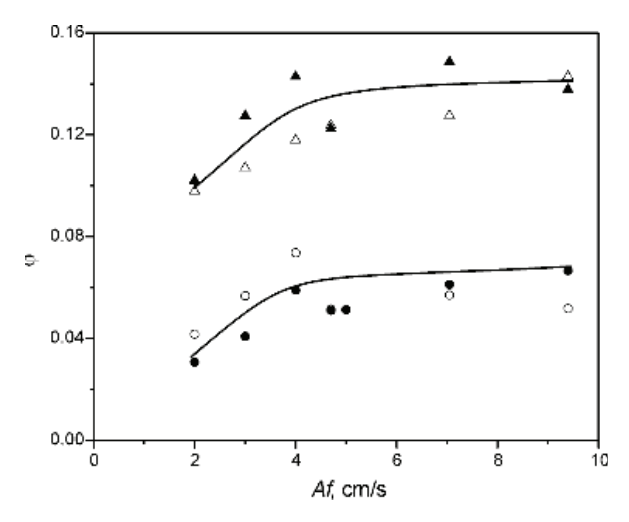


Figure 13.6 Dispersed phase hold-up as a function of the reciprocating intensity (methanol/oil molar ratio; 3:1 – circles, and 6:1 – triangles; temperature: 20 °C – open symbols, and 30 °C – black symbols) (Stamenković et al., 2010a).

The following correlations for dispersed phase holdup were developed (Stamenković et al., 2010a):

- for
$$Af \le 5$$
 cm/s ($\pm 11.4\%$; 13 data)
 $\varepsilon_d = 4.67 \cdot 10^{-5} \left(Af \right)^{0.67} u_d^{-1.22}$ (13.7)
- for $Af \ge 5$ cm/s ($\pm 7.9\%$; 8 data)
 $\varepsilon_d = 4.87 \cdot 10^{-6} u_d^{-1.24}$ (13.8)

where Af is the reciprocating intensity and u_d is the superficial velocity of the dispersed phase.

13.1.2. Drop size and drop size distribution

13.1.2.1. Non-reactive systems

Figure 13.7 displays the Sauter-mean drop diameter along the reactor height for the methanol/oil system, under various conditions: two amplitudes (1.0 and 2.35 cm), two methanol/oil molar ratios (3:1 and 6:1), two temperatures (20 and 30 °C), and three reciprocation frequencies (2.0, 3.0, and 4.0 Hz). For A = 2.35 cm, a temperature of 30 °C, and frequencies of 2.0 and 3.0 Hz, drop size measurements were not

feasible in the upper half of the reactor $(h/h_0 > 0.6)$ due to the formation of an emulsion of small drops. Regardless of the operating conditions, the Sauter-mean drop diameter decreases rapidly from the reactor bottom to approximately one-third of the reactor height, after which it stabilizes in the upper sections of the column. This reduction is particularly pronounced at 30 °C and 2 Hz (Figure 13.7b and d), where unstable, larger methanol drops form and are subsequently disintegrated by the action of the reciprocating perforated plates. Consequently, the reciprocating plate reactor can be divided into two zones (Stamenković et al., 2010a): a lower zone, where the initial large drops are broken down into smaller ones, and an upper zone, comprising most of the reciprocating plate reactor, where a stable dispersion of methanol drops exists, characterized by a constant Sauter-mean drop diameter. The Sauter-mean drop diameter is independent of the methanol/oil molar ratio. It is also well-established that in reciprocating plate reactors with counter-current phase flows, the Sauter-mean drop diameter remains unaffected by phase flow rates (Smith et al., 2008; Stella et al., 2008).

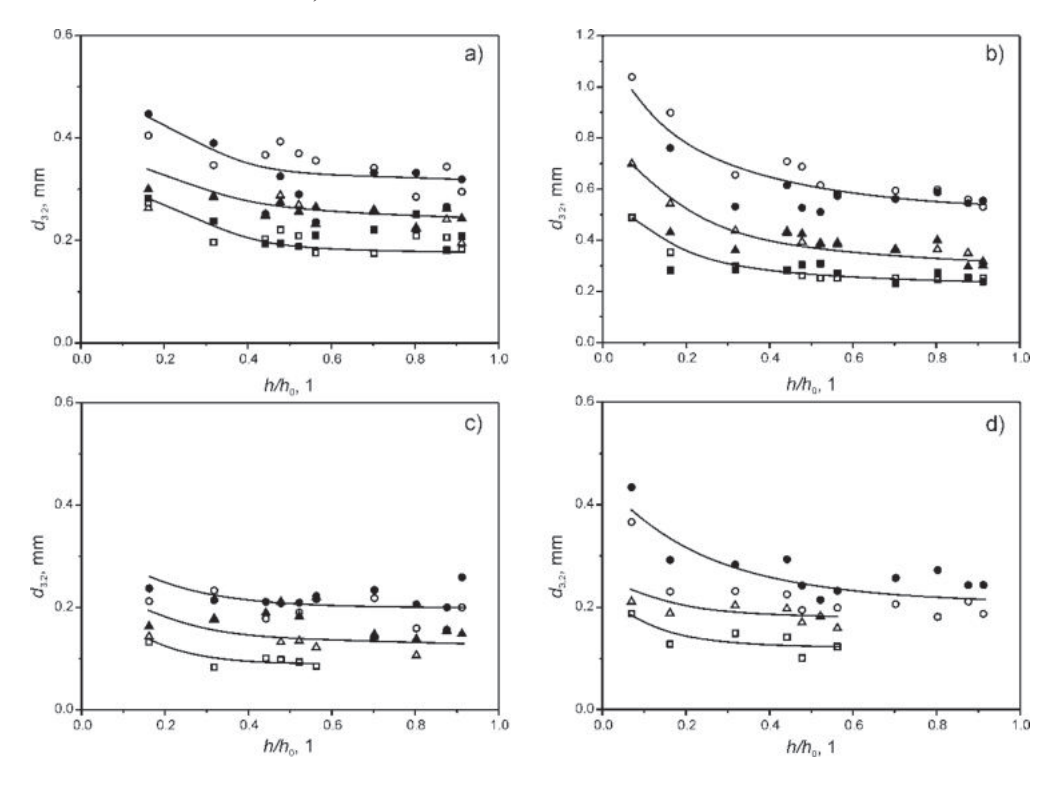


Figure 13.7 Sauter-mean drop diameter along the reactor at (a) A = 1.0 cm and 20 °C, (b) A = 1.0 cm and 30 °C, (c) A = 2.35 cm and 20 °C, and (d) A = 2.35 cm and 30 °C (frequency, Hz: 2.0 - circles, 3.0 - triangles, and 4.0 - squares; methanol/oil molar ratio: 3:1 - open symbols, and 6:1 - black symbols) (Stamenković et al., 2010a).

The Sauter-mean drop diameter decreases with increasing amplitude and frequency of reciprocation, as the enhanced external energy input at higher reciprocating intensities promotes drop breakup. At a given amplitude and frequency of reciprocation, larger Sauter-mean diameter drops form at higher temperatures, while the methanol/oil molar ratio has no significant effect on the mean drop size. The greater viscosity at lower temperatures aids in the drop breakup process, and the reciprocating perforated plates have sufficient capacity to effectively disperse methanol at both methanol/oil molar ratios.

Figure 13.8 illustrates the impact of reciprocating intensity on the Sauter-mean drop diameter in the two distinct zones of the reciprocating plate reactor. As reciprocating intensity increases, the Sauter-mean drop diameter decreases, reflecting the positive influence of external energy on the drop breakup process. This reduction is more pronounced in the lower zone, characterized by unstable dispersion, and at a temperature of 30 °C, compared to the zone of stable dispersion and a temperature of 20 °C. Additionally, the methanol/oil molar ratio does not influence the drop breakup process in either zone. In the upper section of the reciprocating plate reactor, the slopes of the straight lines are calculated to be -0.691 at 20 °C and -0.955 at 30 °C, both of which are lower than the value of -1.2 predicted by the turbulent model (Baird et al., 1994).

Various equations have been developed to predict the Sauter-mean drop diameter in agitated liquid-liquid contactors. However, most of these Equations are limited to the specific systems and operating conditions for which they were derived. Some of these models are based on Kolmogorov's theory of homogeneous isotropic turbulence, which correlates the maximum stable drop diameter with the specific power consumption, using an exponent of -0.4, provided the contactor operates in a fully turbulent regime. For Karr reciprocating plate extraction columns, Stella et al. (2008) validated that the Sauter-mean drop diameter data fit the correlation proposed by Kumar and Hartland (1996), originally developed for countercurrent flow extraction columns:

$$d_{32} = C_{\Psi} \varepsilon^{0.5} / \left\{ \frac{1}{\left[C_{\Omega} \left(\frac{\sigma}{\Delta \rho g} \right)^{0.5} \right]^{2}} + \frac{1}{\left[C_{\Pi} \Psi^{-0.4} \left(\frac{\sigma}{\rho_{c}} \right)^{0.6} \right]^{2}} \right\}^{-0.5}$$
(13.9)

where $d_{3,2}$ is the Sauter mean drop size, ε is the fraction-free plate surface, ψ is the average power consumption per mass unit, g is the gravitational acceleration, σ is the interfacial tension, ρ_e is the continuous phase density, $\Delta \rho$ is the density difference between the two phases, and C_{Ψ} and C_{Π} are the parameters.

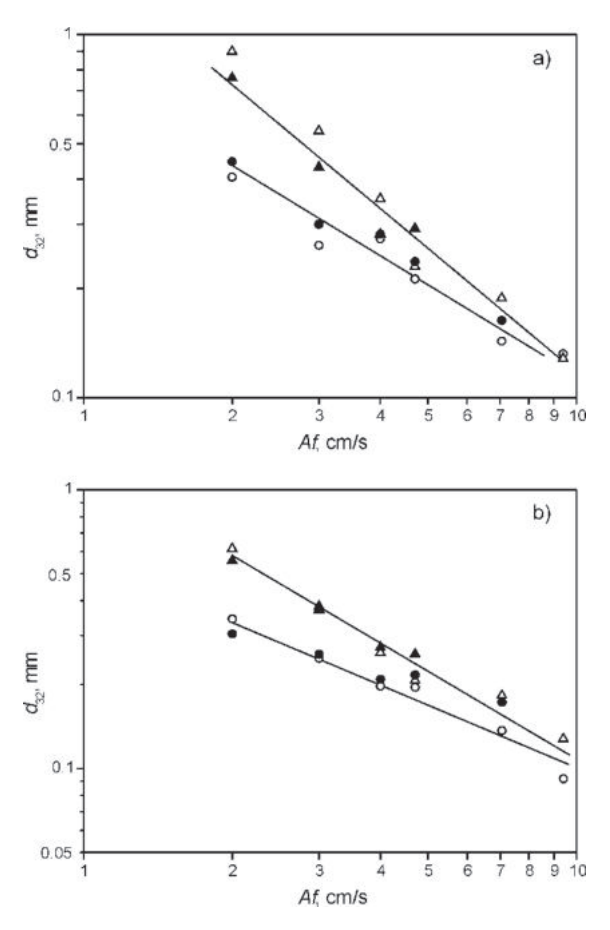


Figure 13.8 Sauter-mean drop diameter (a) at $h/h_0 = 0.162$ (a) and (b) in the upper zone of the reactor as a function of the reciprocating intensity (methanol/oil molar ratio; 3:1 – circles, and 6:1 – triangles; temperature: 20 °C - open symbols, and 30 °C - black symbols) (Stamenković et al., 2010a).

The denominator of Equation (13.9) comprises two additive terms: one representing the ratio of buoyancy to interfacial tension forces, and the other reflecting the energy of turbulent eddies in the continuous phase. In the context of the reciprocating plate reactor under consideration, the first term is negligible compared to the second, allowing Equation (13.9) to be simplified into Equation (13.10) (Stamenković et al., 2010a):

$$d_{32} = C_{\Psi} C_{\Pi} \varepsilon^{0.5} \left(\frac{\sigma}{\rho_{c}} \right)^{0.6} \Psi^{-0.4}$$
 (13.10)

where the specific power consumption is defined as follows:

$$\Psi = \frac{P_{av}}{m_e} \tag{13.11}$$

where $P_{\rm av}$ is the average power consumption and $m_{\rm e}$ is the mass of the emulsion.

Figure 13.9 illustrates the drop size in the upper reactor zone as a function of specific power consumption raised to the power of -0.4. The Sauter-mean drop diameter is observed to correlate with the time-averaged power consumption, as described by Equation (13.12) (Stamenković et al., 2010a):

$$d_{32} = 2.26 \cdot 10^{-4} \, \Psi^{-0.4} \tag{13.12}$$

The average relative standard deviation between the experimental and calculated values of the Sauter-mean drop diameter was determined to be $\pm 11.9\%$ (17 data points) (Stamenković et al., 2010a).

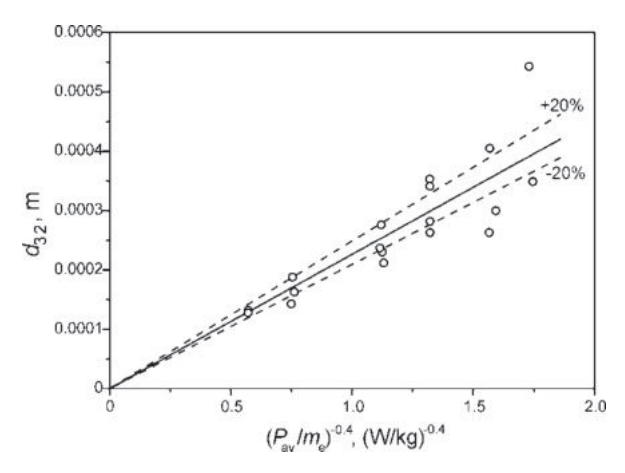


Figure 13.9 Dependence of Sauter-mean drop diameter on time-averaged power consumption (positions along the reactor higher than $h/h_o = 0.162$) (Stamenković et al., 2010a).

For the reactor and the systems under consideration, $\varepsilon = 0.51$ and $\rho_c = 920 \text{ kg/m}^3$ (Table 13.3). Assuming that the interfacial tension of methanol/sunflower oil is equivalent to that of methanol/soybean oil, which is 0.00382 N/m (Wu et al., 2007), the calculated value of $C_{\Psi}C_{\Pi} = 0.596$ from the slope of Equation (13.10) closely matches the value of $C_{\Psi}C_{\Pi} = 0.637$ reported by Kumar and Hartland (1996), resulting in a relative error of 6.3%.

The Sauter-mean drop diameter for the upper reactor zone and the lower third of the reactor is correlated with the time-averaged power consumption, and the following correlations are derived, respectively (Stamenković et al., 2010a):

The Sauter-mean drop diameter for the upper reactor zone and the lower third of the reactor is correlated with the time-averaged power consumption. The following correlations are derived for each zone, respectively (Stamenković et al., 2010a):

$$d_{32} = 0.179 P_{\text{av}}^{0.4} \tag{13.13}$$

and

$$d_{32} = 0.214 P_{\text{av}}^{0.4} \tag{13.14}$$

with the mean relative standard deviation between experimental and calculated values of \pm 18.8% (98 data) and \pm 17.5% (21 data), respectively.

Equations (13.13) to (13.14) require clarification due to the transition from laminar to transitional flow through perforated plates. The mechanism of drop breakage in the reciprocating plate reactor depends on agitation intensity, involving several key factors: shear forces acting on drops passing through plate perforations, collisions of drops with plates, and gravitational flow of drops in the interplate spaces (Joseph and Varma, 1998; Sovova, 1990). Under high agitation intensity, turbulent eddies generated by the reciprocating motion of perforated plates predominantly cause drop disintegration, while under low agitation intensity, all three mechanisms contribute effectively (Sovova, 1990). Equation (13.9) addresses the dissipation rate of energy via turbulent eddies under high agitation intensity. In cases where the dispersed phase viscosity, such as methanol and sunflower oil ($\mu_d/\mu_c = 0.0063$), is significantly lower than that of the continuous phase, the shear force required for drop rupture is substantial, limiting drop breakage to regions with high turbulence intensity (Sajjadi et al., 2002).

In axial dispersion models for both single-phase (Stevens and Baird, 1990) and two-phase (Stella et al., 2008) flows, the reciprocating plate reactor is conceptualized as comprising well-mixed regions around perforated plates and poorly-mixed interplate spaces. Therefore, turbulent eddies induced by the reciprocating plate movement are confined to these well-mixed regions. This results in a locally higher energy dissipation rate around each perforated plate compared to the average rate across the interplate spaces. This two-region model explains the enhanced drop breakage near perforated plates, where the shear forces are stronger due to well-mixed conditions (drops passing through plate holes or colliding with plates), in contrast to the "pure" laminar flow in interplate spaces. This localized energy dissipation and shear force action around perforated plates intensify the drop breakage process, highlighting the significance of agitation intensity in the efficiency of drop disintegration within the reciprocating plate reactor.

To fully characterize liquid-liquid dispersions, the drop size distribution must be considered in addition to the Sauter-mean drop diameter. Figure 13.10 presents drop size distributions along the reactor height for non-reactive systems under three reciprocating frequencies (2.0, 3.0, and 4.0 Hz), two temperatures (20 and 30 °C), and two methanol/oil molar ratios (3:1 and 6:1). Figure 13.11 provides photographs of dispersions along the reactor height for a methanol/oil molar ratio of 6:1 at 2.0 Hz and 30 °C.

Across all operating conditions, an unimodal distribution is observed. At higher reciprocation frequencies (3.0 and 4.0 Hz), the distributions are uniform throughout the reactor height. In contrast, at the lowest frequency (2.0 Hz), uniformity is observed only in the upper part of the reactor. As the reciprocation frequency increases, the drop size distribution becomes narrower with the peak shifting towards smaller drop sizes. At the highest frequency, the distributions are more symmetric, with significantly reduced tails on the large drop size side, particularly evident in systems with a methanol/sunflower oil molar ratio of 6:1 (Figures 13.11a, c, and e).

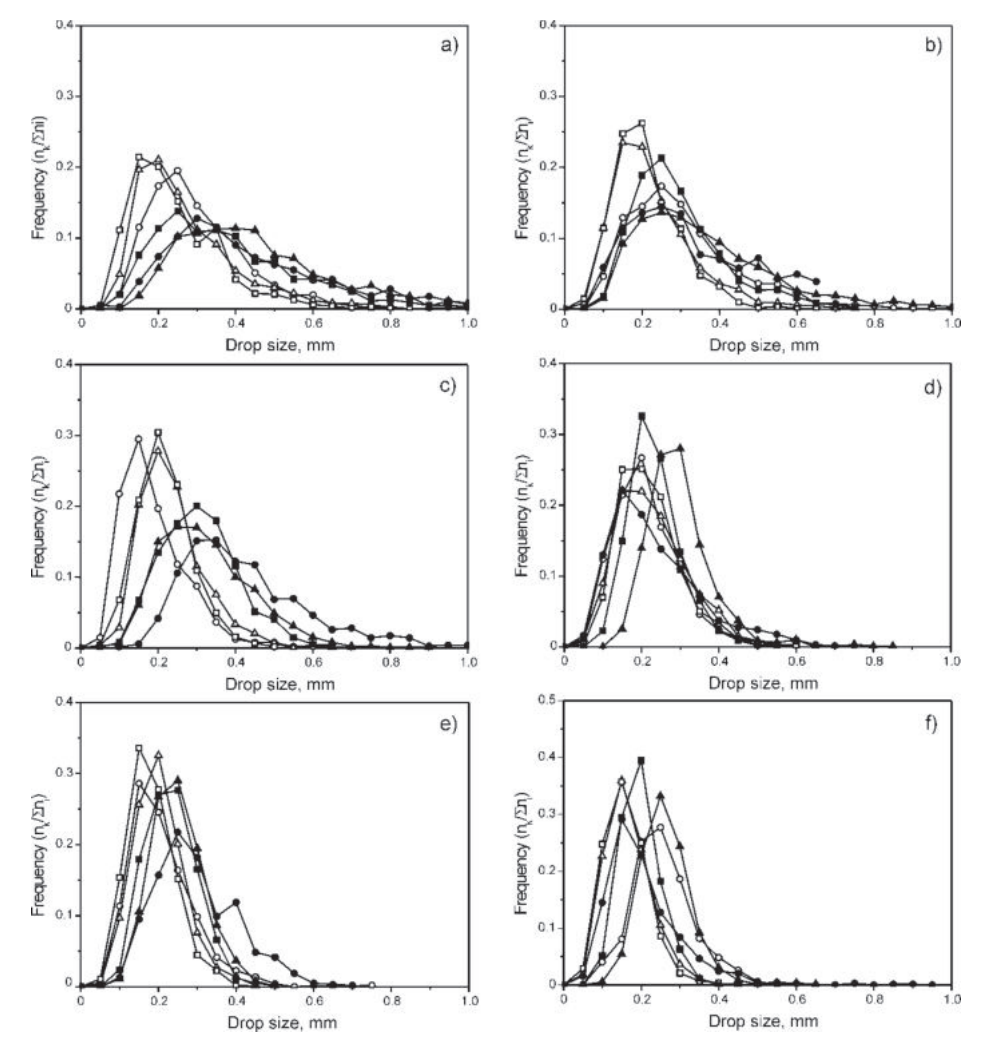


Figure 13.10 Drop size distribution in non-reactive systems for oil-to-methanol molar ratios of 1:3 (a, c, and e) and 1:6 (b, d, and f) at reciprocation frequencies of 2 Hz (a and b), 3 Hz (c and d) and 4 Hz (e and f) (A = 1.0 cm; h/h_0 : 0.162 – circles, 0.478 – triangles, and 0.876 – squares; temperature, °C: 20 - open symbols, and 30 – black symbols) (Stamenković et al., 2010a).

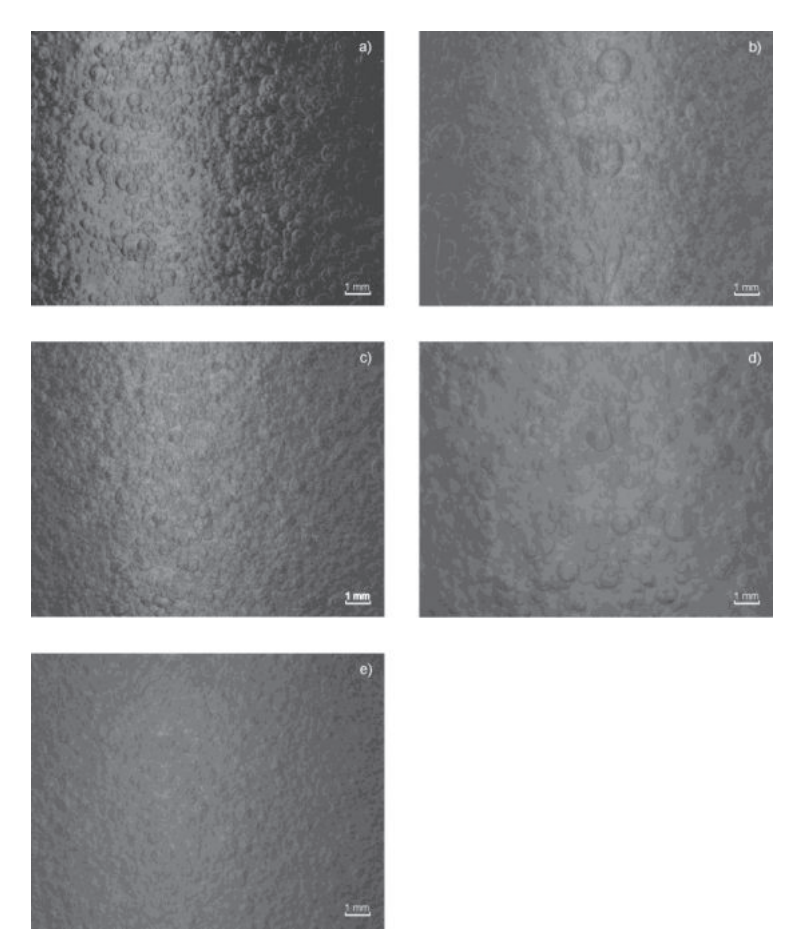


Figure 13.11 Photographs of the dispersion in the non-reactive (a, c and e) and reactive (b and d) systems along the reactor height h/h_0 : 0.162 (a and b), 0.318 (c and d), and 0.876 (e) (A = 1 cm; f = 2.0 Hz; temperature, °C: 30; and methanol/sunflower oil molar ratio: 6:1) (Stamenković et al., 2010a).

At 20 °C, the drop size distributions are narrower with higher peaks at smaller drop sizes and shorter tails compared to those at 30 °C, regardless of reciprocation frequency and molar ratio. The methanol/oil molar ratio does not significantly influence the shape or position of the drop size distribution or the Sauter-mean drop diameter. Generally, reactive systems exhibit narrower drop size distributions with higher peaks at smaller drop sizes compared to their non-reactive counterparts.

13.1.2.2. Reactive systems

Figure 13.12 illustrates the variations in the Sauter-mean drop diameter along the reactor height during the methanolysis reaction at 20 and 30 °C with methanol/oil

molar ratios of 3:1 and 6:1. Due to the formation of an emulsion with very small drops, measurements in the upper half of the reactor (above 0.4) were not feasible. For comparison, the variations in non-reactive systems are also shown.

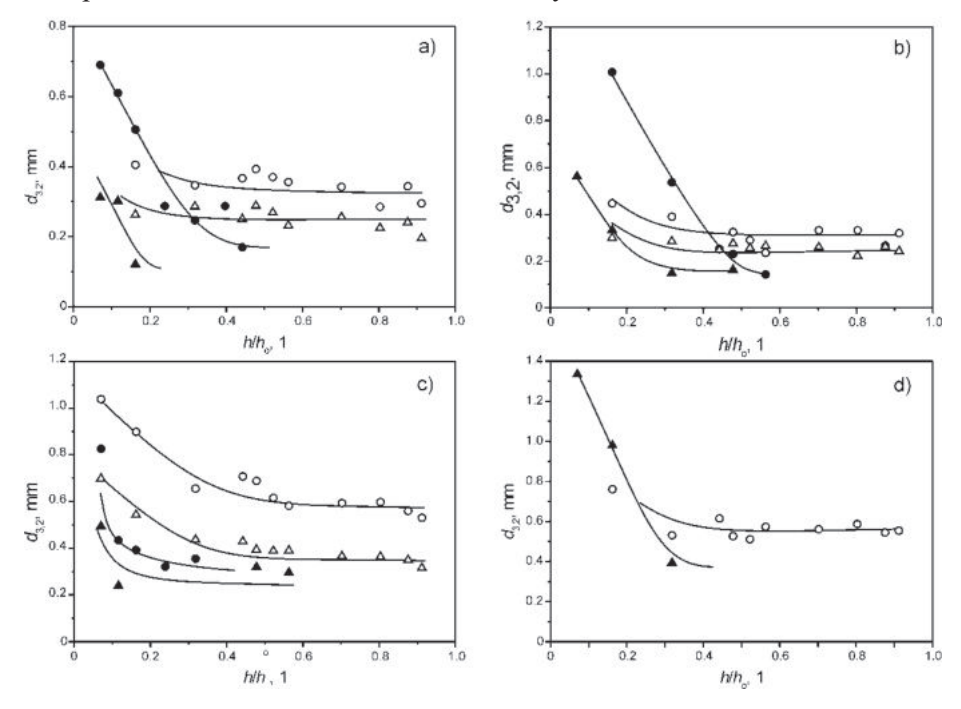


Figure 13.12 Sauter-mean drop diameter along the reactor at 20 °C and methanol/oil molar ratio of (a) 3:1 and (b) 6:1, as well as at 30 °C and methanol/oil molar ratio of (c) 3:1 and (d) 6:1 (A = 1.0 cm; f, Hz: 2.0 – circles and 3.0 – triangles; system without reaction – open symbols, and system with reaction – black symbols) (Stamenković et al., 2010a).

The curve shapes for the Sauter-mean drop diameter along the reactor height are similar for both reactive and non-reactive systems. However, in the upper part of the reactor, the Sauter-mean drop diameter appears smaller in the non-reactive systems compared to the reactive systems under the same conditions. This difference is attributed to the presence of emulsifiers (monoglycerides, diglycerides, and soaps) formed during the methanolysis reaction, which stabilize the smaller drops (Stamenković et al., 2007). It is reasonable to expect that the Sauter-mean drop diameter will remain constant in the upper part of the reciprocating plate reactor throughout its height during the methanolysis reaction.

Figures 13.13 and 13.14 display the drop size distributions in the reactive systems. These distributions narrow and shift towards smaller sizes along the reactor height, a trend previously observed in batch-stirred tank reactors during the methanolysis reaction (Stamenković et al., 2007). Figure 13.11 provides images of the reaction mixtures, illustrating how drop size varies along the reactor height.

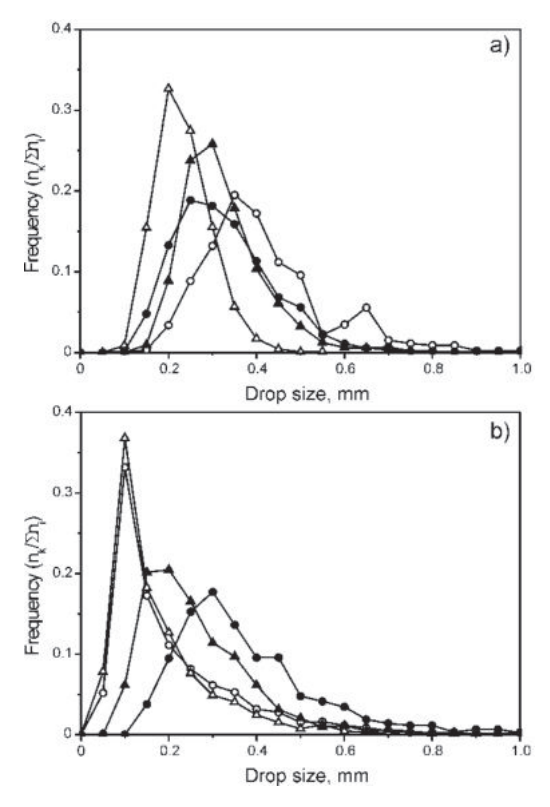


Figure 13.13 Drop size distribution in reactive systems for oil-to-methanol molar ratios of 1:3 (a) and 1:6 (b) at the reciprocation frequency of 2.0 Hz (1% potassium hydroxide based on the oil weight; A = 1.0 cm; h/h_0 : 0.162 – circles, and 0.318 – triangles; temperature, °C: 20 - open symbols, and 30 – black symbols) (Stamenković et al., 2010a).

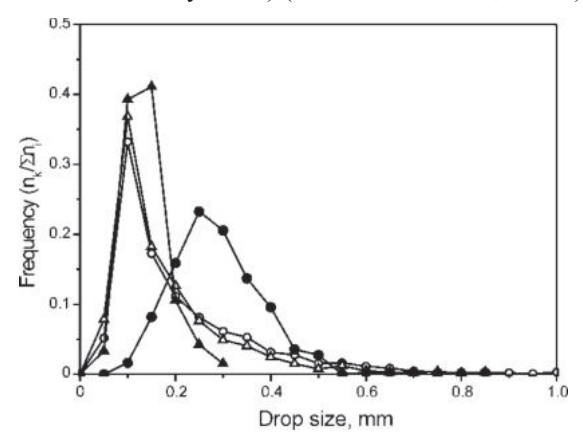


Figure 13.14 Drop size distribution in reactive systems for the oil-to-methanol molar ratio of 1:6 at the temperature of 20 °C (h/h_0 : 0.162 – circles, and 0.318 – triangles; A = 1.0 cm; f, Hz: 2.0 - open symbols, and 3.0 – black symbols) (Stamenković et al., 2010a).

13.1.3. Specific interfacial area

The specific interfacial area increased with increasing both the reciprocating intensity and the sunflower oil-to-methanol molar ratio, i.e., the dispersed phase superficial velocity, as can be seen in Figure 13.15. It was due to the effect of the reciprocating intensity and the sunflower oil-to-methanol molar ratio on the dispersed phase holdup and the Sauter-mean drop diameter. The following correlation was derived by the least square methods ($\pm 12.1\%$, 18 data) (Stamenković et al., 2010a).

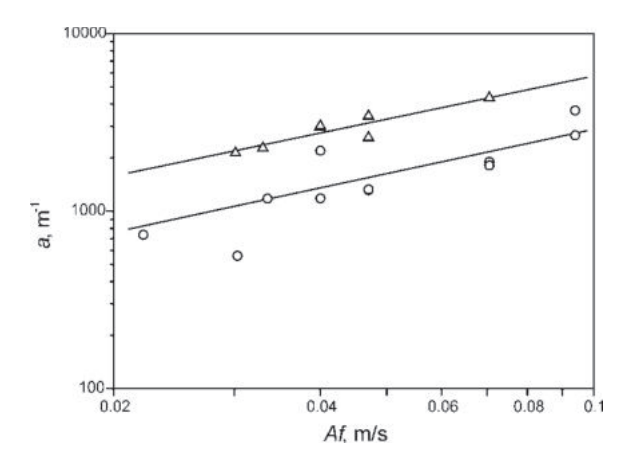


Figure 13.15. The specific interfacial area as a function of the reciprocating intensity at methanol/oil molar ratios of 3:1 (circles) and 6:1 (triangles) (Stamenković et al., 2010a).

Figure 13.15 shows that the specific interfacial area increased with both higher reciprocating intensity and a lower methanol/oil molar ratio, which reflects an increase in the dispersed phase superficial velocity. This effect is attributed to the impact of reciprocating intensity and the molar ratio on the dispersed phase holdup and the Sauter-mean drop diameter. The following correlation was derived using least squares methods (12.1%, 18 data points) (Stamenković et al., 2010a):

$$a = 3.3 \cdot (Af)^{0.74} u_d^{-1.20} \cdot \tag{13.15}$$

where a is the specific interfacial area, Af is the reciprocating intensity, and u_d is the dispersed phase superficial velocity.

13.1.4. Overview of previous research on biodiesel production in reciprocating plate reactors

Reciprocating plate columns have been uniquely explored in Serbia for applications as biodiesel production reactors, both at laboratory and pilot scales.

Additionally, research has extended to their use in biosynthesizing dextransucrase, dextran, and ethanol (Banković Ilić et al., 2024).

Continuous potassium hydroxide-catalyzed biodiesel production from various oily feedstocks (sunflower oil, rapeseed oil, and waste pig-roasting lard) with methanol was carried out in reciprocating plate columns of different diameters (Banković-Ilić et al., 2015; Miladinović et al., 2019; Stamenković, 2014; Stamenković et al., 2010a, 2013). The hydrodynamics of a cocurrent two-phase upflow in a 2.5 cm i.d. reciprocating plate reactor were specifically investigated for the potassium hydroxide-catalyzed methanolysis of sunflower oil (Stamenković et al., 2010a). As detailed in Section 13.1.1.2, this hydrodynamic study confirmed the presence of plug flow of the continuous phase (sunflower oil) through the column, despite the bulk flow regimes through the column and plate openings being predominantly laminar to transitional. Additionally, pressure variation at the reactor bottom and power consumption were shown to be influenced by reciprocating intensity (Equation (13.6) and Table 13.4), while the Sauter-mean drop diameter correlated with specific power consumption (Equations (13.13) and (13.14)). The holdup of the dispersed phase (methanol) (Equations (13.7) and (13.8)) and the specific interfacial area were linked to both reciprocating intensity and the superficial dispersed phase velocity (Equation (13.15)). Therefore, the hydrodynamic study demonstrated that reciprocating plate columns facilitate plug flow, effective twophase mixing, and rapid reactions between immiscible reactants, such as sunflower oil and methanol, at room temperature, along with a straightforward scale-up method consistent with Karr-type reciprocating plate columns (Stamenković et al., 2010a)

13.1.5.1. Effect of operational parameters on biodiesel production

The impact of operational parameters, including the methanol/oil molar ratio, temperature, and the amplitude and frequency of reciprocation, on the efficiency of biodiesel production was investigated for the methanolysis (Stamenković, 2014) and ethanolysis of sunflower oil (Stamenković et al., 2010b)

Figure 13.16 illustrates the effects of reciprocation amplitude and frequency on the methyl ester content at various reaction temperatures and methanol/oil molar ratios during the potassium hydroxide-catalyzed methanolysis of sunflower oil in a 2.54 cm i.d. reciprocating plate reactor. Generally, methyl ester content increases with rising temperature, methanol/oil molar ratio, and reciprocation amplitude and frequency, particularly in the lower sections of the reactor. However, these effects diminish in the uppermost section of the reactor. As the amplitude and frequency of reciprocation, i.e., reciprocating intensity (Af), increase, so does power consumption. For example, under the conditions of A = 2.35 cm and f = 3 Hz, the reciprocating

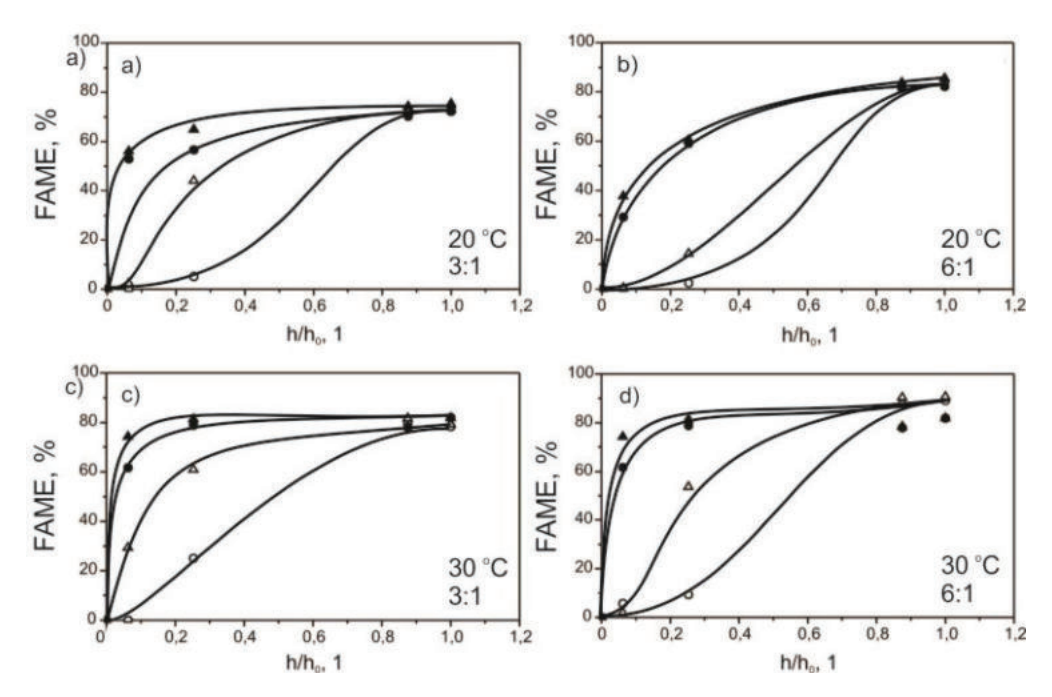


Figure 13.16 The effect of reciprocation frequency and amplitude on the methyl ester content at different reaction temperatures and methanol/oil molar ratios: a) 20 °C and 3:1, b) 20 °C and 6:1, c) 30 °C and 3:1, and d) 30 °C 6:1 (2 Hz – circles and 3 Hz – triangles; and A = 1 cm – open symbols: and A = 2.35 cm – black symbols; $D_c = 2.54$ cm, $n_p = 63$, and 1% potassium hydroxide) (adapted from Stamenković, 2014).

intensity and power consumption are approximately 3.5 and 20 times higher, respectively, compared to the conditions of A=1 cm and f=2 Hz. This increased external energy input promotes better mixing of the immiscible reactants and comminutes the dispersed phase (methanol), enhancing both interfacial mass transfer and reaction rate. Higher temperatures reduce the viscosity of the reaction system (especially sunflower oil) and increase reactant solubility, further accelerating the reaction. The formation of emulsifiers (mono- and diacylglycerols) in the reactor's inlet region stabilizes the emulsion of small methanol droplets, maintaining a high interfacial area and accelerating the reaction in the lower part of the reactor. Additionally, a higher methanol/oil molar ratio increases the reaction rate, driving the methyl ester formation upwards in the reactor.

At lower energy inputs, such as at $A=1\,\mathrm{cm}$, an induction phase is observed in the inlet part of the reactor, resulting in sigmoid curves that indicate the presence of mass transfer limitations. In contrast, at higher energy inputs, like at $A=2.35\,\mathrm{cm}$, no mass transfer limitations are observed, as evidenced by the exponential shape of the curves. Increasing the methanol/oil molar ratio from 3:1 to 6:1 leads to a rise in both

methyl ester content along the reactor and reaction rate in the reactor's inlet region, with the highest methyl ester content observed at the reactor outlet.

Typically, ethanolysis of vegetable oils is conducted near the boiling point of ethanol (approximately 78 °C). To reduce biodiesel production costs, the ethanolysis of sunflower oil with 1% sodium hydroxide catalyst was carried out in a continuous 2.54 cm i.d. reciprocating plate column (Stamenković et al., 2010b) at temperatures of 30 °C, 50 °C, and 70 °C. The process employed a methanol/oil molar ratio of 6:1 and residence times of 6.5 min and 13 min. The reciprocation amplitude was set at 1 cm based on the results of sunflower oil methanolysis. The study found that neither reciprocation frequency (3 Hz or 4 Hz) nor residence time (6.5 min or 13 min) significantly affected the outlet ethyl ester content (Figures 13.17a and b, respectively). Increasing the reaction temperature enhanced ethyl ester content throughout the reciprocating plate column, as depicted in Figure 13.18. Additionally, higher temperatures accelerated reaction rates, particularly in the lower section of

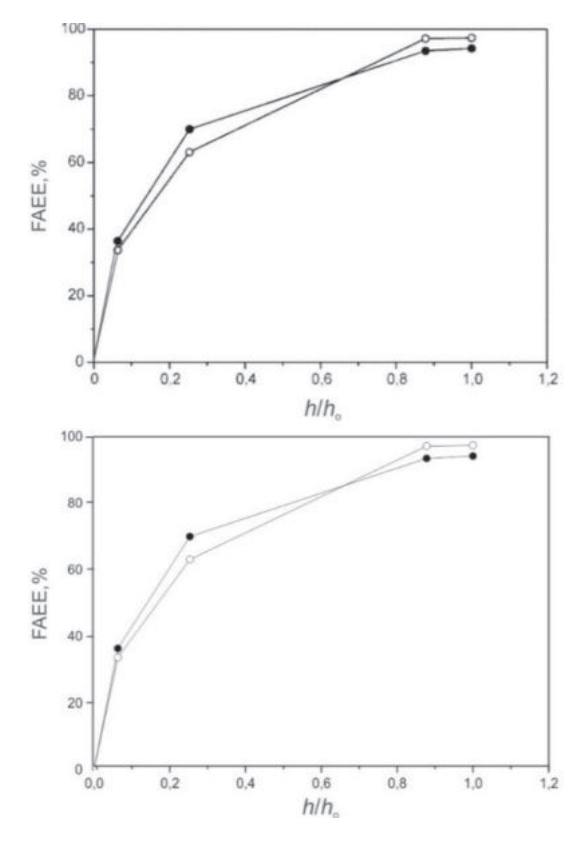


Figure 13.17 The effects of (a) reciprocation frequency at a residence time of 13 min (3 Hz $-\bullet$ and 4 Hz $-\circ$) and (b) residence time at a reciprocation frequency of 3 Hz (6.5 min $-\circ$ and 13 min $-\bullet$) on the ethyl ester content along the reciprocating plate reactor (6:1 methanol/oil molar ratio, 1% NaOH, and 30 °C) (Stamenković et al., 2010b).

the reactor. The differences in ethyl ester contents among the three temperatures diminished along the reactor length, resulting in outlet ethyl ester contents ranging from 94.2% to 97.3%. Subsequently, the outlet reaction mixture underwent gravitational separation with a residence time of 190 min. The crude biodiesel exiting the separator contained approximately 99% ethyl esters.

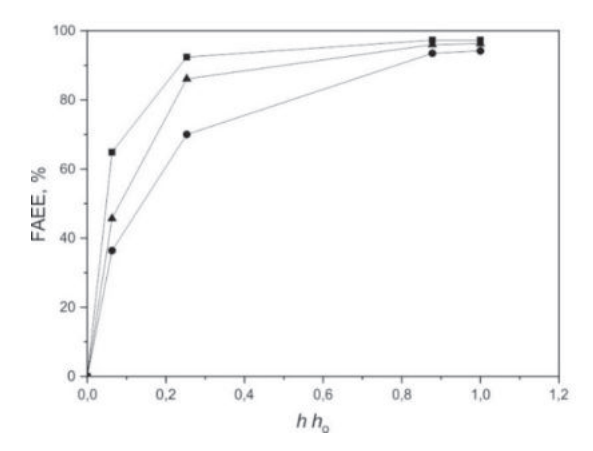


Figure 13.18 The effect of the reaction temperature on the ethyl ester content along the reciprocating plate reactor (6:1 methanol/oil molar ratio, 1% sodium hydroxide, and 3 Hz): $30 \, ^{\circ}\text{C} - \bullet$, $50 \, ^{\circ}\text{C} - \blacktriangle$, and $70 \, ^{\circ}\text{C} - \blacksquare$) (Stamenković et al., 2010b).

13.1.5.2. Two-step biodiesel production by a continuous base-catalyzed methanolysis of vegetable oils

Since the maximum methyl ester content achieved at the outlet of a single reciprocating plate reactor was below the EU biodiesel quality standard of 96.5%, a two-stage continuous process was implemented at the laboratory scale (Stamenković et al., 2008). The production setup, shown in Figure 13.19, consisted of two reciprocating plate reactors with cocurrent upward flows of the reactants, each followed by a gravitational separator. The reaction mixture had a residence time of 13 min.

The continuous methanolysis of sunflower oil was catalyzed by 1% potassium hydroxide in the two reciprocating plate reactors at 30 °C. The process began with sunflower oil and the potassium hydroxide-in-methanol solution being introduced at the bottom of the first reciprocating plate reactor. After the methyl ester phase was separated from the methanol-glycerol phase in the first separator, it was combined with an additional potassium hydroxide-in-methanol solution and pumped into the second reciprocating plate reactor. The crude biodiesel was then separated from the reaction mixture in the second gravitational separator. The methyl ester content in the crude biodiesel was approximately 80% after the first stage and 98–100% after the second stage.

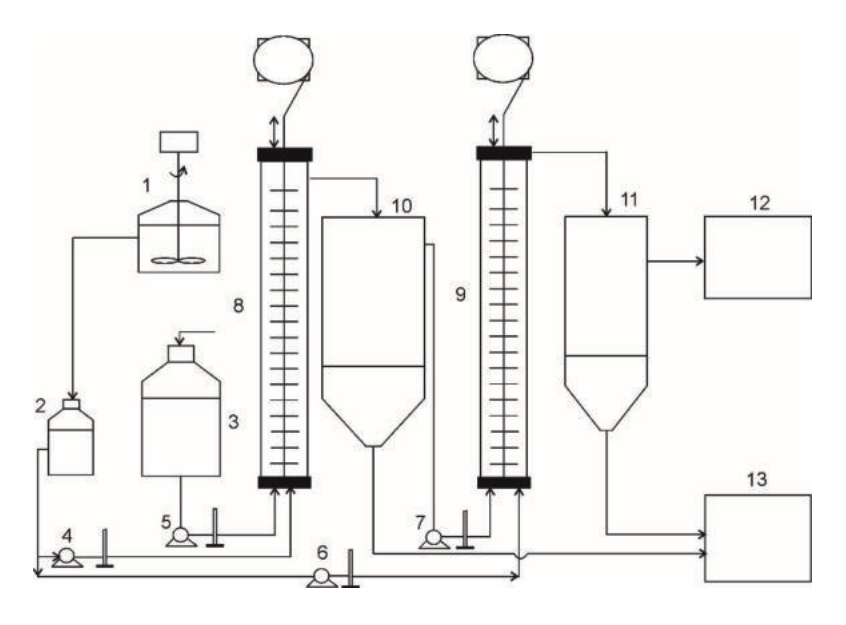


Figure 13.19 Schematic representation of a two-stage biodiesel production plant: 1 – Tank for catalyst solution preparation, 2 – Catalyst solution tank, 3 – Vegetable oil tank, 4 and 6 – Peristaltic pumps for catalyst solution transport, 5 – Peristaltic pumps for oil transport, 7 – Peristaltic pumps for oil-ester phase transport, 6 – Oil and alcohol preheater, 8 and 9 – Reciprocating plate reactors, 10 and 11 – Gravity separators, 12 – Ester tank, and 13 – Glycerol-alcohol phase tank (Stamenković et al., 2013).

The methanolysis of sunflower oil in a continuous two-step process was patented nationally in 2013 (Stamenković et al., 2013). While this process shares similarities with the widely used Lurgi Technology, it features several key differences: (a) a significantly shorter residence time (13 min compared to 60 min), (b) a lower reaction temperature (30 °C versus 60 °C), and (c) vigorous agitation intensity (as opposed to moderate).

13.1.5.3. Biodiesel production in a continuous pilot reciprocating plate reactor

The continuous homogeneous base-catalyzed methanolysis of rapeseed oil was conducted in a pilot plant with a capacity of approximately 74 liters per hour (Stamenković et al., 2010c). As shown schematically in Figure 13.20, the pilot plant's key components include a reciprocating plate reactor and a gravitational separator. The reactor, with an internal diameter of 16.6 cm, is fitted with 15 reciprocating perforated plates (hole diameter: 8 mm, free fraction area: 46.6%, interplate spacing: 5 cm). Additionally, 190 polypropylene spheres, each 8.5 mm in diameter, occupy about 3.8% of each interplate space. The reactor operates with a reciprocation amplitude of 2.35 cm and a frequency of 2 Hz.

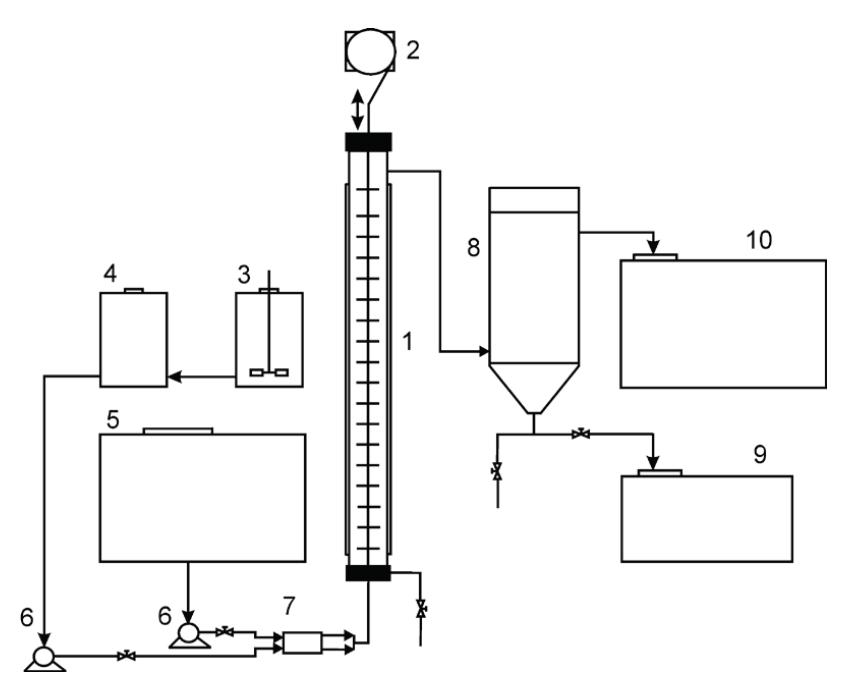


Figure 13.20 Schematic representation of the pilot plant: 1 – reciprocating plate reactor, 2 – electric motor, 3 – tank for catalyst preparation, 4 – tank for catalyst solution in methanol, 5 – tank for vegetable oil, 6 – pumps for transporting vegetable oil and catalyst solution in methanol, 7 – heater, 8 – gravity separator, 9 – glycerol-alcohol phase tank and 10 – ester phase tank (Stamenković et al., 2010c).

The methanolysis reaction takes place at a relatively low temperature of 30 °C, using a methanol/oil molar ratio of 6:1 and potassium hydroxide (1.0% by weight of the oil) as the catalyst. Oil and methanol are pumped through a preheater to the bottom of the reactor, where the reaction mixture is agitated by the reciprocating plates as it flows upward through the reactor, exiting at the top. The mixture is then separated in a gravitational separator into a methyl ester phase (crude biodiesel) and an alcohol phase. Using rapeseed oil, the crude biodiesel leaving the separator achieved a high methyl ester content, ranging from 96.0% to 98.3%.

Consequently, the research conducted by Stamenković and colleagues (Stamenković et al., 2008, 2010a, 2010b, 2010c) provided valuable insights into the optimal operating conditions for potassium hydroxide-catalyzed methanolysis of sunflower oil and demonstrated the process's scalability for industrial applications (Veljković et al., 2024).

13.1.5. Cosolvents in transesterifications in continuous flow reactors

In a typical homogeneous transesterification reaction, alcohol and vegetable oils are immiscible at ambient temperature, resulting in a two-phase mixture. Increasing reaction temperature enhances phase miscibility but requires significant energy. Adding a cosolvent to the reaction mixture can enhance alcohol solubility in the oil phase, reducing the induction period by overcoming initial mass transfer resistance (Sawangkeaw et al., 2010). Additionally, cosolvents improve phase separation (biodiesel and glycerol) and suppress soap formation (Sakthivel et al., 2013).

Cosolvents should be inert and non-reactive with the reactants or catalysts. Low-molecular-weight ethers (e.g., methyl tert-butyl ether, dimethyl ether, diethyl ether) and tetrahydrofuran have been effective in achieving a monophasic mixture when added sufficiently (Boocock et al., 1996). Other organic compounds like propane, heptane, *n*-hexane, and CO₂ have also been utilized. Ionic liquids have emerged as significant cosolvents (Zhao and Baker, 2013), alongside biodiesel itself (Todorović et al., 2019).

Tetrahydrofuran is a widely used cosolvent due to its favorable properties. Its boiling point, close to that of methanol, allows for easy recovery and reuse. Tetrahydrofuran is also cost-effective, non-toxic, chemically inert, and enhances glycerol separation (Boocock et al., 1996). Additionally, it can increase the rate constant of transesterification reactions (Ataya et al., 2006; Doell et al., 2008; Kumar et al., 2011). However, a drawback is its tendency to form peroxides during storage (Guan et al., 2009a).

The impact of cosolvents on the conversion of vegetable oils with alcohol has mainly been studied in homogeneously catalyzed transesterification processes using batch reactors (Banković-Ilić et al., 2015). However, research on continuous biodiesel production with cosolvents is limited (Table 13.6). Existing studies include base-catalyzed methanolysis (Guan et al., 2009a; Guan and Kusakabe, 2012; Shuit, 2010), enzyme-catalyzed methanolysis (Lozano et al., 2012; Royon et al., 2007; Shaw et al., 2008), and transesterification under supercritical CO₂ using methanol (Anitescu et al., 2008; Tang et al., 2008) or ethanol (Bertoldi et al., 2009; da Silva et al., 2010; Trentin et al., 2011a, 2011b) as the acyl acceptor. Various continuous reactors, including tubular, microtube, and packed-bed reactors, have been used, with static mixers added to tubular reactors to enhance mixing and prevent channeling and plugging (Meng et al., 2008).

Using a reciprocating plate reactor for continuous methanolysis of sunflower oil catalyzed by potassium hydroxide demonstrated that the reciprocating motion of perforated plates ensured uniform energy dissipation and maximized the interfacial

Type of	Oil	Type of	Alcohol/oil	Catalyst/	Catalyst/ Cosolvent,	Tempe-	Pressure,	Pressure, Optimal reaction conditions	ion conditions	Reference
reactor		acyl acceptor	molar ratio, mol/mol	loading, conc.	% vol. to alcohol	rature, °C	MPa	Reaction conditions	Yield (conversion), %/Residence time, min	ı
Tubular static mixing	Rapeseed	Methanol	6:1	KOH / 1%	THF, butanon	250-270			6-9 / (06)	Meng et al. (2008)
Microtube	Sunflower	Sunflower Methanol	8:1	KOH / 1%	Diethyl ether, 0.73 ^a	25			(92.8) / 1.55	Guan et al. (2009a)
Electrolysis cell	Corn	Methanol	24:1		THF, 0.25 ^a	25			09/8/60	Guan and Kusakabe (2009, 2012)
Tubular	Rapeseed	Rapeseed Methanol, sc ^b	24:1	Triethyl- Ethyl amine / acetat 0.27:1ª	Ethyl acetate, 1:10	280	25		85 / 145	Tang et al. (2008)
Microtube	Soybean	Ethanol, sc 10:1-40:1	10:1-40:1		CO ₂ , 1:5- 1:10	250-325 10-20	10-20	40:1, 1:5, 325 °C, 20 MPa	54.9 / 35	Da Silva et al. (2010)
Tubular	Soybean	Ethanol, sc	10:1-40:1		CO ₂ , 0:1- 0.5:1°	300-350 7.5-20	7.5-20	40:1, 0.05:1, 70 / 110 250 °C, 10 MPa	70 / 110	Bertoldi et al. (2009)
Tubular	Soybean	Methanol, sc	3:1-6:1		CO ₂ , 4 ^d	350-425 100-250	100-250		(100) / 2-3	Anitescu et al. (2008)
Microtube	Soybean	Ethanol, sc	20:1-40:1		CO ₂ , 0.5:1- 0.2:1°	250-325 10-20		20: 1, 0.2:1, 325 °C, 20 MPa	78 / -	Trentin et al. (2011a)
Microtube	Soybean	Ethanol, sc 20:1-40:1	20:1-40:1		CO ₂ , 0.5:1-	250-325 10-20	10-20	20:1, 0.2:1, 325 °C, 20 MPa	78-84/ 47-49 /	Trentin et al. (2011b)

Continuation of Table 13.6 A review of continuous transesterification processes using cosolvents.

Type of Oil	Oil	Type of	Alcohol/oil	Catalyst/lo	Cosolvent,	Tempe	Pressure,	Optimal reac	Alcohol/oil Catalyst/lo Cosolvent, Tempe Pressure, Optimal reaction conditions	Reference
reactor		acyl acceptor	molar ratio, ading, mol/mol conc.	ading,	% vol. to -rature, MPa alcohol °C	-rature, °C		Reaction conditions	Reaction Yield (conversion), conditions %/Residence time, min	1
Fixed bed Triolein	Triolein	Methanol, sc		Candida t-Bur antractica CO ₂	Candida t-Butanol 45 antractica CO ₂		18		-/ 56	Lozano et al. (2012)
Fixed bed	Fixed bed Cottonseed Methanol	Methanol	6:1	Candida t-Butanc antractica 32.5 %	<i>t</i> -Butanol, 32.5 %	50			95 / 500	Royon et al. (2007)
Packed bed Soybean	Soybean	Methanol	3:1-5:1	Candida n-Hexan antractica Butanol,	<i>n</i> -Hexane: <i>t</i> - 45-65 Butanol,	45-65		4.3:1, 52 °C (75.2) / -	(75.2) / -	Shaw et al. (2008)
RPR	Sunflower Methanol	Methanol	6:1	KOH / 1%	KOH / 1% THF, 1, 10, 20 30 ^f	20			84 / 13	Banković Ilić et al. (2015)

area between the two immiscible reactants (Stamenković, 2014; Stamenković et al., 2010a). Encouraged by positive results, further investigations were conducted using tetrahydrofuran as a cosolvent in continuous reciprocating plate reactor methanolysis (Banković-Ilić et al., 2015). The reaction was performed with a methanol/oil molar ratio of 6:1, 1% potassium hydroxide (by oil mass), at 20°C, and tetrahydrofuran concentrations of 0%, 1%, 10%, and 30% (by oil mass). Sampling valves and photo positions were installed along the reactor to monitor the process. The systems studied were sunflower oil/methanol/tetrahydrofuran (non-reactive) and sunflower oil/methanol/tetrahydrofuran/potassium hydroxide (reactive).

13.3.6.1. Mean drop size and drop size distribution

Figure 13.21 displays variations in the Sauter-mean drop diameter of the dispersed phase along the reactor for non-reactive (methanol/sunflower oil/tetrahydrofuran) and reactive (methanol/potassium hydroxide/sunflower oil/tetrahydrofuran) systems at different tetrahydrofuran concentrations. Figures. 13.22 and 13.23 illustrate the drop size changes with reactor height in non-reactive and reactive systems with 1% tetrahydrofuran, respectively. In reactive systems, drop size measurements are hindered in the upper reactor section ($h/h_0 > 0.5$) at tetrahydrofuran concentrations of 0%, 1%, and 10%, and entirely at 30% tetrahydrofuran due to the formation of a milky white emulsion comprising barely visible and very fine drops.

For both non-reactive and reactive systems at all cosolvent concentrations, the Sauter-mean drop diameter decreases in the lower part of the reactor (Figure 13.21). In non-reactive systems, the drop diameter remains constant in the upper part, and it is likely the same for reactive systems. This behavior, previously observed in the absence of tetrahydrofuran (Stamenković et al., 2010a), can be attributed to the breakup of large drops due to shear forces, collisions, and gravitational flow through plate perforations (Joseph and Varma, 1998; Sovova, 1990). In reactive systems, the reaction of methanol with acylglycerols further reduces the drop size along the reactor. In the upper part, a stable dispersion of methanol drops forms, with a constant Sauter-mean drop diameter, due to the balance between drop breakage from reciprocating plate motion and drop coalescence from extended residence time. The small, stable drops, stabilized by emulsifiers formed during methanolysis and saponification (diacylglycerols, monoacylglycerols, and soaps), increase the interfacial area, enhancing mass transfer and methanolysis reaction rates.

At any reactor location, the Sauter-mean drop diameter is generally smaller in the reactive system than in the non-reactive one under the same conditions and

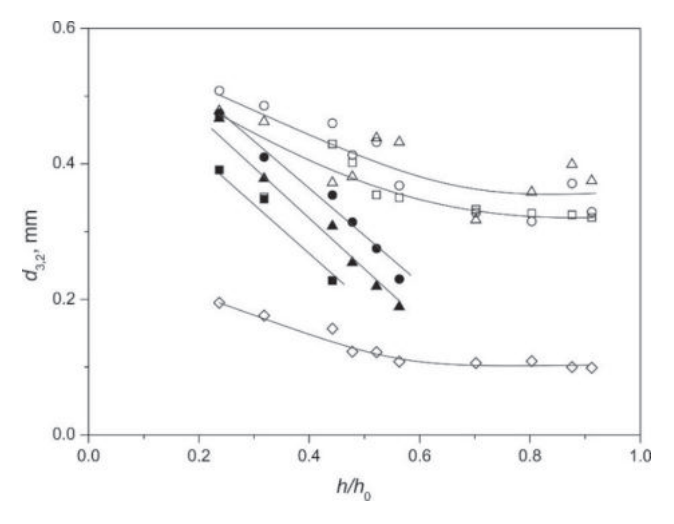


Figure 13.21 The comparison between Sauter-mean drop diameter in non-reactive (open symbols) and reactive (black symbols) systems at different tetrahydrofuran concentrations $(0\% - 0, 1\% - \Delta, 10\% - \Box, \text{ and } 30\% - \Diamond)$ (Banković-Ilić et al., 2015).

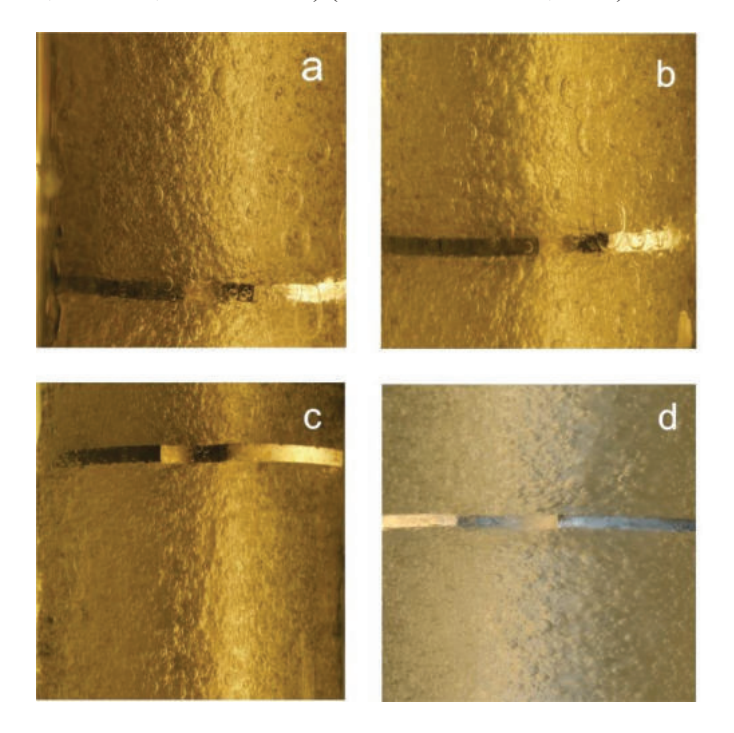


Figure 13.22 The photographs of the dispersion in the non-reactive systems with 1% tetrahydrofuran along the reactor, h/h_0 : a) 0.24, b) 0.52, c) 0.7, and d) 0.91 (Banković-Ilić et al., 2015).

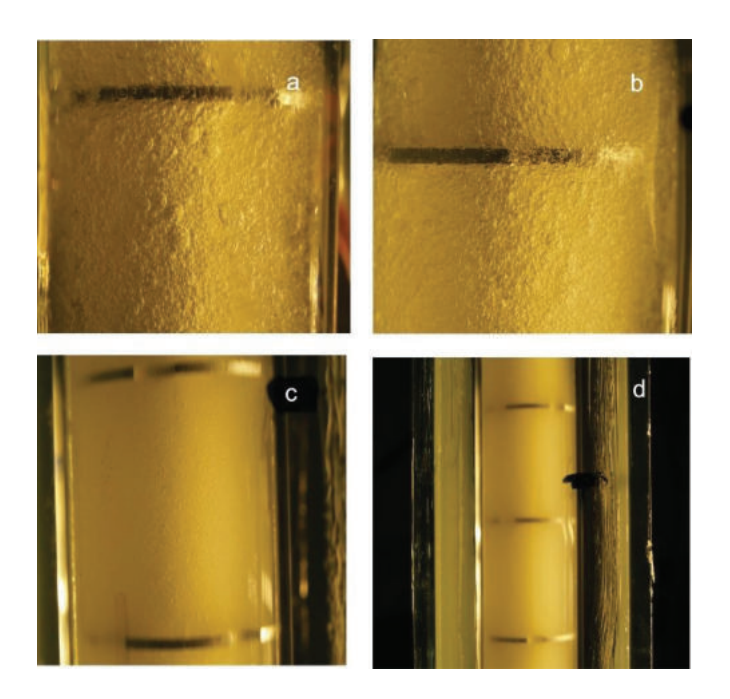


Figure 13.23 The photographs of the dispersion in the reactive systems with tetrahydrofuran 1% along the reactor, h/h_0 : a) 0.24, b) 0.52, c) 0.7, and d) 0.91 (Banković-Ilić et al., 2015).

decreases with increasing cosolvent concentration. In the non-reactive system, a 1% tetrahydrofuran concentration has little effect on drop size, while a 10% concentration leads to a slight reduction of about 7% throughout the reactor. At 30% tetrahydrofuran, the drop size noticeably decreases along the reactor, due to tetrahydrofuran's positive impact on reactant solubility and the drop breakage process.

Figures. 13.24 and 13.25 show the drop size distributions along the reactor height for non-reactive and reactive systems, respectively. Both systems exhibit an unimodal distribution, with a single peak in the low drop size range at all tetrahydrofuran concentrations and reactor locations. In the non-reactive system (Figure 13.24), at low tetrahydrofuran concentrations (0% and 1%), the highest frequency of small drops is observed in the lower third of the reactor. At 30% tetrahydrofuran, the distribution peaks at around 52% frequency indicate a shift toward a stable homogeneous emulsion of smaller drops. Drop size distributions are narrower with shorter tails on the larger drop side as the tetrahydrofuran concentration increased from 0% to 10%. At tetrahydrofuran concentrations ≤10%, the distribution remained uniform in the reactor's upper part, whereas at 30% tetrahydrofuran, a milky-white emulsion of fine drops formed, preventing accurate measurement.

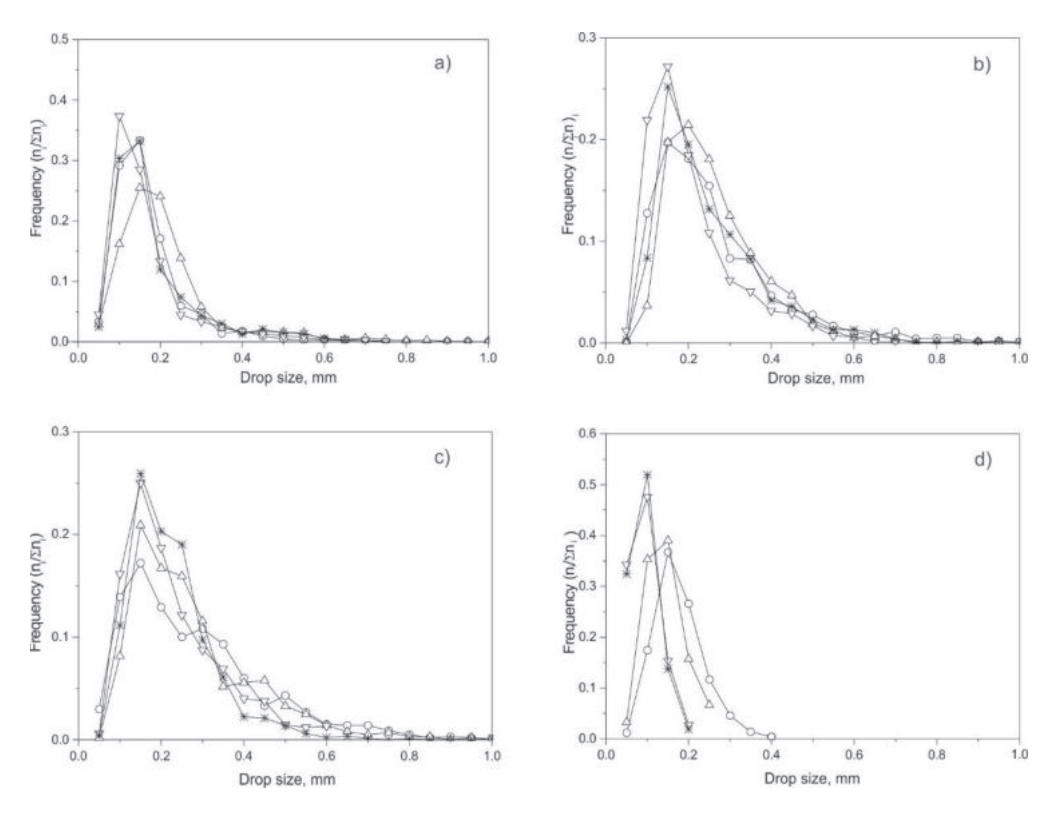


Figure 13.24 Drop size distribution in non-reactive systems at different tetrahydrofuran concentrations: a) 0%, b) 1%, c) 10%, and d) 30% (h/h_0 : 0.24 – o, 0.44 – Δ , 0.7 – ∇ , and 0.91 – *) (Banković-Ilić et al., 2015).

In the reactive system (Figure 13.25), the drop size distribution becomes narrower along the reactor height, consistent with previous observations in systems without cosolvent (Stamenković et al., 2010a) and in a batch stirred tank reactor (Stamenković et al., 2007). The presence of tetrahydrofuran further shifts the distribution towards a stable homogeneous emulsion of smaller drops.

13.3.6.2. Kinetic modeling of the potassium hydroxide-catalyzed methanolysis of sunflower oil in a reciprocating plate column in the presence of a cosolvent

Controversial findings exist regarding the influence of cosolvents on the kinetics of base-catalyzed transesterification of vegetable oils in batch reactors. Karmee et al. (2006) reported no significant rate increase with tetrahydrofuran in pongamia oil methanolysis, suggesting a homogeneous mixture without tetrahydrofuran. However, other studies (Ataya et al., 2006; Doell et al., 2008; Kumar et al., 2011)

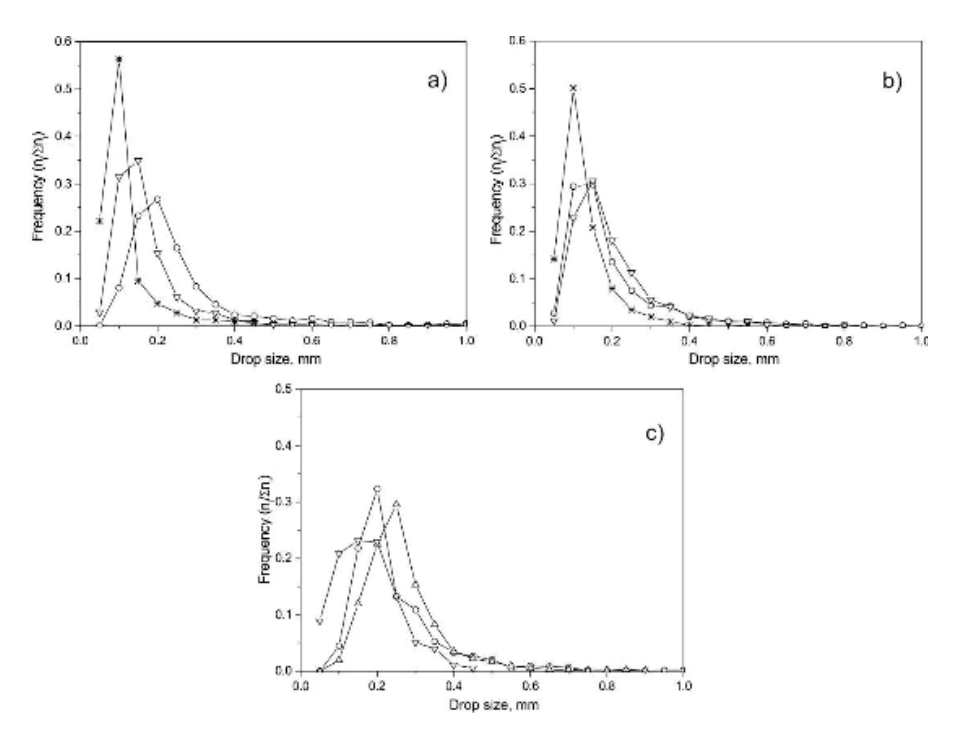


Figure 13.25 Drop size distribution in the reactive system for different tetrahydrofuran concentrations: a) 0%, b) 1%, and c) 10 % (h/h_0 : 0.24 – o, 0.32 – Δ , 0.44 – ∇ , and 0.52 – *) (Banković-Ilić et al., 2015).

have shown that tetrahydrofuran notably enhances the reaction rate, with the effect varying across oils, being highest for soybean, followed by canola, mahua, and jatropha oils. This enhancement is attributed to improved oil solubility in methanol and enhanced reactant contact area (Refaat, 2010; Todorović, 2013). This enhancement is attributed to improved oil solubility in methanol and enhanced reactant contact area (Refaat, 2010; Todorović, 2013). Trentin et al. (2011b) first modeled continuous ethyl ester production under supercritical conditions in microtube reactors using a mass balance approach, assuming first-order reactions.

The overall potassium hydroxide-catalyzed sunflower oil methanolysis reaction can be presented by the following stoichiometric equation:

$$A + 3B \rightleftharpoons 3R + S \tag{13.16}$$

where A is triacylglycerols, B is methanol, R is fatty acid methyl esters, and S is glycerol.

The kinetics of potassium hydroxide-catalyzed sunflower oil methanolysis in continuous flow reactors, with and without tetrahydrofuran, is modeled under the following assumptions:

- (a) Methanolysis progresses through initial heterogeneous followed by pseudo-homogeneous regimes, controlling the kinetics by mass transfer and chemical reaction, respectively. These regimes align with findings in batch reactors with mechanical stirrers (Stamenković et al., 2008) and ultrasound irradiation (Avramović et al., 2012). They are characterized by sigmoidal fatty acid methyl ester and triacylglycerol concentration variations, observed both with and without cosolvent (Ataya et al., 2006; Avramović et al., 2012; Boocock et al., 1996, 1998; Kumar et al., 2011; Todorović et al., 2013). In a continuous reciprocating plate reactor, the former regime takes place in the lower part of the reactor, and the latter regime occurs in the upper part of the reactor (Stamenković et al., 2010a). Also, the flow pattern changes gradually along a microtube reactor where the potassium hydroxide-catalyzed sunflower oil methanolysis occurs in both the absence and presence of diethyl ether as a cosolvent (Guan et al., 2009b).
- (b) In the chemical control regime, the methanolysis behaves as an irreversible second-order reaction initially (Avramović et al., 2012; Darnoko and Cheryan, 2000), becoming reversible near equilibrium (Stamenković et al., 2008). Reverse reactions are negligible in the early period due to excess methanol and low product concentrations. The second-order mechanism for both forward and reverse reactions near equilibrium has already been demonstrated (Vicente et al., 2005, 2006).
- (c) Steady-state plug flow through the reciprocating plate reactor is assumed but verified under specific amplitude and frequency conditions (Stamenković et al., 2010a).
- (d) A free fatty acid neutralization reaction is negligible due to the low oil content in the oil (Avramović et al., 2012; Stamenković et al., 2008).
- (e) Saponification reaction is also negligible at low temperatures and initial catalyst amounts (Vicente et al., 2004), ensuring constant catalyst concentration throughout.

Mass transfer controlled regime: According to assumption (a), mass transfer initially limits the overall reaction rate near the bottom of the reactor. Thus, the triacylglycerol disappearance rate equals its transfer rate from the oil phase into methanol drops across the interfacial area. Assuming plug flow, the kinetic equation is as follows:

$$\left(-r_{\scriptscriptstyle A}\right) = -\frac{\mathrm{d}c_{\scriptscriptstyle A}}{\mathrm{d}\tau} = k_{\scriptscriptstyle c}a\left(c_{\scriptscriptstyle A} - c_{\scriptscriptstyle A,s}\right) \tag{13.17}$$

where k_c is the triacylglycerol mass transfer coefficient, a is the average specific interfacial area, c_A and $c_{A,s}$ are the triacylglycerol concentrations in the oil phase and on the interfacial area, respectively, and τ is the residence time.

The chemical reaction is faster than the mass transfer, $c_{A,s} = 0$, and Equation (13.17) is simplified into the following one:

$$-\frac{\mathrm{d}c_A}{\mathrm{d}\tau} = k_{\mathrm{c}}a \cdot c_{\mathrm{A}} \tag{13.18}$$

The triacylglycerol concentration is related to the triacylglycerol conversion degree as follows:

$$c_{A} = c_{A0} (1 - x_{A}) \tag{13.19}$$

where $c_{A,o}$ is the initial triacylglycerol concentration and x_A is the triacylglycerol conversion degree.

Equation (13.18) can be transformed into Equation (13.20):

$$\frac{\mathrm{d}x_A}{\mathrm{d}\tau} = k_{\mathrm{c}}a(1 - x_{\mathrm{A}}) \tag{13.20}$$

The residence time is defined by Equation (13.21):

$$\tau = \frac{hA_c}{v_o} \tag{13.21}$$

where τ is the residence time, h is the reactor length, v_0 is the volumetric flow rate, and A_c is the cross-sectional area of the reactor, or in a differential form:

$$d\tau = \frac{A_c}{V_o}dh \tag{13.22}$$

Thus, Equation (13.20) can be transformed into Equation (13.23):

$$\frac{\mathrm{d}x_A}{\mathrm{d}h} = \frac{A_c}{v_o} k_c a \left(1 - x_A\right) \tag{13.23}$$

which can be integrated by giving Equation (13.24):

$$-\ln\left(1-x_{\rm A}\right) = \frac{A_{\rm c}}{v_{\rm o}}k_{\rm c}a \cdot h \tag{13.24}$$

Equation (13.24) can be transformed into a dimensionless equation as follows:

$$-\ln\left(1-x_{\rm A}\right) = \frac{h_{\rm o}A_{\rm c}}{v_{\rm o}}k_{\rm c}a\cdot\left(\frac{h}{h_{\rm o}}\right) \tag{13.25}$$

where h_0 is the total reactor height. The dependence of $-\ln(1-x_A)$ versus (h/h_0) is

linear with the slope $\frac{h_{\rm o}A_{\rm c}}{v_{\rm o}}k_{\rm c}a$ from which the volumetric triacylglycerol mass transfer coefficient, $k_{\rm c}a$, can be calculated.

Chemical reaction controlled regime: In the pseudo-homogeneous reaction regime, where the chemical reaction is slower than the triacylglycerol mass transfer (assumption b), the triacylglycerol conversion rate can be expressed as follows:

$$\frac{dx_A}{d\tau} = k_2 c_{Ao} (1 - x_A)^2 \tag{13.26}$$

where k_2 is the rate constant of the irreversible pseudo-second-order reaction.

After including Equations (13.19) and (13.21) into Equation (13.26) and integration, one obtains Equation (13.27):

$$\frac{1}{1 - x_{\rm A}} = \frac{h_{\rm o} A_{\rm c}}{v_{\rm o}} k_2 c_{\rm Ao} \cdot \left(\frac{h}{h_{\rm o}}\right) + C_1 \tag{13.27}$$

where C_1 is the integration constant. The reaction rate constant k_2 and the integration constant C_1 can be estimated from the slope and intercept of the linear dependence of $1/(1 - x_A)$ versus h/h_o , respectively.

According to assumption (b), the methanolysis reaction rate close to the equilibrium is the reversible second-order reaction:

$$\left(-r_{A}\right) = -\frac{\mathrm{d}c_{A}}{\mathrm{d}\tau} = \vec{k}_{2}c_{A}c_{B} - \vec{k}_{2}c_{R}c_{S} \tag{13.28}$$

where \vec{k}_2 and \vec{k}_2 are the reaction rate constants for the forward and reverse reactions, respectively, and c_B , c_R , and c_S are the actual concentrations of methanol, fatty acid methyl esters, and glycerol, respectively. The initial concentrations of fatty acid methyl esters and glycerol are zero, and the initial concentration of methanol is c_{Bo} . Since $c_B = c_{Bo} - 3c_{Ao}x_A$, $c_R = 3c_{Ao}x_A$, and $c_S = c_{Ao}x_A$, it follows:

$$\frac{dx_A}{d\tau} = \vec{k}_2 (1 - x_A)(c_{Bo} - 3c_{Ao}x_A) - 3\vec{k}_2 c_{Ao}x_A^2$$
 (13.29)

Upon integration, the following equation is obtained:

$$\ln \frac{\left[6M(1-K)x_{A} - (1+3M) - \sqrt{-\Delta}\right]}{\left[6M(1-K)x_{A} - (1+3M) + \sqrt{-\Delta}\right]} = \vec{k}_{2}c_{Bo}\tau\sqrt{-\Delta} + C_{2} \tag{13.30}$$

where $K = \vec{k}_2/\vec{k}_2$ is the reciprocal value of the equilibrium constant for the overall methanolysis reaction, $M = c_{A0}/c_{B0}$ is the initial molar ratio of triacylglycerol-to-methanol (=1/6). $\Delta = 4 \cdot 3M(1-K) - (1+3M)^2 < 0$, and C_2 is the integration constant.

Substituting Equation (13.23) into Equation (13.29) and dividing by h_o , Equation (13.31) is obtained:

$$\frac{1}{h_o} \ln \left[\frac{6M(1-K)x_A - (1+3M) - \sqrt{-\Delta}}{6M(1-K)x_A - (1+3M) + \sqrt{-\Delta}} \right] = f(x_A) = \vec{k}_2 c_{Bo} \frac{S}{v_o} \sqrt{-\Delta} \cdot \frac{h}{h_o} + \frac{C_2}{h_o}$$
(13.31)

The reaction rate constant \vec{k}_2 can be calculated from the slope of Equation (13.31). The constant K can be calculated from the equilibrium triacylglycerol conversion degree, x_{Ae} , which can be experimentally determined since it is:

$$\frac{dx_A}{d\tau} = \vec{k}_2 c_{Bo} \left[(1 - x_{Ae})(1 - 3Mx_{Ae}) - 3KMx_{Ae}^2 \right] = 0$$
 (13.32)

or

$$K = \frac{3Mx_{Ae}^2 - (1 + 3M)x_{Ae} + 1}{3Mx_{Ae}^2}$$
 (13.33)

Methanolysis reaction analysis: Figure 13.26 depicts fatty acid methyl ester concentration variations during methanolysis, varying tetrahydrofuran (0% to 30%) and residence times (13 and 26 min). At 0% and low tetrahydrofuran (1% and 10%),

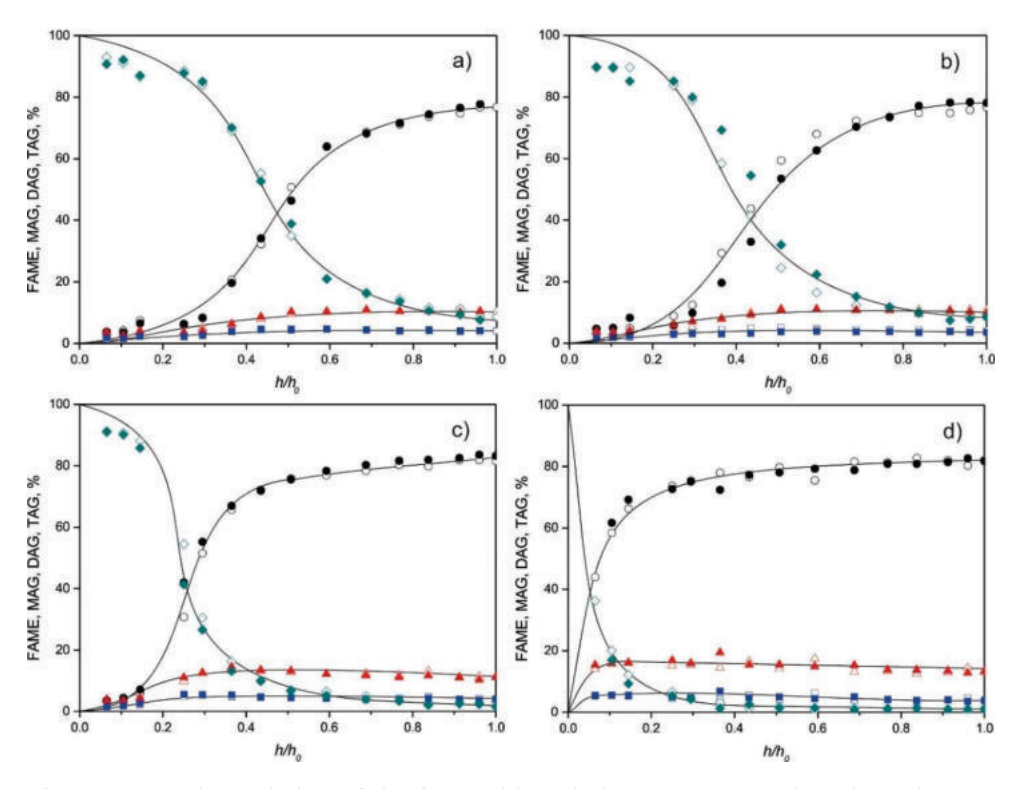


Figure 13.26 The variation of the fatty acid methyl ester concentration along the reactor height for two residence times (13 min – open symbols, and 26 min – black symbols) at different tetrahydrofuran concentrations $(0\% - o, 1\% - \Delta, 10\% - \Box, \text{ and } 30\% - \Diamond)$ (Banković-Ilić et al., 2015).

low fatty acid methyl ester levels (below 10%) in the first third of the reactor reflect mass-transfer limitations at the oil-methanol interface. Higher tetrahydrofuran enhances the interface area by reducing drop size and promotes the reactions in the liquid phase, thus causing higher reaction rates. Concentration profiles shift downwards with increasing tetrahydrofuran, alleviating mass transfer limits entirely at 30%. Along the reactor height, the fatty acid methyl ester concentration started to increase rapidly because the interface area was increased by the dispersion action of reciprocating plates, which increased the reaction rate. In the upper part of the reactor, the reaction approached the equilibrium, and the fatty acid methyl ester concentration reached a maximum value. The maximum fatty acid methyl ester yield increased with increasing tetrahydrofuran concentration. Guan et al. (2009a) and Meng et al. (2008) noted the same variations for the potassium hydroxide-catalyzed methanolysis of sunflower and rapeseed oils, respectively.

For all tetrahydrofuran concentrations, fatty acid methyl ester concentrations for the two residence times (13 and 26 min) are identical at any reactor location (Figure 13.26), confirming steady-state flow (assumption c). At the reactor exit, maximum fatty acid methyl ester concentrations of 78-80% for low (0-1%) and 81-86% for higher (10-30%) tetrahydrofuran concentrations are observed. This suggests: 1) tetrahydrofuran concentration primarily affects the reaction rate and slightly influences equilibrium fatty acid methyl ester concentration, 2) a second reactor is needed to achieve higher fatty acid methyl ester yield (over 96.5% fatty acid methyl esters) to meet biodiesel standards, and 3) a separation unit is necessary to remove glycerol from the exit mixture to favor fatty acid methyl ester synthesis. Therefore, the biodiesel production process should involve two reciprocating plate reactors in series with glycerol separation after each reactor. Additionally, Figure 13.26 shows that equilibrium is reached within the reactor, indicating the reactor column could be shorter and should be designed according to transesterification reaction kinetics.

The fatty acid methyl ester concentration curves along the reactor are sigmoidal for 0%, 1%, and 10% tetrahydrofuran concentrations but exponential for 30% tetrahydrofuran (Figure 13.26). The sigmoidal curves confirm the existence of different kinetic regimes in the reactor: triacylglycerol mass transfer controls the rate in the lower part, while the chemical reaction controls the upper part. The exponential curve at 30% tetrahydrofuran suggests a reaction-controlled regime without mass transfer limitations, where the system transitions from an accelerated to a decelerated phase as it approaches equilibrium. Thus, it is essential to consider reaction kinetics at different reactor heights.

Kinetic models: The kinetic models described by Equations (13.25), (13.27), and (13.31) correspond to mass transfer control, irreversible second-order reaction, and

reversible second-order reaction, respectively. Figure 13.27 shows the linear relationships of $-\ln(1-x_A)$, $1/(1-x_A)$, and $f(x_A)$ (the left-hand sides of Equations (13.25), (13.27), and (13.31)) with the relative reactor height (h/h_0) for different tetrahydrofuran concentrations. The strong correlation between the kinetic equations and experimental data (R > 0.92) across all tetrahydrofuran concentrations validates the proposed models.

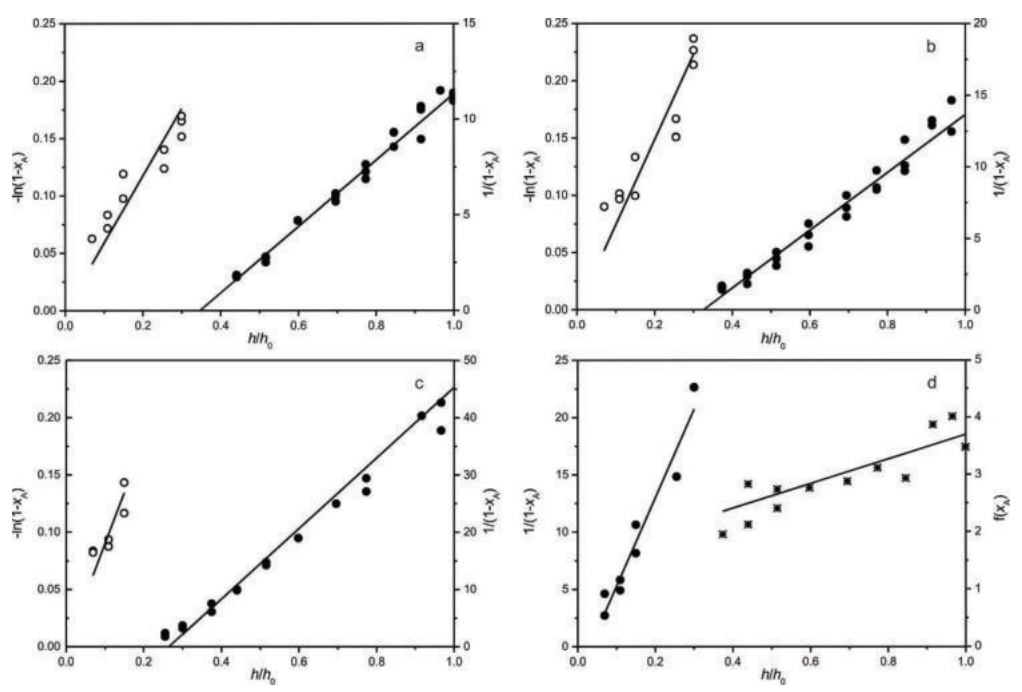


Figure 13.27 The kinetic models of triacylglycerol methanolysis (straight lines) at different tetrahydrofuran concentrations: a) 0%, b) 1%, c) 10%, and d) 30% (experimental data: mass transfer − o; irreversible second-order reaction − •; and reverse second-order reaction − *) (Banković-Ilić et al., 2015).

At low tetrahydrofuran concentrations ($\leq 10\%$), in the reactor's initial section, a heterogeneous system with poor triacylglycerol mass transfer from the bulk of oil to the interface is observed (assumption a: heterogeneous regime), limiting the overall reaction rate. In the upper reactor section, where a stable emulsion of fine drops forms, the kinetics are governed by an irreversible second-order reaction (assumption b: pseudo-homogeneous regime). At the highest tetrahydrofuran concentration (30%), the entire reactor operates under a reaction-controlled regime, with the lower section dominated by an irreversible second-order reaction and the upper section by a reversible second-order reaction.

Table 13.7 presents the rate constants for three kinetic models. The overall volumetric mass transfer coefficient in the mass transfer-controlled regime increases with higher tetrahydrofuran concentrations due to enhanced drop breakage and improved reactant miscibility in the presence of the cosolvent. However, the critical relative height $(h/h_0)_{cr}$, where triacylglycerol mass transfer ceases to control the process, decreases as tetrahydrofuran concentration rises. Additionally, the rate constant for the irreversible second-order reaction also increases with higher tetrahydrofuran concentrations.

Table 13.7 The values of the volumetric mass transfer coefficient for the heterogeneous (mass transfer controlled) regime and the rate constants for the pseudo-homogeneous (chemical reaction controlled) regime (Banković-Ilić et al., 2015).^a

THF	Mass tr	ansfer-	C	hemical	reaction-contro	lled regime		(h)
(%)	contr	olled	Irreversible	second-	Reversible sec	cond-order reac	ction	$\left(\overline{h_0}\right)_{cr}$
	reg	ime	order read	ction				
	$k_{l}a,$	R	k_2 ,	R	\vec{k}_2 ,	k	R	
	min ⁻¹		L/mol·min		<i>n</i> ₂ ,	κ_2		
					L/mol·min	L/mol·min		
0	0.044	0.960	1.551	0.991	-	-		0.30
1	0.056	0.979	1.842	0.975	-	-		0.30
10	0.073	0.987	6.492	0.933	-	-		0.15
30	-		10.834	0.969	0.253	0.0015	0.922	0.30

^a Abbreviations: THF – tetrahydrofuran. Symbols: $k_c a$ is the triacylglycerol mass transfer coefficient, k_2 is the reaction rate constant for the irreversible pseudo-second-order reaction, \vec{k}_2 is the reaction rate constant for the forward second-order reaction, and \vec{k}_2 is the reaction rate constant for the reversible second-order reaction.

No data on the transesterification reaction rate constant in continuous reactors is available in the current literature, except for the study of Banković-Ilić et al. (2015), which was the first attempt to investigate the kinetics of methanolysis of vegetable oils in the presence of a cosolvent in a continuous upflow reciprocating plate reactor. However, some studies have developed kinetic models for vegetable oil methanolysis in batch reactors (Ataya et al., 2006; Doell et al., 2008; Kumar et al., 2011). As shown in Table 13.8, the presence of tetrahydrofuran increases the reaction rate constant compared to systems without the cosolvent. However, the rate-enhancing effect of tetrahydrofuran varies significantly between different oils, indicating that generalizations about its impact on transesterification rates cannot be made (Kumar et al., 2011).

Simulation of the methanolysis process: Figure 13.28 illustrates triacylglycerol conversion variations with reactor height for different tetrahydrofuran concentrations, validating the kinetic models against experimental data. For mass

Table 13.8 Ratios of reaction rate constants for methanolysis of vegetable oils in the presence and the absence of THF (Banković-Ilić et al., 2015).

1						
Reactor type	Oil/catalyst	THF amount	Tempe-	Order and	Ratio of	Reference
			rature,	type of	rate	
			°C	reaction	constants	
Batch vial	Canola oil/	1.25:1	20	First	120	Ataya et al.
	1% NaOH	THF:methanol				(2006)
	Canola oil/	v/v		First	41.9	
	3% NaOH			1 1130	71.7	
Batch flask	Soybean oil/	12:1 THF:oil	50	Second,	1084 ^{a,b}	Doell et al.
Batter Hasir	0.05%	molar ratio	20	forward	632 ^{a,c}	(2008)
	NaOCH ₃	inolal latio		Torwara	574 ^{a,d}	(2000)
Batch flask	Mahua oil/	1.25:1	28	Third,	14.6	Kumar et
	1% KOH	THF:methan	45	irreversible	7.5	al., 2011)
	Jatropha oil/	ol v/v	28		5.5	
	1% KOH		45		3.6	
Continuous	Sunflower	1 wt% THF	20	First, mass	1.27	Banković-
RPR	oil/1% KOH	of the oil		transfer-		Ilić et al.
				controlled		(2015)
				regime		
				Second,	1.19	
				irreversible		
		10 wt% THF		First, mass	1.66	
		of the oil		transfer-		
				controlled		
				regime		
				Second,	4.19	
				irreversible		
		30 wt% THF		Second,	6.99	
		of the oil		irreversible		

^a Taken from Kumar et al. (2011). ^b Triacylglycerols to diacylglycerols. ^c Diacylglycerols to monoacylglycerols. ^d Monoacylglycerols to glycerol. Abbreviations: RPR – reciprocating plate reactor and THF – tetrahydrofuran.

and 10% tetrahydrofuran, and $\pm 2.7\%$, $\pm 3.4\%$, and $\pm 3.0\%$ for irreversible second-order reactions, respectively (Banković-Ilić et al., 2015). At 30% tetrahydrofuran, MRPD values are $\pm 3.1\%$ and $\pm 1.0\%$ for irreversible and reversible second-order reactions, respectively (Banković-Ilić et al., 2015).

13.1.6. Biodiesel production from waste pig-roasting lard in a continuous reciprocating plate reactor

To maximize the benefits of biodiesel, innovative approaches are essential, utilizing inexpensive raw materials like waste lipids or non-edible oils, advanced reactor designs for continuous operation, and optimized reaction conditions. Integrating these elements, along with kinetic studies, represents a promising

strategy for enhancing biodiesel production processes. For instance, biodiesel production from waste pig-roasting lard using a continuous reciprocating plate reactor has been demonstrated (Miladinović et al., 2019).

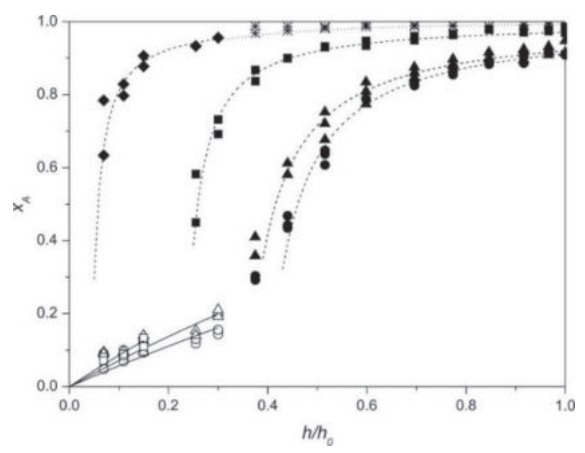


Figure 13.28 The comparison of the triacylglycerol conversion degree calculated by the kinetic model (lines) with the experimental data (symbols) for different tetrahydrofuran concentrations (0% – o, 1% – Δ , 10% – \Box , and 30 % – \Diamond and *; mass transfer-controlled region: open symbols and straight lines; irreversible second-order reaction: black symbols and dash lines; and a reversible second-order reaction: stars and dot line) (Banković-Ilić et al., 2015).

Waste animal fats from meat processing are cost-effective feedstocks for biodiesel production (Banković-Ilić et al., 2014). Commonly used fats include waste and raw lard (Adewale et al., 2016; Jeong et al., 2009; Shin et al., 2012; Stojković et al., 2016a, 2016b), beef tallow (Adewale et al., 2015; Da Cunha et al., 2009; Da Rós et al., 2012), and poultry fat (Boey et al., 2011; Gameiro et al., 2015). Lard transesterification is typically conducted with homogeneous (Jeong et al., 2009; Stojković et al., 2016a), heterogeneous (Stojković et al., 2016b) catalysts, enzymes (Adewale et al., 2016), or under supercritical methanol conditions (Shin et al., 2012). Batch reactors are commonly used, while continuous reactors are less frequent. Among novel reactors, continuous reciprocating plate reactors (Banković-Ilić et al., 2015; Miladinović et al., 2019; Stamenković et al., 2010a) are promising for biodiesel production, offering maximized interfacial mass transfer with low power consumption. Reciprocating plate reactors enhance the process by frequently renewing the interfacial contact area, providing uniform liquid-liquid dispersion, near plug flow, effective two-phase mixing, and rapid potassium hydroxidecatalyzed transesterification at room temperature (Banković-Ilić et al., 2015; Miladinović et al., 2019; Stamenković et al., 2010a).

Since numerous factors impact both biodiesel yield and quality, analyzing each factor individually using the one-factor-at-a-time method is labor-intensive and time-consuming and overlooks potential interactions. Hence, statistical methods like the response surface methodology with diverse experimental designs are increasingly favored to optimize these intricate processes (Montgomery, 2005; Veljković et al., 2012). Moreover, this approach enhances understanding and evaluation of how factors and their interactions influence the biodiesel production process.

Biodiesel production from waste pig-roasting lard in a continuous reciprocating plate reactor presents challenges in achieving high yields and product quality, necessitating a thorough investigation. The reaction conditions' impact on transesterification rates and biodiesel yield is not easily generalized, making the optimization of operating conditions essential for maximizing yield and minimizing costs (Stamenković et al., 2011). Given the numerous factors affecting yield and quality, the one-factor-at-a-time method is inefficient and overlooks interactions. Thus, statistical methods like the response surface methodology are increasingly used to optimize these complex processes, enhancing the understanding of factor interactions and their influence on biodiesel production (Montgomery, 2005; Veljković et al., 2012). On the other hand, enhancing the understanding of the kinetics involved in biodiesel production from waste pig-roasting lard in a continuous reciprocating plate reactor is crucial for improving energy efficiency and product quality and reducing production costs.

Statistical and kinetic modeling have seldom been used to optimize the transesterification conditions of waste animal fats. The batch potassium hydroxide-catalyzed methanolysis of waste lard follows pseudo-first-order kinetics (Stojković et al., 2016a), while the same reaction in a packed-bed reactor adheres to a combination of changing-order and first-order kinetics for triacylglycerols and methyl esters, respectively (Stojković et al., 2016b).

Miladinović et al. (2019) were the first to combine low-cost waste lard with a 2.54 cm i.d. reciprocating plate reactor for continuous biodiesel production via potassium hydroxide-catalyzed transesterification at 60 °C. They optimized key process factors—including the methanol/lard molar ratio (4.5:1 to 7.5:1), catalyst loading (0.5 to 1.0% of lard mass), and reactor height (13 to 192 cm), i.e., residence time—using response surface methodology and factorial design to maximize fatty acid methyl ester content. The study also evaluated existing kinetic models for triacylglycerol conversion along the reactor height.

13.1.7.1. Statistical modeling and optimization

Both the full and reduced quadratic model equations show a significant lack of fit (p > 0.010), indicating they do not accurately represent the observed fatty acid methyl ester content, and their reproducibility within the experimental region is uncertain (Myers and Montgomery, 2002). Therefore, despite high coefficients of determination, these models are not recommended for modeling fatty acid methyl ester content (Veljković, 2014). While the full cubic equation was aliased, its reduced form—excluding statistically insignificant terms—is significant (F-value = 74.7, p < 0.0001) and shows an insignificant lack of fit (p = 0.509) (Table 13.9). This model is represented by the following regression equations (Miladinović et al., 2019):

Actual:

$$Y = -1340.89 + 293.45 X_1 + 2738.57 X_2 + 37.69 X_3 - 496.23 X_1 X_2 + 15.34 X_1 X_3 - 100.29 X_2 X_3 - 15.92 X_1^2 - 1206.95 X_2^2 + 17.27 X_1^2 X_2 + 173.78 X_1 X_2^2$$

$$(13.34)$$

Coded:

$$Y = 83.16 - 7.26 X_1 + 14.92 X_2 + 12.83 X_3 - 10.64 X_1 X_2 + 5.42 X_1 X_3 - 5.90 X_2 X_3 - 6.67 X_1^2 - 10.27 X_2^2 + 9.71 X_1^2 X_2 + 16.29 X_1 X_2^2$$

$$(13.35)$$

where Y is the fatty acid methyl ester content, X_1 is the methanol/lard molar ratio, X_2 is the catalyst loading, and X_3 is the normalized reactor height.

The quality of the fit for the reduced cubic model was evaluated using several statistical criteria. An R^2 -value of 0.944 indicates that the model explains 94.4% of the fatty acid methyl ester content variation, with only 5.6% due to uncontrolled factors. The adjusted $R_{\rm pred}^2$ -value of 0.910 is consistent with the predicted $R_{\rm adj}^2$ of 0.932, showing strong predictive ability. A coefficient of variation of 7.8% suggests good reproducibility, while the mean relative percentage deviation (MRPD) of $\pm 7.1\%$ (55 data points) indicates a close match between actual and predicted data. The Kolmogorov-Smirnov normality test (statistic = 0.171 > p = 0.072) confirms the data are normally distributed, with no outliers detected.

The normalized reactor height, i.e., residence time, has the most significant impact on fatty acid methyl ester content, with the highest *F*-value, surpassing the effects of catalyst loading and the methanol/lard molar ratio. Catalyst loading also has a greater positive impact on fatty acid methyl ester content than the methanol/lard molar ratio, consistent with findings from potassium hydroxide-catalyzed methanolysis of refined lard (Jeong et al., 2009). According to Equation (13.35), while catalyst loading and reactor height positively influence fatty acid methyl ester content, the methanol/lard molar ratio has a negative effect. Thus, increasing catalyst loading and residence time enhances fatty acid methyl ester content. The positive effect of catalyst loading is due to its influence on the reaction rate constant, which

increases with higher catalyst concentrations. This positive impact of catalyst concentration on fatty acid methyl ester formation has also been observed in alkalicatalyzed transesterification of used frying oil under batch conditions (Atapour et al., 2014).

Table 13.9 ANOVA results for the response surface reduced cubic model (Miladinović et al., 2019).

Source	Sum of squares	df	Mean square	F-value	<i>p</i> -value: Prob > F
Model	25738.2	10	2573.8	74.7	< 0.0001
X_{I}	524.6	1	524.6	15.2	0.0003
X_2	2215.0	1	2215.0	64.3	< 0.0001
X_3	4061.1	1	4061.1	117.8	< 0.0001
$X_1 X_2$	2263.8	1	2263.8	65.7	< 0.0001
$X_1 X_3$	394.9	1	394.9	11.5	0.0015
$X_2 X_3$	469.0	1	469.0	13.6	0.0006
X_{1}^{2}	564.1	1	564.1	16.4	0.0002
X_2^2	1335.0	1	1335.0	38.7	< 0.0001
$X_1^2 X_2$	628.8	1	628.8	18.2	0.0001
$X_1X_2^2$	1769.5	1	1769.5	51.3	< 0.0001
Residual	1516.5	44	34.5		
Lack of Fit	1181.4	34	34.7	1.0	0.509
Pure Error	335.0	10	33.5		
Cor Total	27254.7	54			

 $R^2 = 0.944$, $R_{\text{adj}}^2 = 0.932$, $R_{\text{pred}}^2 = 0.910$, C.V. = 7.8% and MRPD = $\pm 7.1\%$ (based on 55 data).

Increasing residence time by raising the reactor height leads to higher fatty acid methyl ester content due to prolonged contact between reactants and the catalyst. This trend is consistent with observations in a liquid-liquid film reactor, where fatty acid methyl ester concentration increased during sodium hydroxide-catalyzed palm oil methanolysis (Narváez et al., 2009). The effect of the methanol/lard ratio is more complex and depends on the other two factors. A positive influence of the methanol/tallow molar ratio on ester yield was noted in potassium hydroxide-catalyzed methanolysis in a batch reactor (Mendonça et al., 2011). However, excessive methanol can increase glycerol solubility, potentially reversing the reaction and reducing fatty acid methyl ester content (Kafuku and Mbarawa, 2010; Lin et al., 2009).

Equation (13.33) reveals three significant two-factor interactions influencing fatty acid methyl ester content, involving all three process factors, indicating that these factors do not act independently. The interaction between catalyst loading and the methanol/lard molar ratio has the most significant impact, with the catalyst

loading quadratic term being more influential than that of the methanol/lard molar ratio. Interactions between catalyst loading and the methanol/lard molar ratio or reactor height negatively affect fatty acid methyl ester content, while the interaction between the methanol/lard molar ratio and reactor height has a positive impact.

The negative interaction between catalyst loading and methanol/lard molar ratio may be due to decreased catalyst concentration and increased glycerol solubility in a larger methanol amount, promoting the reverse reaction. As reactor height increases, higher catalyst loading could lead to fatty acid methyl ester and triacylglycerol saponification, explaining the negative interaction between these factors. Conversely, increased reactor height enhances residence time and the uniform emulsion zone, favoring fatty acid methyl ester synthesis at higher methanol/lard molar ratios. The prevailing interaction depends on the relative importance of these influences under specific process conditions. Aiming at the achievement of the maximum fatty acid methyl ester content in the range of up to 100%, the optimal process factors in the used experimental ranges are found by solving Equation (13.35). The optimal catalyst loading is in the range of 0.9% to 1%, the optimal methanol/lard molar ratio is close to either the lowest or highest level (4.5:1–4.7:1 and 7.3:1–7.4:1, respectively) and the optimal reactor height corresponds to the reactor outlet (Miladinović et al., 2019).

Figure 13.29 illustrates the outlet fatty acid methyl ester content as a function of catalyst loading and the methanol/lard molar ratio, presented as 3D and contour plots from the reduced cubic model. The contour plot indicates that fatty acid methyl ester content exceeding 96.5% can be achieved across the entire methanol/lard ratio range if catalyst loading is sufficiently high (shadowed area). Thus, the minimum methanol/lard ratio is a key criterion for optimizing process conditions. The optimal conditions for achieving a fatty acid methyl ester content greater than 99% are a catalyst loading of 0.9% (of lard mass) and a methanol/lard ratio of 4.5:1. However, experimental results show a fatty acid methyl ester content of 96.2% with a slightly higher catalyst loading (1.0%), suggesting the model may have overestimated fatty acid methyl ester content at high catalyst loading and varying methanol/lard ratios. Hoque et al. (2011) found the optimal methanol/lard ratio for batch methanolysis of various feedstocks, including animal fats, to be between 4.8:1 and 6.5:1.

13.1.7.2. Kinetic analysis

For the kinetic modeling of potassium hydroxide-catalyzed waste lard methanolysis, the presence of heterogeneous and pseudo-homogeneous regimes is assumed, where the reaction is controlled by mass transfer and chemical reaction, respectively. This behavior is similar to that observed for sunflower oil methanolysis with potassium hydroxide in the same reciprocating plate reactor (Banković–Ilić et al., 2015). Two reaction mechanisms: 1) pseudo-first-order kinetics in both regimes and 2) a changing mechanism coupled with triacylglycerol mass transfer throughout the reactor are tested.

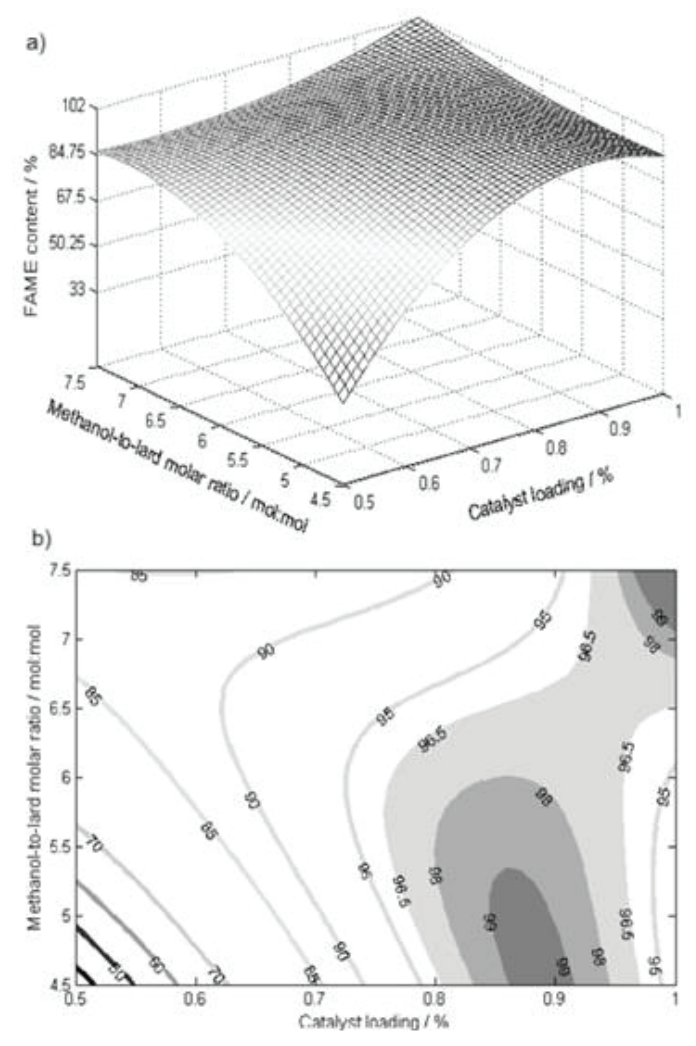


Figure 13.29. Response (a) surface and (b) contour plots for fatty acid methyl ester content as a function of methanol/lard molar ratio and catalyst loading at $h/h_0 = 1.00$ (the reduced cubic model) (Miladinović et al., 2019).

Methanolysis converts triacylglycerols to fatty acid methyl esters and glycerol via intermediates diacylglycerols and monoacylglycerols. Because these intermediates are consumed faster than triacylglycerols, they are not considered in the overall reversible reaction (Equation 13.16). The reciprocating plate reactor operates under an ideal plug flow, as confirmed by previous tests (Banković–Ilić et

al., 2015; Stamenković et al., 2010a). With the FFA content in waste lard at only 0.53%, FFA neutralization is neglected, and saponification of triacylglycerols is also ignored due to the high methanol/lard molar ratio.

Pseudo-first-order reaction in heterogeneous and homogeneous regimes: In the heterogeneous regime, the reaction rate is limited by triacylglycerol mass transfer resistance in the lower part of the reciprocating plate reactor, with the triacylglycerol conversion rate equal to the mass transfer rate into methanol drops. Assuming plug flow, Equation (13.25) describes the variation in conversion degree along the reactor height (Banković–Ilić et al., 2015):

$$-\ln\left(1-x_{\rm A}\right) = \frac{h_{\rm o}A_{\rm c}}{v_{\rm o}}k_{\rm c}a\cdot\left(\frac{h}{h_{\rm o}}\right) \tag{13.25}$$

In the pseudo-homogeneous regime, where the reaction rate is slower than the mass transfer, it limits the overall process rate. Assuming plug flow and an irreversible pseudo-first-order reaction, the rate equation is given by Equation (13.27) (Banković–Ilić et al., 2015):

$$-\ln(1-x_{\rm A}) = \frac{h_{\rm o}A_{\rm c}}{v_{\rm o}}k_{\rm app}\left(\frac{h}{h_{\rm o}}\right) + C_{1}$$
 (13.27)

where k_{app} is the apparent pseudo-first-order reaction rate constant.

Figure 13.30 shows a linear relationship between $-\ln(1 - x_A)$ on h/h_0 . For the lowest catalyst and methanol amounts (0.5% of waste lard and a 4.5:1 methanol/lard molar ratio), only a heterogeneous regime was observed. For other catalyst loadings and methanol/lard ratios, both heterogeneous and pseudo-homogeneous regimes were present. In the initial one-third of the reactor, the reaction rate was slow due to limited triacylglycerol mass transfer. Here, the reaction rate was independent of catalyst concentration and methanol/lard ratio (rate = 0.036 min⁻¹). In the upper reactor, where fatty acid methyl esters acted as a cosolvent and diacylglycerols and monoacylglycerols as emulsifiers, the pseudo-homogeneous system formed, and the reaction rate increased linearly with catalyst amount (Figure 13.31). The reaction rate constant was determined to be 4.70 L/(mol·min) ($R^2 = 0.995$).

Changing mechanism coupled with triacylglycerol mass transfer: Miladinović et al. (2014) originally developed this model for heterogeneously catalyzed sunflower oil methanolysis. The changing mechanism was previously used

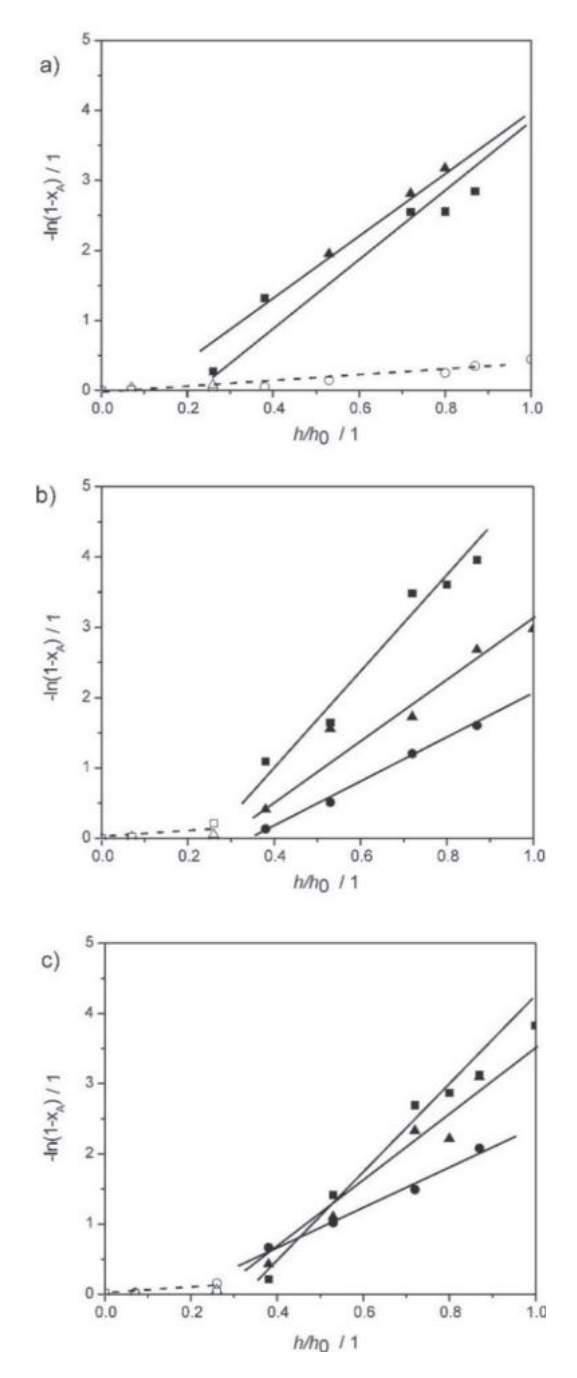


Figure 13.30 The linear dependence of $-\ln(1-x_A)$ on the normalized reactor height at different methanol/lard molar ratios: a) 4.5:1, b) 6.0:1, and c) 7.5:1 (catalyst loading, % of waste lard: 0.50 - circles, 0.75 - triangles and 1.00 - squares; mass transfer-controlled regime: open symbols and chemical reaction-controlled regime: black symbols) (Miladinović et al., 2019).

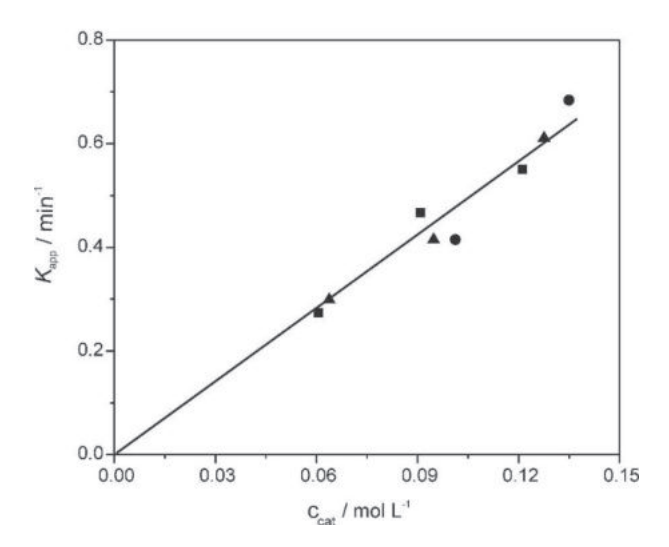


Figure 13.31 Dependence of apparent reaction rate constant on the catalyst concentration for different methanol/lard molar ratios: $4.5:1 - \blacksquare$, $6.0:1 - \blacktriangle$, and $7.5:1 - \blacksquare$) (Miladinović et al., 2019).

for homogeneous alkali-catalyzed methanolysis (Noureddini and Zhu, 1997). This model accounts for the effect of fatty acid methyl ester concentration on the reaction rate, as fatty acid methyl esters act as cosolvents that improve interfacial contact and enhance triacylglycerol mass transfer. Integrated into the steady-state mass balance of the plug flow reciprocating plate reactor, the model yields Equation (13.36) (Miladinović et al., 2015):

$$\left(-\frac{dc_A}{d\tau}\right) = k_m \cdot \frac{c_A}{K + c_A} \cdot \left(c_{R0} + c_R\right) \tag{13.36}$$

where $k_{\rm m}$ is the apparent reaction rate constant, K is the model parameter that takes the triacylglycerol affinity to the catalytical species (methoxide ions) into account, $c_{\rm A}$ is the concentration of triacylglycerols, $c_{\rm R}$ is the concentration of fatty acid methyl esters, and $c_{\rm R0}$ is the hypothetic initial concentration of fatty acid methyl esters that corresponds to the initially available catalytical species near the interfacial area, which is introduced to avoid the fact that $c_{\rm R} = 0$ for $\tau = 0$.

If c_A and c_F are expressed in terms of x_A , Equation (13.34) can be transformed as follows:

$$\frac{dx_{A}}{d\tau} = k_{m} \cdot \frac{(1 - x_{A}) \cdot (c_{R0} + 3 \cdot c_{A0} \cdot x_{A})}{K + c_{A0} \cdot (1 - x_{A})}$$
(13.35)

For the heterogeneous regime, where $K \le c_A$, a simplified Equation is obtained:

$$\frac{dx_A}{d\tau} = k_m \cdot \left(\frac{c_{R0}}{c_{A0}} + 3x_A\right) \tag{13.36}$$

The parameters in Equations (13.35) and (13.36) are determined from experimental data using Polymath software. This software is also used to calculate x_A -values along the reactor height, which are then employed to compute c_A and c_R (= $3c_{A0}x_A$).

After calculating the parameters from Equation (13.36), they were normalized by the initial methanol concentration ($k_{\rm m}/c_{\rm B0}$ and $K/c_{\rm B0}$) and then correlated with catalyst concentration (Miladinović et al., 2014). Figure 13.32 demonstrates linear relationships between $k_{\rm m}/c_{\rm B0}$, $K/c_{\rm B0}$, and catalyst concentration, with slopes indicating

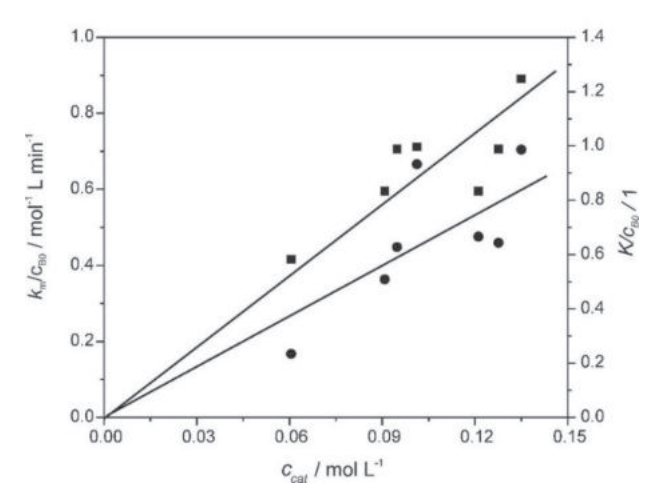


Figure 13.32 The linear dependences of $k_{\rm m}/c_{\rm B0}$ (\bullet) and $K/c_{\rm B0}$ (\blacksquare) on the catalyst concentration for all methanol/lard molar ratios ($R^2 = 0.95$ and 0.98, respectively).

the reaction rate constant ($k_2 = 4.54 \text{ L}^2/(\text{mol}^2 \text{ min})$) and modified triacylglycerol affinity for catalytical species (K' = 8.73 L/mol). Notably, the k_2 -value for the waste lard methanolysis in the reciprocating plate reactor is approximately a hundred times higher than that (0.045 $\text{L}^2/(\text{mol}^2 \text{ min})$) observed for the quicklime-catalyzed methanolysis of sunflower oil in a stirred batch reactor at 60 °C (Miladinović et al., 2014).

Figure 13.33 illustrates the dependence of the parameter c_{R0} on the methanol/lard molar ratio and catalyst concentration. At a constant methanol/lard molar ratio, this parameter increases with catalyst concentration up to about 0.10 mol/L, then levels off despite further catalyst addition. Conversely, as the methanol/lard molar ratio increases, this parameter decreases due to dilution of the reaction mixture, which lowers the catalyst concentration.

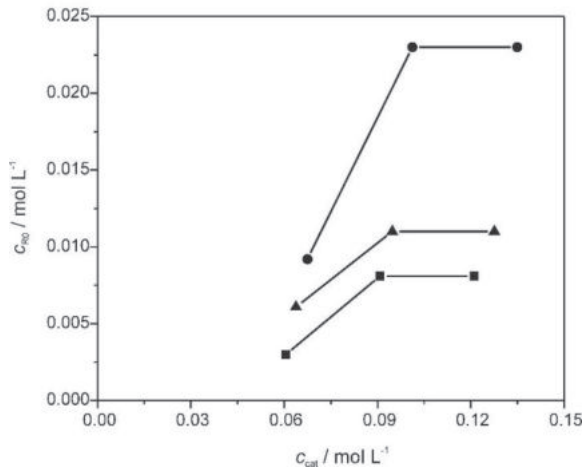


Figure 13.33 The variation of c_{B0} with catalyst concentration at various methanol/lard molar ratios: $4.5:1 - \bullet$, $6.0:1 - \blacktriangle$, and $7.5:1 - \blacksquare$.

Simulation of triacylglycerol and fatty acid methyl ester variation: For the lowest potassium hydroxide concentration (0.5% of waste lard) and the lowest methanol/lard molar ratio (4.5:1), where the reaction rate is limited by triacylglycerol mass transfer, Equations (13.25) and (13.36) were used to calculate x_A , c_A , and c_R . Figures 13.34a and 13.35a compare the actual and predicted values of c_A and c_R , showing acceptable agreement with MRPD values of $\pm 25.2\%$ and $\pm 15.9\%$, respectively. For other conditions, x_A was calculated using Equations (13.25), (13.27), and (13.35).

As shown in Figures 13.34b, 13.34c, 13.35b, and 13.35c, the models fit the experimental data well under different conditions (catalyst loading of 0.75% and 1.00% of waste lard and methanol/lard molar ratios of 6.0:1 and 7.5:1), with lower MRPD values of $\pm 9.2\%$ and $\pm 11.8\%$ for the pseudo-first-order reaction and the model incorporating changing mechanisms with mass transfer. Figures 13.34 and 13.35 also show that the fatty acid methyl ester content increases more in the middle part of the reactor than in the upper part ($h/h_0 > 0.70$), where the increase in fatty acid methyl ester content is less than 2%. Similar behavior was observed during the palm oil methanolysis in a liquid-liquid film reactor (Narváez et al., 2009).

The same model was validated for sunflower oil methanolysis in the same reciprocating plate reactor at a 6:1 methanol/oil molar ratio, 20 °C, and 1.0% potassium hydroxide as indicated by a low MRPD of $\pm 6.4\%$ (Banković–Ilić et al., 2015). The model's validity with waste and sunflower oil suggests its broader applicability for modeling the kinetics of various transesterification reactions.

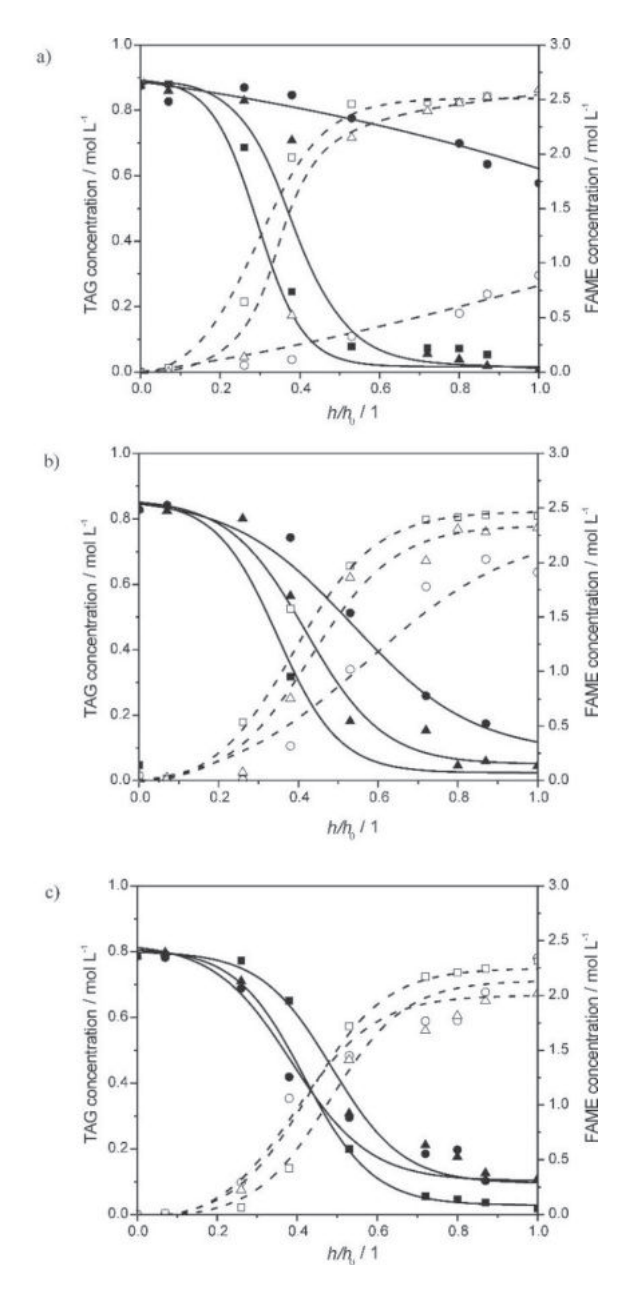


Figure 13.34 Comparison of experimental and predicted values of triacylglycerols (black symbols) and fatty acid methyl esters (open symbols) concentration calculated by two correlations describing the triacylglycerol mass transfer and chemical reaction rates at different methanol/lard molar ratios (a) 4.5:1, (b) 6.0:1, and (c) 7.5:1 (simulation: triacylglycerols – solid lines, fatty acid methyl esters – dash lines; catalyst loadings, % of waste lard: 0.5 – circles, 0.75 – triangles and 1.0 – squares).

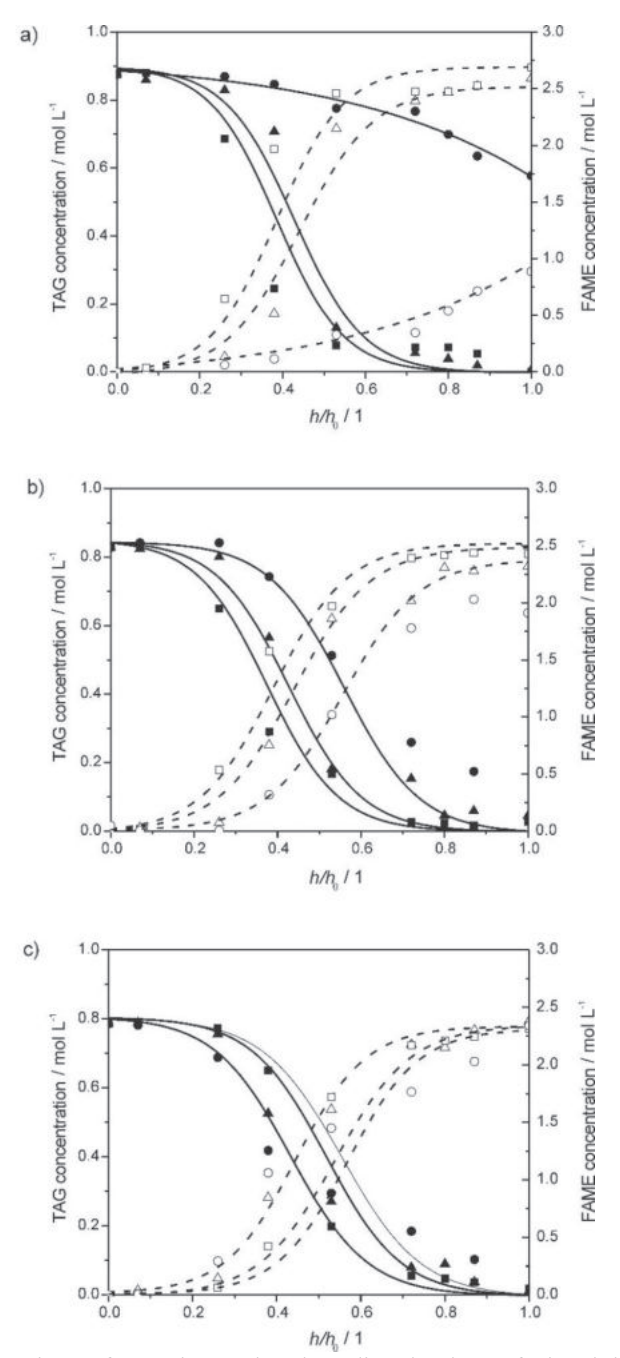


Figure 13.35 Comparison of experimental and predicted values of triacylglycerols and fatty acid methyl ester concentration calculated by kinetic model for overall reaction at different methanol/lard molar ratios: (a) 4.5:1, (b) 6.0:1, and (c) 7.5:1 (simulation: triacylglycerols – solid lines, fatty acid methyl esters – dash lines; catalyst loadings, % of waste lard: 0.5 – circles, 0.75 – triangles and 1.0 – squares).

13.1.7. Comparison of reciprocating plate reactors with other reactor types

Comparing the performance of the reciprocating plate reactor with other reactor types and the catalytic capabilities of potassium hydroxide versus other catalysts (sodium hydroxide, quicklime) in methanolysis under similar conditions is insightful. Table 13.10 summarizes the conversion (or ester yields), capacity, and operating conditions across various reactors, including stirred (Da Cunha et al., 2009), reciprocating plate (Banković–Ilić et al., 2015; Stamenković, 2014; Stamenković et al., 2010a), ultrasonic (Stavarache et al., 2007), zigzag micro-channel (Wen et al., 2009), metal foam (Yu et al., 2010), and packed bed (Miladinović et al., 2015; Stojković et al., 2016b) reactors.

The reciprocating plate reactor used for the waste lard methanolysis under optimal conditions achieved a fatty acid methyl ester content of 96.2% with a capacity of 120 kg/day. In comparison, a batch pilot reactor for the potassium hydroxide-catalyzed methanolysis of beef tallow had a higher capacity (800 kg/day) and similar conversion (>95%) but required a longer reaction time (3 h) with slightly higher catalyst concentration and temperature (Da Cunha et al., 2009). Although ultrasonic irradiation in a tubular reactor offers benefits at lower temperatures (38–40 °C) (Stavarache et al., 2007), it requires a higher methanol/oil molar ratio (7.5:1 for edible oil, 6.0:1 for palm oil) and longer residence time (30 min) to achieve fatty acid methyl ester content over 95% than the process in the reciprocating plate reactor.

A zigzag micro-channel reactor achieved higher reaction efficiency (99.5% fatty acid methyl ester yield in 28 s) than the reciprocating plate reactor under optimal conditions, likely due to more intensive mass transfer from micro-scale static mixing (Wen et al., 2009). However, its capacity (0.28 kg/day) is significantly smaller, requiring many reactors to match the reciprocating plate reactor output. The metal foam reactor also reduces residence time (3.26 min) for a high ester yield (95.2%) at an increased methanol/oil molar ratio (10:1) but has a smaller capacity (13.2 kg/day) (Yu et al., 2010).

The reciprocating plate reactor's shorter residence time and higher production capacity are advantages over a packed-bed reactor for waste lard methanolysis (Stojković et al., 2016b). However, it has a drawback in methyl ester separation from potassium hydroxide. At a lower temperature (20 °C), the potassium hydroxide-catalyzed sunflower oil methanolysis in the same reciprocating plate reactor yielded a lower fatty acid methyl ester content (78–80%) under identical conditions (Banković–Ilić et al., 2015). In contrast, fatty acid methyl ester content of over 99% was achieved using two reciprocating plate reactors in series with a gravitational separator between them (Stamenković et al., 2013).

Table 13.10 Comparison of various reactor and catalyst types for biodiesel production from various feedstocks with methanol.

Reactor (i.d., cm)/ process type	Feedstock	Methanol/ feedstock molar ratio	Catalyst/ loading, % of feedstock	Temperature, °C	Conversion (yield), %/ residence time, min	Capa- city, kg/day	Reference
RPR (2.54)/ continuous	Waste lard	4.5:1	KOH/1.0	60	96.2/10	120	Miladinović et al. (2019)
RPR (2.54)/ continuous	Sunflower oil	6:1	KOH/1.0	20	78–84/13	98	Banković– Ilić et al. (2015)
RPR (2.54), two in series/ continuous	Sunflower	6:1	KOH/1.0	30	80/12 ^a 100/30 ^b	98 ^a 42 ^b	Stamenković et al. (2013)
Pilot RPR (16)/ continuous	Rapeseed oil	6:1	KOH/1.0	30	73.6/13	70°	Stamenković et al. (2010c)
Pilot stirred/ batch	Beef tallow	6:1	KOH/1.5	65	>95/180 ^d	800	Da Cunha et al. (2009)
Ultrasonic tubular/ continuous	Palm oil	6:1	KOH/-	38–40	95/20	165	Stavarache et al. (2007)
Zigzag micro- channel/ continuous	Soybean oil	9:1	NaOH/1.2	56	(99.5)/ 0.5	0.28	Wen et al. (2009)
Zigzag metal foam/ continuous	Soybean oil	10:1	NaOH/ 1.0	55	(95.2/3.26	13.2	Yu et al. (2010)
Packed bed (3)/ continuous	Sunflower oil	6:1–18:1	Quicklime bits	60	98.5/60 -120	2.1	Miladinović et al. (2015)
Packed bed/ continuous	Waste lard	6:1	Quicklime bits	60	>96.5/60	3.6	Stojković et al. (2016b)

^a The first reactor in the series; ^b The second reactor in the series; ^c dm³/h. ^d Reaction time.

Mass transfer resistance in the inlet part of the reciprocating plate reactor slows the transesterification reaction due to the immiscibility of waste lard and methanol (Stamenković et al., 2010a). This resistance results in large methanol droplets and a small specific interfacial area, leading to slow triacylglycerol mass transfer, which limits the reaction rate. Improving methanol dispersion in the initial part of the reciprocating plate reactor can enhance performance. Inserting inert packing in the

interplate spaces intensifies mixing and reduces mass transfer resistance. The positive effects of added spheres (Aleksić, 2006; Banković–Ilić et al., 2001a, 2001b), Rashig rings (Aleksić, 2006; Sundaresan and Varma, 1990b), and pall rings (Prabhavathy et al., 1996) on mass transfer in reciprocating plate reactors have been demonstrated for both gas-liquid and liquid-liquid systems. This approach was successful in the rapeseed oil methanolysis in a 16 cm i.d. reciprocating plate reactor with spherical packing in interplate spaces, achieving a fatty acid methyl ester content of 98% (Stamenković et al., 2010c).

13.2.8. A short overview of other applications of reciprocating plate reactors in Serbia

Besides biodiesel production at laboratory and pilot levels (Banković-Ilić et al., 2015; Miladinović et al., 2019; Stamenković, 2014; Stamenković et al., 2010a, 2014), reciprocating plate reactors have been used in Serbia to study biosyntheses of dextransucrase, dextran (Veljković, 1985; Veljković et al., 1990), and ethanol (Nikolić, 2013).

A 2.54 cm i.d. reciprocating plate column was used as a bioreactor for alcoholic fermentation of a glucose medium (40 g/L) with *Saccharomyces cerevisiae* immobilized on macroporous polymer particles ($\varepsilon_s = 0.236$) at 30 °C and a liquid flow rate of ~1.2 L/day (Nikolić, 2003). The dispersion model was validated by comparing predicted and measured glucose concentrations at the bioreactor exit. Axial dispersion did not affect glucose conversion with zero-order kinetics, but positively influenced glucose conversion and ethanol yield under Monod kinetics.

Furthermore, the biosynthesis of dextransucrase by *Leuconostoc mesenteroides* Zdravlje S-P strain was investigated in a 2.5 cm i.d. reciprocating plate column, a bubble column, and a stirred vessel at 25 °C (Veljković, 1985; Veljković et al., 1990). Maximum power consumption was calculated from the maximum pressure variation at the reactor bottom (Veljković and Skala, 1986), and volumetric oxygen mass transfer was determined using a dynamic method during aerobic microbial growth (Veljković and Skala, 1988). The reciprocating plate column showed the highest aeration capacity among the bioreactors for the same specific power consumption and at a much lower superficial gas velocity (Veljković et al., 1990). However, this capacity exceeded the optimal level for maximum enzyme biosynthesis, leading to the selection of the aerated stirred tank bioreactor for dextransucrase production (Veljković, 1985; Veljković et al., 1990).

13.2 Oscillatory flow reactors in biodiesel production

13.2.1. Reactor design and flow regime

Oscillatory flow reactors represent a subtype of continuous plug flow reactors characterized by equally spaced orifice plate baffles within a tube, as illustrated in Figure 13.36. Oscillatory flow within the reactor is commonly created by a piston, which induces a pulsed flow that creates eddies in the vicinity of the baffles, thereby improving heat transfer and mixing around the baffles (Harvey et al., 2001; Law et al., 2018; Mackley and Stonestreet, 1995). As the piston advances, turbulence is generated in the upstream direction through the orifices, while as the piston retracts, turbulence occurs downstream below the baffles.

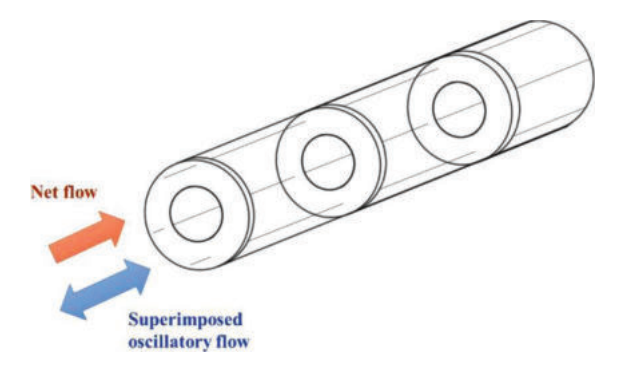


Figure 13.36 Oscillatory flow reactor with the most commonly used sharp-edged orifice baffles: oscillatory flow is superimposed on bulk flow by a piston (Harvey et al., 2003).

Unlike conventional tubular reactors, where mixing depends on net flow, oscillatory flow reactors achieve independent mixing behavior. This unique design enables them to exhibit plug flow characteristics even under laminar flow conditions, allowing for significantly shorter reactor lengths compared to conventional plug flow reactors. This reduction in length/diameter ratio extends residence times effectively. Additionally, oscillatory flow reactors offer reduced power consumption relative to equivalent stirred tank reactors (Abbott et al., 2014). Moreover, their scalable design suggests the potential for direct translation to large-scale production without the need for intermediate scale-up trials (Masngut et al., 2010). Furthermore, oscillatory flow reactors feature narrow residence time distributions, facilitating staged additions and customizable parameter profiles along their length (Masngut et al., 2010).

The mechanism of eddy formation in oscillatory flow reactors has been well-documented in the literature (Brunold et al., 1989; Gough et al., 1997; Mazubert et al., 2016a; McDonough et al., 2015; Ni et al., 2002). Typical flow patterns in

continuous oscillatory flow reactors equipped with orifice baffles are shown in Figure 13.37. During flow acceleration (Figure 13.37a), eddies form downstream of the baffles, causing flow separation. As the oscillatory velocity increases (Figure 13.37b), these eddies fill the baffle cavity. In the flow reversal phase (Figure 13.37c), the eddies detach, creating a free vortex that is engulfed by the bulk flow and interacts with vortices from previous cycles (Figure 13.37d), before the cycle repeats.

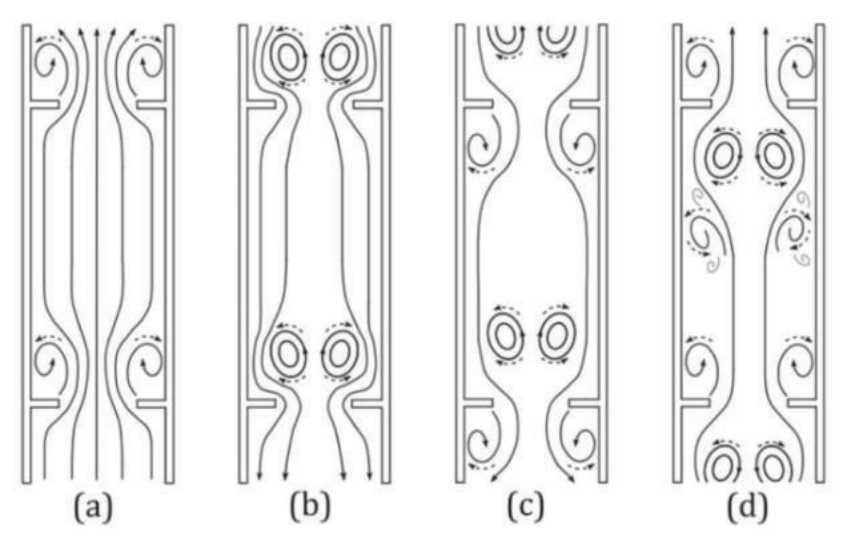


Figure 13.37 Eddy formation in a continuous oscillatory flow reactor equipped with orifice baffles (McDonough et al., 2015).

Several baffle designs are used in the research of oscillatory flow reactors (Avilaa et al., 2022), as shown in Figure 13.38. These include the most common sharp-edged single-orifice plates (Figure 13.38), along with periodic smooth constrictions (mesoscales), multi-orifice plates, disc-and-doughnut configurations, various helical forms (e.g., round wires, sharp-edged and alternating ribbons, double ribbons with a central rod), central disc baffles, and wire wool.

The geometrical parameters of oscillatory flow reactors influence the shape and size of the vortices generated, which need sufficient space to fully expand in each baffle cavity. The primary design parameters for oscillatory flow reactors are based on the single orifice baffle design. Table 13.11 lists the most commonly used values, now often considered standard design guidelines. However, it is important to note that these values were defined under specific conditions from the original studies and have not been optimized for a wide range of operating conditions or applications (Avilaa et al., 2022).

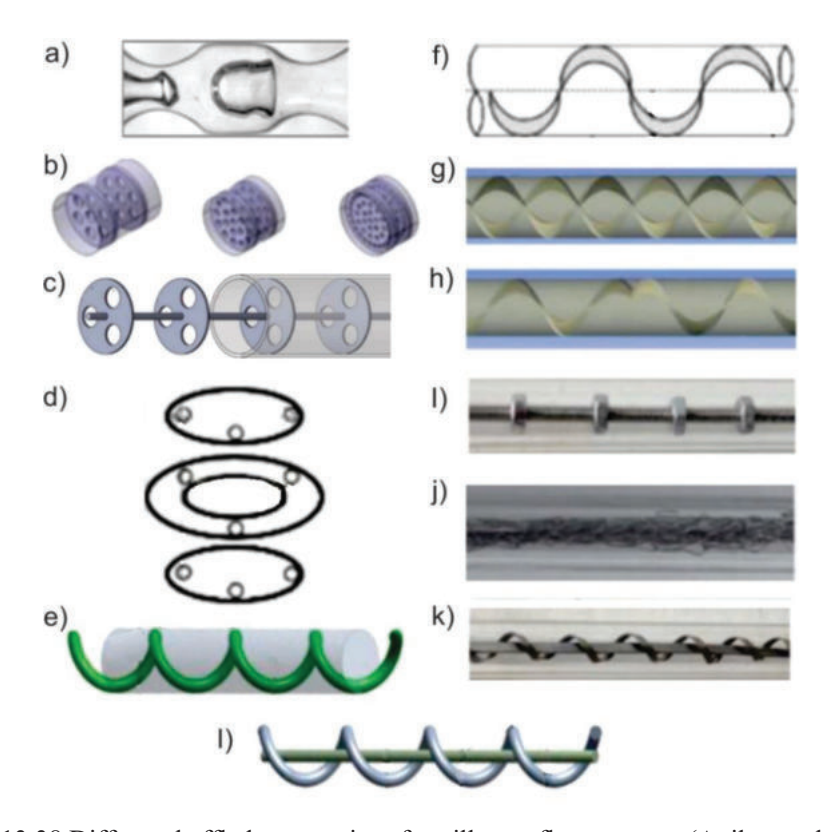


Figure 13.38 Different baffled geometries of oscillatory flow reactors (Avilaa et al., 2022).

Table 13.11 Main geometrical parameters of oscillatory flow reactor design.

Parameter	Symbol	Most common values
Reactor diameter	D_{c}	15–150 mm
Baffle spacing	h	$1.5 D_{\rm c}$
Baffle orifice diameter	d_{o}	$0.45 – 0.5 D_{c}$
Fractional free baffle area (%)	${\cal E}$	20–25
Baffle thickness	δ	2–3
Oscillation amplitude	A	0.25–0.6 h

13.2.2. Overview of previous research on biodiesel production in oscillatory flow reactors

The results from previous studies on biodiesel production in oscillatory flow reactors, summarized in Table 13.2, indicate that near-complete conversion can be achieved in relatively short residence times. These studies predominantly use vegetable oils like rapeseed and sunflower oil, as well as waste cooking oil, as

feedstocks. Methanol is exclusively used, with alcohol/oil molar ratios ranging from 3:1 to 18:1, depending on the catalyst and feedstock, but most frequently at a 6:1 ratio. Alkali catalysts, primarily potassium hydroxide at a dosage of about 1% of the oil, are commonly employed to accelerate transesterification reactions, typically at 60 °C, whereas 4-dodecylbenzenesulfonic acid has been used as an acid catalyst (Al-Saadi et al., 2019). Some studies also utilize heterogeneous catalysts, such as basic mixed CaO/MgO (Ali et al., 2022, 2023) and calcined date seeds (Khelafi et al., 2022), as well as an acid sulfonated glucose catalyst (Kefas et al., 2019). Masngut et al. (2010) reported that biodiesel production directly from oilseeds like rapeseed, jatropha, and pongamia was investigated using in situ transesterification and examining the suspension characteristics of rapeseed particles in oscillatory flow reactors. However, no experimental results were provided.

Residence times vary from 60 seconds to 120 minutes, influenced by the type of catalyst, feedstock, and the reactor's design, geometry, and operational conditions. Notably, in advanced systems combining oscillatory flow reactors with cold plasma or hydrodynamic systems, residence times can be as short as 90 seconds (Taki et al., 2023, 2024). To optimize operational variables, some studies employ response surface methodology with Box-Behnken design (Al-Saadi et al., 2019, 2020; Kouhifaiegh et al., 2024; Soufi et al., 2017; Taki et al., 2022, 2023, 2024), one-factor-at-a-time methods (Ali et al., 2022; Kefas et al., 2019; Syam et al., 2012), and occasionally ANN modeling (Ali et al., 2023). Additionally, incurring low capital and running costs, mesoscale oscillatory flow reactors are particularly suitable for screening tests and determining optimal operating conditions of transesterification systems reactions (Al-Saadi et al., 2019; Phan et al., 2011; Zheng et al., 2007).

This configuration is particularly advantageous for multiphase reactions such as the transesterification process used in biodiesel production (García-Martín et al., 2018; Kefas et al., 2019; Soufi et al., 2017) because the recirculation flow increases the interfacial area in the liquid phase, which consequently enhances the rate of mass transfer. Moreover, an oscillatory flow reactor provides better yields along with high oscillation amplitudes and low Strouhal numbers (Harvey et al., 2003; Zheng et al., 2007). Distinct baffle configurations also showed good multiphase contact and high mass transfer rates, allowing for diverse applications (McDonough et al., 2015).

Oscillatory flow reactors (OFRs) have the potential to achieve higher biodiesel yields compared to stirred tank reactors (García-Martín et al., 2018). Additionally, similar conversions can be attained between batch and continuous mesoscale OFRs and batch-stirred tank reactors, often within approximately the same reaction times (Zheng et al., 2007). However, a significant drawback of OFRs is the absence of an integrated separation unit for the final products (Phan et al., 2011). Despite their

advantages, including enhanced mixing intensity, improved heat and mass transfer, and higher biodiesel yields, the complex design of OFRs remains a barrier to commercial application. Furthermore, achieving optimal mixing in OFRs requires large reactor dimensions, which adds another layer of complexity (Masngut et al., 2010).

Among various baffle designs, the smooth constriction geometry has been shown to achieve the highest biodiesel yield (82%), outperforming the wire wool baffle and sharp-edged helical baffle with a central rod (74–76%). This design enables stable conversion rates and better process performance, reaching a steady state 33% faster than the other baffle geometries (Harvey et al., 2003; Mazubert et al., 2014; Phan et al., 2012). A higher velocity ratio, which represents the relationship between oscillatory and net flow, is necessary for effective liquid-liquid dispersion (Al-Saadi et al., 2019; Mazubert et al., 2015; Phan et al., 2012).

For example, the sharp-edged helical baffles have demonstrated superior biodiesel yields compared to the coiled wire helical baffles due to their higher shear rates, which enhance liquid-liquid phase mixing (Phan et al., 2011). Additionally, the helical and alternating helical baffles offer improved plug flow behavior compared to the single orifice and disc-and-doughnut baffles while maintaining significant shear strain rates, crucial for droplet breakup (Mazubert et al., 2016a,b). However, vortical flow is less pronounced in the alternating helical blade, with streamlines from the inlet occupying less reactor volume, suggesting less efficient flow turnover near the walls, which could potentially hinder heat transfer (Mazubert et al., 2016a).

13.2.3. Analysis of homogeneous transesterification reactions

These studies collectively demonstrate the potential of oscillatory flow reactors in biodiesel production, offering advantages such as reduced reaction times and improved yields through enhanced mixing and mass transfer.

13.2.3.1. Base catalysis

Harvey et al. (2003) pioneered transesterification in continuous oscillatory flow reactors with single-orifice baffles using methanol and rapeseed oil. Operating at temperatures of 50°C and 60°C with a methanol/oil molar ratio of 1.5:1 and a methanol/sodium hydroxide mass ratio of 24.4:1, they achieved over 99% conversion to methyl esters meeting EU biodiesel standards. Their residence times of 10 min and 20 min at 50 °C and 60 °C were significantly shorter compared to traditional stirred batch reactors (at least 75% lower).

In early studies, researchers compared the performance of batch and continuous oscillatory flow meso reactors with stirred tank reactors. Zheng et al. (2007) examined this in the alkali-catalyzed transesterification of refined vegetable oil. They observed comparable biodiesel yields across all three reactor types. The continuous oscillatory flow reactor, operating at 60°C with a 4.2% sodium methoxide solution in methanol at a flow rate of 126 mL/h, achieved nearly complete conversion to biodiesel. The study concluded that this reactor is well-suited for continuous laboratory-scale biodiesel production. Similarly, García-Martín et al. (2018) compared a batch-mode oscillatory flow reactor with a stirred tank reactor for biodiesel production from waste cooking oil using 1% sodium hydroxide. The oscillatory flow reactor outperformed the stirred tank reactor, achieving a 72.5% ester yield in half the time. Optimal conditions of the oscillatory flow reactor included a 6:1 methanol/oil molar ratio, 0.67 Hz oscillation frequency, and a 30minute residence time, resulting in a maximum ester yield of 78.8%. Increasing oscillation frequency and Reynolds number further improved ester yield by enhancing mass and heat transfer. The biodiesel's composition and properties were independent of the reactor type.

Phan et al. (2011, 2012) explored continuous transesterification in mesoscale oscillatory flow reactors, focusing on various baffle designs (integral, wire wool, and helical baffles) and using potassium hydroxide and sodium methoxide catalysts. They found that potassium hydroxide provided slightly higher conversions (97% vs. 94–96%) and faster reaction times (5 min vs. 5–10 min) (Phan et al., 2012). The induction time decreased with increasing oscillatory Reynolds number, achieving stable steady states in 1.5 to 4.0 residence times, depending on the baffle type. Optimal residence times were crucial, as longer times reduced ester content due to saponification. A conversion higher than 95 % was achieved in a residence time lower than 5 min. To improve mixing, reactors were designed with sharp-edged helical baffles fixed on a central rod, which outperformed standard helical baffles by enhancing shear force and reducing phase separation (Phan et al., 2011). This design generated faster and more uniform mixing at low flow rates and low oscillatory Reynolds numbers.⁵ The resulting ester yields ranged from 70% to 90%, depending on operational conditions, with a conversion exceeding 95% in 5 min and consistent methyl ester quality.

-

$$Re_o = \frac{2\pi A f \rho_1 D_c}{\mu_1}$$

⁵ The oscillatory Reynolds number describes the intensity of mixing in the reactor:

Several research groups (Al-Saadi et al., 2020; Kouhifaiegh et al., 2024; Mazubert et al., 2014; Muhammed Niyas et al., 2023; Santikunaporn et al., 2020; Soufi et al., 2017; Syam et al., 2012; Taki et al., 2022) further investigated parameters such as temperature, catalyst type, and residence time in continuous oscillatory flow reactors, showing improvements in biodiesel yield and process efficiency compared to conventional reactors. For instance, Syam et al. (2012) optimized the transesterification of pre-treated jatropha oil with methanol in a continuous oscillatory flow reactor with annular baffles. They evaluated the effects of temperature, catalyst type, and methanol/oil molar ratio on biodiesel yield. The optimal conditions— a 6:1 methanol/oil molar ratio, 1% potassium hydroxide, and 60°C—achieved a 99.7% ester yield in just 10 min. Similarly, Kouhifaiegh et al. (2024) conducted optimization studies on the continuous production of biodiesel from sunflower oil, varying parameters such as methanol/oil molar ratio, temperature, reactor length, and catalyst concentration. Their findings identified optimal conditions: operating at 51°C with an 8.5:1 methanol/oil ratio, 1% potassium hydroxide catalyst concentration, and utilizing a 3-meter reactor. These conditions achieved an actual conversion rate of 89%, closely aligned with the predicted 92%. Soufi et al. (2017) investigated the impact of oscillation frequency, baffle spacing, and temperature on ester yield in a 1% potassium hydroxide-catalyzed transesterification of waste cooking oil over a 5-minute reaction period. They found temperature to be the primary factor affecting ester yield, while interbaffle spacing had no significant impact. The highest yield of 81.9% was achieved at an oscillation frequency of 4.1 Hz, an interbaffle spacing of 5 cm, and 60 °C, though similar yields were also attainable with different spacings.

Al-Saadi et al. (2020) optimized the homogeneous base transesterification of refined and low-grade rapeseed oils. For refined rapeseed oil, they achieved 99% conversion with a 13:1 methanol/oil molar ratio, 0.5% catalyst, 50 °C, and 16 minutes residence time. For low-grade oil, 90% conversion was attained with an 18:1 methanol/oil molar ratio, 2% catalyst, 50 °C, and 4.25-minute residence time. Techno-economic analysis using Aspen HYSYS indicated that the single-step process for low-quality rapeseed oil was more cost-effective than the conventional process with refined oil or the two-step process with waste cooking oil.

Moreover, biodiesel production from waste cooking oils was studied at low temperatures and varying operational variables (Mazubert et al., 2014; Santikunaporn et al., 2020; Taki et al., 2022). Mazubert et al. (2014) achieved 92.1% conversion in 6 min with a 6:1 methanol/oil molar ratio and 1% potassium hydroxide catalyst at 40 °C, comparable to batch reactor results (95% in 10 min) but achieved more quickly due to improved mixing. Santikunaporn et al. (2020) found that

residence time and methanol/oil molar ratio significantly impacted ester content at 65 °C. Optimal conditions were a 60-second residence time, 3.0% potassium hydroxide loading, and an 11:1 methanol/oil molar ratio. Taki et al. (2022) found that among the studied variables—temperature, catalyst amount, residence time, and methanol/oil molar ratio—the methanol/oil ratio had minimal impact on methyl ester conversion. Increasing this ratio decreased reaction efficiency. Longer reactor lengths and increased baffling enhanced mixing and prolonged residence time, thereby improving efficiency. The highest biodiesel conversion achieved was 74.5%. Specifically, Muhammed Niyas et al. (2023) found that a solar-powered rotating flask oscillatory flow reactor achieved a 93.7% ester yield from coconut waste cooking oil in 30 min, comparable to the yield in the stirred tank reactor, which took 60 min.

13.2.3.2. Acid catalysis

Acid catalysts have rarely been used in biodiesel production in oscillatory flow reactors. Only Al-Saadi et al. (2019) studied the effects of operating conditions, including methanol/oil molar ratio, catalyst/oil molar ratio, and residence time, on methyl ester production from rapeseed oil using 4-dodecylbenzenesulfonic acid as the catalyst. Complete conversion was achieved at 60°C using optimal conditions: methanol/oil molar ratio of 10:1 with a catalyst concentration of 0.99 M for a 60-minute residence time, or a methanol/oil molar ratio of 6.5:1 with a catalyst concentration of 0.5 M for a 120-minute residence time.

13.2.4. Analysis of heterogeneous transesterification reactions

13.2.4.1. Base catalysis

Heterogeneous base catalysis in oscillatory flow reactors has been studied far less than homogeneous catalysis (Ali et al., 2022, 2023; Khelafi et al., 2022). Khelafi et al. (2022) found that an oscillatory flow reactor outperformed a stirred tank reactor in sunflower oil transesterification with methanol, catalyzed by calcined data seed at lower agitation speeds, but the stirred tank reactor was more effective at higher speeds. To reduce biodiesel production costs, Ali et al. (2022) developed a CaO/MgO catalyst from calcined low-cost natural dolomite and used it to transesterify oleic acid at a 6:1 methanol/oil ratio. Optimal conditions (60°C, 4.3 Hz, 8 mm amplitude, 40 min residence) achieved 96% conversion, outperforming a stirred tank reactor (77.4% at 60°C, 40 min). However, an ANN model predicted a 98.6% conversion under slightly adjusted conditions (Ali et al., 2023).

13.2.4.1. Acid catalysis

Kefas et al. (2019) studied biodiesel production from palm fatty acid distillate (over 90% free fatty acid) and methanol using a modified sulfonated glucose catalyst in a continuous oscillatory flow reactor. Optimal conditions—9:1 methanol/oil molar ratio, 2.5% catalyst loading, 60 °C, 50 min residence time, and 6 Hz oscillation frequency—resulted in 97% conversion and 94.2% ester yield. The catalyst maintained about 80% conversion after four reuse cycles.

13.2.5. Advanced oscillatory flow reactor technology

Advancements in biodiesel production technologies are aimed at achieving higher conversion rates and shorter reaction times through several key strategies. These include refining reactor design, optimizing reaction conditions such as catalyst selection, and improving mixing techniques. In addition to optimizing transesterification conditions, innovations in reactor technology have shown promise in accelerating reactions and enhancing conversion efficiency. For example, recent studies have investigated innovative methods, such as integrating an oscillatory flow reactor with a hydrodynamic reactor (Taki et al., 2023) or employing cold plasma pretreatment of the reactants before entering the reactor (Taki et al., 2024).

Taki et al. (2023) demonstrated the effectiveness of a combined oscillatory-hydrodynamic reactor in producing biodiesel from sunflower oil. Initially, increasing residence time led to higher biodiesel conversion rates, albeit reaching a plateau due to the reaction's reversibility. In contrast, using only the oscillatory flow reactor resulted in a lower conversion of 74.5%. However, by atomizing reactants with a plasma jet (20 kV, 20 kHz) before introducing them into the reactor, conversion rates improved significantly, reaching 94.6% under optimal conditions (Taki et al., 2024). The study highlighted key operational variables such as methanol/oil ratio, catalyst loading, plasma exposure time, and residence time, which critically influence biodiesel production efficiency. Therefore, coupling an oscillatory flow reactor with either upstream plasma pretreatment or downstream hydrodynamic reactors holds great promise for significantly enhancing biodiesel production efficiency. This approach offers substantial advantages over conventional reactor technologies.

REFERENCES

Abbott, M. S. R., Harvey, A. P., Valente Perez, G., Theodorou, M. K. (2013). Biological processing in oscillatory baffled reactors: operation, advantages and potential. Interface Focus 3, 20120036. https://doi.org/10.1098/rsfs.2012.0036.

Abbott, M. S. R., Valente Perez, G., Harvey, A. P., Theodorou, M. K. (2014). Reduced power consumption compared to a traditional stirred tank reactor (STR) for enzymatic saccharification of alpha-cellulose using oscillatory baffled reactor (OBR) technology. Chemical Engineering Research and Design **92**, 1969–1975. https://doi.org/10.1016/j.cherd.2014.01.020.

Adewale, P., Dumont, M.–J., Ngadi, M. (2015). Enzyme–catalyzed synthesis and kinetics of ultrasonic–assisted biodiesel production from waste tallow. Ultrasonic Sonochemistry **27**, 1–9.

Adewale, P., Dumont, M.–J., Ngadi, M. (2016). Enzyme-catalyzed synthesis and kinetics of ultrasonic assisted methanolysis of waste lard for biodiesel production. Chemical Engineering Journal **284**, 158–165. https://doi.org/10.1016/j.cej.2015.08.053.

Akita, K., Yoshida, F. (1974). Bubble size, interfacial area and liquid-phase mass transfer coefficient in bubble columns. Industrial and Engineering Chemistry Process Design and Development 13, 84–91. https://doi.org/10.1021/i260049a016.

Al Taweel, A. M., Landau, J., Boyle, J., Gomaa, H. G. (1995). Operational characteristics of a novel reciprocating plate multi-phase contactor. Transactions of the Institution of Chemical Engineers **73**, 707–712.

Aleksić, M. (2006). Hydrodynamic and mass-transfer characteristics of a multiphase reciprocating plate reactor [Hidrodinamičke i maseno-prenosne karakteristike višefaznog reaktora sa vibracionom mešalicom]. Doctoral dissertation, University of Niš, Niš, Serbia (in Serbian). https://doi.org/10.2298/HEMIND0210409A

Aleksić, M., Veljković, V. B., Banković-Ilić, I. B., Lazić, M. L., Skala, D. U. (2002a). The influence of Rashig rings and the rheological properties of the liquid phase on the pressure drop at the bottom of a reciprocating plate column. Hemijska Industrija **56**, 409–414. https://doi.org/10.2298/HEMIND0303107A

Aleksić, M., Veljković, V. B., Banković-Ilić, I. B., Lazić, M. L., Skala D. U. (2002b). Gas holdup in a gassed reciprocating plate column with Rashig rings placed in interplate spaces. Canadian Journal of Chemical Engineering **80**, 485–490. https://doi.org/10.1002/cjce.5450800318.

Aleksić, M., Veljković, V., Banković-Ilić, I., Lazić, M., Skala, D. (2003). Effects of Rashig rings placed in interplate spaces and the rheological properties of the liquid

- phase on power consumption in a gassed reciprocating plate column. Hemijska Industrija **57**, 107–113. https://doi.org/10.2298/HEMIND0303107A.
- Aleksić, M., Veljković, V., Banković-Ilić, I., Lazić, M., Skala, D. (2004). The effects of operating conditions on the gas holdup in a multiphase reciprocating plate column with Rashig rings placed in interplate spaces, 16th International Congress of Chemical and Process Engineering, CHISA, Prague, Czech Republic, CD-ROM of Full Texts 0755.pdf.
- Aleksić, M., Vasić, Lj., Banković-Ilić, I., Veljković, V., Lazić, M., Skala D. (2006). Correlation for volumetric mass transfer coefficient in a reciprocating plate column of different diameter, 5th International Conference of the Chemical Societies of the South-east European Countries, Book of Abstracts, 1, 213, Ohrid, Sept. 10–14
- Ali, M. M., Ahmed, S. M., Aqar, D. Y., Gheni, S. A., Abdullah, G. H., Mahmood, M. A., Habeeb, O. A., Harvey, A., Phan, A. N. (2022). Use of dolomite catalyst in biodiesel production via transesterification of waste cooking oil in oscillatory baffled reactor. AIChE J **68**, e17751. https://doi.org/10.1002/aic.17751.
- Ali, M. M., Gheni, S. A., Ahmed, S. M. R., Hmood, H. M., Hassan, A. A., Mohammed, H. R., Mohammed, S. T., Karakullukcu, N. T. (2023). Catalytic production of biodiesel from waste cooking oil in a two-phase oscillatory baffled reactor: Deactivation kinetics and ANN modeling study. Energy Conversion and Management 19, 100383. https://doi.org/10.1016/j.ecmx.2023.100383.
- Al-Masry, W. A., Dukkan, A. R. (1998). Hydrodynamics and mass-transfer studies in a pilot-plant airlift reactor: Non-Newtonian systems. Industrial Engineering and Chemical Research 37, 41–48. https://doi.org/10.1021/ie960378z.
- Al-Saadi, L. S., Alegría, A., Eze, V. C., Harvey, A. P. (2019). Rapid screening of an acid-catalyzed triglyceride transesterification in a mesoscale reactor, Chemical Engineering and Technology **42**, 539–548, https://doi.org/10.1002/ceat.201800203.
- Al-Saadi, L. S., Eze, V. C., Harvey, A. P. (2020). A techno-economic analysis based upon a parametric study of alkali-catalysed biodiesel production from feedstocks with high free fatty acid and water contents. Biofuels **13**, 401–413. https://doi.org/10.1080/17597269.2020.1727688.
- Anitescu, G., Deshpande, A., Tavlarides, L. L. (2008). Integrated technology for supercritical biodiesel production and power cogeneration. Energy and Fuel **22**, 1391–1399. https://doi.org/10.1021/ef700727p.
- Atapour, M., Kariminia, H.-R., Moslehabadi, P. M. (2014). Optimization of biodiesel production by alkali-catalyzed transesterification of used frying oil. Process Safety and Environmental Protection **92**, 179–185.
- Ataya, F., Dube, M. A., Ternan, M. (2006). Single-phase and two-phase base-catalyzed transesterification of canola oil to fatty acid methyl esters at ambient conditions. Industrial and Engineering Chemistry Research **45**, 5411–5417. https://doi.org/10.1021/ie0601520.

- Audet, J., Lounes, M., Thibault, J. (1996). Pullulan fermentation in a reciprocating plate bioreactor. Bioprocess Engineering **15**, 209–214. https://doi.org/10.1007/BF00369484.
- Avilaa, M., Kawas, B., Fletcher, D. F., Poux, M., Xuereb, C., Aubin, J. (2022). Design, performance characterization and applications of continuous oscillatory baffled reactors. Chemical Engineering and Processing: Process Intensification **180**, 108718. https://doi.org/10.1016/j.cep.2021.108718.
- Avramović, J. M., Stamenković, O. S., Todorović, Z. B., Lazić, M. L., Veljković, V. B. (2012). Empirical modeling of ultrasound assisted base-catalyzed sunflower oil methanolysis kinetics. Chemical Industry and Chemical Engineering Quarterly 18, 115–127. https://doi.org/10.2298/CICEQ110705053A.
- Baird, M. H. I., Garstang, J. H. (1972). Gas absorption in a pulsed bubble column. Canadian Journal of Chemical Engineering **27**, 823–833. https://doi.org/10.1016/0009-2509(72)85016-4.
- Baird, M. H. I., Lane, S. J. (1973). Drop size and holdup in a reciprocating plate extraction column. Canadian Journal of Chemical Engineering **28**, 947–957. https://doi.org/10.1016/0009-2509(77)80029-8.
- Baird, M. H. I., Rama Rao, N. V. (1988). Characteristics of a countercurrent reciprocating plate bubble column. II Axial mixing and mass transfer. Canadian Journal of Chemical Engineering **66**, 222–231. https://doi.org/10.1002/cjce. 5450660206.
- Baird, M. H. I., Rama Rao, N. V. (1991). Axial mixing in a reciprocating plate with very small density gradients. AlChE J. **37**, 1019–1026 (1991). https://doi.org/10.1002/aic.690370707.
- Baird, M. H. I., Rama Rao, N. V., Vijayan, S. (1992). Axial mixing and mass transfer in a vibrating perforated plate extraction column, Canadian Journal of Chemical Engineering **70**, 69–76. https://doi.org/10.1002/cjce.5450700111.
- Baird, M. H. I., Rama Rao, N. V. (1995). Power dissipation and flow patterns in reciprocating baffle-plate columns. Canadian Journal of Chemical Engineering 73, 417–425. https://doi.org/10.1002/cjce.5450730401.
- Baird, M. H. I., Rama Rao, N. V. (1997). Pressure drops in gas-liquid flow in a 15 cm reciprocating plate column. Canadian Journal of Chemical Engineering **75**, 282–289. https://doi.org/10.1002/cjce.5450750202.
- Baird, M. H. I., Rama Rao, N. V., Procházka, J., Sovova, H. (1994). Reciprocating plate columns, In: *Liquid-Liquid Extraction Equipment* (Godfrey, J. C., Slater, M. J., Eds), John Wiley & Sons Ltd., pp. 307–362.
- Baird, M. H. I., Lo, T. C., Rama Rao, N. V., Stonestreet, P. (1996). Power dissipation and holdup in a gassed reciprocating baffle-plate column. Transactions of the

American Institute of Chemical Engineers **74**, 463–470. https://doi.org/10.1002/cjce. 5450730401.

Baird, M. H. I., Rice, R. G. (1975). Axial dispersion in large unbaffled column. Chemical Engineering Journal **9**, 171–174. https://doi.org/10.1016/0300-9467(75)80010-4.

Baird, M. H. I., Rohatgi, A. (1989). Mass transfer from discrete gas bubbles in a reciprocating plate column. Canadian Journal of Chemical Engineering **67**, 682–685. https://doi.org/10.1002/cjce.5450670423.

Baird, M. H. I., Stonestreet, P. (1995). Energy dissipation in oscillatory flow within a baffled tube. Transactions of the Institution of Chemical Engineers **73A**, 503–511.

Banković-Ilić, I. (1993). A study of power consumption and gas holdup in a three-phase reciprocating plate column [Ispitivanje snage mešanja i sadržaja gasa u trofaznoj koloni sa vibracionom mešalicom]. Master's thesis, Faculty of Technology and Metallurgy, University of Belgrade, Belgrade, Serbia (in Serbian).

Banković-Ilić, I. B. (1999). Hydrodynamics and mass transfer of gas-liquid-solid reciprocating plate columns [Hidrodinamika i prenos mase u sistemima gas-tečnost-čvrsto u koloni s vibracionom mešalicom]. Doctoral dissertation, Faculty of Technology in Leskovac, University of Niš, Niš, Serbia (in Serbian).

Banković-Ilić, I., Veljković, V., Lazić, M., Skala, D. (1993). Hydrodynamics of a gas-liquid-solid reciprocating plate column, *11th International Congress of Chemical and Process Engineering*, *CHISA*, Prague, Czech Republic, E4.27

Banković-Ilić, I., Veljković, V., Skala, D. (1994). Gas holdup in three phase reactors of the bubble column type. Hemijska Industrija **48**, 397–402.

Banković-Ilić, I., Veljković, V., Lazić, M., Skala, D. (1995). Power consumption and gas holdup in a gas-liquid reciprocating plate column. Chemical Engineering Communications **134**, 17–32. https://doi.org/10.1080/00986449508936320.

Banković-Ilić, I., Veljković, V., Lazić, M., Skala, D. (1996). Power consumption and pressure fluctuation at the column base in gas-liquid-solid reciprocating plate columns, *12th International Congress of Chemical and Process Engineering CHISA*, Prague, Czech Republic P3.89

Banković-Ilić, I., Veljković, V., Lazić, M., Skala, D. (1997). Analysis of the orifice coefficient in a reciprocating plate column. Hemijska Industrija **51**, 501-508.

Banković-Ilić, I. B., Veljković, V. B., Lazić, M. L., Skala, D. U. (1998a). Influence of liquid properties on power consumption in reciprocating plate columns. I. Newtonian fluids, 13th International Congress of Chemical and Process Engineering, CHISA, Prague, Czech Republic, P3.37 (CD-ROM of full texts 0195.pdf)

Banković-Ilić, I. B., Veljković, V. B., Lazić, M. L., Skala, D. U. (1998b). Influence of liquid properties on power consumption in reciprocating plate columns. II. Non-

newtonian fluids, 13th International Congress of Chemical and Process Engineering, CHISA, Prague, Czech Republic, P3.38 (CD-ROM of full texts 0196.pdf).

Banković-Ilić, I. B., Veljković, V. B., Lazić, M. L., Skala, D. U. (2000). Mass transfer in reciprocating plate columns: I. Volumetric mass transfer coefficient, *14th International Congress of Chemical and Process Engineering, CHISA*, Prague, Czech Republic P.3.34, (CD-ROM of full texts 0487.pdf).

Banković-Ilić, I. B., Veljković, V. B., Lazić, M. L., Skala, D. U. (2001a). Mass transfer in a multiphase vibration column. I. The volumetric mass transfer coefficient. Hemijska Industrija **55**, 376–382.

Banković-Ilić, I. B., Veljković, V. B., Lazić, M. L., Skala, D. U. (2001b). Mass transfer in a multiphase vibration column. II. Interfacial area. Hemijska Industrija **55,** 383–388.

Banković-Ilić, I. B,. Stamenković, I., Stamenković, O., Lazić, M. L., Veljković, V. B., Skala D. U. (2004a). Pressure variation at the bottom of a reciprocating plate reactor filled with non-Newtonian liquids, *18th Congress of Chemists and Technologists of Macedonia*, Ohrid, 23–25. September, CD-ROM of Extended Abstracts, CHE–Bankovic-IlicIvana-effects-e.pdf.

Banković-Ilić, I. B,. Aleksić, M., Veljković, V. B., Lazić, M. L., Skala D. U. (2004b). Effects of size of Rashig rings placed in interplate spaces and fractional plate free area on the gas holdup in a reciprocating plate Reactor, *18th Congress of Chemists and Technologists of Macedonia*, Ohrid, 23–25. September, CD-ROM of Extended Abstracts, CHE-11-Bankovic-IlicIvana-effects-e.pdf.

Banković-Ilić, I., Veljković, V., Skala, D. (2009). [Hydrodynamic and mass transfer characteristics of reciprocating plate columns with gas-liquid and gas-liquid-solid systems - monograph] Hidrodinamičke i masenoprenosne karakteristike kolone sa vibracionom mešalicom za sisteme gas-tečnost i gas-tečnost-čvrsta faza – monografija, Univerzitet u Nišu, Tehnološki fakultet, Leskovac. ISBN 978-86-82367-80-2 (in Serbian).

Banković-Ilić, I. B., Stojković, I. J., Stamenković, O. S., Veljković, V. B., Hung, Y.-T. (2014). Waste animal fats as feedstocks for biodiesel production. Renewable and Sustainable Energy Reviews **32**, 238–254. https://doi.org/10.1016/j.rser.2014.01.038.

Banković-Ilić, I. B., Todorović, Z. B., Avramović, J. M., Veličković, A. V., Veljković, V. B. (2015). The effect of tetrahydrofuran on the base-catalyzed sunflower oil methanolysis in a continuous reciprocating plate reactor. Fuel Processing Technology 137, 339–350. https://doi.org/10.1016/j.fuproc.2015.03.023.

Banković-Ilić, I., Miladinović, M., Veljković, V. (2024). Continuous reciprocating plate and packed bed multiphase reactors in biodiesel production: Advancements and challenges. Hemijska Industrija. 78, 205–225. https://doi.org/10.2298/HEMIND 230630010B.

- Bertoldi, C., Silva, C., Bernardon, J. P., Corazza, M. L., Filho, L. C., Oliveira, J. V. (2009). Continuous production of biodiesel from soybean oil in supercritical ethanol and carbon dioxide as cosolvent. Energy and Fuel 23, 5165–5172. https://doi.org/10.1021/ef900402r.
- Boey, P.–L., Maniam, G. P., Hamid, S. A., Ali, D. M. H. (2011). Crab and cockle shells as catalysts for the preparation of methyl esters from low free fatty acid chicken fat. Journal of the American Oil Chemists' Society 88, 283–288. https://doi.org/10.1007/s11746-010-1660-4.
- Boocock, D. G. B., Konar, S. K., Mao, V., Lee, C. (1996). Fast one-phase oil-rich processes for the preparation of vegetable oil methyl esters. Biomass and Bioenergy 11, 43–50. https://doi.org/10.1016/0961-9534(95)00111-5.
- Boocock, D. G. B., Konar, S. K., Mao, V., Lee, C., Buligan, S. (1998). Fast formation of high purity methyl esters from vegetable oils. Journal of the American Oil Chemists' Society **75**, 1167–1172. https://doi.org/10.1007/s11746-998-0130-8.
- Bouaifi, M., Roustan, M. (1998). Bubble size and mass transfer coefficients in dual-impeller agitated reactors. Canadian Journal of Chemical Engineering **76**, 390–397. https://doi.org/10.1002/cjce.5450760307.
- Boyle, J. (1975). Gas-liquid contacting in a reciprocating plate column. Doctoral dissertation, University of New Brunswick, Fredericton, Canada.
- Brauer, H. (1985). Biological waste water treatment in a reciprocating jet bioreactor. In: *Biotechnology* (Rehm, H. J., Read, G., eds), Vol. 2, Weinheim: VCH-Verlagsgesellshaft mbH, pp. 519-535
- Brauer, H. (1991). Growth of fungi and bacteria in the reciprocating jet bioreactor, Bioprocess Engineering 6, 1–15. https://doi.org/10.1007/BF00369272.
- Brauer, H., Sucker, D. (1979). Biological wastewater treatment in a high efficiency reactor. German Chemical Engineering **2**, 77–86.
- Brunold C. R., Hunns J. C. B., Mackley M. R., Thompson, J. W. (1989). Experimental observations on flow patterns and energy losses for oscillatory flow in ducts containing sharp edges. Chemical Engineering Science 44, 1227–1244, https://doi.org/10.1016/0009-2509(89)87022-8.
- Calabrese, G. S., Pissavini, S. (2011). From batch to continuous flow processing in chemicals manufacturing. AIChE J. 57, 828–834. https://doi.org/10.1002/aic.12598.
- Calderbank, P. H. (1958). Physical rate processes in industrial fermentation. Part I: the interfacial area in gas-liquid contacting with mechanical agitation. Transactions of the American Institute of Chemical Engineers **36**, 443–460.
- Chavarria-Hernandez, N., Tecante, A., Brito de la Fuente, E., Tanguy, P. (1996). Gas-liquid mass transfer in Newtonian and non-Newtonian liquids in a stirred tank agitated with dual turbine-helical ribbon impeller, *12th International Congress of Chemical and Process Engineering*, *CHISA*, Prague, Czech Republic, D1.6

Chen, B. H., Yang, N. S., McMillan, A. F. (1986). Gas holdup and pressure drop for air-water flow through plate bubble columns. Canadian Journal of Chemical Engineering **64**, 387–392. https://doi.org/10.1002/cjce.5450640305.

Cova, D. R. (1974). Axial mixing in the liquid phase in gas-sparged column. Industrial and Engineering Chemistry Process Design and Development **13**, 292–301. https://doi.org/10.1021/i260051a018.

Da Cunha, M. E., Krause, L. C., Aranda Moraes, M. S., Schmitt Faccini, C., Assis Jacques, R., Rodrigues Almeida, S., Alves Rodrigues, M. R., Bastos Caramão, E. (2009). Beef tallow biodiesel produced in a pilot scale. Fuel Processing Technology **90**, 570–575. https://doi.org/10.1016/j.fuproc.2009.01.001.

Da Rós, P. C. M., De Castro, H. F., Carvalho, A. K. F., Soares, C. M. F., De Moraes, F. F., Zanin, G. M. (2012). Microwave-assisted enzymatic synthesis of beef tallow biodiesel. Journal of Industrial Microbiology and Biotechnology **39**, 529–536. https://doi.org/10.1007/s10295-011-1059-8.

Darnoko, D. Cheryan, M. (2000). Kinetics of palm oil transesterification in a batch reactor. Journal of the American Oil Chemists' Society 77, 1263–1267. https://doi.org/10.1007/s11746-000-0198-y.

Da Silva, C., de Castilhos, F., Oliveira, J. V., Filho, L. C. (2010). Continuous production of soybean biodiesel with compressed ethanol in a microtube reactor. Fuel Process. Technol. **91**, 1274–1281. https://doi.org/10.1016/j.fuproc.2010.04. 009.

Deshusses, M. A., Chen, W., Mulchandani, M. (1997). Innovative bioreactors, Biochemical Engineering **8** 165–168. https://doi.org/10.1016/S0958-1669(97) 80096-1.

Dhanasekaran, S., Karunanithi, T. (2010a). Axial mixing in a novel perforated plate bubble column. International Journal of Chemical Reaction Engineering **8**, A118. https://doi.org/10.2202/1542-6580.2332.

Dhanasekaran, S., Karunanithi, T. (2010b). Mass transfer studies in a novel perforated plate. International Journal of Chemical Reaction Engineering **8**, A116. https://doi.org/10.2202/1542-6580.2340.

Dhanasekaran, S., Karunanithi, T. (2012a). Improved gas holdup in novel bubble column. Canadian Journal of Chemical Engineering 90, 126-136. https://doi.org/10.1002/cjce.20509.

Dhanasekaran, S., Karunanithi, T. (2012b). Statistical analysis of experimental variables on gas holdup in novel bubble column using Box-Behnken design. International Journal of Chemical Reaction Engineering **10**, A21. https://doi.org/10.1515/1542-6580.2908.

Dhanasekaran, S., Karunanithi, T. (2012c). Bubble diameter and effective interfacial area in a novel hybrid rotating and reciprocating perforated plate bubble column.

International Journal of Chemical Reaction Engineering **10**, A21. https://doi.org/10.1515/1542-6580.2914.

Dhanasekaran, S., Karunanithi, T. (2012d). Statistical analysis of effects of experimental variables on mass transfer coefficient in a novel hybrid bubble column using Box–Behnken design. Canadian Journal of Chemical Engineering **9999**, 1-12. https://doi.org/10.1002/cjce.2172612.

Doell, R., Konar, S. K., Boocock, D. G. B. (2008). Kinetic parameters of a homogeneous transmethylation of soybean oil. J. Am. Oil. Chem. Soc. **85**, 271–276.

Gagnon, H., Lounes, M., Thibault, J. (1998). Power consumption and mass transfer in agitated gas-liquid columns: A comparative study. Canadian Journal of Chemical Engineering **76**, 379–389. https://doi.org/10.1002/cjce.5450760306.

Gameiro, M., Lisboa, P., Paiva, A., Barreiros, S., Simões, P. (2015). Supercritical carbon dioxide—based integrated continuous extraction of oil from chicken feather meal, and its conversion to biodiesel in a packed—bed enzymatic reactor, at pilot scale. Fuel **153**, 135–142. https://doi.org/10.1016/j.fuel.2015.02.100.

García-Martín, J. F., Barrios, C. C., Alés-Álvarez, F. J., Dominguez-Sáez, A., Alvarez-Mateos, P.P. (2018). Biodiesel production from waste cooking oil in an oscillatory flow reactor. Performance as a fuel on a TDI diesel engine. Renewable Energy **125**, 546–556. https://doi.org/10.1016/j.renene.2018.03.002.

Gavrilescu, M., Tudose, R. Z. (1997). The specific interfacial area in external-loop airlift bioreactors. Bioprocess Engineering **16**, 127–133. https://doi.org/10.1007/s004490050299.

Ghirardini, M., Donati, G., Rivati, F. (1992). Gas lift reactors: Hydrodynamics, mass transfer and scale up. Chemical Engineering Science 47, 2209–2214. https://doi.org/10.1016/0009-2509(92)87036-P.

Gomaa, H. G., Landau, J., Al Taweel, A. M. (1991). Gas-liquid contacting in reciprocating plate columns: I. Hydrodynamics. Canadian Journal of Chemical Engineering **69**, 228–239. https://doi.org/10.1002/cjce.5450690127.

Gomaa, H. G., Al Taweel, A. M. (2005). Axial mixing in a novel pilot scale gasliquid reciprocating plate column. Chemical Engineering and Processing **44** 1285–1295. https://doi.org/10.1016/j.cep.2005.04.003

Gopi, R., Thangarasu Vinoth, Angkayarkan Vinayakaselvi, M., Ramanathan, A. (2022). A critical review of recent advancements in continuous flow reactors and prominent integrated microreactors for biodiesel production. Renewable and Sustainable Energy Reviews 154(C). https://doi.org/10.1016/j.rser.2021.111869.

Gorodeckij, I. J., Vasin, A. A., Olevskij, B. M., Lupanov, P. A. (1980). Vibracionnye Massoobmennye Apparaty, Moscow: Himia.

- Gough, P., Ni, X., Symes, K. C. (1997). Experimental flow visualisation in a modified pulsed baffled reactor. Journal of Chemical Technology and Biotechnology **69**, 321–328, https://doi.org/10.1002/(SICI)1097-4660(199707)69.
- Guan, G., Kusakabe, K. (2009). Synthesis of biodiesel fuel using an electrolysis method. Chemical Engineering Journal **153**, 159–163. https://doi.org/10.1016/j.cej. 2008.10.009.
- Guan, G., Kusakabe, K. (2012). Development of advanced biodiesel fuel production process. Journal of the Japan Petroleum Institute **55**, 171–181. https://www.jstage.jst.go.jp/article/jpi/55/3/55_171/_pdf.
- Guan, G., Sakurai, N., Kusakabe, K. (2009a). Synthesis of biodiesel from sunflower oil at room temperature in the presence of various cosolvents. Chemical Engineering Journal **146**, 302–306. https://doi.org/10.1016/j.cej.2008.10.009.
- Guan, G., Kusakabe, K., Sakurai, N., Moriyama, K. (2009b). Transesterification of vegetable oil to biodiesel fuel using acid catalysts in the presence of dimethyl ether. Fuel **88**, 81–86. https://doi.org/10.1016/j.fuel.2008.07.021.
- Gupta, J., Agarwal, M., Dalai, A.K. (2020). An overview on the recent advancements of sustainable heterogeneous catalysts and prominent continuous reactor for biodiesel production. Journal of Industrial and Engineering Chemistry **88**, 58–77. https://doi.org/10.1016/j.jiec.2020.05.012.
- Hafez, M. M., Baird, M. H. I. (1978). Power consumption in a reciprocating plate extraction column. Transactions of the American Institute of Chemical Engineers **56**, 229–238.
- Hafez, M., Procházka, J. (1974a). The dynamic effects in a vibrating plate and pulsed extractors. I. Theory and experimental technique. Chemical Engineering Science **29**, 1745–1753. https://doi.org/10.1016/0009-2509(74)87033-8.
- Hafez, M., Procházka, J. (1974b). The dynamic effects in a vibrating plate and pulsed extractors II. The forces under the steady and pulsating single-phase flow. Chemical Engineering Science **29**, 1755–1762. https://doi.org/10.1016/0009-2509(74)87034-X.
- Harikrishnan, T. L., Varma, Y. B. G. (1992). Analysis of flow, pressure drop and power requirement in pulsed columns. Industrial and Engineering Chemistry Research **31**, 1352–1361. https://doi.org/10.1021/ie00005a015.
- Harvey, A. P., Mackley, M. R., Stonestreet, P. (2001). Operation and optimization of an oscillatory flow continuous reactor. Industrial Engineering and Chemical Research **40**, 5371–5377. https://doi.org/10.1021/ie0011223.
- Harvey, A. P., Mackley, M. R., Seliger, T. (2003). Process intensification of biodiesel production using a continuous oscillatory flow reactor. Journal of Chemical Technology and Biotechnology **78**, 338–41. https://doi.org/10.1002/jctb.782.

- He, H., Wang, T., Zhu, S. (2007). Continuous production of biodiesel fuel from vegetable oil using supercritical methanol process. Fuel **86**, 442–447. https://doi.org/10.1016/j.fuel.2006.07.035.
- Holmes, T., Karr, A. E., Baird, M. (1991). Effect of unfavorable continuous phase density gradient on axial mixing. AIChE Journal **37**, 360-366. https://doi.org/10.1002/aic.690370306.
- Hoque, M. E., Singh, A., Chuan, Y. L. (2011). Biodiesel from low cost feedstocks: The effects of process parameters on the biodiesel yield. Biomass Bioenergy **35**, 1582–1587. https://doi.org/10.1016/j.biombioe.2010.12.024.
- Hu, X., Wang, X., Yang, H. (2003). Caffeine Extraction with a Karr reciprocating Plate Column. Engineering in Life Sciences **3**, 10. https://doi.org/10.1002/elsc. 20031798
- Jealous, A. C., Johnson, H. F. (1955). Power requirements for pulse generation in pulse column. Industrial Engineering and Chemistry 47, 1159–1166. https://doi.org/10.1021/ie50546a021.
- Jeong, G.-T., Yang, H.-S., Park, D.-H. (2009). Optimization of transesterification of animal fat ester using response surface methodology. Bioresource Technology **100**, 25–30.
- Joseph, S., Varma, Y. B. G. (1998). A correlation for drop size and slip velocity in reciprocating plate column. Bioprocess Engineering **18**, 367-371. https://doi.org/10.1007/s004490050457.
- Kafuku, G., Mbarawa, M. (2010). Alkaline catalyzed biodiesel production from *Moringa oleifera* oil with optimized production parameters. Applied Energy. **87**, 2561–2565. https://doi.org/10.1016/j.apenergy.2010.02.026.
- Kagan, S. Z., Veisbein, B. A., Trukhanov, V. G., Musychenko, L.A. (1973). Longitudinal mixing and its effect on mass transfer in pulsed-screen extractor. International Journal of Chemical Engineering. 13, 217–219.
- Karmee, S. K., Chandna, D., Ravi, R., Chadha, A. (2006). Kinetics of base-catalyzed transesterification of triglycerides from *Pongamia* oil. Journal of the American Oil Chemists' Society **83**, 873–877. https://doi.org/10.1007/s11746-006-5040-z.
- Karr, A. E. (1959). Performance of reciprocating plate extraction columns. AIChE Journal **5**, 446–452. https://doi.org/10.1002/aic.690050410.
- Karr, A. E., Ramanujam, S., Lo, T. C., Baird, M. H. I. (1980). Extraction of whole fermentation broth with Karr reciprocating plate extraction column. Canadian Journal of Chemical Engineering **58**, 249–252. https://doi.org/10.1002/cjce. 5450580217.
- Karr, A. E., Gebert, W., Wang, M. (1987). Axial mixing and scaleup of reciprocating plate columns. Canadian Journal of Chemical Engineering **65**, 373–381. https://doi.org/10.1002/cjce.5450650304.

Kato, Y., Nishiwaki, A. (1972). Longitudinal dispersion coefficient of a liquid in a bubble column. International Chemical Engineering **125**, 182-187. https://doi.org/10.1252/KAKORONBUNSHU1953.35.912.

Kawase, Y., Umeno, S., Kumagai, T. (1992). The prediction of gas hold-up in bubble column reactors: Newtonian and non-Newtonian fluids. Chemical Engineering Journal **50**, 1–7. https://doi.org/10.1016/0300-9467(92)80001-Q.

Kayode Coker, A. (2001). Modeling of chemical kinetics and reactor design, 2nd ed. Woburn: Butterworth-Heinemann.

Kažić, N. (1979). Investigation of pressure change to define hydromechanical forces in a vibrating extractor [Proučavanje promene pritiska u cilju definisanja hidromehaničkih sila u vibracionom ekstraktoru]. Master's thesis, University of Belgrade, Mechanical Engineering, Belgrade (in Serbian).

Kefas, H. M., Yunus, R., Rashid U., Taufiq-Yap, Y.H. (2019). Enhanced biodiesel synthesis from palm fatty acid distillate and modified sulfonated glucose catalyst via an oscillation flow reactor system. Journal of Environmental Chemical Engineering 7, 102993. https://doi.org/10.1016/j.jece.2019.102993.

Khelafi, M. Djaafri, S. Kalloum, M. R. Atelge, S. Abut, A. (2022). Dahbi, M. Bekirogullari, A.E. Atabani, Effect of stirring speeds on biodiesel yield using an innovative oscillatory reactor and conventional STR (A comparative study). Fuel **325**, 124856. https://doi.org/10.1016/j.fuel.2022.124856.

Kim, S. D., Baird, M. H. I. (1976a). Axial dispersion in a reciprocating plate extraction column. Canadian Journal of Chemical Engineering **54**, 81–89. https://doi.org/10.1002/cjce.5450540112.

Kim, S. D., Baird, M. H. I. (1976b). Effect of hole size on hydrodynamics of a reciprocating perforated plate extraction column. Canadian Journal of Chemical Engineering **54**, 235–237. https://doi.org/10.1002/cjce.5450540320.

Kolmogorov, A. N. (1941). The local structure of turbulence in incompressible viscous fluid for very large Reynolds numbers. Doklady Akademii Nauk SSSR **30**, 301–304 [Kolmogorov, A. N. (1991). The local structure of turbulence in incompressible viscous fluid for very large Reynolds numbers. Proceedings of the Royal Society of London. Series A, Mathematical and Physical Science **434**, 9–13. http://doi.org/10.1098/rspa.1991.0075.]

Kostanyan, A. E., Pebalk, V. L., Pelevina, T. K. (1980). Investigation of the operating characteristics of column extractors with vibrating plates. Theoretical Foundations of Chemical Engineering **14**, 115–118.

Kouhifaiegh, M., Hosseinzadeh Samani, B., Ebrahimi, R., Taki, K. (2024). Design and construction of a single orifice oscillatory flow reactor for the continuous production of biodiesel from sunflower oil. Biofuels **15**, 1041–1050. https://doi.org/10.1080/17597269.2024.2330187.

Kumar, A., Hartland, S. A. (1995). Unified correlation for the prediction of dispersed-phase hold-up in liquid-liquid extraction equipment. Industrial and Engineering Chemistry Research **34**, 3925–3940. https://doi.org/10.1021/ie00038 a032.

Kumar, A., Hartland, S. (1996). Unified correlations for the prediction of drop size in liquid-liquid extraction columns. Industrial and Engineering Chemistry Research **35**, 2682–2695. https://doi.org/10.1021/ie950674w.

Kumar, G. R., Ravi, R., Chadha, A. (2011). Kinetic studies of base-catalyzed transesterification reactions of non-edible oils to prepare biodiesel: The effect of cosolvent and temperature. Energ. Fuel. **25**, 2826–2832. https://doi.org/10.1021/ef200469u.

Landau, J., Boyle, J., Al Taweel, A. (1976). Pressure variation in reciprocating plate columns. Chemie Ingenieur Technik **48**, 1077. https://doi.org/10.1002/cite.33048 1131.

Law, R., Ahmed, S. M. R., Tang, N., Phan, N., Harvey, A. P. (2018). Development of a more robust correlation for predicting heat transfer performance in oscillatory baffled reactors. Chemical Engineering and Processing – Process Intensification 125, 133–138. https://doi.org/10.1016/j.cep.2018.01.01.

Leevijit, T., Wisutmethangoon, W., Prateepchaikul, G., Tongurai, C., Allen, M. (2006). Design and test of a continuous reactor for palm oil transesterification. Songklanakarin Journal of Science and Technology **28**, 791–802.

Leevijit, T., Tongurai, C., Prateepchaikul, G., Wisutmethangoon, W. (2008). Performance test of 6-stage continuous reactor for palm methyl ester production. Bioresource Technology **99**, 214–221. https://doi.org/10.1016/j.biortech.2006.11. 052.

Lertsanthapornsuk, V., Pairintra, R., Aryusuk, K., Krisnangkura, K. (2008). Microwave assisted in continuous biodiesel production from waste frying palm oil and its performance in a 100 kW diesel generator. Fuel Processing Technology **89**, 1330–1336. https://doi.org/10.1016/j.fuproc.2008.05.024.

Levenspiel, O. (1979). Osnovi teorije i projektovanja hemijskih reaktora, prevod na srpski jezik, TMF-ICS, Beograd [Chemical Reaction Engineering; an Introduction to the Design of Chemical Reactors, First Edition. John Wiley and Sons, New York, 1962.]

Liao, B. Q., Wang, J., Wan, C. R. (2005). Separation and Recovery of Rare Earths in Reciprocating Extraction Columns. Separation Science and Technology **40**, 1685-1700. http://dx.doi.org/10.1081/SS-200059604

Lin, L., Ying, D., Chaitep, S., Vittayapadung, S. (2009). Biodiesel production from crude rice bran oil and properties as fuel. Applied Energy **86**, 681–688. https://doi.org/10.1016/j.apenergy.2008.06.002.

- Linek, V., Vacek, V., Benes, P. (1987). A critical review and experimental verification of the correct use of the dynamic method for the determination of oxygen transfer in aerated agitated vessels to water. Chemical Engineering Journal **34**, 11–34. https://doi.org/10.1016/0300-9467(87)85003-7.
- Liu, C. H., Chen, B. H. (1993). Characteristics of reciprocating screen-plate bubble column with dilute alcohol solutions. Canadian Journal of Chemical Engineering **71**, 464–467. https://doi.org/10.1002/cjce.5450710318.
- Lo, T. C., Procházka, J. (1983). Reciprocating plate extraction columns. In: *Handbook of Solvent Extraction* (Lo, T. C., Baird, M. H. I., Hanson, C., Eds), Wiley, pp. 373–389.
- Lo, T. C., Baird, M. H. I., Rama Rao, N. V. (1992). The reciprocating plate column development and applications. Chemical Engineering Communications **116**, 67–88. https://doi.org/10.1080/00986449208936044.
- Lounes, M., Thiboult, J. (1993). Hydrodynamics and power consumption of a reciprocating plate gas-liquid column. Canadian Journal of Chemical Engineering **71**, 497–506. https://doi.org/10.1002/cjce.5450710401.
- Lounes, M., Thiboult, J. (1994). Mass transfer in a reciprocating plate bioreactor. Chemical Engineering Communications **127**, 169–189. https://doi.org/10.1080/00986449408936231.
- Lounes, M., Thiboult, J. (1996). Axial dispersion in a reciprocating plate column. Canadian Journal of Chemical Engineering **74**, 187–194. https://doi.org/10.1002/cjce.5450740203.
- Lounes, M., Audet, J., Thiboult, J., LeDuy, A. (1995). Description and evaluation of a reciprocating plate bioreactor. Bioprocess Engineering **13**, 1–11. https://doi.org/10.1007/BF00368758.
- Lozano, P., García-Verdugo, E., Bernal, J. M., Izquierdo, D. F., Burguete, M. I., Sánchez-Gómez, G., Luis, S. V. (2012). Immobilised lipase on structured supports containing covalently attached ionic liquids for the continuous synthesis of biodiesel in sc CO₂. ChemSusChem **5**, 790–798. https://doi.org/10.1002/cssc.201100692.
- Mackay, M. E., Mackley, M. R., Wang., Y. (1991). Oscillatory flow within tubes containing wall or central baffles. Transactions of the American Institute of Chemical Engineers **69**, 506–513.
- Mackley, M. R., Stonestreet, P. (1995). Heat transfer and associated energy dissipation for oscillatory flow in baffled tubes. Chemical Engineering Science **50**, 2211–2224. https://doi.org/10.1016/0009-2509(95)00088-M.
- Mackley, M. R., Stonestreet, P., Thurston, N. C., Wiseman, J. S. (1998). Evaluation of a novel self-aerating, oscillating baffle column. Canadian Journal of Chemical Engineering **76**, 5–10. https://doi.org/10.1002/cjce.5450760102.

Mar, B. W., Babb, A. L. (1959). Longitudinal mixing in a pulsed sieve-plate extraction column. Industrial-Engineering Chemistry **51**, 1011–1014.

Masngut, N., Harvey, A. P., Ikwebe, J. (2010). Potential uses of oscillatory baffled reactors for biofuel production. Biofuels 1, 605–619. https://doi.org/10.4155/bfs.10.38.

Masuik, S., Rakoczy, R. (2007). Power consumption, mixing time, heat and mass transfer measurements for liquid vessels that are mixed using reciprocating multiplates agitators. Chemical Engineering and Processing: Process Intensification 46, 89–98. https://doi.org/10.1016/j.cep.2006.05.002.

Mazubert, A., Aubin, J., Elgue, S., Poux, M. (2014). Intensification of waste cooking oil transformation by transesterification and esterification reactions in oscillatory baffled and microstructured reactors for biodiesel production. Green Processes and Synthesis. **3**, 419–429, http://dx.doi.org/10.1515/gps-2014-0057.

Mazubert, A., Crockatt, M., Roelands, M. (2015). Reactor comparison for the esterification of fatty acids from waste cooking oil. Chemical Engineering and Technology **38**, 2161–2169. https://doi.org/10.1002/ceat.201500138.

Mazubert, A., Fletcher, D. F., Poux, M., Aubin, J. (2016a). Hydrodynamics and mixing in continuous oscillatory flow reactors—Part I: Effect of baffle geometry. Chemical Engineering and Processing: Process Intensification **108**, 78–92. https://doi.org/10.1016/j.cep.2016.07.015.

Mazubert, A., Fletcher, D. F., Poux, M., Aubin, J. (2016b). Hydrodynamics and mixing in continuous oscillatory flow reactors—Part II: Characterisation methods. Chemical Engineering and Processing: Process Intensification **102**, 102–116. https://doi.org/10.1016/j.cep.2016.01.009.

McDonough, J. R., Phan, A. N., Harvey, A. P. (2015). Rapid process development using oscillatory baffled mesoreactors — a state-of-the-art review, Chemical Engineering Journal **265**, 110–121. https://doi.org/10.1016/j.cej.2014.10.113.

Mendonça, D. R., Andrade, H. M. C., Guimarães, P. R. B., Vianna, R. F., Meneghetti, S. M. P., Pontes, L. A. M., Teixeira, L. S. G. (2011). Application of full factorial design and Doehlert matrix for the optimisation of beef tallow methanolysis via homogeneous catalysis. Fuel Processing Technology **92**, 342–348. https://doi.org/10.1016/j.fuproc.2010.09.026.

Meng, M., Jiang, J., Li, X., Ying, H., Xu, Y. (2008). Continuous preparation of biodiesel with co-solvent in tubular static mixer. Nongye Gongcheng Xuebao/Transactions of the Chinese Society of Agricultural Engineering **24**, 193–196.

Michell, R. W., Furzer, I. A. (1972). Mixing in trickle flow through packed beds. Chemical Engineering Journal **4**, 53–63. https://doi.org/10.1016/0300-9467(72) 80053-4.

Miladinović, M. R., Krstić, J. B., Tasić, M. B., Stamenković, O. S., Veljković, V. B. (2014). A kinetic study of quicklime–catalyzed sunflower oil methanolysis. Chemical Engineering Research and Design **92**, 1740–1752. https://doi.org/10.1016/j.cherd. 2013.11.023.

Miladinović, M. R., Stamenković, O. S., Veljković, V. B., Skala, D. U. (2015). Continuous sunflower oil methanolysis over quicklime in a packed-bed tubular reactor. Fuel **154**, 301–307. https://doi.org/10.1016/j.fuel.2015.03.057.

Miladinović, M. R., Stojković, I. S., Veličković, A. V., Stamenković, O. S., Banković-Ilić, I. B., Veljković, V. B. (2019). Optimization and kinetic modeling of waste lard methanolysis in a continuous reciprocating plate reactor. Chinese Journal of Chemical Engineering 27, 2481–2490. https://doi.org/10.1016/j.cjche.2019.02.019.

Miller, D. N. (1974). Scale-up of agitated vessels gas-liquid mass transfer. AIChE Journal **20**, 445–453. https://doi.org/10.1002/aic.690200303.

Miyanami, K., Tojo, K., Yano, T. (1974). Liquid-phase mixing in a multistage vibrating-disc column with concurrent gas-liquid flow. Journal of Chemical Engineering of Japan 6, 518–522.

Miyanami, K., Tojo, K., Minami, I., Yano, T. (1978). Gas-liquid mass transfer in vibrating disc column. Chemical Engineering Science **33**, 601–608. https://doi.org/10.1016/0009-2509(78)80022-0.

Miyanami, K., Tojo, K., Yano, T., Miyaji, K., Minami, I. (1975). Drop size distribution and holdups in a multistage vibrating disc column. Chemical Engineering Science **30**, 1415–1420. https://doi.org/10.1016/0009-2509(75)85073-1.

Miyauchi, T., Oya, H. (1965). Longitudinal dispersion in pulsed perforated-plate columns. AlChE J. 11, 395–402. https://doi.org/10.1002/aic.690110307.

Montgomery, D. C. (2005). Design and analysis of experiments. 6th ed. New York: John Wiley & Sons, Inc.

Muhammed Niyas, M., Shaija, A. (2023). Biodiesel production from coconut waste cooking oil using novel solar-powered rotating flask oscillatory flow reactor and its utilization in diesel engine. Thermal Science and Engineering Progress **40**, 101794. https://doi.org/10.1016/j.tsep.2023.101794.

Murthy, V. V. P. S., Ramachandran, K. B., Ghose, T. K. (1987). Gas hold-up and power consumption in an air-pulsed column bioreactor. Process Biochemistry **22**, 3–8.

Myers, R. H., Montgomery, D. C. (2002). Response Surface Methodology: Process and Product Optimization using Designed Experiments, 2nd ed., John Wiley and Sons, New York.

- Narváez, P. C., Sánchez, F. J., Godoy-Silva, R. D. (2009). Continuous methanolysis of palm oil using a liquid-liquid film reactor. Journal of the American Oil Chemists' Society **86**, 343–352. https://doi.org/10.1007/s11746-009-1356-9.
- Naseva, O. (2002). Uticaj reoloških osobina tečne faze na snagu mešanja u bioreaktoru sa vibracionom mešalicom [Influence of the rheological properties of the liquid phase on the power consumption in a reciprocating plate bioreactor]. Master's thesis, University of Niš, Faculty of Technology in Leskovac, Niš, Serbia.
- Naseva, O., Stamenković, I., Banković-Ilić, I., Lazić, M., Veljković, V., Skala D. (2002). Sadržaj gasa u bioreaktoru sa vibracionom mešalicom tečna faza je nenjutnovski fluid [Gas holdup in a reciprocating plate bioreactor: Non-newtonian liquid phase]. Hemijska Industrija (Chemical Industry) **56**, 198–203. https://doi.org/10.2298/HEMIND0205198N.
- Naseva, O., Stamenković, I., Banković-Ilić, I., Lazić, M., Veljković, V., Skala D. (2003). Snaga mešanja nenjutnovskih tečnosti u višefaznom reaktoru sa vibracionom mešalicom [The power consumption in a multiphase reciprocating plate reactor filled with the non-newtonian liquids]. Procesna tehnika **1**, 185–187. https://izdanja.smeits.rs/index.php/procteh/article/view/3688/3867.
- Nemecek, M., Procházka, J. (1974). Longitudinal mixing in a vibrating-sieve-plate column two-phase flow. Canadian Journal of Chemical Engineering **52**, 739–749. https://doi.org/10.1002/cjce.5450520607.
- Ni, X., Jian, H., Fitch, A.W. (2002). Computational fluid dynamic modelling of flow patterns in an oscillatory baffled column. Chemical Engineering Science **57**, 2849–2862, https://doi.org/10.1016/S0009-2509(02)00081-7.
- Nikolić, Lj. B. (2003). Backmixing in the liquid phase and the kinetics of the alcoholic fermentation in a three-phase reciprocating plate bioreactor [Povratno mešanje tečne faze i kinetika procesa alkoholne fermentacije u trofaznom bioreaktoru sa vibracionom mešalicom]. Doctoral dissertation, University of Niš, Faculty of Technology in Leskovac, Niš, Serbia. http://doiserbia.nb.rs/phd/fulltext/NI20031003NIKOLIC.pdf (in Serbian).
- Nikolić, Lj., Đoković, N., Veljković, V., Skala, D. (1999). Aksijalno mešanje u koloni sa vibracionom mešalicom. Hemijska Industrija **53**, 300–308.
- Nikolić, Lj., Stojanović, S., Veljković, V., Skala, D. (2003). The model of back-flow mixed tanks-in-series used for representing the liquid flow in a reciprocating plate column. Hemijska Industrija **57**, 269–275. https://doi.org/10.2298/HEMIND 0306269N.
- Nikolić, Lj. B., Nikolić, V. D., Veljković, V. B., Lazić, M. L., Skala, D. U. (2004). Axial dispersion of the liquid phase in a three-phase Karr reciprocating plate column, Journal of the Serbian Chemical Society **69** (7), 581–599. https://doi.org/10.2298/JSC0407581N.

Nikolić, Lj., Veljković, V., Skala, D. (2001a). Analysis of liquid flow in a Karr reciprocating plate column. Hemijska Industrija **55**, 249–254. http://www.ache.org.rs/HI/2001/No06/skala.pdf.

Noh, S. H., Baird, M. H. I. (1984). Mass transfer and pressure drop in a cocurrent reciprocating plate extraction column. AIChE Journal **30**, 120–127. https://doi.org/10.1002/aic.690300117.

Noureddini, H., Harkey, D., Medikonduru, V. (1998). Continuous process for the conversion of vegetable oils into methyl esters of fatty acids. Journal of the American Oil Chemists' Society **75**, 1775–1783. https://doi.org/10.1007/s11746-998-0331-1.

Noureddini, H., Zhu, D. (1997). Kinetics of transesterification of soybean oil. Journal of the American Oil Chemists' Society **74**, 1457–1463. https://doi.org/10.1007/s11746-997-0254-2.

Ohki, Y., Inoue, H. (1970). Longitudinal mixing of the liquid phase in bubble columns. Chemical Engineering Science **25**, 1–16. https://doi.org/10.1016/0009-2509(70)85016-3.

Panton, R., Goldman, A. (1976). Correlation of nonlinear orifice impedance, The Journal of the Acoustical Society of America **60**, 1390–1396. https://doi.org/10.1121/1.381232.

Parthasarathy, P. (1981). The bubble size distribution. Master's thesis, Madras

Parthasarathy, P., Sriniketan, Srinivas, N. S., Varma, Y. B. G. (1984). Axial mixing of continuous phase in reciprocating plate columns. Chemical Engineering Science **39**, 987–995. https://doi.org/10.1016/0009-2509(84)87006-2.

Pavasović, V. (1975). The study of hydrodynamics in a vibrating extractor [Ispitivanje hidrodinamike u vibracionom ekstraktoru], Doctoral dissertation, University of Belgrade, Faculty of Technology and Metallurgy, Belgrade.

Peterson, C. L., Cook, J. L., Thompson, J. C., Taberski, J. S. (2002). Continuous flow biodiesel production. Applied Engineering in Agriculture **18**, 5–11. https://doi.org/10.13031/2013.7702.

Petrović, D. (1989). The study of hydrodynamics and mass transfer in a three-phase bubble column with a concentric draught-tube [Ispitivanje hidrodinamike i prenosa mase u trofaznoj barbotažnoj koloni sa koncentričnom cevi]. Doctoral dissertation, University of Novi Sad, Faculty of Technology, Novi Sad, Serbia.

Phan, A. N., Harvey, A. P., Rawcliffe, M. (2011). Continuous screening of base-catalysed biodiesel production using new designs of mesoscale oscillatory baffled reactors. Fuel Processing Technology **92**, 1560–1567. https://doi.org/10.1016/j.fuproc.2011.03.022.

Phan, A. N., Harvey, A. P., Eze, V. (2012). Rapid production of biodiesel in mesoscale oscillatory baffled reactors, Chemical Engineering and Technology **35**, 1214–1220, https://doi.org/10.1002/ceat.201200031.

Pietzsch, W., Pilhofer, T. H. (1985). Calculation of the drop size in pulsed sieveplate extraction columns. Chemical Engineering Science **39**, 961–965. https://doi.org/10.1016/0009-2509(84)87003-7.

Pošarac, D. (1988). The study of hydrodynamics and mass transfer in a three-phase reactor with external recirculation [Ispitivanje hidrodinamike i prenosa mase u trofaznom reaktoru sa spoljnom recirkulacijom]. Doctoral dissertation, University of Novi Sad, Faculty of Technology, Novi Sad, Serbia (in Serbian).

Prabhavathy, N. K., Joseph, S., Varma, Y. B. G. (1996). Influence of added packing on the volumetric efficiency in a Karr column. Bioprocess Engineering **15**, 109–115. https://doi.org/10.1007/BF00372986.

Pratt, H. R. C., Baird, M. H. I. (1983). Axial dispersion, Chapter 6, *Handbook of Solvent Extraction*, Lo, T. C., Baird, M. H. I., Hanson, C., eds., New York: Wiley-Interscience, pp. 199–248.

Prochazka, J., Hafez, M. M. (1972). The analysis of the dynamic effects in vibrating and pulse plate extraction columns. Collection of Czechoslovak Chemical Communications 37, 3725-3734. https://doi.org/10.1135/cccc19723725

Rama Rao, N. V., Baird, M. H. I. (1986). Gas-liquid pressure drop studies in a reciprocating plate column. Canadian Journal of Chemical Engineering **64**, 42–47. https://doi.org/10.1002/cjce.5450640106.

Rama Rao, N. V., Baird, M. H. I. (1988). Characteristics of a countercurrent reciprocating plate bubble column. I. Holdup, pressure drop and bubble diameter. Canadian Journal of Chemical Engineering **66**, 211–221. https://doi.org/10.1002/cjce.5450660205.

Rama Rao, N. V., Baird, M. H. I. (1998). Back mixing in a reciprocating plate column with stable density gradients. AIChE Journal 44, 659–663. https://doi.org/10.1002/aic.690440411

Rama Rao, N. V., Baird, M. H. I. (2003). Gas-liquid mass transfer in a 15 cm diameter reciprocating plate column. Journal of Chemical Technology and Biotechnology **78**, 134–137. https://doi.org/10.1002/jctb.704.

Rama Rao, N. V., Srinivas, N. S., Varma, Y. B. G. (1983). Dispersed phase holdup and drop size distributions in reciprocating plate columns. Canadian Journal of Chemical Engineering **61**, 168–177. https://doi.org/10.1002/cjce.5450610204.

Rama Rao, N. V., Vijayan, S., Baird, M. H. I. (1991). Hydrodynamics of a vibrating perforated plate extraction column. Canadian Journal of Chemical Engineering **69**, 212–221. https://doi.org/10.1002/cjce.5450690125.

Refaat, A. A. (2010). Different techniques for the production of biodiesel from waste vegetable oil. International Journal of Environmental Science and Technology 7, 183–213. https://doi.org/10.1016/0300-9467(85)80061-7.

Reschke, M., Schügerl, K. (1985). Continuous reactive extraction of penicillin-G in a Karr column. Chemical Engineering Journal **31**, B19–B26. https://doi.org/10.1016/0300-9467(85)80061-7.

Roman, R. V., Tudose, R. Z. (1997). Studies on transfer processes in mixing vessels: effect of particles on gas-liquid mass transfer using modified Rushton turbine agitators. Bioprocess Engineering 17, 361–365. https://doi.org/10.1007/s004490050398.

Royon, D., Daz, M., Ellenrieder, G., Locatelli, S. (2007). Enzymatic production of biodiesel from cotton seed oil using *t*-butanol as a solvent. Bioresource Technology **98**, 648–653. https://doi.org/10.1016/j.biortech.2006.02.021.

Sajjadi, S., Zerfa, M., Brooks, B. W. (2002). Dynamic behaviour of drops in oil/water/oil dispersions. Chemical Engineering Science 57, 663–675. https://doi.org/10.1016/S0009-2509(01)00415-8.

Sakthivel, S., Halder, S., Gupta, P. D. (2013). Influence of co-solvent on the production of biodiesel in batch and continuous process. International Journal of Green Energy **10**, 876–884. https://doi.org/10.1080/15435075.2012.727365.

Santikunaporn M., Techopittayakul T., Echaroj S., Chavadej S., Chen Y.-H., Yuan M.-H., Asavatesanupap C. (2020). Optimization of biodiesel production from waste cooking oil in a continuous mesoscale oscillatory baffled reactor. Engineering Journal **24**, 19–28. https://doi.org/10.4186/ej.2020.24.2.19.

Sater, V. E., Levenspiel, O. (1966). Two-phase flow in packed beds. Industrial and Engineering Chemistry Fundamentals 5, 86–92.

Sawangkeaw, R., Bunyakiat, K., Ngamprasertsith, S. (2010). A review of laboratory-scale research on lipid conversion to biodiesel with supercritical methanol. Journal of Supercritical Fluids **55**, 1–13. https://doi.org/10.1016/j.supflu.2010.06.008.

Šerbak, V., Selga, S., Sakse, A. (1978). Isplanie pnevmatičeskogo fermentatora s perforirovannlimi tarelkami primenitellino k processam biosinteza lizina, *Tehnologija mikrobnogo sinteza*, Riga: Zinatne, pp. 125–130.

Serieys, M., Goma, G., Durand, G. (1978). Design and oxygen transfer potential of a pulsed continuous tubular fermentor. Biotechnology and Bioengineering **20**, 1393–1406. https://doi.org/10.1002/bit.260200906.

Sharma, R. N., Baird, M. H. I. (1978). Solvent extraction of copper in a reciprocating plate column. Canadian Journal of Chemical Engineering **56**, 310–315. https://doi.org/10.1002/cjce.5450560307.

Shaw, J. F., Chang, S. W., Lin, S. C., Wu, T. T., Ju, H. Y., Akoh, C. C., Chang, R. H., Shieh, C. J. (2008). Continuous enzymatic synthesis of biodiesel with Novozym 435. Energy and Fuel **22**, 840–844. https://doi.org/10.1021/ef7005047.

- Shin, H.–Y. Lee, S.–H., Ryu, J–H, Bae, S.–Y. (2012). Biodiesel production from waste lard using supercritical methanol. Journal of Supercritical Fluids **61**, 61–68. https://doi.org/10.1016/j.supflu.2011.09.009.
- Shuit, S. H., Lee, K. T., Kamaruddin, A. H., Yusup, S. (2010). Reactive extraction and in situ esterification of *Jatropha curcas* L. seeds for the production of biodiesel. Fuel **89**, 527–530. https://doi.org/10.1016/j.fuel.2009.07.011.
- Skala, D. U. (1976). Investigation of axial mixing in a Karr column [Ispitivanje aksijalnog mešanja u Karovoj koloni], Master's thesis, University of Belgrade, Faculty of Technology and Metallurgy, Belgrade, Serbia (in Serbian).
- Skala, D. U. (1980). Analysis of the gas-liquid system in a reciprocating plate column [Analiza sistema gas-tečnost u koloni sa vibracionom mešalicom]. Doctoral dissertation, University of Belgrade, Faculty of Technology and Metallurgy, Belgrade, Serbia (in Serbian).
- Skala, D., Mićić, J. (1982). Uticaj raspodele vremena zadržavanja na proračun hemijskih reaktora. Hemijska Industrija **36**, 28, 75, 105, 136, 163.
- Skala, D., Veljković, V. (1987a). Zadržavanje gasa u trofaznoj koloni sa vibracionom mešalicom, *II Jugoslovenski kongres za hemijsko inženjerstvo i procesnu tehniku sa međunarodnim učešćem*, Dubrovnik, Zbornik radova II, 56–59.
- Skala, D., Veljković, V. (1987b). Gas holdup in a Karr reciprocating plate column, 9th International Congress of Chemical and Process Engineering, CHISA, Prague, Czech Republic.
- Skala, D., Veljković, V. (1988). Mass transfer characteristics in a gas-liquid reciprocating plate column. I. Liquid phase volumetric mass transfer coefficient. Canadian Journal of Chemical Engineering **66**, 192–199. https://doi.org/10.1002/cjce.5450660203.
- Skala, D., Veljković, V. (1996). Gas holdup in three-phase reciprocating columns, *Mixed-Flow Hydrodynamics: Advances in Engineering Fluid Mechanics*, Cheremisinoff, N. P., ed., Houston: Gulf Publ. Co., pp. 803-810.
- Skala, D., Veljković, V., Janjić, V., Lazić, M., Banković-Ilić, I. (1993). Gas holdup in a gas-liquid-solid reciprocating plate column. Canadian Journal of Chemical Engineering 71, 817–820. https://doi.org/10.1002/cjce.5450710521.
- Skala, D., Zubović, S., Mićić, J. (1981). Ispitivanje proticanja tečne faze u koloni sa vibracionom mešalicom pri suprotnostrujnom toku gas-tečnost [Investigation of liquid flow in a reciprocating plate column at countercurrent gas-liquid flow]. Glasnik Hemijskog Društva Beograd (Bulletin de la Société Chimique Beograd) **46**, 513–525. JSCS Vol-46 1981.pdf, https://www.shd.org.rs/JSCS/Start.html.
- Smith, K. H., Browser, T., Stevens, G. W. (2008). Performance and scale-up of Karr reciprocating plate extraction columns. Industrial and Engineering Chemistry Research 47, 8368–8375. https://doi.org/10.1021/ie800581u.

Soufi, M. D., Ghobadian, B., Najafi, G., Mohammad Mousavi, S., Aubin, J. (2017). Optimization of methyl ester production from waste cooking oil in a batch tri-orifice oscillatory baffled reactor. Fuel Process Technology **167**, 641. https://doi.org/10.1016/j.fuproc.2017.07.030.

Sovova, H. (1990). Countercurrent pulsed and reciprocating plate extractors. Prediction of Sauter mean drop diameter. Collection of Czechoslovak Chemical Communications 55, 409–425. https://doi.org/10.1135/cccc19900409.

Stamenković, I. (2005). The influence of the rheological properties of the liquid phase on the gas holdup and the pressure variation at the bottom of the reciprocating plate reactor [Uticaj reoloških osobina tečne faze na sadržaj gasa i promenu pritiska na dnu reaktora sa vibracionom mešalicm]. Master's thesis, University of Niš, Faculty of Technology in Leskovac, Niš, Serbia (in Serbian).

Stamenković, I.S. (2014). Continuous homogenously base—catalyzed alcoholysis of vegetable oils in a reciprocating plate reactor [Kontinualna homogena bazno katalizovana alkoholiza biljnih ulja u reaktoru sa vibracionom mešalicom]. Doctoral dissertation, University of Niš, Faculty of Technology in Leskovac, Niš, Serbia (in Serbian).

Stamenković, O. S., Stamenković, I. S., Banković-Ilić, I. B., Lazić, M. L., Veljković, V. B., Skala D. U. (2002). Snaga mešanja njutnovske tečnosti u reaktoru sa vibracionom mešalicom. Procesna tehnika **2–3**, 100–103. https://izdanja.smeits.rs/index.php/procteh/article/view/3542.

Stamenković, I. S., Stamenković, O. S., Banković-Ilić, I. B., Lazić, M. L., Veljković, V. B., Skala D. U. (2004). The pressure variation at the bottom of a reciprocating plate bioreactor filled with non-Newtonian liquids, *16th International Congress of Chemical and Process Engineering, CHISA*, 22–26. August, Prague, Czech Republic. CD-ROM of Full Texts 0763.pdf

Stamenković, I. S., Stamenković, O. S., Banković-Ilić, I. B., Lazić, M., Veljković, V., Skala, D. (2005). The gas holdup in a multiphase reciprocating plate column filled with carboxymethylcellulose solutions. Journal of the Serbian Chemical Society 70 1533–1544. https://doi.org/10.2298/JSC0512533S.

Stamenković, O. S., Lazić, M. L., Todorović, Z. B., Veljković, V. B., Skala, D. U. (2007). The effect of agitation intensity on alkali-catalyzed methanolysis of sunflower oil. Bioresource Technol **98**, 2688–2699. https://doi.org/10.1016/j.biortech.2006.09.024.

Stamenković, O. S., Todorović, Z. B., Lazić, M. L., Veljković, V. B., Skala, D. U. (2008). Kinetics of sunflower oil methanolysis at low temperatures. Bioresource Technology **99**, 1131–1140. https://doi.org/10.1016/j.biortech.2007.02.028.

Stamenković, I. S., Banković-Ilić, I. B., Jovanić, P. B., Veljković, V. B., Skala, D. (2010a). Hydrodynamics of a cocurrent upflow liquid-liquid reciprocating plate

reactor for homogeneously base-catalyzed methanolysis of vegetable oils. Fuel **89**, 3971–3984. http://www.doi:10.1016/j.fuel.2010.06.026.

Stamenković, I., Stamenković, O., Todorović, Z., Banković Ilić, I., Lazić, M., Veljković, V., Skala, D. (2010b). A continuous process of sunflower oil ethanolysis in a reciprocating plate reactor [Kontinualni proces etanolize suncokretovog ulja u reaktoru sa vibracionom mešalicom], II konferencija "Održivi razvoj i klimatske promene" SUSTAINNIS 2010, CD ROM str. 291–295. Niš, Srbija, 13–15. September 2010.

Stamenković, I., Stamenković, O., Todorović, Z., Banković Ilić, I., Lazić, M., Veljković, V., Skala, D., (2010c). Pilot plant for production of fatty acid methyl esters from vegetable oils [Poluindustrijsko postrojenje za dobijanje metil estara masnih kiselina iz biljnih ulja]. II konferencija "Održivi razvoj i klimatske promene" SUSTAINNIS 2010, CD ROM str. 180–184. Niš, Srbija, 13–15. September 2010.

Stamenković, O. S., Veličković, A. V., Veljković, V. B. (2011). The production of biodiesel from vegetable oils by ethanolysis: Current state and perspectives. Fuel **90**, 3141–3155. https://doi.org/10.1016/j.fuel.2011.06.049.

Stamenković, I., Stamenković, O., Banković-Ilić, I., Todorović, Z., Lazić, M., Veljković, V., Skala, D. (2013). Production of fatty acid esters by continuous alcoholysis of vegetable oils [Dobijanje estara masnih kiselina postupkom alkoholize biljnih ulja]. RS 52398, Intellectual Property Gazette (Glasnik intelektualne svojine). 1, 51 (in Serbian). https://www.zis.gov.rs/wp-content/uploads/GIS 2013 1.pdf

Stavarache, C., Vinatoru, M. Y., Maeda, H., Bandow, H. (2007). Ultrasonically driven continuous process for vegetable oil transesterification. Ultrasonic Sonochemistry **14**, 413–417. https://doi.org/10.1016/j.ultsonch.2006.09.014.

Stegeman, D., Knop, P. A., Wijnands, A. J. G., Westerterp, K. R. (1996). Interfacial area and gas holdup in a bubble column reactor at elevated pressures, Industrial and Engineering Chemistry Research **35**, 3842–3847. https://doi.org/10.1021/ie960325h.

Stella, A., Pratt, H. R. C., Mensforth, K. H., Stevens, G. W., Bowser, T. (2006). Backmixing in Karr reciprocating-plate extraction columns. Industrial and Engineering Chemistry Research 45, 6555–6562. https://doi.org/10.1021/ie060390j.

Stella, A., Mensforth, K. H., Bowser, T., Stevens, G. W., Pratt, H. R. C. (2008). Mass transfer performance in Karr reciprocating plate extraction columns. Industrial and Engineering Chemistry Research 47, 3996–4007. https://doi.org/10.1021/ie071623p.

Stephens, G. G., Mackley, M. R. (2002). Heat transfer performance for batch oscillatory flow mixing, Experimental Thermal and Fluid Science **25**, 583–594. https://doi.org/10.1016/S0894-1777(01)00098-X

Stevanović, R., Pavasović, V., Simonović, D., Nemoda, S. (1980). The study of pressure variations at the bottom of a vibrating plate extraction column, Proceedings

- of the 2nd Yugoslav-Italian-Austrian Chemical Engineering Conference, (Levec, J., ed.), September 15-18, Bled, Ljubljana, pp. 186-197.
- Stevens, G. W., Baird, M. H. I. (1990). A model for axial mixing in reciprocating plate columns. Chemical Engineering Science **45**, 457–465. https://doi.org/10.1016/0009-2509(90)87032-N.
- Stojković, I. J., Banković–Ilić, I. B., Veličković, A. V., Avramović, J. M., Stamenković, O. S., Povrenović, D. S., Veljković, V. B. (2016a). Waste lard methanolysis catalyzed by potassium hydroxide at moderate temperatures. Chemical Engineering and Technology **39**, 741–750. https://doi.org/10.1002/ceat.201400705.
- Stojković, I. J., Miladinović, M. R., Stamenković, O. S., Banković–Ilić, I. B., Povrenović, D. S., Veljković, V. B. (2016b). Biodiesel production by methanolysis of waste lard from piglet roasting over quicklime. Fuel **182**, 454–466. https://doi.org/10.1016/j.fuel.2016.06.014.
- Sundaresan, A., Varma, Y. B. G. (1990a). Dispersed phase holdup and bubble size distributions in gas-liquid cocurrent upflow and countercurrent flow in reciprocating plate column. Canadian Journal of Chemical Engineering **68**, 560–568. https://doi.org/10.1002/cjce.5450680405.
- Sundaresan, A., Varma, Y. B. G. (1990b). Interfacial area and mass transfer in gasliquid cocurrent upflow and countercurrent flow in reciprocating plate column. Canadian Journal of Chemical Engineering **68**, 951–958. https://doi.org/10.1002/cjce.5450680610.
- Sater, V. E., Levenspiel, O. (1966). Two-phase flow in packed beds. Evaluation of axial dispersion and holdup by moment analysis. Industrial & Engineering Chemistry Fundamentals 5, 1, 86-92. https://doi.org/10.1021/i160017a015
- Syam, A. M., Yunus, R., Ghazi, T. I. M., Choong, T. S. Y. (2012). Synthesis of Jatropha curcas oil-based biodiesel in a pulsed loop reactor. Industrial Crops and Products **37**, 514–519. https://doi.org/10.1016/j.indcrop.2011.07.030.
- Taki, K., Hosseinzadeh Samani, B., Rostami, S., Besharati, S. (2022). Design and fabrication of smooth periodic constriction reactor to biodiesel production from waste cooking oil. Biofuels **13**, 1007–1013. https://doi.org/10.1080/17597269.2022. 2062976.
- Taki, K., Hosseinzadeh Samani, B., Rostami, S., Besharati, S. (2023). Combination of oscillatory and hydrodynamic system for biodiesel production from sunflower oil. Biofuels **14**, 235–242. https://doi.org/10.1080/17597269.2022.2130510.
- Taki, K., Hosseinzadeh Samani, B., Anasari Ard**ali**, A. (2024). Unleashing the power of plasma and flow: A novel cold plasma-oscillatory system for enhanced continuous biodiesel production from sunflower oil. Energy Technology **12**, 2301164. https://doi.org/10.1002/ente.202301164.

- Tang, Z., Wang, L., Yang, J. (2008). Transesterification of rapeseed oil catalyzed by liquid organic amine in supercritical methanol in a continuous tubular-flow reactor. European Journal of Lipid Science and Technology **110**, 747–753. https://doi.org/10.1002/ejlt.200700256.
- Thornton, J. D. (1957). Liquid-Liquid Extraction. Part XIII: The effect of pulse wave form and plate geometry on the performance and throughput of a pulsed column. Transactions of the American Institute of Chemical Engineers (London) **35**, 316–330.
- Todorović, Z. B., Stamenković, O. S., Stamenković, I. S., Avramović, J. M., Veličković, A. V., Banković-Ilić, I. B., Veljković, V. B. (2013). The effects of cosolvent on homogeneously and heterogeneously base-catalyzed methanolysis of sunflower oil. Fuel **107**, 493–502. https://doi.org/10.1016/j.fuel.2012.11.049.
- Todorović, Z. B., Troter, D. Z., Đokić-Stojanović, D. R., Veličković, A. V., Avramović, J. M., Stamenković, O. S., Veselinović, Lj. M., Veljković, V. B. (2019). Optimization of CaO-catalyzed sunflower oil methanolysis with crude biodiesel as a cosolvent. Fuel **237**, 903–910. https://doi.org/10.1016/j.fuel.2018.10.056
- Tojo, K., Miyanami, K., Yano, T. (1974a). Gas holdup and pressure drop in multistage vibrating disc column with cocurrent gas-liquid flow. Journal of Chemical Engineering of JapanJpn. 7, 123–126. https://doi.org/10.1252/jcej.7.123.
- Tojo, K., Miyanami, K., Yano, T. (1974b). Mass transfer in multistage vibrating disc column with cocurrent gas-liquid flow. Journal of Chemical Engineering of Japan 7, 126–130. https://doi.org/10.1252/jcej.7.126.
- Tojo, K., Miyanami, K., Yano, T. (1979). Power dissipation in a vibrating disc column. Chemical Engineering Journal 17, 211–218. https://doi.org/10.1016/0300-9467(79)85015-7.
- Trentin, C. M., Lima, A. P., Alkimim, I. P., Silva, C., de Castilhos, F., Mazutti, M. A., Oliveira, J. V. (2011a). Continuous production of soybean biodiesel with compressed ethanol in a microtube reactor using carbon dioxide as co-solvent. Fuel Process Technology 92, 952–958. https://doi.org/10.1016/j.fuproc.2010.12.016.
- Trentin, C. M., Lima, A. P., Alkimim, I. P., Silva, C., de Castilhos, F., Mazutti, M. A., Oliveira, J. V. (2011b). Continuous catalyst-free production of fatty acid ethyl esters from soybean oil in microtube reactor using supercritical carbon dioxide as co-solvent. Journal of Supercritical Fluids 56, 283–291. https://doi.org/10.1016/j.supflu.2010.10.037.
- Van Dierendonck, L. L., Fortuin, M. H., Venderbos, D. (1971). The specific contact area in gas-liquid reactors. *4th Europ. Symp. Chem. Reaction Engineering*, Brussels, 1968, Pergamon Press, pp. 205-215.
- Van Dijck, W. J. D. (1935). Tower with internal perforated suitable for extracting liquids by treatment with other liquids and for similar cocurrent processes. US Patent 2, 011, 186.

Vasić, Lj. S. (2006). Oxygen mass transfer rate as a criterion for scaling up a reciprocating plate column [Brzina prenosa mase kiseonika kao kriterijum za povećanje razmere kolone sa vibracionom mešalicom]. Master's thesis, University of Niš, Faculty of Technology in Leskovac, Niš, Serbia (in Serbian).

Vasić, Lj., Banković-Ilić, I., Lazić, M., Veljković, V., Skala, D. (2005a). The effects of operating conditions on the pressure variation at the bottom of a 16.6 cm i.d. reciprocating plate column. Chemical Industry and Chemical Engineering Quarterly 11, 195–202. https://doi.org/10.2298/CICEQ0504195V.

Vasić, Lj., Banković-Ilić, I., Lazić, M., Veljković, V., Skala, D. (2005b). Gas-holdup in a 16.6 cm I.D. reciprocating plate column. Hemijska Industrija **59**, 263–266. https://doi.org/10.2298/HEMIND0510263V.

Vasić, Lj., Banković-Ilić, I., Lazić, M., Veljković, V., Skala, D. (2006a). The power consumption in a 16,6 cm i.d. multiphase reciprocating plate column filled with nonnewtonian liquids [Snaga mešanja nenjutnovskih tečnosti u višefaznoj koloni sa vibracionim mešanjem prečnika 16,6 cm]. *19. Međunarodni kongres o procesnoj industriji, Procesing 2006*, Beograd, 14-16. Jun 2006., Zbornik rezimea radova 17, 35 [Zbornik Međunarodnog kongresa o procesnoj industriji – Procesing, [S.l.], 19(1), 2024. https://izdanja.smeits.rs/index.php/ptk/article/view/7633].

Vasić, Lj., Banković-Ilić, I., Lazić, M., Veljković, V., Skala, D. (2006b). The gas hold-up in a 16.6 cm i.d. multiphase reciprocating plate column. 5th International Conference of the Chemical Societies of the South-East European Countries, Book of Abstracts, 1, 238, Ohrid, September 10–14, 2006.

Vasić, Lj., Banković-Ilić, I., Lazić, M., Veljković, V., Skala, D. (2007). Oxygen mass transfer in a 16.6 i.d. multiphase reciprocating plate column. Journal of the Serbian Chemical Society **72**, 523–531. https://doi.org/10.2298/JSC0705523V.

Veljković, V. (1985). The study of hydrodynamic and mass-transfer characteristics of different reactors and selection of the optimal type for dextransucrose biosynthesis [Ispitivanje hidrodinamičkih i maseno-prenosnih karakteristika različitih reaktora i izbor optimalnog tipa za biosintezu dekstran-saharaze]. Doctoral dissertation, Faculty of Technology and Metallurgy, University of Belgrade, Belgrade, Serbia (in Serbian).

Veljković, V. (1994). Osnovi biohemijskog inženjerstva. Tehnološki fakultet, Leskovac [Fundamentals of Biochemical Engineering, Faculty of Technology, Leskovac, Serbia] (in Serbian).

Veljković, V. B. (2014). Comment on "Study of fuel properties of rubber seed oil based biodiesel" [Energy Convers Manage 2014;78:266–75] by Ahmad et al. Energy Conversion and Management **86**, 1186–1188. https://doi.org/10.1016/j.enconman. 2014.05.048.

Veljković, V., Skala, D. (1985). Influence of different liquid flow models on the determination of oxygen mass transfer in a reciprocating plate column. Journal of the Serbian Chemical Society **50**, 427–434.

Veljković, V., Skala, D. (1986). Hydrodynamic investigation of gas-liquid contacting in a reciprocating plate column. Canadian Journal of Chemical Engineering **64**, 906–914. https://doi.org/10.1002/cjce.5450640604.

Veljković, V., Skala, D. (1988). Mass transfer characteristics in a gas-liquid reciprocating plate column. II. Interfacial area. Canadian Journal of Chemical Engineering **66**, 200–210. https://doi.org/10.1002/cjce.5450660204.

Veljković, V., Skala, D. (1989). On the possibility of general prediction of gas holdup in reciprocating plate column. Canadian Journal of Chemical Engineering **67**, 1015–1018.https://doi.org/10.1002/cjce.5450670622.

Veljković, V. B., Lazić, M. L., Rutić, D. J., Jovanović, S. M., Skala, D. U. (1990). Selection of a bioreactor and the optimal aerobic conditions for dextransucrase fermentation by *Leuconostoc mesenteroides*. Journal of the Serbian Chemical Society **35**, 483–490.

Veljković, V., Banković-Ilić, I., Lazić, M., Skala, D. (1996). Gas holdup in threephase reciprocating plate columns, *12th International Congress of Chemical and Process Engineering*, *CHISA*, Prague, Czech Republic, P3.90

Veljković, V. B., Avramović, J. M., Stamenković, O. S. (2012). Biodiesel production by ultrasound-assisted transesterification: State of the art and the perspectives. Renewable and Sustainable Energy Reviews **16**, 1193–209. https://doi.org/10.1016/j.rser.2011.11.022.

Veljković, V. B., Banković-Ilić, I., Skala, D. (2024). Reciprocating plate column – fundamental research and application in Serbia from 1970 to 2020: Review paper. Hemijska Industrija (Chemical Industry) 78, 197-203. https://doi.org/10.2298/HEMIND2303200.

Vicente, G., Martinez, M., Aracil, J. (2004). Integrated biodiesel production: A comparison of different homogenous catalysts system. Bioresource Technology **92**, 297–305. https://doi.org/10.1016/j.biortech.2003.08.014.

Vicente, G., Martinez, M., Aracil, J., Esteban, A. (2005). Kinetics of sunflower oil methanolysis. Industrial and Engineering Chemistry Research 44, 5447–5454. https://doi.org/10.1021/ie040208j.

Vicente, G., Martinez, M., Aracil, J., Esteban, A. (2006) Kinetics of *Brassica carinata* oil methanolysis. Energy Fuel **20**, 1722–1726. https://doi.org/10.1021/ef060047r.

Vogelpohl, A. (1985). Biologische Reinigung von Abwässern mit dem Kompaktraktor. Chemische Industrie (Düsseldorf) **37**, 43–46.

- Weiland, P., Onken, U. (1981). Fluid dynamics and mass transfer in an airlift fermenter with external loop. German Chemical Engineering 4, 42–50.
- Wen, Z., Yu, X., Tu, S.–T., Yan, J., Dahlquist, E. (2009). Intensification of biodiesel synthesis using zigzag micro-channel reactors. Bioresource Technology **100**, 3054–3060. https://doi.org/10.1016/j.biortech.2009.01.022.
- Wu, P., Yang, Y., Colucci, J. A., Grulke, E. A. (2007). Effect of ultrasonication on droplet size in biodiesel mixtures. Journal of the American Oil Chemists' Society **84**, 877–884. https://doi.org/10.1007/s11746-007-1114-9.
- Wu, Y., Vovers, J., Lu, H. T., Li, W., Stevens, G. W., Mumford, K. A. (2022). Investigation of the extraction of natural alkaloids in Karr reciprocating plate columns: Fluid dynamic study. Chemical Engineering Science **264**, 118090. https://doi.org/10.1016/j.ces.2022.118090
- Yang, N. S., Shen, Z. Q., Chen, B. H., McMillan, A. F. (1986a). Pressure drop, gas holdup and interfacial area for gas-liquid contact in Karr columns. Industrial and Engineering Chemistry Process Design **25**, 660–664. https://doi.org/10.1021/i200034a011.
- Yang, N. S., Shen, Z. Q., Chen, B. H., McMillan, A. F. (1986b). Axial mixing and mass transfer in gas-liquid Karr columns. Industrial and Engineering Chemistry Process Design **25**, 776–780. https://doi.org/10.1021/i200034a031.
- Yoshida, Y., Muira, Y. (1963). Gas absorption in agitated gas-liquid contactors. Industrial and Engineering Chemistry Process Design **2**, 263–268. https://doi.org/10.1021/i260008a002.
- Yu, X., Wen, Z., Lin, Y., Tu, S.–T., Wang, Z., Yan, J. (2010). Intensification of biodiesel synthesis using metal foam reactors. Fuel **89**, 3450–3456. https://doi.org/10.1016/j.fuel.2010.06.011.
- Yung, K. K. L., Smith, C. D., Bowser, T., Perera, J. P., Stevens, G. W. (2012). The use of an ionic liquid in a Karr reciprocating plate extraction column. Chemical engineering research and design **90**, 2034–2040. https://doi.org/doi:10.1016/j.cherd. 2012.03.006
- Yung, K. K. L., Smith, C. D., Bowser, T., Perera, J. P., Stevens, G. W. (2012). The use of an ionic liquid in a Karr reciprocating plate extraction column: Dispersed phase hold-up prediction. Separation Science and Technology 47, 346–353 https://doi.org/doi:10.1080/01496395.2011.593604
- Yung, K. K. L., Smith, C. D., Bowser, T., Perera, J. P., Stevens, G. W. (2012). The use of an ionic liquid in a Karr reciprocating plate extraction column: Drop size distribution. Separation Science and Technology 47, 1733–1739. http://dx.doi.org/10.1080/01496395.2012.681000

Zhao, H., Baker, G. A. (2013). Ionic liquids and deep eutectic solvents for biodiesel synthesis: a review. Journal of Chemical Technology and Biotechnology **88**, 3–12. https://doi.org/10.1002/jctb.3935.

Zheng, M., Sketon, R. L., Mackley, M. R. (2007). Biodiesel reaction screening using oscillatory flow meso reactors. Process Safety and Environmental Protection **85**,365–371. https://doi.org/10.1205/psep07030.

Živković, S. B., Veljković, M. V., Banković–Ilić, I. B., Krstić, I. M., Konstantinović, S. S., Ilić, S. B., Avramović, J. M., Stamenković, O. S., Veljković, V. B. (2017). Technological, technical, economic, environmental, social, human health risk, toxicological and policy considerations of biodiesel production and use. Renewable and Sustainable Energy Reviews **79**, 222–247. https://doi.org/10.1016/j.rser.2017. 05.048.

List of Tables

- Table 1.1 Types of reciprocating plate columns (Banković-Ilić et al., 2009).
- Table 1.2 Application of reciprocating plate columns.
- Table 1.3 Overview of previous research related to the reciprocating plate column.
- Table 4.1 Theoretical correlations for the pressure variation at the bottom of pulsation and reciprocating plate columns.
- Table 4.2 Empirical correlations for the pressure variation at the column bottom of reciprocating plate columns.
- Table 4.3 Physical properties of liquids (20 °C) used in the hydrodynamic research in reciprocating plate columns.
- Table 5.1 Review of theoretical equations for the calculation of power consumption in pulsed and reciprocating columns.
- Table 5.2 Empirical correlations for the power consumption of reciprocating plate columns.
- Table 6.1 Influence of the system geometry on the mean plate opening coefficient.
- Table 6.2 The plate opening coefficient calculated by Equations (6.2), (6.3), and (6.6) for single-phase systems (Banković-Ilić et al., 1997).
- Table 7.1 Empirical correlations for the dispersed phase holdup in pulsation and vibration devices.
- Table 7.2 Physical properties of CMC solution (Naseva et al., 2002).
- Table 8.1 Empirical correlations for Sauter and mean bubble diameters in reciprocating (vibrating) devices.
- Table 9.1 Models and methods of calculating flow model parameters in reciprocating plate columns.
- Table 9.2 Empirical correlations for the axial dispersion coefficient in reciprocating plate columns.
- Table 10.1 Correlations for volumetric oxygen mass transfer coefficient.
- Table 11.1 Correlations for the specific interfacial area in reciprocating plate columns.
- Table 12.1 Correlations for mass transfer coefficient.
- Table 13.1 Major characteristics, advantages, and drawbacks of oscillatory reactors.
- Table 13.2 Continuous reciprocating plate column and oscillatory flow reactors for biodiesel production.
- Table 13.3 Physical properties of the liquid phase (Stamenković et al., 2010a).
- Table 13.4 Parameters of correlations for time-averaged and maximum pressure variations at the reactor bottom, Equation (13.4) (Stamenković et al., 2010a).
- Table 13.5. Parameters of correlations for time-averaged and maximum power consumption, Equation (13.4) (Stamenković et al., 2010a).
- Table 13.6. A review of continuous transesterification processes using cosolvents.

- Table 13.7. The values of the volumetric mass transfer coefficient for the heterogeneous (mass transfer controlled) regime and the rate constants for the pseudo-homogeneous (chemical reaction controlled) regime (Banković-Ilić et al., 2015).
- Table 13.8. Ratios of reaction rate constants for methanolysis of vegetable oils in the presence and the absence of tetrahydrofuran (Banković-Ilić et al., 2015).
- Table 13.9. ANOVA results for the response surface reduced cubic model (Miladinović et al., 2019).
- Table 13.10 Comparison of various reactor and catalyst types for biodiesel production from various feedstocks with methanol.
- Table 13.11 Main geometrical parameters of oscillatory flow reactor design.

List of Figures

- Figure 1.1 Types of reciprocating plate column plates (Lo et al., 1992): (a) Karr type, (b) Procházka type, (c) Karpacheva and Gorodetsky type without the drain on plates KRIMZ, and (d) Karpacheva and Gorodetsky with the drain on plates GIAP.
- Figure 1.2 Types of reciprocating plate column (Baird et al., 1994): KRPC Karr-type reciprocating plate column, PRPC Procházka-type reciprocating plate column, and VDC vibrating disc column.
- Figure 2.1 Characteristic fluid flow between two adjacent perforated plates in a single-phase system in a reciprocating plate column (Brauer, 1991): (a) upwards motion of plates and (b) downwards motion of plates.
- Figure 2.2 Photographs of the gas-liquid dispersion in a reciprocating plate column with the countercurrent gas-liquid flow: (a) A = 0.65 cm, f = 1.17 Hz, (b) A = 0.65 cm, f = 6.17 Hz, (c) A = 2.00 cm, f = 1.17 Hz, and (d) A = 2.00 cm, f = 6.17 Hz ($D_c = 2.54$ cm, $n_p = 65$, $d_o = 0.8$ cm, cm, $\varepsilon = 51\%$, $u_g = 0.823$ cm/s, and $u_l = 0.443$ cm/s).
- Figure 3.1 Scheme of the transmission mechanism (Banković-Ilić, 1993).
- Figure 4.1 The momentum balance for the controlled volumes in a batch reciprocating plate column (Banković-Ilić, 1993): (a) an entire column with the reciprocating plate stack and (b) a column part comprising the liquid surrounding a reciprocating plate.
- Figure 4.2 A typical instantaneous pressure variation at the column bottom Δp for a non-gassed system (water, A = 2.35 cm, and f = 2.5 s⁻¹).
- Figure 4.3 Dependence of the total and mean pressure variation at the column bottom filled with "pure" liquids on the reciprocating intensity: $D_c = 2.54$ cm (Δp^* open symbols and $\Delta p_{\rm av}$ black symbols; water circles, glycerol triangles, 0.5% n-butanol squares, 0.8 M Na₂SO₄ rhombuses, 1% CMC stars, and 2% CMC— crosses) (Banković-Ilić, 1999).
- Figure 4.4 Dependence of the total and mean pressure variation at the column bottom filled with "pure" liquids on the reciprocating intensity: $D_{\rm c} = 9.2$ cm (Δp^* open symbols and $\Delta p_{\rm av}$ black symbols; water circles, glycerol triangles, 0.5% n-butanol squares, 0.8 M Na_SO₄ rhombuses, 1% CMC stars, and 2% CMC crosses) (Banković-Ilić, 1999).
- Figure 4.5 Dependence of the total (open symbols) and mean (close symbols) pressure variation at the column bottom filled with "pure" liquids on the reciprocating intensity: $D_c = 16.6$ cm, water circle, 0.5% CMC triangle, and 1.0% CMC square (Vasić et al., 2005a).
- Figure 4.6 Effect of the superficial gas velocity on the total (black symbols) and mean (open symbols) pressure variation at the column bottom (distilled water: u_g (cm/s): 0.5

- squares and 1.5 triangles; aqueous CMC solution: u_g (cm/s): 0.5 circles and 1.5 inverted triangles) (Aleksić et al., 2002a)
- Figure 4.7 Dependence of the mean pressure variation at the column bottom on the reciprocating intensity for two-phase (liquid-solid) systems: (a) distilled water and (b) aqueous 1% CMC solution (ε_s , %: $0 \square$, $0.35 \circ$, 0.87Δ , 1.74∇ , and $3.2 \Diamond$ (Aleksić et al., 2002a).
- Figure 4.8 Effect of the superficial gas velocity on the pressure variation at the column bottom (spheres open symbols and Rashig rings black symbols; u_g cm/s: 0.5 squares and 1.5 triangles) (Aleksić et al., 2002a).
- Figure 4.9 Influence of the properties of the liquid phase on the total and mean pressure variation at the column bottom with a two-phase (liquid-solid) system: (a) $D_c = 2.54$ cm and $\varepsilon_s = 6.6\%$ and (b) $D_c = 9.2$ cm and $\varepsilon_s = 3.8\%$ (Δp^* open symbols and $\Delta p_{\rm av}$ black symbols; water circles, 64% glycerol triangles, 0.5% n-butanol squares, 0.8 M Na₂SO₄ rhombuses, 1% CMC stars, and 2% CMC crosses) (Banković-Ilić, 1999).
- Figure 5.1 The influence of reciprocating intensity on the mean and total power consumption of 'pure' liquids (P_{av} open symbols and P^* black symbols; distilled water squares and aqueous CMC solution circles) (Aleksić et al., 2003).
- Figure 5.2 Dependence of the power number of 'pure' liquids on the Reynolds number: 1) $D_c = 14.96 \text{ cm}, \ \varepsilon = 0.12 \oplus \text{ and } \varepsilon = 0.53 +: \text{ water (Hafez and Baird, 1978); 2)}$ $D_c = 10.2 \text{ cm}, \ \varepsilon = 0.28 \text{: water} \bullet \text{ and } 100\% \text{ glycerol} \blacktriangle \text{ (Lounes and Thibault, 1993); and 3)}$ $D_c = 2.54 \text{ cm}, \ \varepsilon = 0.51 \text{: water} \odot, 64\% \text{ glycerol} \Box, 1\% \text{ CMC} \Theta, \text{ and } 2\% \text{ CMC} \Theta; D_c = 9.2 \text{ cm}, \ \varepsilon = 0.45 \text{: water} \odot, 100\% \text{ glycerol} \Delta, 69\% \text{ glycerol} \lozenge, 64\% \text{ glycerol} \Box, 40\% \text{ glycerol} \blacktriangledown, 1\% \text{ CMC} *, \text{ and } 2\% \text{ CMC} \times \text{ (Banković-Ilić, 1999)}.$
- Figure 5.3 Influence of the degree of polymerization and solution concentration on the total (open symbols) and mean (black symbols) power consumption of 'pure' liquids (liquid: aqueous carboxymethylcellulose solutions; PP 50: 0.5% circles, 1% triangles, and 2% squares; PP 200: 0.5% rhombuses, 1% inverted triangles, and 2% +; PP 500: 0.5% crosses and 1% stars; and PP 1000: 0.5% dashes and 1% up dashes) (Naseva, 2002).
- Figure 5.4 Dependence of corrected total and mean power consumption of two-phase (gas-liquid) systems on reciprocating intensity at a constant superficial gas velocity: a) $D_c = 2.54$ cm and b) $D_c = 9.2$ cm (liquid: water; P^* open symbols and $P_{\rm av}$ black symbols; single-phase system dashed line, $u_{\rm g}$ cm/s: 0.5 squares, 1.0 triangles, 1.5 squares, and 3.0 –stars (Banković-Ilić, 1999).
- Figure 5.5 Dependence of mean and total power consumption of two-phase (liquid-solid) systems on reciprocating intensity ($D_c = 9.2$ cm): (a) distilled water and (b) aqueous 1% CMC solution (ε_s , % vol.: 0 squares; 0.35 circles; 0.87 triangles; 1.74 inverted triangles, and 3.2 rhombuses; P^* black symbols and P_{av} open symbols) (Aleksić et al., 2003).

- Figure 5.6 Effect of a solid phase (spheres: 8.3 mm) on the total and mean power consumption (liquid: 0.5 % CMC solution; $D_{\rm c} = 9.2$ cm; $u_{\rm g}$, cm/s: 0.5 cm/s; liquid-solid system squares; three-phase system: $\varepsilon_{\rm s}$, %: 3.84 circles; 6.61 triangles; P^* open symbols and $P_{\rm av}$ black symbols) (Stamenković et al., 2002).
- Figure 5.7 Effect of superficial gas velocity on the power consumption of three-phase systems (distilled water; Rashig rings (0.8 cm): 3.2%; D_c : 9.2 cm; P^* black symbols and $P_{\rm av}$ open symbols; $u_{\rm g}$, cm/s: 0.5 squares, 1.0 triangles, and 1.5 rhombuses; 1% CMC solution: $u_{\rm g}$, cm/s: 0.5 circles, 1.0 inverted triangles, and 1.5 stars) (Aleksić et al., 2003).
- Figure 5.8 The influence of the number of spheres (spheres: 8.3 mm) in the interplate space on the total power consumption of a three-phase system (liquid: water; D_c : 2.54 cm; $u_g = 0.5$ cm/s: 5 spheres per interplate space $-\circ$, 5 spheres per second interplate space $-\Delta$, 5 spheres per third interplate space $-\Box$, and 10 spheres per second interplate space $-\Box$; $u_g = 1.5$ cm/s: 5 spheres per second interplate space $-\times$) (Banković-Ilić, 1999).
- Figure 5.9 The influence of the type of solid particles ($D_c = 9.2$ cm; spheres: 8.3 mm, ε_s : 3.8 vol.% open symbols; and Rashig rings: 8×8 mm, ε_s : 3.2 vol.% black symbols) on the total power consumption of three-phase systems as a function of the reciprocating intensity at different superficial gas velocities: (liquid: distilled water; u_g , cm/s: 0.5 squares, 1.0 circles, and 1.5 triangles) (Aleksić et al., 2003).
- Figure 6.1 Changes in the vibrating plate velocity, the pressure at the column bottom, and the square of the plate opening coefficient with time during one cycle of reciprocating motion (liquid: distilled water; $D_c = 9.2 \text{ cm}$; f = 5.9 Hz; Δ_P and C_o^2 : solid line recorded signal, and dashed line processed signal) (Banković-Ilić et al., 1997).
- Figure 6.2 Comparison of plate opening coefficients determined based on the processed and recorded pressure signals at the column bottom: (a) gas-liquid and (b) liquid (D_c , cm: 2.54 black symbols, and 9.2 open symbols; water circles, 0.5% n-butanol triangles, 0.8M sodium sulfite squares, 40% glycerol +, 64% glycerol inverted triangles, 100% glycerol *, 1% CMC rhombuses, and 2% CMC + squares and × squares, respectively; adapted from Banković-Ilić et al., 1997).
- Figure 6.3 Comparison of the value of the plate opening coefficient calculated based on Equations (6.4) and (6.6) for the laminar regime of the liquid flow (symbols the same as in Figure 6.2) (Banković-Ilić et al., 1997).
- Figure 6.4 The influence of reciprocating intensity on the plate opening coefficient for (a) Newtonian liquids of low and medium viscosity and (b) highly viscous Newtonian and non-Newtonian liquids (symbols as in Figure 6.2) (Banković-Ilić et al., 1997).

- Figure 6.5 Dependence of the plate opening coefficient calculated based on the processed pressure signal on the Reynolds number (symbols same as in Figure 6.2; Lounes and Thibault, 1993: water ⊙ and glycerol □) (Banković-Ilić et al., 1997).
- Figure 6.6 The dependence of the plate opening coefficient calculated from the mean pressure variation at the column bottom on the reciprocating intensity ($D_c = 9.2$ cm; u_g , cm/s: 0.5 open symbols, 1.0 black symbols, and 1.5 bullet symbols; water circles, 64% glycerol triangles, and 1% CMC squares) (Banković-Ilić et al., 1997).
- Figure 6.7 Dependence of the mean plate opening coefficient, calculated based on the slope of the linear part of the log $[\Delta p/(1-\varepsilon_g)]$ versus log (Af) relationship, on the superficial gas velocity (symbols the same as in Figure 6.2) (Banković-Ilić et al., 1997).
- Figure 6.8 Dependence of the mean plate opening coefficient on the Reynolds number in two-phase (liquid-solid phase: water circles and 64% glycerol tringles) and three-phase (gas-liquid-solid: water squares and 64% glycerol rhombuses; u_g , cm/s: 0.5) systems ($D_c = 2.54$ cm; ε_s %: 6.6 open symbols and 3.8 black symbols) (Banković-Ilić, 1999).
- Figure 6.9 Dependence of the mean plate opening coefficient on the Reynolds number in two-phase (liquid-solid) and three-phase (gas-liquid-solid) systems ($D_c = 9.2$ cm; symbols as in Figure 6.8) (Banković-Ilić, 1999).
- Figure 7.1 Dependence of gas holdup on reciprocating intensity: (a) $D_c = 2.54$ cm, (b) $D_c = 9.2$ cm (Banković-Ilić, 1999), and (c) $D_c = 16.6$ cm (Vasić, 2005) (liquid: water; ε_s , %: 0 lines [u_g , cm/s: 0 - -, 0.5 ----, and 1.5 —], 3.8 black symbols, and 6.6 open symbols; u_g , cm/s: 0.5 circles, 1.0 triangles, and 1.5 squares).
- Figure 7.2 The influence of the free surface of the plate on the gas holdup of the two-phase systems: a) distilled water and b) 1% CMC solution (ε , %: 45,4; u_g , cm/s: 0,5 \blacksquare , 1,0 \bullet , and 1,5 \blacktriangle ; ε , %: 31,9; u_g , cm/s: 0,5 \blacktriangledown , 1,0 \bullet , and 1,5 *; ε , %: 26,3; u_g , cm/s: 0,5 \square ; 1,0 \circ , and 1.5 Δ) (Aleksić, 2006).
- Figure 7.3 Influence of the fraction of Rashig rings on the gas holdup: u_g , cm/s: a) 0.5, b) 1.0, and c) 1.5 (*Af*, cm/s: 0.045 circles, 0.06 triangles, 0.08 squares, 0.1 rhombuses, and 0.12 inverted triangles) (Aleksić et al., 2002b).
- Figure 7.4 The effect of the size of Rashig rings on the gas holdup (distilled water; ε , %: 45.4; ε _s, % vol.: 2.66; diameter of Rashig rings, mm: 8 open symbols and 12 black symbols; u_g, cm/s: 0.5 squares, 1.0 circles, and 1.5 triangles) (Banković-Ilić et al., 2004b).
- Figure 7.5 Comparison of the effect of solid particles on the gas holdup (distilled water; ε , %: 45.4; u_g , cm/s: 0.5 squares, 1.0 circles, and 1.5 triangles; Rashig rings with a diameter of 8 mm: black symbols; ε_s , % vol.: 3.20; spheres with a diameter of 8.3 mm: open symbols; ε_s , % vol.: 3.80) (Aleksić, 2006).
- Figure 7.6 Effect of CMC (PP 200) concentration on gas holdup of two-phase and threephase systems at $u_g = 0.5$ cm/s (ε_s , %: 0 – circles, 3.84 – triangles, and 6.61 –

- squares; CMC, %: 0.5 open symbols and 1.0 black symbols; adapted from Naseva et al., 2002).
- Figure 7.7 Effect of CMC concentration (PP 1000) on the gas holdup of two-phase and three-phase systems at (a) $u_g = 0.5$ cm/s and (b) $u_g = 1.5$ cm/s (ε_s , %: 0 circles, 3.84 triangles, and 6.61 squares; CMC, %: 0.5 open symbols and 1.0 black symbols) (Naseva et al., 2002).
- Figure 7.8 The influence of the degree of polymerization of the CMC solution on the gas holdup of two-phase and three-phase systems at $u_g = 1$ cm/s: a) 0.5 % CMC and b) 1.0 % CMC (ε_s , %: 0 circles and 3.84 triangles; CMC: PP 200 open symbols and PP 1000 black symbols) (Naseva et al., 2002).
- Figure 7.9 Dependence of the gas holdup on the specific power consumption (u_g , cm/s: 0.5 circle, 1.0 triangle, and 1.5 square): D_c = 2.54 cm black symbols; D_c = 9.2 cm open symbols (Banković-Ilić, 1999); and D_c = 9.2 cm crossed out symbols (Vasić et al., 2005b).
- Figure 7.10 Comparison of gas holdup in different reactors (system: gas-liquid) (Banković-Ilić, 1999): RPC1 D_c = 2.54 cm (Banković-Ilić, 1999), RPC2 D_c = 9.2 cm (Banković-Ilić, 1999), BC (Stegeman et al., 1996), ALCDT (Al-Masry and Dukkan, 1998), ALELC (Gavrilescu et al., 1998), and ST stirred tank (Gagnon et al., 1998).
- Figure 8.1 Effect of agitation on bubble size (Experiments symbols; Equation (8.1) lines; D_c , cm: 9.2 open symbols and 2.54 black symbols; water circles, solid line, 64% glycerol triangles, solid line, 0.5% n-butanol squares, dotted line, and 0.8M Na₂SO₄ rhombuses, dashed line) (Banković-Ilić, 1999).
- Figure 8.2 Dependence of the Sauter bubble diameter on reciprocating intensity (liquid: water; D_c , cm: 2.54 black symbols and 9.2 open symbols; ug, cm/s: 0.5 circles, 1.0 triangles, and 1.5 squares) (Banković-Ilić, 1999).
- Figure 8.3 The effect of liquid properties on bubble size in a gassed reciprocating plate column ($D_c = 9.2$ cm) filled with (a) water, (b) 64% glycerol, (c) 0.8 M Na₂SO₄, and (d) 0.5% *n*-butanol ($f \approx 3 \text{ s}^{-1}$, $u_g = 0.5 \text{ cm/s}$).
- Figure 8.4 Bubble size distribution histograms: (a) $u_g = 0.5$ cm/s and f = 3 s⁻¹, (b) $u_g = 0.5$ cm/s, and f = 4.9 s⁻¹, and (c) $u_g = 1$ cm/s and f = 4 s⁻¹ ($D_c = 2.54$ cm; liquid: water) (Banković-Ilić, 1999).
- Figure 8.5 Bubble size distribution histograms: (a) 64% glycerol, $f = 1.8 \text{ s}^{-1}$, (b) 0.5% n-butanol, $f = 2.1 \text{ s}^{-1}$, and (c) 0.8M Na₂SO₄, $f = 2.2 \text{ s}^{-1}$ ($D_c = 2.54 \text{ cm}$; $u_g = 0.5 \text{ cm/s}$) (Banković-Ilić, 1999).
- Figure 8.6 Bubble size distribution histograms: (a) $f = 2.3 \text{ s}^{-1}$ and (b) $f = 3.7 \text{ s}^{-1}$ ($D_c = 9.2 \text{ cm}$; $u_g = 0.5 \text{ cm/s}$; liquid: water) (Banković-Ilić, 1999).
- Figure 8.7 Bubble size distribution histograms: $(u_g = 1.5 \text{ cm/s})$: (a) $f = 0 \text{ s}^{-1}$ and (b) $f = 3.2 \text{ s}^{-1}$ ($D_c = 9.2 \text{ cm}$; liquid: water) (Banković-Ilić, 1999).
- Figure 8.8 Bubble size distribution histograms: (a) 64% glycerol: $f = 2.4 \text{ s}^{-1}$, (b) 0.8 M Na₂SO₄: $f = 2 \text{ s}^{-1}$, and (c) 1% CMC: $f = 1.9 \text{ s}^{-1}$ ($D_c = 9.2 \text{ cm}$; $u_g = 0.5 \text{ cm/s}$) (Banković-Ilić, 1999).

- Figure 9.1 Comparison of the axial dispersion coefficient of different multiphase devices: dependence of the axial dispersion coefficient on (a) reciprocating intensity, (b) superficial liquid velocity, and (c) superficial gas velocity: reciprocating plate column: 1) $D_c = 2.54$ cm (Nikolić et al., 2004); 2) $D_c = 2.54$ cm (Skala, 1980); 3) $D_c = 9.2$ cm (Nikolić, 2003); 4) $D_c = 9.3$ cm (Parthasarathy et al., 1984); 5) $D_c = 10.2$ cm (Lounes and Thibault., 1996); packed column (Rashg rings): 6) $D_c = 5.1$ cm (Michel and Furzer, 1972); 7) $D_c = 10.2$ cm (Sater and Levenspel, 1966); and bubble column: 8) $D_c = 1.97$ cm (Cova, 1974); 9) $D_c = 4$ cm (Ohki and Inoue, 1970); 10) $D_c = 6.6$ cm (Kato and Nishiwaki, 1972); 11) $D_c = 9.2$ cm (Baird and Rice, 1975).
- Figure 10.1 Dependence of the volumetric oxygen mass transfer coefficient on reciprocating intensity (gas-liquid system dashed line; gas-liquid-solid system solid line): (a) $D_c = 2.54$ cm (Skala and Veljković, 1988), (b) $D_c = 9.2$ cm (Banković-Ilić, 1999), (c) $D_c = 16.6$ cm (Vasić, 2005): (liquid: 0.8 M Na₂SO₄, ε_s , %: 0.5 *, 0.5 *, 0.5 *, and 0.5 +; 0.5 *, 0.5 circles, 0.5 triangles, and 0.5 squares).
- Figure 10.2 Comparison of the volumetric oxygen mass transfer coefficient in different devices for the gas-liquid system (Banković-Ilić, 1999): RPC1 D_c = 2.54 cm (Veljković, 1985); RPC2 D_c = 9.2 cm (Banković-Ilić, 1999); RPC3 D_c = 9.3 cm (Sundaresan and Varma, 1990a); RPC4 D_c = 5.08 cm (Yang et al., 1986); BC and ALCDT (Al-Masry and Dukkan, 1998; Petrović, 1989); ALELC (Weiland and Onken, 1981); ST1 (Bouaifi and Roustan, 1998); and ST2 (Chavarria-Hernandez et al., 1996).
- Figure 10.3 Comparison of volumetric oxygen mass transfer coefficient in different devices for the gas-liquid-solid phase system: RPC1 D_c = 2.54 cm (Banković-Ilić, 1999); RPC2 D_c = 9.2 cm (Banković-Ilić, 1999); BKKC (Petrović, 1989); BKSR (Pošarac, 1988); and SM (Roman and Tudose, 1997).
- Figure 10.4 Comparison of volumetric mass transfer coefficient in Karr-type reciprocating plate columns of different geometries for the gas-liquid system: RPC1 D_c = 16.6 cm (Vasić et al., 2007); RPC2 D_c = 9.2 cm (Banković Ilić, 1999); RPC3 D_c = 2.54 cm (Veljković, 1985); RPC4 (Rama Rao and Baird, 2003); RPC5 (Gagnon et al., 1998); RPC6 (Baird and Rama Rao., 1988); RPC7 (Lounes et al., 1995); and RPC8 (Lounes and Thibault., 1994).
- Figure 10.5 Comparison of the volumetric mass transfer coefficient in reciprocating plate columns of different geometries: $D_c = 2.54$ cm (RPC1) (Skala and Veljković, 1988) and $D_c = 9.2$ cm (RPC2) (Banković-Ilić, 1999).
- Figure 10.6 The influence of the shape of solid particles on the volume coefficient of oxygen mass transfer (spheres with a diameter of 8.3 mm; ε_s , % vol.: 3.80; open symbols; u_g ; cm/s: 0.5 squares, 1.0 circles and 1.5 triangles (Banković-Ilić, 1999); Rashig rings with a diameter of 8 mm; ε_s , % vol.: 3.20; black symbols; u_g ; cm/s: 0.5 square, 1.0 circle and 1.5 triangle (Aleksić, 2006).

- Figure 11.1 Dependence of the specific interfacial area on the reciprocating intensity: (a) D_c = 2.54 cm and (b) D_c = 9.2 cm (liquid: 0.8 M sodium sulfite, ε_s , %: 0, u_g , cm/s: 0 *, $0.5 \times$, and 1.5 +; ε_s , %: 3.8 open symbols, and 6.6 black symbols, u_g , cm/s: 0.5 circles, 1.0 triangles, and 1.5 squares) (Banković-Ilić (1999).
- Figure 11.2 Dependence of gas holdup, Sauter bubble diameter, and specific interfacial area on Morton's number (*Z*) ($D_c = 2.54$ cm, u_g , cm/s: 0.5; *Af*, cm/s: 5.2 open symbols and 7.1 black symbols) (Banković-Ilić, 1999).
- Figure 11.3 Comparison of the specific interfacial area in reciprocating plate columns of different geometry: $D_c = 2.54$ cm (RPC1) and $D_c = 9.2$ cm (RPC2); gas-liquid system open area and gas-liquid-solid system solid area (Banković-Ilić, 1999).
- Figure 11.4 Comparison of the specific interfacial area of different reactors for gas-liquid systems (Banković-Ilić, 1999): RPC1 D_c = 2.54 cm (Skala, 1980), RPC2 D_c = 9.2 cm (Banković-Ilić, 1999), RPC3 (Yang et al., 1986a), RPC4 (Gooma et al., 1991), BC (Stegeman et al., 1996), ALELC (Ghirardini et al., 1992), and ST (Bouaifi and Roustan, 1998).
- Figure 12.1 Comparison of the mass transfer coefficient in the liquid film in different devices for the gas-liquid system (adapted from Banković-Ilić, 1999): RPC1 D_c = 2.54 cm (Veljković and Skala, 1986), RPC2 D_c = 9.2 cm (Banković-Ilić, 1999), RPC3 (Baird and Rama Rao, 1988), PBC pulsed bubble column (Baird and Garstang, 1972), VDC vibration disc column (Mianami et al., 1978), and ST (Miller, 1974).
- Figure 13.1 Pressure variation at the reactor bottom (a) and power consumption (b) as a function of reciprocating intensity under batch or single-phase conditions (sunflower oil; 30°C; batch reactor; *A*, cm: 1.0 circle and 2.35 triangle; single-phase flow reactor; *A*, cm: 1.0 square and 2.35 diamond; time-averaged pressure variation and power consumption: open symbols; maximum pressure variation and power consumption: black symbols) (Stamenković et al., 2010a).
- Figure 13.2 Pressure variation at the reactor bottom (a) and power consumption (b) as a function of reciprocating intensity under two-phase co-current flow conditions (A, cm: 1.0 and 2.35; sunflower-methanol molar ratio, 1:3: 20 °C circles, and 30 °C up triangles; sunflower-methanol molar ratio, 1:6: 20 °C squares, and 30 °C diamonds; time-averaged pressure variation and power consumption: open symbols; maximum pressure variation and power consumption: black symbols) (Stamenković et al., 2010a).
- Figure 13.3 The dependences of $\frac{\Delta p_{\rm av}}{\rho_e}$, $\frac{\Delta p^*}{\rho_e}$, $\frac{P_{\rm av}}{\rho_e}$ or $\frac{P^*}{\rho_e}$ on the reciprocating intensity (batch conditions: circles; single phase flow: triangles; and two-phase flow: squares; time-averaged pressure variation and power consumption: open symbols, and total pressure variation and power consumption: black symbols; Equation (15) for batch and single phase flow: solid lines, and Equation (15)

for two-phase flow: dashed lines) (Stamenković et al., 2010a).

- Figure 13.4 The power number as a function of the reciprocation Reynolds number (present study: sunflower oil, batch circles, sunflower oil, single phase flow up triangles, and sunflower oil-methanol, concurrent flow squares; water, batch diamonds; and a 64% aqueous solution of glycerol, batch down triangles) (Stamenković et al., 2010a).
- Figure 13.5 The plate opening coefficient as a function of the reciprocation Reynolds number (present study: sunflower oil, batch circles, and single-phase flow up triangles; water, batch squares, and 64% glycerol, batch diamonds; A, cm: 1.0 open symbols, and 2.35 black symbols) (Stamenković et al., 2010a).
- Figure 13.6 Dispersed phase hold-up as a function of the reciprocating intensity (methanol/oil molar ratio; 3:1 circles, and 6:1 triangles; temperature: 20 °C open symbols, and 30 °C black symbols) (Stamenković et al., 2010a).
- Figure 13.7 Sauter-mean drop diameter along the reactor at (a) A = 1.0 cm and 20 °C, (b) A = 1.0 cm and 30 °C, (c) A = 2.35 cm and 20 °C, and (d) A = 2.35 cm and 30 °C (frequency, Hz: 2.0 circles, 3.0 triangles, and 4.0 squares; methanol/oil molar ratio: 3:1 open symbols, and 6:1 black symbols) (Stamenković et al., 2010a).
- Figure 13.8 Sauter-mean drop diameter (a) at $h/h_0 = 0.162$ (a) and (b) in the upper zone of the reactor as a function of the reciprocating intensity (methanol/oil molar ratio; 3:1 circles, and 6:1 triangles; temperature: 20 °C open symbols, and 30 °C black symbols) (Stamenković et al., 2010a).
- Figure 13.9 Dependence of Sauter-mean drop diameter on time-averaged power consumption (positions along the reactor higher than $h/h_0 = 0.162$) (Stamenković et al., 2010a).
- Figure 13.10 Drop size distribution in non-reactive systems for oil-to-methanol molar ratios of 1:3 (a, c, and e) and 1:6 (b, d, and f) at reciprocation frequencies of 2 Hz (a and b), 3 Hz (c and d) and 4 Hz (e and f) (A = 1.0 cm; h/h_0 : 0.162 circles, 0.478 triangles, and 0.876 squares; temperature, °C: 20 open symbols, and 30 black symbols) (Stamenković et al., 2010a).
- Figure 13.11 Photographs of the dispersion in the non-reactive (a, c and e) and reactive (b and d) systems along the reactor height h/h_0 : 0.162 (a and b), 0.318 (c and d), and 0.876 (e) (A = 1 cm; f = 2.0 Hz; temperature, °C: 30; and methanol/sunflower oil molar ratio: 6:1) (Stamenković et al., 2010a).
- Figure 13.12 Sauter-mean drop diameter along the reactor at 20 °C and methanol/oil molar ratio of (a) 3:1 and (b) 6:1, as well as at 30 °C and methanol/oil molar ratio of (c) 3:1 and (d) 6:1 (A = 1.0 cm; f, Hz: 2.0 circles and 3.0 triangles; system without reaction open symbols, and system with reaction black symbols) (Stamenković et al., 2010a).
- Figure 13.13 Drop size distribution in reactive systems for oil-to-methanol molar ratios of 1:3 (a) and 1:6 (b) at the reciprocation frequency of 2.0 Hz (1% potassium hydroxide based on the oil weight; A = 1.0 cm; h/h_0 : 0.162 circles, and 0.318

- triangles; temperature, °C: 20 open symbols, and 30 black symbols) (Stamenković et al., 2010a).
- Figure 13.14 Drop size distribution in reactive systems for the oil-to-methanol molar ratio of 1:6 at the temperature of 20 °C (h/h_o : 0.162 circles, and 0.318 triangles; A = 1.0 cm; f, Hz: 2.0 open symbols, and 3.0 black symbols) (Stamenković et al., 2010a).
- Figure 13.15 The specific interfacial area as a function of the reciprocating intensity at methanol/oil molar ratios of 3:1 (circles) and 6:1 (triangles) (Stamenković et al., 2010a).
- Figure 13.16 The effect of reciprocation frequency and amplitude on the methyl ester content at different reaction temperatures and methanol/oil molar ratios: a) 20 °C and 3:1, b) 20 °C and 6:1, c) 30 °C and 3:1, and d) 30 °C 6:1 (2 Hz circles and 3 Hz triangles; and A = 1 cm open symbols: and A = 2.35 cm black symbols; $D_c = 2.54$ cm, $n_p = 63$, and 1% potassium hydroxide) (adapted from Stamenković, 2014).
- Figure 13.17 The effects of (a) reciprocation frequency at a residence time of 13 min (3 Hz − and 4 Hz − ∘) and (b) residence time at a reciprocation frequency of 3 Hz (6.5 min − ∘ and 13 min − •) on the ethyl ester content along the reciprocating plate reactor (6:1 methanol/oil molar ratio, 1% NaOH, and 30 °C) (Stamenković et al., 2010b).
- Figure 13.18 The effect of the reaction temperature on the ethyl ester content along the reciprocating plate reactor (6:1 methanol/oil molar ratio, 1% sodium hydroxide, and 3 Hz): 30 °C − •, 50 °C − ▲, and 70 °C − ■) (Stamenković et al., 2010b).
- Figure 13.19 Schematic representation of a two-stage biodiesel production plant: 1 Tank for catalyst solution preparation, 2 Catalyst solution tank, 3 Vegetable oil tank, 4 and 6 Peristaltic pumps for catalyst solution transport, 5 Peristaltic pumps for oil transport, 7 Peristaltic pumps for oil-ester phase transport, 6 Oil and alcohol preheater, 8 and 9 Reciprocating plate reactors, 10 and 11 Gravity separators, 12 Ester tank, and 13 Glycerol-alcohol phase tank (Stamenković et al., 2013).
- Figure 13.20 Schematic representation of the pilot plant: 1 reciprocating plate reactor, 2 electric motor, 3 tank for catalyst preparation, 4 tank for catalyst solution in methanol, 5 tank for vegetable oil, 6 pumps for transporting vegetable oil and catalyst solution in methanol, 7 heater, 8 gravity separator, 9 glycerolalcohol phase tank and 10 ester phase tank (Stamenković et al., 2010c).
- Figure 13.21 The comparison between Sauter-mean drop diameter in non-reactive (open symbols) and reactive (black symbols) systems at different tetrahydrofuran concentrations (0% o, 1% Δ, 10% □, and 30 % ◊) (Banković-Ilić et al., 2015).

- Figure 13.22 The photographs of the dispersion in the non-reactive systems with 1% tetrahydrofuran along the reactor, h/h_0 : a) 0.24, b) 0.52, c) 0.7, and d) 0.91 (Banković-Ilić et al., 2015).
- Figure 13.23 The photographs of the dispersion in the reactive systems with tetrahydrofuran 1% along the reactor, h/h_0 : a) 0.24, b) 0.52, c) 0.7, and d) 0.91 (Banković-Ilić et al., 2015).
- Figure 13.24 Drop size distribution in non-reactive systems at different tetrahydrofuran concentrations: a) 0%, b) 1%, c) 10%, and d) 30% (h/h_0 : 0.24 o, 0.44 Δ , 0.7 ∇ , and 0.91 *) (Banković-Ilić et al., 2015).
- Figure 13.25 Drop size distribution in the reactive system for different tetrahydrofuran concentrations: a) 0%, b) 1%, and c) 10 % (h/h_0 : 0.24 o, 0.32 Δ , 0.44 ∇ , and 0.52 *) (Banković-Ilić et al., 2015).
- Figure 13.26 The variation of the fatty acid methyl ester concentration along the reactor height for two residence times (13 min open symbols, and 26 min black symbols) at different tetrahydrofuran concentrations (0% o, 1% Δ, 10% □, and 30 % ◊) (Banković-Ilić et al., 2015).
- Figure 13.27 The kinetic models of triacylglycerol methanolysis (straight lines) at different tetrahydrofuran concentrations: a) 0%, b) 1%, c) 10%, and d) 30% (experimental data: mass transfer o; irreversible second-order reaction •; and reverse second-order reaction *) (Banković-Ilić et al., 2015).
- Figure 13.28 The comparison of the triacylglycerol conversion degree calculated by the kinetic model (lines) with the experimental data (symbols) for different tetrahydrofuran concentrations (0% − 0, 1% − Δ, 10% − □, and 30 % − ◊ and *; mass transfer-controlled region: open symbols and straight lines; irreversible second-order reaction: black symbols and dash lines; and a reversible second-order reaction: stars and dot line) (Banković-Ilić et al., 2015).
- Figure 13.29 Response (a) surface and (b) contour plots for fatty acid methyl ester content as a function of methanol/lard molar ratio and catalyst loading at $h/h_0 = 1.00$ (the reduced cubic model) (Miladinović et al., 2019).
- Figure 13.30 The linear dependence of $-\ln(1-x_A)$ on the normalized reactor height at different methanol/lard molar ratios: a) 4.5:1, b) 6.0:1, and c) 7.5:1 (catalyst loading, % of waste lard: 0.50- circles, 0.75- triangles and 1.00- squares; mass transfer-controlled regime: open symbols and chemical reaction-controlled regime: black symbols) (Miladinović et al., 2019).
- Figure 13.31 Dependence of apparent reaction rate constant on the catalyst concentration for different methanol/lard molar ratios: 4.5:1 −●, 6.0:1 − ▲, and 7.5:1 − ■) (Miladinović et al., 2019).
- Figure 13.32 The linear dependences of $k_{\rm m}/c_{\rm B0}$ (\bullet) and $K/c_{\rm B0}$ (\blacksquare) on the catalyst concentration for all methanol/lard molar ratios ($R^2=0.95$ and 0.98, respectively).
- Figure 13.33 The variation of c_{B0} with catalyst concentration at various methanol/lard molar ratios: $4.5:1 \bullet$, $6.0:1 \blacktriangle$, and $7.5:1 \blacksquare$.

- Figure 13.34 Comparison of experimental and predicted values of triacylglycerols (black symbols) and fatty acid methyl esters (open symbols) concentration calculated by two correlations describing the triacylglycerol mass transfer and chemical reaction rates at different methanol/lard molar ratios (a) 4.5:1, (b) 6.0:1 and (c) 7.5:1 (simulation: triacylglycerols solid lines, fatty acid methyl esters dash lines; catalyst loadings, % of waste lard: 0.5 circles, 0.75 triangles and 1.0 squares).
- Figure 13.35 Comparison of experimental and predicted values of triacylglycerols and fatty acid methyl ester concentration calculated by kinetic model for overall reaction at different methanol/lard molar ratios: (a) 4.5:1, (b) 6.0:1, and (c) 7.5:1 (simulation: triacylglycerols solid lines, fatty acid methyl esters dash lines; catalyst loadings, % of waste lard: 0.5 circles, 0.75 triangles and 1.0 squares).
- Figure 13.36 Oscillatory flow reactor with the most commonly used sharp-edged orifice baffles: oscillatory flow is superimposed on bulk flow by a piston (Harvey et al., 2003).
- Figure 13.37 Eddy formation in a continuous oscillatory flow reactor equipped with orifice baffles (McDonough et al., 2015).
- Figure 13.38 Different baffled geometries of oscillatory flow reactors (Avilaa et al., 2022).

